

Electronic Thesis and Dissertation Repository

8-19-2021 10:30 AM

Hydrogen Production Via Photocatalytic Water Splitting Under Near-UV and Visible Light Using Doped Pd TiO₂

Bianca Rusinque, *The University of Western Ontario*

Supervisor: de Lasa, Hugo, *The University of Western Ontario*

A thesis submitted in partial fulfillment of the requirements for the Doctor of Philosophy degree in Chemical and Biochemical Engineering

© Bianca Rusinque 2021

Follow this and additional works at: <https://ir.lib.uwo.ca/etd>

 Part of the [Catalysis and Reaction Engineering Commons](#)

Recommended Citation

Rusinque, Bianca, "Hydrogen Production Via Photocatalytic Water Splitting Under Near-UV and Visible Light Using Doped Pd TiO₂" (2021). *Electronic Thesis and Dissertation Repository*. 8053.
<https://ir.lib.uwo.ca/etd/8053>

This Dissertation/Thesis is brought to you for free and open access by Scholarship@Western. It has been accepted for inclusion in Electronic Thesis and Dissertation Repository by an authorized administrator of Scholarship@Western. For more information, please contact wlsadmin@uwo.ca.

Abstract

The present PhD thesis reports the modification of titanium dioxide (TiO₂) with palladium (Pd), to enhance hydrogen production via water splitting, using 2.0v/v% ethanol as a scavenger. Titanium dioxide was used as photocatalyst, given its ability to absorb photons, producing e⁻/h⁺ pairs. Mesoporous TiO₂ was synthesized using a soft template, following the sol-gel method, to modify its morphological properties. Palladium was used as co-catalyst doping TiO₂ agent, narrowing the band gaps down to 2.51 eV, and creating additional active metal sites.

Water splitting experiments under near-UV and visible light irradiation were carried out in the Photo-CREC Water-II Reactor (PCW-II) unit. It allows precise irradiation measurements, for macroscopic irradiation energy balances.

Redox reactions in the PCW-II led to hydrogen production and by-product compounds formation such as methane, ethane, ethylene, acetaldehyde, carbon monoxide, carbon dioxide and hydrogen peroxide. It was found that this redox reaction followed an “*in series-parallel*” network, involving the organic scavenger ethanol. Carbon balances, OH• and H• radical balances were obtained to validate the proposed reaction network. Furthermore, a kinetic model for photocatalytic water splitting for hydrogen production was developed, with the proposed kinetics and the associated kinetic parameters, being validated with experimental data, obtained in PCW-II unit.

Regarding energy efficiencies (QY%), it was observed that the prepared TiO₂-Pd photocatalyst presented a promising QY% based on H• produced of up to 69.4% under near-UV irradiation, and of 17.6% under visible light for hydrogen production.

Keywords

Hydrogen, Palladium, TiO₂, Visible Light, Near UV-Light, Photo-CREC Water-II Reactor, Kinetic Modelling, Quantum Yield.

Summary for Lay Audience

The world community has been working towards the production of alternative energy sources to guarantee a sustainable life on Earth. Researchers have been exploring diverse alternatives in search of a clean and emission-free energy vector that can work as an alternative fuel. Hydrogen has attracted the attention of scientists and governments around the globe, given its great value as energy carrier with net-zero CO₂ emissions when burned.

Photocatalysis is a promising environmentally friendly technology used to produce hydrogen via water splitting. It involves the use of sunlight, which is one of the most inexhaustible and renewable energy sources, to produce highly efficient and low-cost hydrogen. However, the photocatalytic water splitting reaction is not a spontaneous process in nature, it requires a semiconductor material capable of absorbing irradiation and a sacrificial agent such as ethanol, to allow the reaction to occur.

The present PhD thesis reports the modification of the titanium dioxide (TiO₂) photocatalyst with palladium (Pd), in order to produce hydrogen via water splitting using 2.0v/v% ethanol as scavenger. Water splitting experiments under near-UV and visible light irradiation were carried out in the Photo-CREC Water-II Reactor (PCW-II) unit leading to hydrogen production and by-products formation such as methane, ethane, ethylene, acetaldehyde, carbon monoxide, carbon dioxide and hydrogen peroxide.

It was observed that the prepared Pd-TiO₂ photocatalyst presented promising quantum efficiencies under Near UV light of up to 69.4%, and under visible light irradiation of 17.6% towards hydrogen production via water splitting.

Co-Authorship Statement

This PhD thesis encloses materials that are published in peer reviewed journals as listed below:

1. Title: Photocatalytic Hydrogen Production Under Near-UV Using Pd-Doped Mesoporous TiO₂ and Ethanol as Organic Scavenger

Authors: Bianca Rusinque, Salvador Escobedo and Hugo de Lasa

Author contributions: conceptualization, investigation and supervision, H.d.L.; proposed methodology and supervision, S.E.; validation, formal analysis and writing, B.R.

Reference: Rusinque, B.; Escobedo, S.; de Lasa, H. Photocatalytic Hydrogen Production Under Near-UV Using Pd-Doped Mesoporous TiO₂ and Ethanol as Organic Scavenger. *Catalysts* 2019, 9, 33. <https://doi.org/10.3390/catal9010033>

2. Title: Photoreduction of a Pd-Doped Mesoporous TiO₂ Photocatalyst for Hydrogen Production under Visible Light

Authors: Bianca Rusinque, Salvador Escobedo and Hugo de Lasa

Author contributions: conceptualization, investigation and supervision, H.d.L.; proposed methodology and supervision, S.E.; validation, formal analysis and writing, B.R.

Reference: Rusinque, B.; Escobedo, S.; de Lasa, H. Photoreduction of a Pd-Doped Mesoporous TiO₂ Photocatalyst for Hydrogen Production under Visible Light. *Catalysts* 2020, 10, 74. <https://doi.org/10.3390/catal10010074>

3. Title: Hydrogen Production via Pd-TiO₂ Photocatalytic Water Splitting under Near-UV and Visible Light: Analysis of the Reaction Mechanism

Authors: Bianca Rusinque, Salvador Escobedo and Hugo de Lasa

Author contributions: conceptualization, investigation, review, editing, and supervision: H.d.L.; proposed methodology for adsorption constants evaluation, review, editing, and technical co-supervision: S.E.; conceptualization, investigation, methodology for hydrogen peroxide detection, pH analysis, reaction mechanism, components balance, formal analysis, and writing: B.R.

Reference: Rusinque, B.; Escobedo, S.; de Lasa, H. Hydrogen Production via Pd-TiO₂ Photocatalytic Water Splitting under Near-UV and Visible Light: Analysis of the Reaction Mechanism. *Catalysts* 2021, 11, 405. <https://doi.org/10.3390/catal11030405>

Acknowledgments

I thank God for giving me the strength not to despair in difficult times.

I would like to thank my supervisor Dr. Hugo de Lasa, for offering his expertise, knowledge, support and guidance in the development of this work. I am grateful for his helpful comments, suggestions and constructive criticism throughout this entire project. To Dr. Salvador Escobedo for sharing with me his valuable knowledge, for his continuous support, suggestions and collaboration.

My gratitude to my lab coworkers and friends Abdu, Cesar, Cindy, Imtiaz, Jose, Maureen, Nicolas, Samira, Steve and Sandra. Thank you for your friendship, for offering me advice, and supporting me through this entire process. I would like to thank Florencia de Lasa who assisted with the editing of this PhD dissertation.

I am grateful to my family for their advice, motivation and constant support. Thank you to my Mom and Dad and to my two sisters Michelle and Ashly. Thanks for your never-ending encouragement. I could not be more blessed for having you in my life. To my aunt Vilma for always being there for me and for being the best aunt I could have had. To Myriam Delgado and Julian Acosta for opening the doors of your home and family. Eternally grateful to you.

I would like to thank my husband Aidan Collins for being so supportive, for his many constructive suggestions and very interesting discussions. Thanks for being my best friend and company. To my dear friends Jony, Vanessa and Phillip for their company and valuable friendship.

To my grandma who is with me from heaven and who I will always remember, love and carry in my heart.

Table of Contents

Abstract.....	i
Summary for Lay Audience.....	ii
Co-Authorship Statement.....	iii
Acknowledgments.....	iv
Table of Contents.....	v
List of Tables.....	x
List of Figures.....	xiii
List of Appendices.....	xxiii
Nomenclature.....	xxiv
Chapter 1.....	1
1 Introduction.....	1
Chapter 2.....	5
2 Literature Review.....	5
2.1 Hydrogen Production.....	5
2.1.1 Photocatalysis.....	6
2.1.2 Photocatalytic Cycle.....	7
2.1.3 Water Splitting.....	9
2.1.4 Photocatalyst.....	10
2.1.5 Titanium Dioxide (TiO ₂).....	11
2.1.6 Photocatalyst Doping.....	16
2.1.7 Light Source.....	18
2.2 Sacrificial Agent.....	19
2.3 Photocatalytic Reactor.....	19

2.4 Kinetics of H ₂ Production	21
2.5 Quantum Yield (QY)	22
2.6 Conclusions.....	23
2.7 Scope of the Research.....	24
2.7.1 General Objectives.....	24
2.7.2 Specific Objectives	24
Chapter 3.....	25
3 Equipment, Materials, Photocatalyst Synthesis and Experimental Methods.....	25
3.1 Photo-CREC Water-II Reactor	25
3.2 Lamp Characterization.....	27
3.3 Synthesis Methods	30
3.3.1 Sol-gel Method.....	30
3.3.2 Copolymers	33
3.3.3 Photocatalyst Preparation.....	36
3.4 Photocatalytic Experiments	37
3.5 Analytical Techniques	38
3.6 Determination of H ₂ O ₂ Concentrations	39
3.7 pH Measurements	41
3.8 Conclusions.....	41
Chapter 4.....	42
4 Photocatalyst Characterization.....	42
4.1 N ₂ Physisorption	42
4.2 Temperature Programmed Reduction (TPR)	47
4.3 Pulse Hydrogen Chemisorption	49
4.4 X-Ray Diffraction	50
4.5 Band Gap	54

4.6 X-ray Photoelectron Spectroscopy (XPS)	58
4.7 Conclusions.....	62
Chapter 5.....	63
5 Macroscopic Irradiation Energy Balance (MIEB).....	63
5.1 Irradiation and Measurements.....	63
5.2 Macroscopic Irradiation Energy Balance (MIEB).....	65
5.3 Near-UV-Light MIEB.....	67
5.4 Visible light MIEB.....	68
5.5 Conclusions.....	70
Chapter 6.....	71
6 Hydrogen Production Yields and By-Products	71
6.1 Photocatalytic Mechanism	71
6.2 Hydrogen Production	74
6.2.1 Hydrogen Production Under Near-UV Light	75
6.2.2 Effect of Catalyst Concentration on Hydrogen Production	77
6.2.3 Gas Phase By-Products Formed during Photocatalytic Hydrogen Production under Near-UV Light	78
6.3 Hydrogen Production under Visible Light.....	79
6.3.1 Photocatalyst Photoreduction.....	81
6.3.2 By-Product Formation during the Photocatalytic Hydrogen Production under Visible Light in the Gas Phase.....	85
6.3.3 By-Product Formation during the Photocatalytic Hydrogen Production in the Liquid Phase.....	86
6.4 Conclusions.....	89
Chapter 7.....	90
7 Analysis of the Reaction Mechanism, Carbon Element Balance, OH• and H• radicals Balances	90

7.1 Photocatalytic Hydrogen Production under Near-UV Light and Visible Light using 0.25wt% Pd-TiO ₂	90
7.2 By-Product Formation under Near-UV Light and Visible Light using a 0.25wt% Pd-TiO ₂ Photocatalyst	93
7.3 Carbon Element Balance.....	94
7.4 H [•] and OH [•] Radical Balance	96
7.4.1 OH [•] Radical Analysis Including Hydrogen Peroxide	99
7.4.2 Hydrogen Peroxide Formation from OH [•] Radicals	100
7.4.3 Adsorption of Hydrogen Peroxide	101
7.4.4 Effect of the pH on the Photocatalytic Reaction.....	103
7.5 Conclusions.....	107
Chapter 8.....	108
8 Kinetics for Hydrogen Production and Formation of By-Products	108
8.1 Langmuir-Hinshelwood Model.....	108
8.2 Reaction Mechanism for the <i>In Series-Parallel</i> Kinetic Reaction Network.....	111
8.3 L-H Equations Applied to the Proposed <i>In Series-Parallel</i> Reaction Network .	113
8.4 Kinetic Parameters Estimation.....	118
8.4.1 Kinetic Parameters Estimation under Near-UV Light.....	119
8.4.2 Kinetic Parameters Estimation under Visible Light	124
8.5 Conclusions.....	134
Chapter 9.....	135
9 Quantum Yield (QY) Evaluation	135
9.1 Evaluation of Quantum Yields under Near-UV Light.....	135
9.1.1 Effect of Photocatalyst Concentration on Quantum Yields	137
9.2 Evaluation of Quantum Yields under Visible Light	138
9.2.1 Effect of Photoreduction Time on Quantum Yields	141

9.3 Theoretical Quantum Yields	143
9.4 Conclusions.....	144
Chapter 10.....	145
10 Conclusions and Recommendations	145
10.1 Conclusions.....	145
10.2 Recommendations.....	147
Bibliography	148
Appendices.....	165
Curriculum Vitae	174

List of Tables

Table 1 Traditional Hydrogen Production Technologies.....	5
Table 2 Properties of TiO ₂ for Rutile, Anatase and Brookite.	12
Table 3 Rutile, Anatase and Brookite Applications.....	12
Table 4 Metal-Doped TiO ₂ Photocatalysts under Near-UV and Visible Light	17
Table 5 Sacrificial Agents and Hydrogen Evolution Rate when Using 20 vol% Organic Alcohols and Amines.....	19
Table 6 Quantum Yield Definition in terms of OH· Radicals and Photons Absorbed.	22
Table 7 Quantum Yield for Hydrogen Production.	22
Table 8 PCW-II Dimensions.....	27
Table 9 Reported Synthesis of TiO ₂ Nanoparticles via Sol–Gel Method.....	32
Table 10 Surface Area and Pore Diameter Using a Pluronic F-127 Template.....	46
Table 11 Surface Area and Pore Diameter Using Palladium.....	46
Table 12 Chemisorption Analysis: Metal Dispersion.....	50
Table 13 Photocatalyst Crystallite Sizes.....	53
Table 14 Lattice Parameters for TiO ₂ and Pd doped TiO ₂	53
Table 15 Optical Band Gap for a Photocatalyst Modified by Pt and Pd.	57
Table 16 High-Resolution X-Ray Photoelectron Spectroscopy (XPS) Spectra Binding Energies and Peak Areas for the 0.25 wt% Pd–TiO ₂ , Before Photoreduction and After 60 min of Photoreduction Using Near-UV Irradiation.....	60

Table 17 Comparison between High-Resolution X-Ray Photoelectron Spectroscopy (XPS) Spectra Binding Energies and Peak Areas for the 0.25 wt% Pd–TiO ₂ Before and After 24 Hours of Near-UV Light Exposure.....	61
Table 18 Absorbed Photon Rates on TiO ₂ Photocatalysts, at Different Pd Metal Loadings, under Near- UV Light.....	67
Table 19 Rate of Absorbed Photons at a 1.00 g L ⁻¹ Catalyst Concentration under Near-UV Light.....	68
Table 20 Visible Light Absorbed Photon Rates on TiO ₂ Photocatalysts, at Different Metal Loadings, after 1 Hour of Near-UV Irradiation.....	69
Table 21 Rate of Absorbed Photons under Visible Light after 24 h Near-UV Irradiation.	69
Table 22. Net μMoles of H [•] formed and OH [•] consumed, following 6 h of irradiation using the Pd-TiO ₂ -nUV and Pd-TiO ₂ -VIS.	99
Table 23. Cumulative H [•] Formed/Consumed, and OH [•] Consumed Considering H ₂ and Gas Phase By-Products as established in this study.....	101
Table 24. Adsorption Constants for Hydrogen Peroxide.....	103
Table 25. Cumulative H [•] Formed/Consumed and OH [•] Consumed Considering H ₂ O ₂ Formation and Adsorption.....	103
Table 26. Cumulative H [•] Formed/Consumed and Cumulative μmoles of OH [•] Consumed Considering H ₂ O ₂ (formation, adsorption, dissociation), and pH Changes.....	105
Table 27. Adsorption Constants for Ethanol for the 0.25wt% Pd-TiO ₂	110
Table 28. Reaction Rates for the Chemical Species Involved in the Photocatalytic Water Splitting Reaction using Ethanol as an Organic Scavenger.....	118
Table 29. Intrinsic Kinetic Rate Constants for Hydrogen and By-Products under Near-UV light at 2.0%v/v Ethanol. The adsorption constant for ethanol was set to 1.26 mol ⁻¹ L, as shown in Section 8.1.....	123

Table 30. Intrinsic Kinetic Rate Constants for Hydrogen and By-Products under Visible Light at 2% v/v Ethanol.....	128
Table 31. Cross-Correlation Coefficients for Photocatalytic Hydrogen Production via Water Splitting, under Near-UV Light.	129
Table 32. Cross-Correlation Coefficients for Photocatalytic Hydrogen Production via Water Splitting under Visible Light.	129
Table 33. Quantum Yield (%QY) for the Pd–TiO ₂ photocatalyst when using 0.15g/L of TiO ₂ under near-UV irradiation. All reported data are average values of three repeats.	136
Table 34. QYs% for Pd-TiO ₂ Photocatalysts at Different Metal Loadings (0.25, 0.50, 1.00, 2.50, and 5.00 wt%) under: (a) Visible light irradiation only, (b) Using near-UV light for 1hour, followed by visible light irradiation for 5 hours.	139
Table 35. Theoretical Quantum Yields using 0.25% wt Pd – TiO ₂ photocatalyst.....	143

List of Figures

Figure 1 Energy supply in Canada.....	1
Figure 2. Vision for Hydrogen in Canada in 2050.....	2
Figure 3 Comparison Homogeneous and Heterogeneous Photocatalysis.....	7
Figure 4 Photocatalytic Reaction Cycle.....	8
Figure 5 Photocatalytic Reaction Pathway with an Organic Scavenger.....	9
Figure 6 Steps in a Photocatalytic Process when Using Sacrificial Agents.	10
Figure 7 Classification of Porous Materials.....	13
Figure 8 Electronic Band Structure of Insulators, Semiconductors and Metals.	14
Figure 9 Schematic Representation of Conductivity Band Potentials of Different Semiconductors.....	15
Figure 10 Formation of Photogenerated Electron-Hole Pairs and Hydrogen under Near-UV Light.....	16
Figure 11 Schematics of the Photo-CREC Water-II Reactor. Components: (a) Opaque polyethylene tube, (b) Fused silica windows, (c) Flow distributor, (d) Gas sampling port, (e) Jet driving mixing port, (f) Self-driven mixing impeller, (g) Centrifugal pump, (h) Pyrex tube, (i) Draining gas valve, (j) Purging gas injector, and (k) Slurry sampling port.....	21
Figure 12 Schematics Representation of the Photo-CREC Water-II Reactor with a H ₂ Mixing/Storage Tank: (A) partial longitudinal cross-section of the PCW- II unit showing the downflow circulation of the slurry in the annular channel, (B) overall view of PCW-II showing windows, near-UV lamp and recirculation pump (C) hydrogen storage tank with its components, (D) detail of a photocatalyst particle. Notes: (a) The opaque polyethylene is black in colour. However, it has been shown in grey in this figure, for diagrammatic purposes. (b) The diagram shows a near-UV light in the PCW-II. However, a visible light lamp can also be used.	26

Figure 13 Near-UV Lamp Irradiation Spectrum.....	28
Figure 14. Visible Lamp Irradiation Spectrum.	29
Figure 15 Near-UV and Visible Light Lamp Axial Distribution.....	30
Figure 16 Hydrolysis of an Alkoxide Precursor.	31
Figure 17 Condensation of an Alkoxide Precursor.....	31
Figure 18 Schematic Diagram of the Formation of the Synthesized Mesoporous TiO ₂	34
Figure 19 Pluronic F-127 Structure.	35
Figure 20 Schematic Diagram of the Formation of the Synthesized Mesoporous TiO ₂	35
Figure 21 Description of the Four Consecutive Steps Used during Pd-Doped TiO ₂ Photocatalyst Preparation: (a) Ethanol enters the interface between the hydrophilic (PEO) and hydrophobic (PPO) chains and attaches to the hydrophobic core, (b) A hydrophobic block (PPO) is placed in a central location surrounded by the PEO tails forming micelles, (c) The PEO tails become attached to the TiO ₂ , leaving a hybrid outer layer with a dominant TiO ₂ composition, and (d) Calcination for 6 to 8 hours at 500°C of the resulting photocatalyst precursor yields a TiO ₂ with a 3D mesoporous structure.	36
Figure 22. Calibration curve of H ₂ O ₂ measurements by colorimetric method.	40
Figure 23 BET and BJH. Process description.....	43
Figure 24 N ₂ Adsorption-Desorption Isotherms for Mesoporous TiO ₂ at Different Palladium Loadings.....	45
Figure 25 Temperature Programmed Reduction (TPR) of TiO ₂ and 0.25 wt% Pd-TiO ₂	48
Figure 26 X-Ray Diffractograms for Pd-Doped TiO ₂ Photocatalysts. XRDs for A = anatase and Pd = palladium are shown as a reference.	51
Figure 27 Comparative Analysis of 0.25 wt% Pd-TiO ₂ Photocatalysts Before and After Reduction. A = anatase, PdO = palladium oxide and Pd ⁰ = metallic palladium.	52

Figure 28 XRD Diffractograms for the Pd-Doped TiO ₂ After 6h of Photocatalytic Water Splitting. XRD for anatase, rutile and undoped TiO ₂ are reported, as a reference for comparison: A = anatase, R= Rutile, Pd=Palladium.	54
Figure 29 Band Gap Calculation Using the Tauc Plot Method and the Straight Line Extrapolation for the Following Photocatalysts: a) TiO ₂ , b) 0.25wt%Pd- TiO ₂ , c) 0.50wt%Pd-TiO ₂ , d) 1.0wt%Pd- TiO ₂ , e) 2.5wt%Pd-TiO ₂ and f) 5.0wt%Pd-TiO ₂	56
Figure 30 High-Resolution X-Ray Photoelectron Spectroscopy (XPS) Spectra for 0.25 wt% Pd–TiO ₂ : (a) Before near-UV photoreduction and (b) After 1 hour of near-UV photoreduction. Note: Continuous lines represent Pd ⁰ at (i) 3d _{5/2} and (ii) 3d _{3/2} . Broken lines represent PdO at (iii) 3d _{5/2} and (iv) 3d _{3/2}	59
Figure 31 High-Resolution X-Ray Photoelectron Spectroscopy (XPS) Spectra for 0.25 wt% Pd–TiO ₂ Before Near-UV Photoreduction and After 24 Hours of Near-UV Photoreduction.	61
Figure 32 Survey Scan Analysis for 0.25 wt% Pd–TiO ₂	62
Figure 33 Schematic Representation of the 6000 cm ³ Slurry Control Volume Used to Obtain Macroscopic Irradiation Balances.....	63
Figure 34 Photo-CREC Water-II Reactor with Optical Fibre Sensors in Place to Measure Transmitted Radiation.....	64
Figure 35 Macroscopic Irradiation Balance in a TiO ₂ Water Suspension.	65
Figure 36 Hydrogen Reactions Steps using Pd-TiO ₂ as a Photocatalyst and Ethanol as an Organic Scavenger.	72
Figure 37. Cumulative Hydrogen Volume STP (standard temperature and pressure) Obtained Using Pd at Different Metal Loadings (0.25, 1.50, 1.00, 2.50 and 5.00 wt%). Conditions: photocatalyst concentration of 0.15g L ⁻¹ , 2.0 v/v% ethanol, initial pH = 4 ± 0.05 and near-UV light.	76

Figure 38 Cumulative Hydrogen Production Using 0.25wt% Pd-TiO ₂ at Catalyst Concentrations of 0.15 and 1.00 g L ⁻¹ . Conditions: 2.0 v/v% ethanol, initial pH=4 ± 0.05 and near-UV light.	78
Figure 39. Cumulative Amounts of Carbon Dioxide (CO ₂), Methane (CH ₄), Acetaldehyde (C ₂ H ₄ O), Ethane (C ₂ H ₆), and Ethylene (C ₂ H ₄) Obtained Using a 0.25 wt% Pd-TiO ₂ . Conditions: photocatalyst concentration of 0.15 g L ⁻¹ , 2.0 v/v% ethanol, near-UV light irradiation, and argon atmosphere.....	79
Figure 40 Cumulative Hydrogen Volume STP Produced when Using Pd – TiO ₂ at Different Loadings (0.25, 0.50, 1.00, 2.50 and 5.00wt%). Conditions: Photocatalyst concentration: 0.15g L ⁻¹ , 2.0 v/v% ethanol, pH=4 ± 0.05 and visible light.....	80
Figure 41. Schematic Representation of: (a) The synthesized photocatalysts following calcination at 500 °C, with most of the Pd being present as PdO, (b) The photoreduction of the PdO to Pd ⁰ using a near-UV Lamp, (c) The H ₂ production using a photoreduced Pd-TiO ₂ , with molecular H ₂ being generated on the semiconductor.	82
Figure 42 Cumulative Hydrogen Volume Produced at Different 0.25, 0.50, 1.00, 2.50 and 5.00 wt% Pd Loadings on a Photocatalyst Photoreduced with 1 hour Near-UV Light, and Further Exposed to 6 Hours of Visible Light, to Produce Hydrogen. Conditions: Photocatalyst concentration: 0.15g L ⁻¹ , 2.0 v/v% ethanol, initial pH = 4 ± 0.05.	83
Figure 43. Hydrogen Volume Obtained Using Photocatalysts with 0.25wt%Pd Loadings, Photocatalyst photo-reduced with Near-UV Light during 1hour and 24 hours prior to a run with visible light. Conditions: Photocatalyst concentration: 0.15g L ⁻¹ , 2.0 v/v% ethanol, initial pH = 4 ± 0.05.	84
Figure 44 By-Product Changes with Irradiation Time: a) Methane (CH ₄), b) Ethane (C ₂ H ₆), c) Ethylene (C ₂ H ₄), d) Acetaldehyde(C ₂ H ₄ O) and e) Carbon dioxide (CO ₂) at 0.25%w/w Pd-TiO ₂ . 1 hour near-UV light and 6 hours of visible light were used to produce hydrogen. Conditions: Photocatalyst concentration: 0.15g L ⁻¹ , 2.0 v/v% ethanol, initial pH=4 ± 0.05..	85
Figure 45 Ethanol and CO Changes with Irradiation Time. Conditions: Photocatalyst concentration 0.15g L ⁻¹ , at 0.25% w/w Pd-TiO ₂ , 2.0 v/v% ethanol, initial pH=4 ± 0.05, 6 hours	

of visible light. Notes: a) Ethanol and CO concentrations are defined considering ethanol in the liquid phase, and CO in the gas phase, b) Ethanol in the gas phase and CO in the liquid phase are considered negligible in this analysis. 86

Figure 46. Cumulative H₂O₂ Volume Formed as a Function of Irradiation Time, in the Presence of 0.25 wt% Pd-TiO₂, under: a) Near-UV and b) Visible light (1 h photoreduction under Near-UV followed by 5 h of visible light irradiation). Conditions: Photocatalyst concentration 0.15g L⁻¹, 2.0 v/v% ethanol, initial pH=4 ± 0.05. 88

Figure 47. Cumulative Hydrogen Formed Using the 0.25 wt% Pd-TiO₂-near UV. Conditions: photocatalyst concentration: 0.15 g/L, 2.0 v/v% ethanol. 91

Figure 48. Cumulative Hydrogen Formed with a 0.25 wt% Pd-TiO₂-VIS Photocatalyst, which was Photoreduced during 1 h of Near-UV Light Exposure, and then Exposed to 5 h of Visible Light. Conditions: photocatalyst concentration: 0.15 g L⁻¹, scavenger concentration: 2.0 v/v% ethanol. 92

Figure 49. Cumulative Carbon Dioxide (CO₂), Methane (CH₄), Acetaldehyde (C₂H₄O), Ethane (C₂H₆), and Ethylene (C₂H₄) obtained using a 0.25 wt% Pd-TiO₂-nUV. Conditions: photocatalyst concentration of 0.15 g/L, 2.0 v/v% ethanol, near-UV light irradiation, and argon atmosphere. 93

Figure 50. Cumulative Amounts of Carbon Dioxide (CO₂), Methane (CH₄), Acetaldehyde (C₂H₄O), Ethane (C₂H₆), and Ethylene (C₂H₄) Obtained using a 0.25 wt% Pd-TiO₂-VIS. Conditions: combined near-UV irradiation (1h) and visible light irradiation (5 h), photocatalyst concentration of 0.15 g/L, 2.0 v/v% ethanol, and argon atmosphere. 94

Figure 51. Total Elemental Carbon from Carbon Containing Species, at the Beginning of the Reaction and after 6 Hours of Near-UV Irradiation. Conditions: argon atmosphere, 0.25 wt% Pd-TiO₂-nUV photocatalyst, 2.0 v/v% ethanol. SD for repeats: ± 0.2%. 95

Figure 52. Total Carbon in all Carbon Containing Species at the Beginning of the Reaction and after Combined Near-UV Irradiation (1 h) and Visible Light Irradiation (5 h). Conditions: argon atmosphere, 0.25 wt% Pd-TiO₂-VIS photocatalyst, 2.0 v/v% ethanol. SD for repeats: ± 4.6%. 96

Figure 53. Calibration Curve of H ₂ O ₂ Measurements by Colorimetric Method.	100
Figure 54. Cumulative H ₂ O ₂ Formed as a Function of Irradiation Time, using a 0.25 wt% Pd-TiO ₂ -nUV and 0.25 wt% Pd-TiO ₂ -VIS (1 h photoreduction under near-UV followed by 5 h of visible light irradiation). Conditions: argon atmosphere, 0.15 g/L Pd-TiO ₂ photocatalyst, 2.0 v/v% ethanol.	100
Figure 55. (a) Hydrogen Peroxide Adsorption Isotherm on a Pd-TiO ₂ Photocatalyst and (b) Linearized Langmuir Equilibrium Isotherm for Hydrogen Peroxide on Pd-TiO ₂	102
Figure 56. pH Changes with Irradiation time Using a 0.25 wt% Pd-TiO ₂ -nUV and a 0.25 wt% Pd-TiO ₂ -VIS.	104
Figure 57. (a) μ moles of OH [•] and H [•] Radicals Formed after 6 h of Photocatalytic Hydrogen Production under Near-UV Light, and (b) Percentual H [•] and OH [•] μ mole Balances at Different Irradiation Times under Near-UV Light. The 95% confidence and prediction intervals are reported in red and blue, respectively. SD for the repeats: $\pm 0.8\%$	106
Figure 58. (a) μ Moles of OH [•] and H [•] Radicals Formed after 6 h of Photocatalytic Hydrogen Production (1 Hour of Near-UV Light Photoreduction and 5 Hours of Visible Light), and (b) Percentual OH [•] and H [•] Balances at Different Irradiation Times under Visible Light. The 95% confidence and prediction intervals are reported in red and blue, respectively. SD for the repeats: $\pm 2.5\%$	106
Figure 59. Ethanol Adsorbed on 0.25wt% Pd-TiO ₂ Photocatalyst.....	110
Figure 60. Linearized Langmuir Equilibrium Isotherm for Ethanol on 0.25wt% Pd-TiO ₂	110
Figure 61. Cumulative Methane Volume (STP) after 6 Hours of Irradiation. Experimentally observed runs are represented by (○). Model predictions are represented by (—). Experimental conditions: a) near-UV irradiation, b) 0.25wt% Pd-TiO ₂ photocatalyst and 0.15 g L ⁻¹ photocatalyst loading, c) Initial pH = 4.0.	119
Figure 62. Cumulative Ethane Volume (STP) Obtained after 6 Hours of Irradiation. Experimentally observed runs are represented by (○). Model predictions are represented by	

(—). Experimental conditions: a) near-UV irradiation, b) 0.25wt% Pd-TiO₂ photocatalyst and 0.15 g L⁻¹ photocatalyst loading, c) Initial pH = 4.0..... 120

Figure 63. Cumulative Ethylene Volume (STP) Obtained after 6 Hours of Irradiation. Experimentally observed runs are represented by (○). Model predictions are represented by (—). Experimental conditions: a) near-UV irradiation, b) 0.25wt% Pd-TiO₂ photocatalyst and 0.15 g L⁻¹ photocatalyst loading, c) Initial pH = 4.0..... 120

Figure 64. Cumulative Acetaldehyde Volume Obtained after 6 Hours of Irradiation. Experimentally observed runs are represented by (○). Model predictions are represented by (—). Experimental conditions: a) near-UV irradiation, b) 0.25wt% Pd-TiO₂ photocatalyst and 0.15 g L⁻¹ photocatalyst loading, c) Initial pH = 4.0..... 121

Figure 65. Cumulative CO₂ Volume after 6 Hours of Irradiation. Experimentally observed runs are represented by (○). Model predictions are represented by (—). Experimental conditions: a) near-UV irradiation, b) 0.25wt% Pd-TiO₂ photocatalyst and 0.15 g L⁻¹ photocatalyst loading, c) Initial pH = 4.0..... 121

Figure 66. Cumulative Hydrogen Peroxide Volume Obtained after 6 Hours of Irradiation. Experimentally observed runs are represented by (○). Model predictions are represented by (—). Experimental conditions: a) near-UV irradiation, b) 0.25wt% Pd-TiO₂ photocatalyst and 0.15 g L⁻¹ photocatalyst loading, c) Initial pH = 4.0..... 122

Figure 67. Cumulative Hydrogen Volume Obtained after 6 Hours of Irradiation. Experimentally observed runs are represented by (○). Model predictions are represented by (—). Experimental conditions: a) near-UV irradiation, b) 0.25wt% Pd-TiO₂ photocatalyst and 0.15 g L⁻¹ photocatalyst loading, c) Initial pH = 4.0..... 122

Figure 68. Cumulative Methane Volume after 6 hours of Irradiation. Experimentally observed runs are represented by (○). Model predictions are represented by (—). Experimental conditions: a) 0.25wt% Pd-TiO₂ photocatalyst and 0.15 g L⁻¹ photocatalyst loading, b) Initial pH = 4.0, c) 1 hour near-UV light plus 5 hours under visible light..... 124

Figure 69. Cumulative Ethane Volume after 6 Hours of Irradiation. Experimentally observed runs are represented by (○). Model predictions are represented by (—). Experimental

conditions: a) 0.25wt% Pd-TiO₂ photocatalyst and 0.15 g L⁻¹ photocatalyst loading, b) Initial pH = 4.0, c) 1 hour near-UV light plus 5 hours under visible light. 125

Figure 70. Cumulative Ethylene Volume after 6 Hours of Irradiation. Experimentally observed runs are represented by (○). Model predictions are represented by (—). Experimental conditions: a) 0.25wt% Pd-TiO₂ photocatalyst and 0.15 g L⁻¹ photocatalyst loading, b) Initial pH = 4.0, c) 1 hour near-UV light plus 5 hours under visible light. 125

Figure 71. Cumulative Acetaldehyde Volume after 6 Hours of Irradiation. Experimentally observed runs are represented by (○). Model predictions are represented by (—). Experimental conditions: a) 0.25wt% Pd-TiO₂ photocatalyst and 0.15 g L⁻¹ photocatalyst loading, b) Initial pH = 4.0, c) 1 hour near-UV light plus 5 hours under visible light. 126

Figure 72. Cumulative CO₂ Volume after 6 Hours of Irradiation. Experimentally observed runs are represented by (○). Model predictions are represented by (—). Experimental conditions: a) 0.25wt% Pd-TiO₂ photocatalyst and 0.15 g L⁻¹ photocatalyst loading, b) Initial pH = 4.0, c) 1 hour near-UV light plus 5 hours under visible light. 126

Figure 73. Cumulative Hydrogen Peroxide Volume after 6 Hours of Irradiation. Experimentally observed runs are represented by (○). Model predictions are represented by (—). Experimental conditions: a) 0.25wt% Pd-TiO₂ photocatalyst and 0.15 g L⁻¹ photocatalyst loading, b) Initial pH = 4.0, c) 1 hour near-UV light plus 5 hours under visible light. 127

Figure 74. Cumulative Hydrogen Volume after 6 hours of Irradiation. Experimentally observed runs are represented by (○). Model predictions are represented by (—). Experimental conditions: a) 0.25wt% Pd-TiO₂ photocatalyst and 0.15 g L⁻¹ photocatalyst loading, b) Initial pH = 4.0, c) 1 hour near-UV light plus 5 hours under visible light. 127

Figure 75. Reconciliation Plot for Predicted and Experimentally Observed Volumes at STP for CO₂, H₂O₂, CH₄, C₂H₄O, C₂H₆, C₂H₄, and H₂. Notes: a) Species Volumes: 0 to 113 cm³ STP, b) Species Volumes: 0 to 1.8 cm³, and c) Species Volumes: 0 to 0.0022 cm³ STP. Conditions: 0.25wt% Pd-TiO₂ photocatalyst, Near-UV Light irradiation and Experimental error: ±5.8% Legends: Blue: Methane, Red: Ethane, Yellow: Acetaldehyde, Black: Carbon Dioxide, Violet: Hydrogen Peroxide, Orange: Ethylene and, Green: Hydrogen. 130

Figure 76. Reconciliation Plot for Predicted and Experimentally Observed Volumes at STP for CO₂, H₂O₂, CH₄, C₂H₄O, C₂H₆, C₂H₄, and H₂. Notes: a) Species Volumes: 0 to 10 cm³ STP, b) Species Volumes: 0 to 0.5 cm³, and c) Species Volumes: 0 to 0.0022 cm³ STP. Conditions: 0.25wt% Pd-TiO₂ photocatalyst, Visible Light irradiation and Experimental error: ±15% Legends: Blue: Methane, Red: Ethane, Yellow: Acetaldehyde, Black: Carbon Dioxide, Violet: Hydrogen Peroxide, Orange: Ethylene and, Green: Hydrogen..... 131

Figure 77. Residuals Plot for the Photocatalytic Hydrogen Generation 0.25wt% Pd-TiO₂ under Near-UV Light. Notes: a) Residual volumes between 0 to 113 cm³ STP, and b) Residual volumes between 0 and 1.8 cm³ at STP. Legends: Blue: Methane, Red: Ethane, Yellow: Acetaldehyde, Black: Carbon Dioxide, Violet: Hydrogen Peroxide, Orange: Ethylene and, Green: Hydrogen..... 132

Figure 78. Residuals Plot for the Photocatalytic Hydrogen Generation 0.25wt% Pd-TiO₂ under Near-UV Light. Notes: a) Residual volumes between 0 to 10 cm³ STP, and b) Residual volumes between 0 and 0.35 cm³ at STP. Legends: Blue: Methane, Red: Ethane, Yellow: Acetaldehyde, Black: Carbon Dioxide, Violet: Hydrogen Peroxide, Orange: Ethylene and, Green: Hydrogen..... 133

Figure 79. QY% at Various Irradiation Times, under Near-UV Light and 0.15g L⁻¹ of Photocatalyst Concentration, and Using Pd at Different Loadings (0.25, 0.50, 1.00, 2.50 and 5.00 wt%)..... 137

Figure 80. QY% at various Irradiation Times under near-UV Irradiation Using 0.15, and 1.00g L⁻¹ Photocatalyst Concentrations. Note: Loading was 0.25 wt% Pd on TiO₂. 138

Figure 81. QY% at Various Irradiation Times, under Visible Light, using a 0.15 g L⁻¹ Photocatalyst Concentration. Note: Pd-TiO₂ photocatalyst with different palladium loadings: 0.25, 0.50, 1.00, 2.50, and 5.00 wt% are used. 140

Figure 82. QY% at Various Irradiation Times, under Visible Light, and Using a 0.15g L⁻¹ TiO₂ Photocatalyst Concentration. Photocatalysts were photoreduced using Near-UV light during the first 1 hour..... 141

Figure 83. QY% at Various Irradiation Times under 1 hour near-UV photoreduction, followed by 6 hours of visible light irradiation, and 24 hours near-UV photoreduction, followed by 6 hours of visible light irradiation. Note that the reactions were performed using a 0.15 g L^{-1} photocatalyst concentration and 0.25 wt% Pd on TiO_2 142

List of Appendices

Appendix A. Detection of H ₂ and Carbon Containing Species by a Shimadzu CG 2010	165
Appendix B. Carbon Containing Species Balance	168
Appendix C. H [•] and OH [•] Radicals Balance	170
Appendix D. Quantum Yield Calculation.....	173

Nomenclature

c	Speed of light (3.0E8 m/s)
C_e	Equilibrium concentration in the liquid (mol L ⁻¹)
C_0	Initial concentration (mol L ⁻¹)
D_p	Pore diameter (cm)
e^-	Electron
h^+	Hole
h	Planck's constant (6.63E-34 J/s)
E_{bg}	Energy band gap (eV)
E_{av}	Average Energy of a photon (kJ/mol photon)
F-127	Poly (ethylene oxide)/poly (propylene oxide) / poly (ethylene oxide)
H_2PtCl_6	Chloroplatinic Acid
$H\bullet$	Hydrogen radical
$I(\lambda)$	Intensity of light (W/cm ²)
OH^-	Hydroxide ions
$OH\bullet$	Hydroxyl radicals
k_i	Reaction kinetic Constant (h ⁻¹)
k_i^*	Limiting rate constant of the reaction
K or K_i^A	Adsorption constant of component i
P_o	Rate of photons emitted by the BLB Lamp (einsteins/s)
P_a	Rate of absorbed photons (einstein/s)
P_{a-wall}	Rate of photons absorbed by the inner Pyrex glass (einstein/s)
P_{bs}	Rate of backscattered photons exiting the system (einstein/s)
Pd	Palladium
$PdCl_2$	Palladium II chloride
PEO	Poly (ethylene oxide)
Q_e	Equilibrium adsorbent-phase concentration
$Q_{e,max}$	Maximum adsorption capacity (mol g ⁻¹)
P_{fs}	Rate of forward-scattered radiation (einstein/s)
P_i	Rate of photons reaching the reactor inner surface (einstein/s)

P_{ns}	Rate of transmitted non-scattered radiation (einstein/s)
PPO	Poly (propylene oxide)
Pt	Rate of transmitted photons (einstein/s)
Pt	Platinum
$q(\theta, z, \lambda, t)$	Net radiative flux over the lamp emission spectrum ($\mu\text{W}/\text{cm}^2$)
Redox	Reduction Oxidation Reactions
t	Time (h)
TiO ₂	Titanium dioxide
V	Total volume of the gas chamber (5716 cm ³)
$V_{i,exp}$	Experimentally observed volume at cm ³ STP conditions
$V_{i,model}$	Calculated volume at cm ³ STP
W	Weight (g)
wt%	Weight percent (% m/m)

Greek symbols

θ	Diffraction angle, also scattering angular angle (o)
λ	Wavelength (nm)
ϕ	Efficient quantum yield (%)

Acronyms

BJH	Barrett–Joyner–Halenda model
BLB	Black Light Blue lamp
BET	Brunauer-Emmett-Teller Surface Area Method
CB	Conduction Band
DP25	Degussa P ₂₅ (TiO ₂)
EtOH	Ethanol
LVREA	Local Volumetric Rate of Energy Absorption
LVRPA	Local rate of photon absorption
MREB	Macroscopic Radiation Energy Balance
PCW-II	Photo CREC Water II reactor
STP	Standard Temperature and Pressure (273 K and 1 atm)
TPR	Temperature Programmed Reduction
UV	Ultraviolet

VIS	Visible
VB	Valence Band
XPS	X-ray photoelectron spectroscopy

Subscripts

bg	Band gap
----	----------

Superscripts

0	Basal state
---	-------------

Chapter 1

1 Introduction

The world community has been working towards the production of alternative energy sources while providing sustainable lifestyles for its populations[1]. In Canada, as shown in Figure 1, hydroelectric, wind and solar energy are the most recognized renewable sources of energy. The use of these alternative energy sources has grown significantly in the last few years [2].

In this respect, researchers worldwide have been investigating clean and emission-free energy vectors that could work as alternative fuels. Hydrogen has attracted the attention of the scientific community and governments around the globe, given its great value as a fuel with net-zero CO₂ emissions when burned.

Today, Canada can be considered a leader in the use of renewable energies, and non-Greenhouse Gases emitting energy sources, which account for 65% and 80% respectively, of Canada’s electricity production.

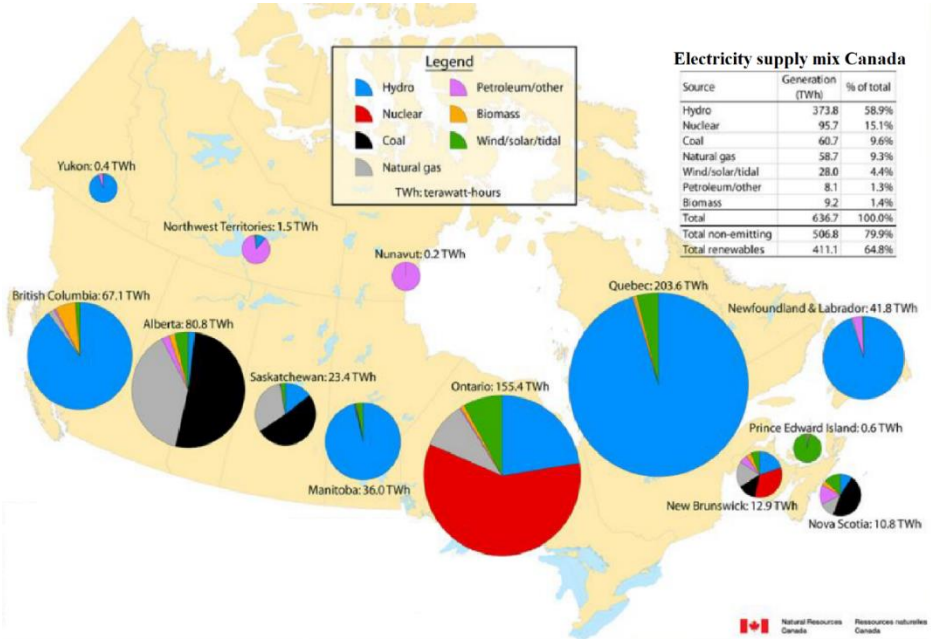


Figure 1 Energy supply in Canada [3].

Note: Sectors in the pie charts report electricity generation in Canada on a per province basis.

In 2019, Natural Resources Canada together with stakeholder groups, provincial, federal, territorial and indigenous groups, worked towards the development and establishment of a strategy to meet Canada's climate change goals, with the objective of achieving a net-zero carbon footprint by 2050[4].

Clean hydrogen is expected to position Canada as a global industrial leader of clean renewable fuels, by contributing to economic recovery and providing at the same time, a domestic low-carbon fuel with reduced carbon emissions (Figure 2). It is anticipated that the implementation of hydrogen production will generate over 350,000 jobs in R&D, manufacturing, and services, while meeting both decarbonization goals and energy demand[4]. This strategy will focus on energy-intensive applications of hydrogen, in transportation, power generation for heating and cooling in buildings, as well as a feedstock in industry.

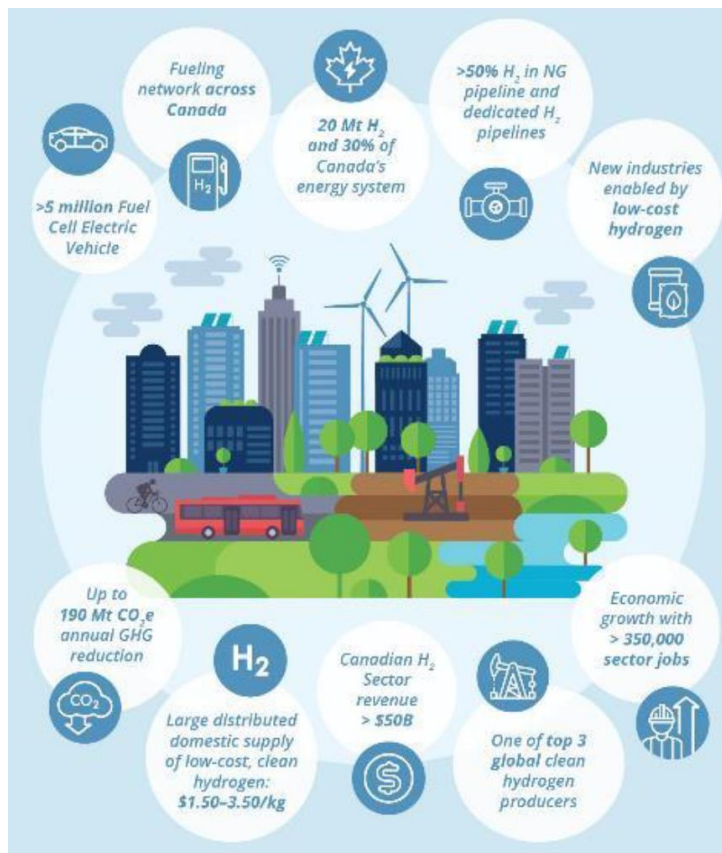


Figure 2. Vision for Hydrogen in Canada in 2050[4].

Hydrogen is one of the most abundant elements on earth that can be extracted from a variety of feedstocks[5]. It also offers a high calorific value (143 MJ/kg) and releases clean emissions to the atmosphere [6], [7].

Hydrogen is now commonly produced via steam methane reforming. This process occurs in industry, at high temperatures and high pressures with carbon dioxide being a main by-product [8]. Furthermore, hydrogen can also be manufactured via autothermal methane reforming, using water and oxygen as methane co-reactants. While energetically more acceptable, autothermal methane reforming, also leads to significant CO₂ emissions. Finally, high temperature and energy intensive methane pyrolysis, provides another alternative for hydrogen manufacturing, with elemental carbon produced creating a complex disposal problem [9]. These aforementioned high temperature processes are energy intensive, and lead to significant greenhouse gas emissions, in most cases.

Water electrolysis is a second most common alternative for hydrogen production. This process is penalized by its high maintenance electrolyte cell costs, lack of reliability and safety issues[10]. In addition, in water electrolysis, various activation energy barriers have to be overcome, setting an extra and unavoidable energy requirement, which limits electrolysis process efficiency. Furthermore, if fossil fuels are used to provide the needed electrical energy, hydrogen production via water electrolysis can be assessed as a process that significantly contributes in overall to greenhouse gas emissions.

Hydrogen can be a main by-product from biomass gasification. Gasification can be appraised as a carbon emission neutral process: carbon contained in biomass is emitted as CO₂ during gasification, while this carbon can be recovered as biomass via photosynthesis. Biomass gasification can use a plurality of carbon sources such as agricultural residues, landfill, and/or organic waste. These reactions have the intrinsic complexity of taking place at high temperatures, over 650-700°C.

Photocatalysis provides a promising approach for hydrogen production. In contrast with the other processes for hydrogen production, photocatalysis takes place at room temperature and close to atmospheric pressure. Photocatalysis uses a semiconductor that generates electron-hole pairs e^-/h^+ , following semiconductor irradiation and upon photon interaction having the

needed energy content. In photocatalysis, the generated e^-/h^+ pairs produce both OH^\bullet and H^\bullet radicals, which are responsible of the hydrogen formation.

Currently, titanium dioxide (TiO_2) is the most frequently used semiconductor in photocatalysis, with anatase being the most photoactive phase. TiO_2 has been proven to be stable, resistant to corrosion, environmentally friendly, largely available in nature and inexpensive [11], [12]. However, its main limitation is its wide band gap (c.a 3.0 eV). Due to this, only 5% of the solar spectrum can be used to activate titanium dioxide. Therefore, the use of sunlight as a source of energy in photocatalysis for hydrogen production, leads to a low efficiency process requiring further improvements [13], [14].

Given these facts, research is required to develop modified photocatalysts for water splitting, meeting the following criteria: a) narrow band gaps to absorb visible light, b) chemical stability under redox conditions, c) inexpensiveness, d) reusability, f) safe to work with, and g) suitable for large-scale hydrogen production[15], [16]. To fully benefit from photocatalysis for hydrogen production, these modified photocatalysts should be used in photocatalytic reactors with high photon absorption efficiencies.

The present doctoral thesis reports hydrogen production via water splitting, using palladium as a TiO_2 dopant. Palladium is a noble metal that modifies the TiO_2 photocatalyst making it active under near-UV and visible light. In the present study, a synthesized mesoporous photocatalyst ($Pd-TiO_2$) was photo reduced under near-UV light irradiation, yielding a 100% of Pd^0 phase and a diminished band gap. The prepared photocatalyst was evaluated in a Photo-CREC Water-II Reactor, under both near-UV and visible light using 2v/v% ethanol as an organic scavenger. A reaction mechanism was proposed using carbon balances, and H^\bullet and OH^\bullet radical balances. This also allowed to establish rate equations using a redox kinetics. In addition, and by using macroscopic energy balances in the Photo-CREC Water Reactor II, quantum yields were calculated for the $Pd-TiO_2$ photocatalysts. On the basis of these findings, it can be stated as reported in this PhD dissertation, that the mesoporous $Pd-TiO_2$ presents important opportunity, to successfully address the challenges of water splitting for hydrogen production via photocatalysis activated with both visible light and near UV irradiation.

Chapter 2

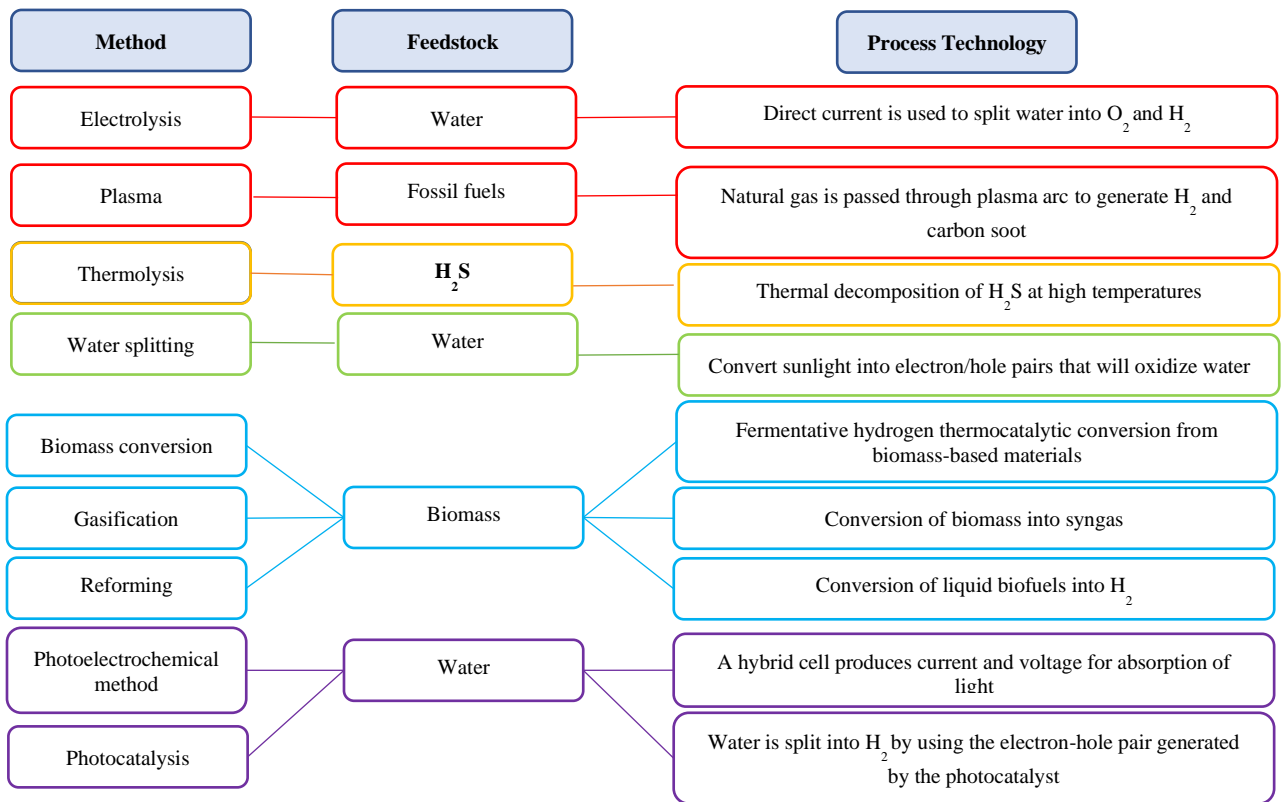
2 Literature Review

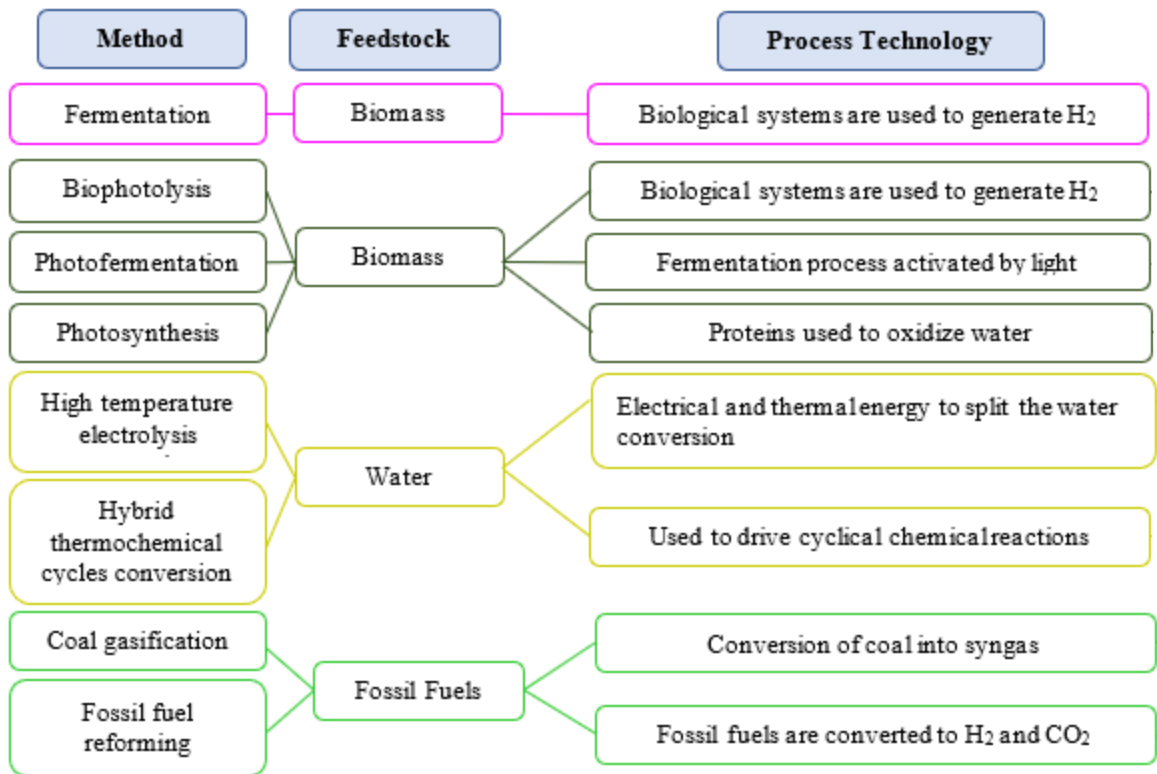
The production of hydrogen has strategic value given that hydrogen is a low-emission, environmentally friendly, clean and sustainable fuel [17]. Hydrogen will likely play a key role, as a fuel, by 2050, given its net-zero CO₂ combustion emissions.[18]. [19]. Hydrogen can be produced, by using water and sunlight as primary sources, in a process designated a water splitting [20].

2.1 Hydrogen Production

Hydrogen is currently produced via different processes such as electrolysis, thermolysis, water splitting, gasification, and fermentation. Table 1 reports the main methods for hydrogen production used today.

Table 1 Traditional Hydrogen Production Technologies [21]–[39]





Despite the diversity of processes, to produce hydrogen, photocatalytic water splitting has greater potential over many of the other above-mentioned production techniques. Photocatalytic water splitting is a process that takes place at low temperatures while using a stable, effective and non-costly semiconductor material or photocatalyst [40]. Nevertheless, water splitting still presents some challenges, such as improving the photon absorption energy efficiency [41].

2.1.1 Photocatalysis

“Photocatalysis” can be defined as the acceleration of a chemical reaction by irradiation (ultraviolet, visible or infrared), which lowers the activation energy for the reaction to occur [42]. In photocatalysis, a semiconductor or photocatalyst material participates in the chemical reaction without being consumed [43].

Photocatalysts can be primarily categorized into two types: (1) Homogeneous and (2) Heterogeneous. Homogeneous photocatalysis, refers to photo induced catalytic reactions where the catalyst is in the same phase as the reactants (liquid phase, generally) whereas in

heterogeneous catalysis, catalysts and reagents are in a different phase (solid-gas, solid-liquid, gas-liquid)[44].

Figure 3 reports some advantages and disadvantages of homogeneous and heterogeneous catalytic processes.

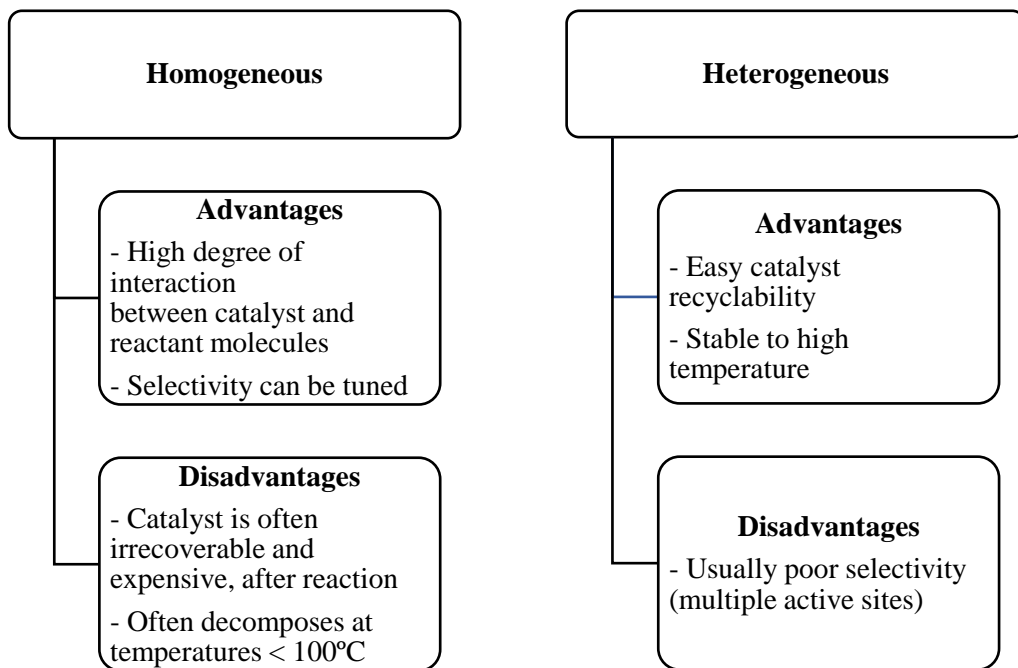


Figure 3 Comparison Homogeneous and Heterogeneous Photocatalysis[45].

As shown in Figure 3, heterogeneous photocatalysis has important advantages over homogeneous photocatalysis. The most relevant ones are the photocatalyst recyclability and thermal stability. These advantages are key, when working with expensive doping noble metals at ambient temperatures [46].

2.1.2 Photocatalytic Cycle

The photocatalytic water splitting reaction for hydrogen production involves the following series of steps[47], [48]:

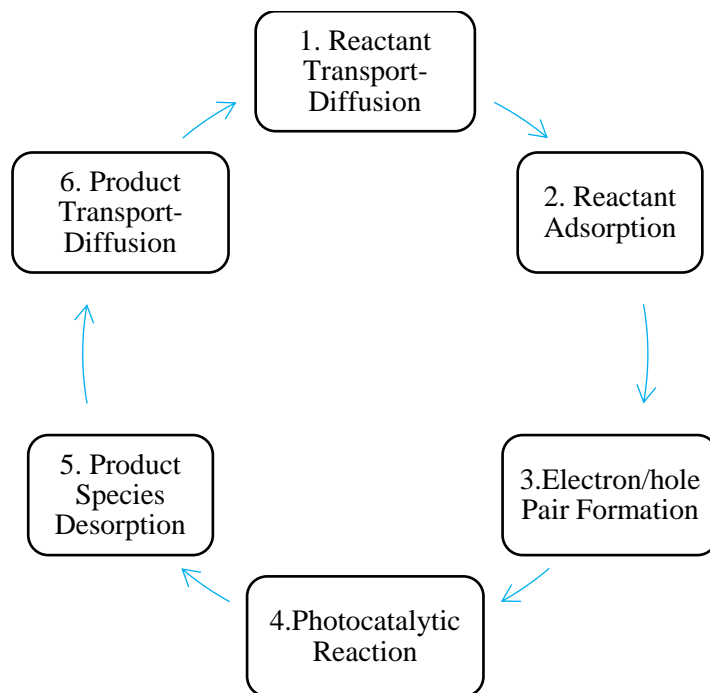


Figure 4 Photocatalytic Reaction Cycle.

1. *Chemical Species Reactant Transport-Diffusion*. This step involves the transfer of the chemical species from the bulk fluid to the external surfaces of the photocatalyst, and from there to the internal surfaces of the photocatalyst via the semiconductor inner pores.
2. *Reactant Adsorption*. This step encompasses the adsorption of the chemical species on photocatalyst active sites.
3. *Electron/hole Pair generation*. This step involves the generation of electron/hole pairs from photon absorption on the semiconductor surfaces.
4. *Photocatalytic Reaction*. This step accounts for the formation of OH^\cdot radicals on semiconductor holes.
5. *Product Species Desorption*. This step involves the desorption of product species from the photocatalyst active sites.

6. *Chemical Species Product Transport and Diffusion.* This step encompasses the transport of products from the photocatalyst surfaces into the bulk fluid.

In photocatalysis, active sites involve an array of sites which are close to energetically identical [49]. These sites provide a lower energy path for molecules, with the purpose of breaking and creating new bonds [50]. When the chemical species are adsorbed on the active sites of the photocatalyst, new reaction intermediates or by-products are generated, with lower energy barriers helping to form products of interest [51][52]. In general, in photocatalytic reactions, the semiconductor material or photocatalyst should lead to the generation of electron-hole pair sites, for the reaction to occur [52].

2.1.3 Water Splitting

Water splitting is a non-spontaneous reaction, that generally takes place at ambient temperature and pressure, with a Gibbs free energy of +237.2kJ/mol and a standard redox potential ΔE equal to 1.23 eV[53].

Processes for water splitting display low efficiencies and are not cost effective. However, photocatalysis offers a path to split water that is inexpensive, and efficient, producing photoproducts such as hydrogen. Despite water splitting thermodynamic constraints, activated photocatalysts and a sacrificial agent can help the reaction to proceed [54]–[56], with the sacrificial agent reducing electron-hole recombination [57].

It is speculated that water splitting under the influence of a semiconductor and an organic sacrificial agent occurs via a distinctive path as shown in Figure 5:

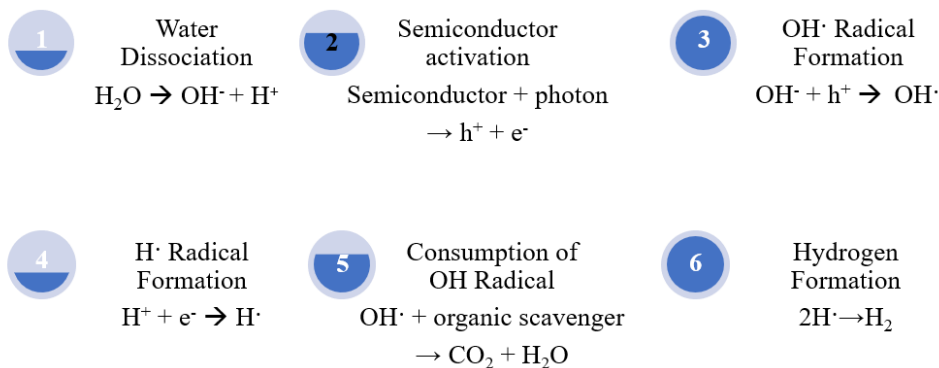


Figure 5 Photocatalytic Reaction Pathway with an Organic Scavenger [58], [59].

Thus, and on this basis one can consider that a photocatalytic reaction involves the following steps:

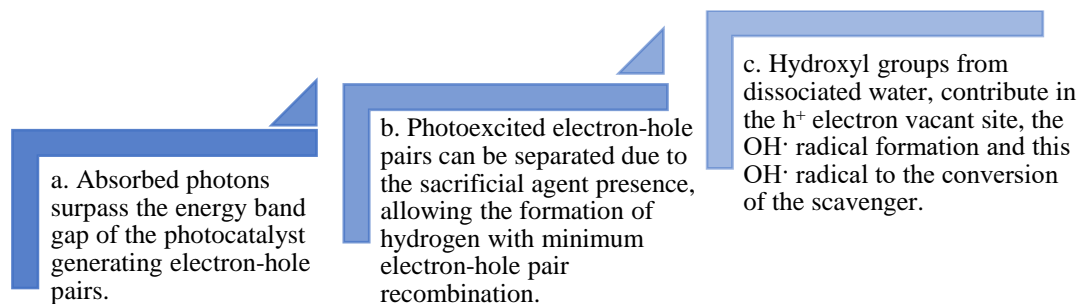


Figure 6 Steps in a Photocatalytic Process when Using Sacrificial Agents [57]–[59].

Therefore, and in order to produce hydrogen via photocatalytic water splitting, three main components are required in a photocatalytic unit:

1. A photocatalyst
2. A light source (Near UV-light or Visible Light)
3. An organic based sacrificial agent

2.1.4 Photocatalyst

The concept of water splitting using a photoelectrical cell was initially introduced by Fujishima and Honda in 1972. The proposed mechanism involved (a) generation of electron-hole pairs using light irradiation in a photoelectrical cell, (b) water oxidation reactions promoting O_2 and H^+ formation, (c) electrons transfer through an external circuit to the cathode, and (d) reduction of H^+ protons, producing molecular hydrogen H_2 [17].

Given their high stability, metal oxides are the most documented semiconductor materials used for water splitting. These oxides have the redox potential required to dissociate a water molecule. Some of the metals used for this purpose are TiO_2 , ZnO , Fe_2O_3 , WO_3 , $BiVO_4$ and $SrTiO_3$ [60]–[62].

Mesoporous photocatalysts appear to display intrinsic advantages for use in photocatalytic processes such as a) relatively larger surface area with adequate pore size, c) high light absorption, d) good electron and chemical species transport properties [63], [64].

The photocatalytic reaction cycle involves the transfer of scavenger chemical species to photocatalyst active sites via chemical species diffusion. Thus, mesoporous semiconductors with larger pore sizes and adequate shapes may be used to enhance organic scavenger diffusivity and the overall reaction rate [65].

It is anticipated that the semiconductor physicochemical properties and photocatalytic efficiency may also depend on the preparation method. Among these methods, sol-gel has been the most commonly used, as it offers opportunity to change the semiconductor texture, composition, homogeneity and structural properties of nanostructures [66] [67].

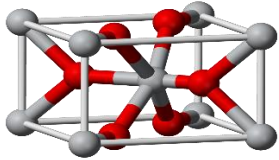
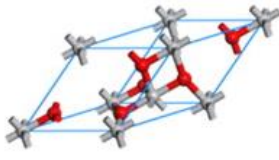
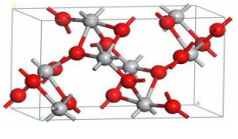
Photocatalyst preparation by the sol-gel method requires the formation of a hydrogel by precipitation, followed by maturation, solvent removal by calcination and, heat treatment reduction. It is after calcination that the formed xerogel phase creates a 3D porous structure resulting in a well defined crystalline mesostructured photocatalyst [68].

2.1.5 Titanium Dioxide (TiO₂)

Titanium dioxide is one of the most used photocatalyst materials. It has multiple advantages such as being stable, chemically active, inexpensive, widely available, non-polluting, having a high dielectric constant and high photocatalytic activity [12]. One of the drawbacks of TiO₂ however, is its relatively high 3.2eV band edge, showing as a result, a very low photocatalytic activity under visible light [11].

Titanium dioxide can be found in three allotropic phases: anatase, rutile, and brookite. Anatase has been reported to have superior photocatalytic properties, whereas rutile exhibits a high thermodynamic stability, among the different polymorphs structures [69]. Table 2 displays some of the properties of each one of the TiO₂ allotropic phases.

Table 2 Properties of TiO₂ for Rutile, Anatase and Brookite [70].

Properties	Rutile	Anatase	Brookite
Crystal Structure	Tetragonal	Tetragonal	Orthorhombic
Lattice Constant	a= 4.5936 c= 2.9587	a = 3.784 c = 9.515	a = 9.184 b = 5.447 c = 5.154
Density (g/cm ³)	4.13	3.79	3.99
Band gap at 10 K (ϵ_0 , in MHz range)	3.051 eV	3.46 eV	
Dielectric constant	173	48	
Refractive Index	2.609	2.488	2.583
Structure			

The rutile allotropic phase of TiO₂ has a tetragonal unit cell with titanium being surrounded by an octahedron of 6 oxygen atoms. Rutile is more stable than the anatase, with both edge and corner being shared. However, the TiO₆ octahedron of the anatase phase shows a larger distortion, with cell units that only share one edge. Additionally, the brookite phase of the TiO₂, display a larger cell volume, with 8 TiO₂ groups per unit cell, connected via the edges of neighbouring units.

Table 3 reports some of the main applications of the TiO₂ phases [71].

Table 3 Rutile, Anatase and Brookite Applications [72].

Rutile	Anatase	Brookite
<ul style="list-style-type: none"> • Paint • Plastics • Paper • Sunscreen • Photocatalysis 	<ul style="list-style-type: none"> • Gems • Paints • Paper • Ceramic • Photocatalysis 	<ul style="list-style-type: none"> • Photovoltaic devices • Photocatalysis • Jewellery

Furthermore, enhancing the photocatalytic activity of a semiconductor material requires an improvement of the semiconductor pore morphology and pore size.

2.1.5.1 Porosity

The surface properties of TiO_2 have a great influence on the photocatalytic activity. Grain size, crystallite form, surface area and porosity are factors that affect the performance of a photocatalyst [73]. Porous photocatalysts can be classified based on pore size, which is defined as the distance between opposite pore walls (width, d_p) as observed in Figure 7 [74].

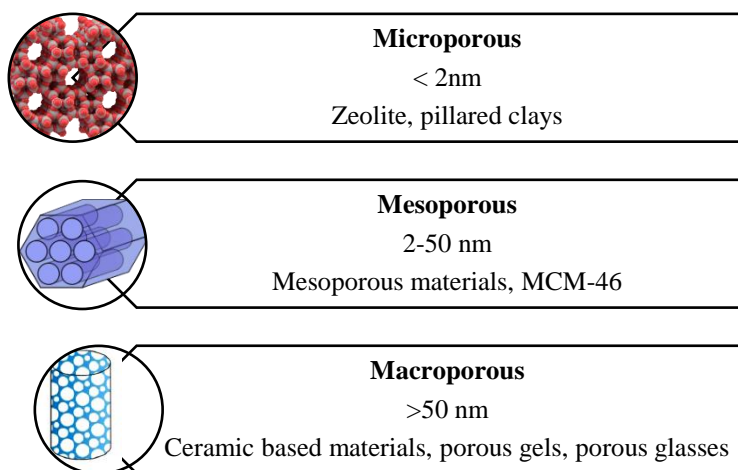


Figure 7 Classification of Porous Materials [71].

Mesoporous TiO_2 ($2\text{nm} < d_p < 50\text{nm}$) has provided good photocatalytic activity, due to its high specific surface area and uniform pore diameter [74], and this given TiO_2 pore structure has a significant influence on (a) the adsorption of electrons, (b) the adsorption of both reagents and products. One can also mention that the mesoporous TiO_2 can also provide the support for metal doping leading to a semiconductor with enhanced photocatalytic activity [75].

Some polymers can act as soft templates¹ and can contribute to TiO_2 synthesis. These polymers are formed by chains of condensed ethylene oxide and propylene oxide molecules. Soft templates are commercially available as Pluronic® F-127 and Pluronic® P-123. The choice of

¹ A soft template does not have a fixed rigid structure, being relatively easily to synthesize and remove producing nanomaterials of various sizes, and with various structure types.

these templates may also be used to optimize the TiO₂ pore structure network during semiconductor synthesis, contributing to both pore size and pore shape modifications [76].

2.1.5.2 Band Gap

The band gap in a semiconductor is determined by the difference between the top value of the valence band (VB) and the bottom value of the conduction band (CB). [77]. The size of the band gap has important implications for photocatalyst applications. A wide band gap provides a good insulator, while a narrow band gap a good conductor. In this respect, a metal is characterized by the overlapping of the valence band with the conduction band, as reported in Figure 8.

Figure 8 also reports the Fermi level, the energy of the least tightly held electrons within a solid, defined at 0 K. This Fermi level is defined as relative value with respect to the conduction band and show the electrical properties of a particular material.

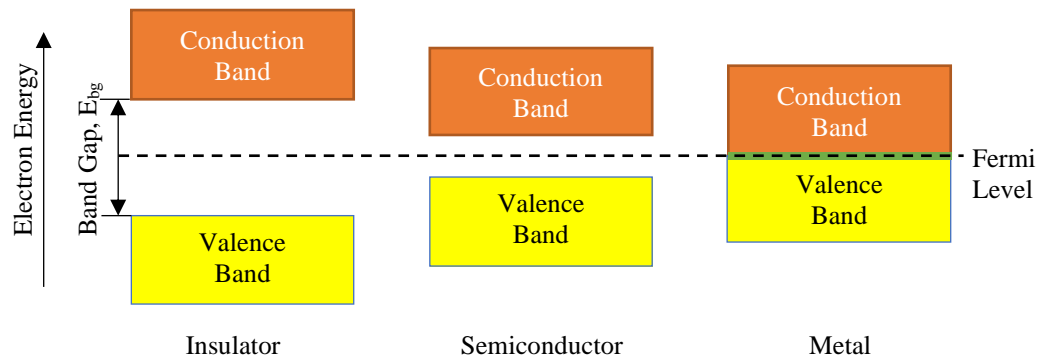


Figure 8 Electronic Band Structure of Insulators, Semiconductors and Metals.

Figure 9 reports the band gap conductivities of various semiconductors of interest. One can see that for anatase and rutile they are approximately. 3.2 eV and 3.0 eV, respectively [78].

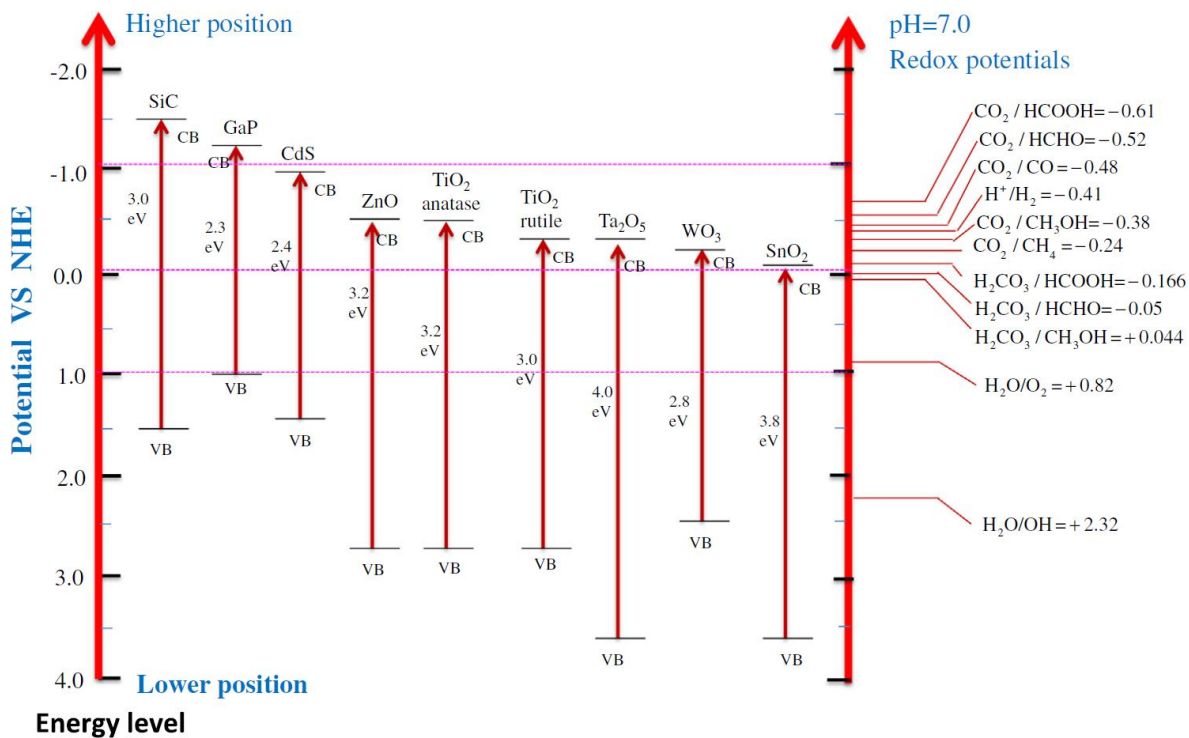


Figure 9 Schematic Representation of Conductivity Band Potentials of Different Semiconductors[79].

Regarding the photocatalytic properties of TiO₂, they are closely related to the formation of electron-hole pairs. Light is absorbed by the semiconductor material, promoting the generation of electron-hole pairs, as shown in Equation 1. The formed electron (e⁻) moves from the valence band to the conduction band, leaving behind a hole (h⁺). The hole, with an absent electron in a bonding orbital, normally placed at the TiO₂ particle irradiated surface, can react with the adsorbed water, producing hydroxyl radicals (OH[·]) [80].



Formed OH[·] radicals may oxidize near organic scavenger molecules, preventing hole and electron recombination and yielding carbon containing oxidized species, whereas the H[·] radicals may form molecular hydrogen (Figure 10) [81].

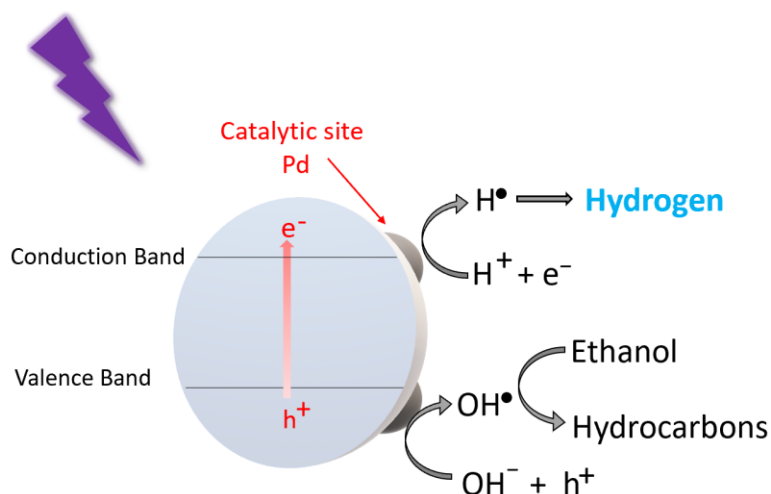


Figure 10 Formation of Photogenerated Electron-Hole Pairs and Hydrogen under Near-UV Light.

2.1.6 Photocatalyst Doping

In order to improve photocatalyst efficiency, various approaches have been carried out including doping, dye sensitization, composite material inclusion and others. The doping of photocatalysts with metals can narrow band gaps, and improve the optoelectronic semiconductor properties [82]. The photoexcitation of these metals leads to the generation of free charge carriers, allowing hydrogen formation. These metals or co-photocatalysts, can be either a noble metal, a metal oxide or a metal hydroxide [83].

In the specific case of TiO_2 , it is reported as shown in Table 4 that metal doping enable hydrogen production, allowing TiO_2 activation by both visible and near-UV spectrum photons [82],[68],[69]. One should mention as well, that some proposed TiO_2 co-photocatalysts include Pt, Pd, Ni, Ru, Rh, Ir and others. These co-photocatalysts can create extra photocatalytic active sites acting as electron collectors and facilitating as a result, the water splitting process.

Table 4 Metal-Doped TiO₂ Photocatalysts under Near-UV and Visible Light [85]–[87]

Dopant	Light Source	H ₂ Rate (μmol h ⁻¹ g ⁻¹)
Pt - 0.5 wt%	500W Hg-Xe lamp with dichroic filter (280 – 400 nm)	27600
Ni- 1 wt% Atomic ratio 1:10 (Ni : Pd)	UV- vis light (400W mercury arc)	200
Ru- 3 wt %	500W Xe lamp with a light cut-off filter UV light: (280–400 nm)	4700
1 wt % Ni	UV (450W Hg)	3390
6.9 wt % F	300W Xe	18270
1 wt % Cu	UV (450W Hg)	793.86
1 wt % Co	Solar and UV (400W Hg vapour lamp)	11,021
Co, Ni, and Cu-doped TiO ₂	UV light irradiation	85
Fe-Ni/Ag/TiO ₂	500 W Xe lamp	7.94E-04
Ag-Ce/TiO ₂	Xenon lamp ≥ 400 nm cut-off filter	1.47
Ga/N - TiO ₂	125 W Hg lamp ≥ 400 nm	35
Ga- TiO ₂	150 W Xe (310 nm < λ < 625 nm)	5722000
Cu ⁺ /Cu ⁰ –TiO ₂	Solar light	1000
Ni(OH) ₂ /TiO ₂	3 W UV-LEDs lamps	3056
Bi-doped TiO ₂	125 W Hg lamp, 500 W Xe	4500
Cu ₂ O/TiO ₂	300 W Xe lamp/simulated sunlight	400
W-TiO ₂ /Au hybrid Au-1.93 wt % - W- 0.83 wt %	300W Xe	24000
Ni/TiO ₂ 1 wt %	UV (450W Hg)	3390
Fe/Ni-TiO ₂ Fe- 5 wt %	UV and visible light	361.64
Pt/TiO ₂ 1 wt %	AM 1.5 G solar simulator	11200
N–TiO ₂ / Pt Pt- 0.2 wt %	500W Xe	570
N/Pt-TiO ₂ 4.6 wt %	Visible light	11.34
Cu/S-TiO ₂ Cu- 5 wt %	500W Xe lamp with UV cut off filter	7500
Pt/Ga-TiO ₂ Ga -3.125 wt %	150W Xe	5722
Gd/N-TiO ₂ Gd 2 wt %	150W Xe	10764
Rh/Nb-TiO ₂ Rh – 0.2 wt %	300W Xe	7850
Ru-TiO ₂ Ru- 3 wt %	500W Xe lamp with a light cut-off filter UV light: (280–400 nm)	4700
TiO ₂ /Pt/rGO Pt - 0.5 wt%	9W 4 Philips PL-S lamp (315 - 400 nm)	2411000
NY TiO ₂ -Pt Pt – 0.188 wt%	Visible light and UV (PLSSXE-300C Xe lamp)	20880
Ni ₁ -Pd ₁₀ /TiO ₂ Ni- 1 wt% Atomic ratio 1:10 (Ni : Pd)	UV- vis light (400W mercury arc)	200
Co-TiO ₂ Co-1 wt %	Solar and UV (400W Hg vapour lamp)	11,021

Palladium, specifically, has a lower Fermi level while compared to TiO₂. When used as a co-photocatalyst, it leads to an effective transference of electrons to metal sites, reducing the electron/hole recombination and promoting enhanced photocatalytic activity [88]. Palladium is a very stable metal, with the palladium precursor reagents being approximately 20% less expensive than those of the platinum.

In summary, modified TiO₂ semiconductors may provide enhanced band gaps and light absorption, as well as (a) higher refractive indexes, (b) slower recombination dynamics and (c) enhanced rate of charge transfers across interfaces. All this favours photocatalytic activity [89].

2.1.7 Light Source

The water splitting reaction is not a spontaneous process that occurs under solar visible light irradiation when using TiO₂ alone as a photocatalyst [90]. Titanium dioxide is only active under ultraviolet light at short wavelengths (200-400 nm). However, most of the solar radiation spectrum is in the visible light range (400 nm to 700 nm), making TiO₂ as a photocatalyst, poorly efficient, under visible light conditions.

In order to reach high sunlight utilization efficiencies, the TiO₂ photocatalyst has to be modified. This can be achieved by surface modification by either using soft templates or doping with a noble metal such as palladium. Additionally, an uniformly irradiated surface area of the photocatalyst should be achieved in order to avoid internal and external diffusion transport phenomena[91]. With this purpose, choosing an adequate light source is essential.

Certain types of lamps have been used for water spitting processes. The most well-known lamps are a) 150 W Xenon arc, b) 300W Xenon cut-off filter and c) 300 W solar simulated radiation [92]. Regarding near-UV and visible light lamps, two types are more commonly used due to their low cost and easy accessibility: a) 15W BLB (Black Light Blue) for near-UV and b) 15W Hg for visible light [93].

2.2 Sacrificial Agent

Organic molecules or sacrificial agents perform as electron donors to prevent electron/hole recombination. Common sacrificial agents are methanol, triethanolamine, ethanol, acids and inorganic compounds, as indicated in Table 5. [94].

Table 5 Sacrificial Agents and Hydrogen Evolution Rate when Using 20 vol% Organic Alcohols and Amines[94].

Sacrificial Agents	H ₂ evolution rate ($\mu\text{mol h}^{-1} \text{g}^{-1}$)
Methanol	599
Ethanol	111
Ethylene glycol	116
Triethanolamine	1197
Methylamine	279
Ethylamine	101
Ethylenediamine	84.2

As shown in Table 5, sacrificial agents with lower oxidation potential and higher permittivity led to higher photocatalytic activity with higher H₂ formation rates. Among the sacrificial agents used, ethanol is one of the most investigated. It has the potential to provide high quantum efficiencies, and can be easily obtained from renewable sources, while being widely available and inexpensive. [95].

Scavengers with lower oxidation potential can be more easily oxidized and can more efficiently trap holes. Ethanol with its 1.1 eV oxidation potential, a possible organic scavenger, can likely display ability to provide electrons. In water splitting process however, using an organic scavenger, photocatalytic reactions may also lead to undesired and unavoidable oxidation by-products.[96].

2.3 Photocatalytic Reactor

Researchers working on H₂ production have designed various photoreactor prototypes. Some of the photoreactors are made out of quartz or pyrex with volumes between 50 ml to 100 ml. Most commonly, these small photoreactors use Xenon lamps with 300W to 500W nominal

power as sources of irradiation. The radiation lamp can be placed either inside (Type I) or outside the reactor (Type II). Type I reactors are generally more advantageous for an efficient photon utilization, because light spreads in all directions (symmetry of irradiation), covering more of the photocatalyst surface area.

A photocatalytic reactor for hydrogen production of the slurry type, should comply with the following criteria: (a) uniform light distribution inside the reactor, (b) no external or internal chemical species diffusive transport limitations, (c) uniform photocatalyst distribution, (d) high surface/volume reactor ratio and, e) minimum photocatalyst fouling effects, (f) well-mixed photocatalyst suspension, (g) low pressure drop, (h) good near-UV and visible light transmittance above 90%, (i) good chemical resistance to the chemicals used (e.g. ethanol) and (j) pH in the 4 to 7 range [97].

The Photo-CREC Water-II Reactor, designed and developed at the Chemical Reactor Engineering Center (CREC)-UWO (Figure 11) satisfies all these design criteria for successful hydrogen production via water splitting [98]. A schematic figure of Photo-CREC Water-II Reactor and its auxiliary components for hydrogen production, is given in Figure 11. In Chapter 3, additional information about the technical characteristics of this unit, is also provided.

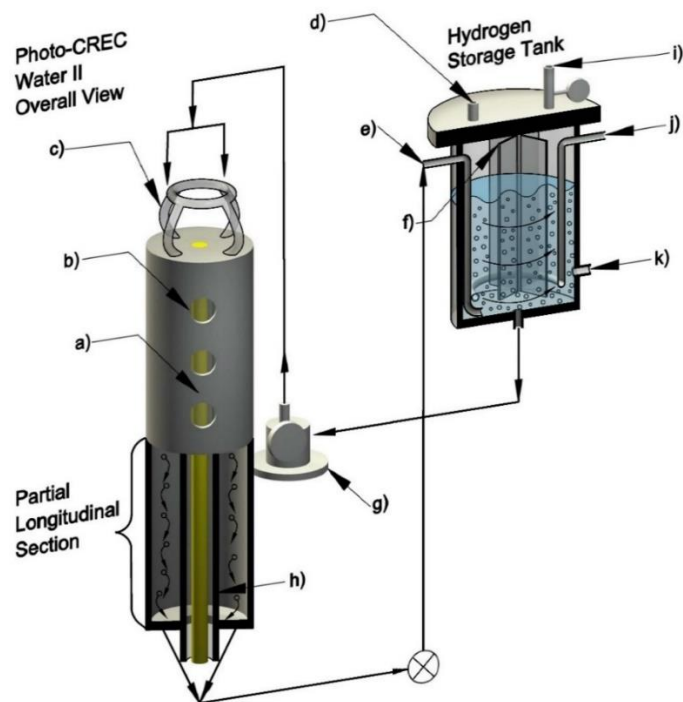


Figure 11 Schematics of the Photo-CREC Water-II Reactor. Components: (a) Opaque polyethylene tube, (b) Fused silica windows, (c) Flow distributor, (d) Gas sampling port, (e) Jet driving mixing port, (f) Self-driven mixing impeller, (g) Centrifugal pump, (h) Pyrex tube, (i) Draining gas valve, (j) Purging gas injector, and (k) Slurry sampling port [99].

2.4 Kinetics of H₂ Production

Regarding kinetics, the Langmuir-Hinshelwood (LH) model is the most commonly used model to express the rate of H₂ and the formation of by-products, when utilizing a sacrificial agent.

The rate of the reaction can be expressed, as in Equation 2:

$$\text{Rate} = \frac{k K [\text{sacrificial agent}]}{1 + K[\text{sacrificial agent}]} \quad \text{Equation 2}$$

where K is the adsorption constant of the sacrificial agent on the photocatalyst surface, and where k is the intrinsic kinetic constant.

One of the main advantages of the L-H model is that it accounts for both chemical species adsorption and intrinsic kinetics. Additionally, when using L-H model, the derived rate equation can be extrapolated, in order to accurately predict the concentrations of the by-products beyond the experimental data[100].

Very few researchers have worked on the kinetics of noble metal doped TiO₂[85]. Those who have done so, have found that the rate of H₂ production when using an Au/TiO₂ and Pd/TiO₂ photocatalyst can be explained by the L-H model. At high sacrificial agent concentrations, the hydrogen evolution rate should become of order zero and remain constant. However, at low scavenger concentrations, the H₂ production rate may become proportional to the concentration of the sacrificial agent, resulting in a first order kinetics[85].

2.5 Quantum Yield (QY)

Equation 3 provides a photonic efficiency (PE) definition as,

$$PE = \frac{\text{Rate of reactant molecules transformed}}{\text{Rate of incident photons}} \quad \text{Equation 3}$$

Furthermore, the quantum yield (QY) for water splitting reactions, as shown in Table 6, can be established on the basis of the rate of hydroxyl radicals (OH[•]) consumed over the number of photons absorbed by the photocatalyst. When compared to the PE, the QY can be considered to be a more adequate parameter to describe photochemical activity and the utilization of absorbed photons[101].

Table 6 Quantum Yield Definition in terms of OH[•] Radicals and Photons Absorbed [98].

Quantum Yield (QY)	$\frac{\text{No. of Consumed OH}^\bullet \text{ radicals moles}}{\text{No. of photons absorbed by the photocatalyst (Pa)}}$
--------------------	---

The quantum yield equations for hydrogen production are shown in Table 7.

Table 7 Quantum Yield for Hydrogen Production[102].

Theoretical QY Based on the Moles of H ₂ Produced	$QY_{H_2} = \frac{\text{moles of H}_2 \text{ produced}}{\text{moles of irradiated photons}}$
Overall QY for H ₂ Production	$QY_{H^\bullet + OH^\bullet} = \frac{\text{moles of H}^\bullet + \text{moles of OH}^\bullet}{\text{moles of photons}}$
QY in terms of the Moles of H [•] Radicals Produced or Two Times the Moles of H ₂ Produced	$QY_{H^\bullet} = \frac{\text{moles of H}^\bullet \text{ produced}}{\text{moles of photons absorbed by the photocatalyst}}$

2.6 Conclusions

Based on the above discussion of the technical literature, the following relevant conclusions can be drawn:

- a) New semiconductors are required for photocatalytic hydrogen production from water splitting. These photocatalysts should be synthesized with enhanced morphologies, involving narrower band gaps, and higher H₂ production activity under near-UV and visible light.
- b) The new synthesized photocatalysts should be very active for hydrogen production via water splitting, and evaluated in engineered units, as is the case of the Photo-CREC Water-II Reactor. Using these novel units allow the assessment of the photocatalysts through macroscopic irradiation energy balances and Quantum Yield efficiencies.
- c) The established performance of the synthesized photocatalysts leads to the establishment of reaction mechanisms for hydrogen production via water splitting. These kinetic models allow determination of the reaction progress as well as, the by-products formed, in scaled-up photocatalytic units. This reaction mechanism should be the foundation of new kinetics models.

2.7 Scope of the Research

2.7.1 General Objectives

- To further develop a doped TiO₂ photocatalysts with palladium. The photocatalyst synthesis will be carried out using a sol-gel method and modified by the Pluronic F-127 polymer.
- To test of the photocatalyst developed under near UV and visible light for hydrogen production at different metal loadings.
- To establish a reaction mechanism for water splitting process using Pd-TiO₂.
- To determine the quantum yield of the photocatalytic process.

2.7.2 Specific Objectives

- To determine the optimum palladium loading (0.25 to 5.00%wt Pd) on the titanium dioxide photocatalyst.
- To thoroughly characterize the synthesized photocatalysts by using physical and chemical techniques such as Nitrogen physisorption, temperature programmed reduction, chemisorption, X-Ray diffraction, X-ray Photoelectron Spectroscopy and UV-Vis Absorption.
- To carry out experiments to measure the extent of influence of the photocatalyst on hydrogen production under Near-UV and visible light irradiation.
- To evaluate the irradiation absorbed by the photocatalyst using an experimental macroscopic irradiation balance.
- To determine reaction pathways to produce hydrogen and its by-products.
- To develop a kinetic model that constitutes the mathematical description of the course of the water splitting reaction for each reaction step.
- To evaluate the quantum yield for the photocatalytic water splitting process.

Chapter 3

3 Equipment, Materials, Photocatalyst Synthesis and Experimental Methods

This chapter introduces the equipment, materials, photocatalyst synthesis and experimental methods employed in this thesis. The Photo-CREC Water-II Reactor unit is described as this is used for photocatalytic water splitting reactions, leading to the production of hydrogen. The photoreactor operation and conditions are reported as well as the light sources used in Photo-CREC Water-II Reactor. Finally, the methods considered in the present study for the development of an efficient photocatalyst as well as the experimental methods used for hydrogen production, are discussed.

3.1 Photo-CREC Water-II Reactor

The Photo-CREC Water-II (PCW-II) Reactor is an innovative unit for hydrogen production. It is a 5.7 L slurry batch reactor configured with two concentric tubes: (a) an inner tube made from transparent borosilicate (Pyrex) and (b) an outer tube made from opaque polyethylene. The fluorescent lamp is placed inside this inner Pyrex tube. Furthermore, the suspended photocatalyst flows in the annular space between the outer polyethylene tube and the inner Pyrex transparent tube, which only absorbs 5% of the near-UV light emitted by the lamp[103].

The PCW-II unit is equipped with a sealed storage feed tank where the photocatalyst remains under agitation. This tank has two (2) ports for periodic liquid and gas phase sampling. Figure 12 describes the main components of PCW-II: The Photo-CREC Water-II Reactor, the centrifugal pump, and the sealed storage tank.

The black polyethylene outer tube minimizes radiation reflection. The external tube is equipped with seven (7) axially and equally spaced silica windows used for irradiation measurements. The Pyrex inner tube absorbs only up to five percent (5%) of the near-UV or visible light emitted by the lamp and protects the light source from any contact with the circulating water along the reactor [104].

The hydrogen storage/mixing tank in the Photo-CREC Water-II Reactor is connected to a centrifugal pump that promoted water recirculation in the concentric channel (space between the outer polyethylene tube and the Pyrex tube), where the photocatalytic reaction takes place.

As seen in Figure 12, the PCW-II is composed of: (1) A 15-W fluorescent visible light lamp or near-UV light, (2) A Pyrex glass inner tube where the lamp is placed, (3) A black polyethylene outer tube with fused silica windows for irradiation measurements, (4) A centrifugal pump, (5) Two sampling ports which allow the photocatalyst suspension to always be kept sealed under agitation; one port for the liquid phase and the other one for the gas phase, (6) A hydrogen storage tank [103]. See reactor dimensions in Table 8.

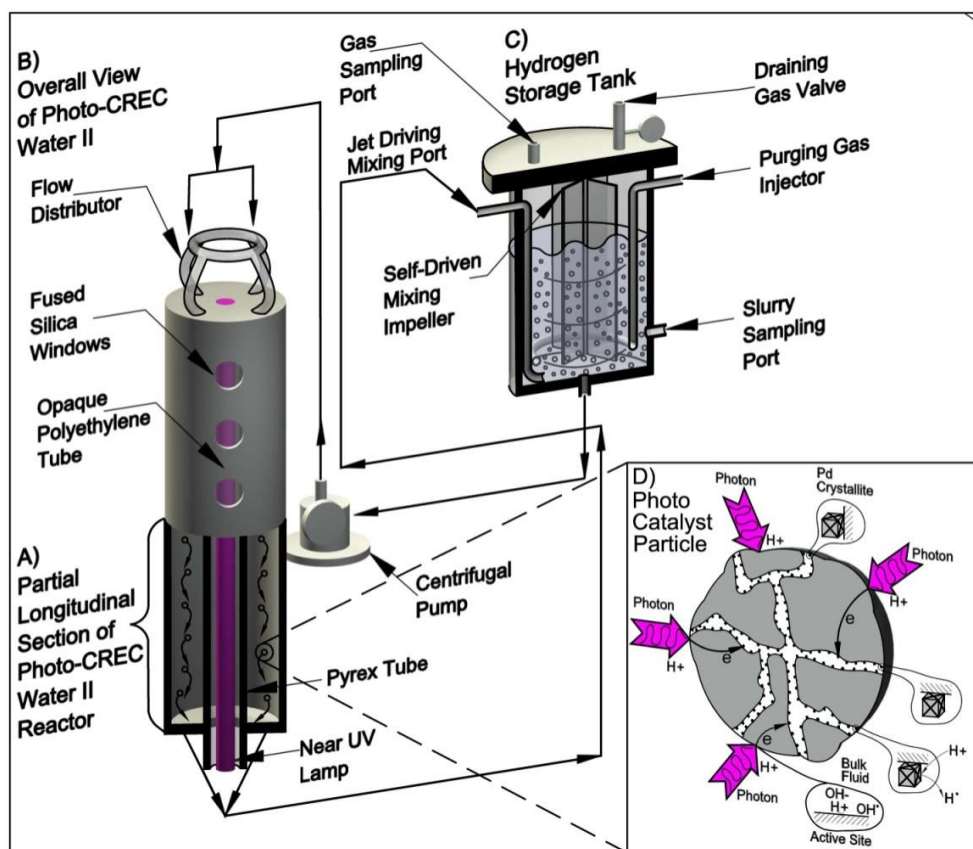


Figure 12 Schematics Representation of the Photo-CREC Water-II Reactor with a H₂ Mixing/Storage Tank: (A) partial longitudinal cross-section of the PCW- II unit showing the downflow circulation of the slurry in the annular channel, (B) overall view of PCW-II showing windows, near-UV lamp and recirculation pump (C) hydrogen storage tank with its components, (D) detail of a photocatalyst particle. Notes: (a) The opaque polyethylene is black in colour. However, it has been shown in grey in this figure, for diagrammatic purposes. (b) The diagram shows a near-UV light in the PCW-II. However, a visible light lamp can also be used.

The Photo-CREC Water-II Reactor is also equipped with gauges to monitor pH, temperature, and pressure. There is an additional entrance port that allows the circulation of inert gas in the storage tank for oxygen removal. The centrifugal pump is a class B, 115V, 2.4A, 60 Hz and 3100 rpm unit and the electrical ballast was designed to operate at 120 VAC, 60 Hz and 0.75 A[105].

Table 8 PCW-II Dimensions.

Component	Height (cm)	Inner radius (cm)	External radius (cm)
Pyrex glass	61	1.505	1.75
External Tube	45	1.75	4.5
Windows	-	-	0.5
H ₂ mixing/storage tank	21	22.5	31
Internal tank impeller	16.5	-	2.25

3.2 Lamp Characterization

Two lamps are used for the photocatalytic water splitting experiments: a) Near-UV lamp and b) Visible light lamp. Each lamp can be placed inside the Pyrex tube, one at a time, providing a 15W of near-UV light or 15 W fluorescent visible light, respectively.

The emitted radiation from the lamps used is measured using the Stellar Net EPP2000-25 Spectroradiometer. The Stellar Net EPP2000-25 Spectroradiometer is an instrument that measures the wavelength, the amplitude of the light emitted from a light source, and the number of photons absorbed after they pass through the slurry medium. This instrument is equipped with fibre optics to effectively measure the spectral irradiance, the radiance, and the Watt flux over the wavelength radiation in the 300-700 nm range, at variable distances and various locations of the PCW-II unit. This spectroradiometer unit was also provided with a high speed parallel digitizer interface [106].

Figure 13 reports the spectrum of the polychromatic BLB Ushio near-UV lamp used, with an observed output power of 1.61 W, an average of 325.1 kJ/photon moles of emitted photon energy and a spectral peak at 368 nm in the 300-420 nm emission range [107].

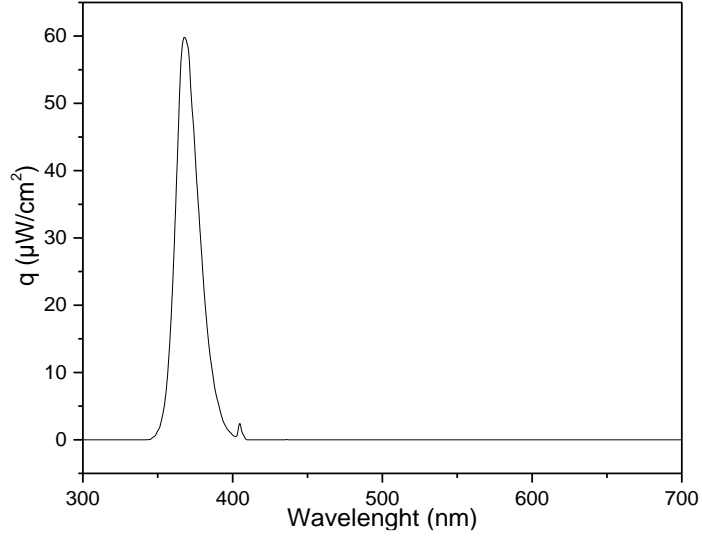


Figure 13 Near-UV Lamp Irradiation Spectrum.

The average emitted photon energy can be calculated using the recorded irradiation spectrum as follows [108]:

$$E_{av} = \frac{\int_{\lambda_{min}}^{\lambda_{max}} I(\lambda) E(\lambda) d\lambda}{\int_{\lambda_{min}}^{\lambda_{max}} I(\lambda) d\lambda} \quad \text{Equation 4}$$

where,

$$E(\lambda) = \frac{hc}{\lambda} \quad \text{Equation 5}$$

With h being the Planck constant (6.34×10^{-34} J s/photon), c representing the speed of light in a vacuum (3.00×10^8 m/s²) and λ denoting the wavelength expressed in nanometers (nm). I is the emitted photons intensity (W/cm²), assessed as $I(\lambda) \approx q(\theta, z, \lambda, t) d\lambda$ and measured with a spectroradiometer. The irradiance is represented by $q(\theta, z, \lambda, t) d\lambda$ and given by the spectrum of the lamps, as shown in Figure 13.

Furthermore, the average emitted photon energy can be calculated as shown in Equation 4, and must be expressed in terms of λ_{max} or the equivalent E_{min} (see Equation 5), required to surpass the TiO₂ band gap [109].

$$E_{av} = \frac{\int_{\lambda_{min}}^{\lambda_{max}} I(\lambda) E(\lambda) d\lambda}{\int_{\lambda_{min}}^{\lambda_{max}} I(\lambda) d\lambda} = \frac{\int_{\lambda_{min}}^{\lambda_{max}} \frac{hc}{\lambda} * q(\theta, z, \lambda, t) d\lambda}{\int_{\lambda_{min}}^{\lambda_{max}} q(\theta, z, \lambda, t) d\lambda} \quad \text{Equation 6}$$

$$E_{av} = 5.36 \times 10^{-19} \text{ J/mol photon} = 325.1 \text{ KJ/mol photo} \quad \text{Equation 7}$$

Similarly, the Stellar Net EPP2000-25 Spectroradiometer can be used to determine the irradiation spectrum of the mercury Philips visible light lamp, as shown in Figure 14. This cool white light lamp has an output power of 1.48 W and an average emitted photon energy of 274.5 kJ/photon mole.

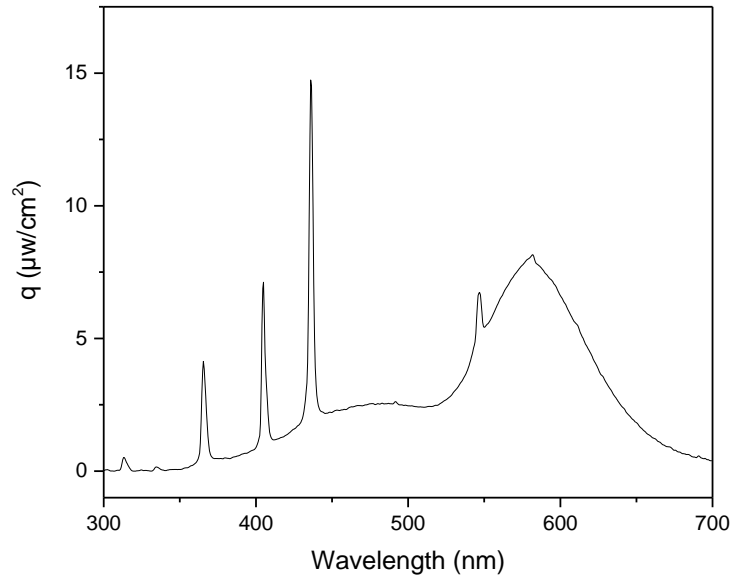


Figure 14. Visible Lamp Irradiation Spectrum.

Furthermore, the axial distribution of the radiative flux can be determined using the Stellar Net EPP2000-25 Spectroradiometer, the fibre optic system and the PVC black collimators. Figure 15 displays the observed axial visible lamp radiation distribution, with a radiation profile showing no significant changes in radiation levels, in the central section of the PCW-II. On the other hand, significant radiation decay can be seen approaching the endpoints of the lamp[110].

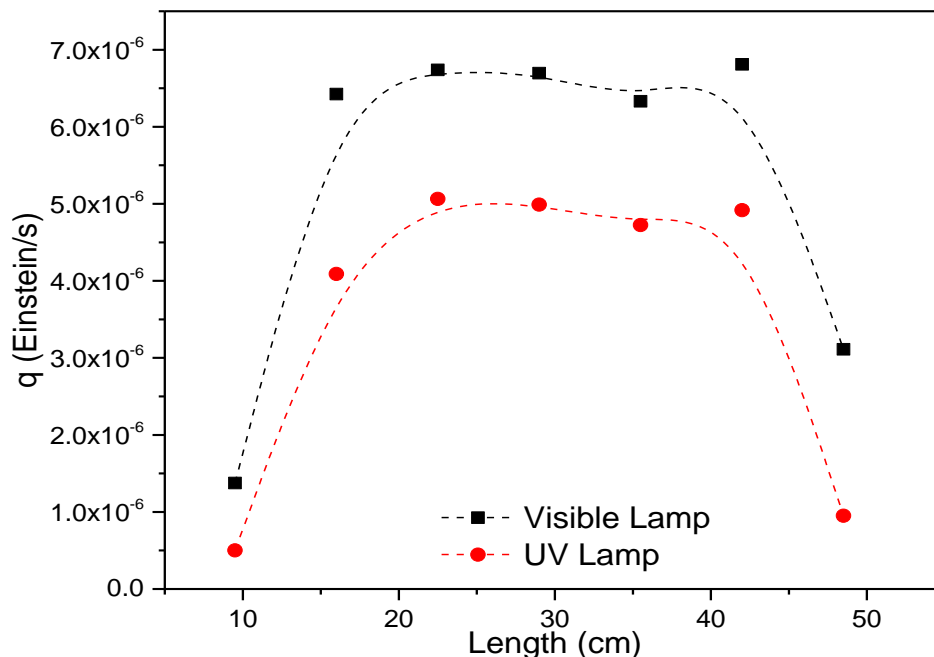


Figure 15 Near-UV and Visible Light Lamp Axial Distribution.

3.3 Synthesis Methods

Modifications made to the photocatalyst synthesis may lead to improvements in the semiconductor surface properties, such as particle diameter and specific surface area, and thus, to enhanced photocatalytic hydrogen production rates. In this respect, the sol-gel method considered in the present study, is considered the best approach for the modification of a semiconductor.

3.3.1 Sol-gel Method

The sol-gel method can be used for photocatalyst synthesis by converting monomers into colloids, and thus promoting a gel structure formation [111]. The sol-gel method for TiO₂ synthesis can be modified, leading to improvements in photocatalyst structural properties such as particle diameter and surface area. Therefore, this also leads to improved photocatalytic activity[66].

The sol-gel method is a well established approach used to control the texture and surface properties of a semiconductor material [112]. It is based on the conversion of monomers into

colloids (sol phase), promoting a gel structure formation [111]. The sol-gel method used in this research, can be described in five (5) stages, beginning with the hydrolysis of a metal precursor, followed by condensation, aging and drying forming 3D structure network [113].

a. Step 1: Hydrolysis

This involves the dissolution of a precursor (metal alkoxide) in an organic solvent (alcohol), as observed in Figure 16. A strong acid or base addition is beneficial to accelerate the hydrolytic process. Hydrolysis leads to a sol and to the dispersion of colloidal particles in the liquid[114].



Figure 16 Hydrolysis of an Alkoxide Precursor.

b. Step 2. Condensation

The condensation of adjacent molecules forms spiral/linear chains of TiO_6 octahedrals. Polymeric networks grow to form colloidal structures, as observed in Figure 17. The condensation process occurs via alkoxylation and oxolation. In the alkoxylation process, two metal centres form a hydroxyl (M-OH-M) bond, under the release of an alcohol. In the oxolation process, two hydroxylated metal species form an oxo (M-O-M) bond, producing water.

Note that there is a visible change in the solvent viscosity during this stage. An interconnected, rigid and porous inorganic network is formed[115]. The size and cross-linked colloid structure is dependent on the metal alkoxide used and the pH of the solution.



Figure 17 Condensation of an Alkoxide Precursor.

c. Step 3. Aging

This involves the polycondensation of the monomeric chains with the gel precipitating during this period of time.

d. Drying

Organic components are being removed from the gel phase. This step could involve drying processes such as evaporation, supercritical drying, and freeze drying, among others. The most common technique used is thermal drying, under ambient conditions. During this time, shrinkage of the pores occurs, yielding a xerogel.

e. Calcination

Water molecules and residues are being removed from the xerogel, using high temperatures. The calcination temperature and rate of heating are key conditions to control the morphological properties of the resulting semiconductor such as pore size and material density.

The particle nucleation in the sol-gel process used in this research, led to a homogeneous structure during colloidal deposition. This yielded a well-controlled particle size, shape, surface area to volume ratio, and porosity[116].

Table 9 reports results found in the literature, on the synthesis and operation conditions of TiO₂ photocatalysts using the sol-gel methodology.

Table 9 Reported Synthesis of TiO₂ Nanoparticles via Sol–Gel Method.

Precursor	Process Conditions	Result	Reference
TTIP, isopropanol, deionized water and glacial acetic acid	Stirring: 2 h, pH: 1 Drying: 1 h, 80 °C Calcination: 2 h, 450–700 °C	Agglomeration of anatase and rutile phase Crystallite size: 13 and 100 nm	[117]
TTIP, hydrochloric acid, ethanol and deionized water	Stirring: 2 h, at room Temperature, pH 3–8 Drying: 100 °C, 1 h Calcination: 350–750 °C	Particle agglomerate. Anatase turns into rutile when increasing temperature. Crystallite size: 12 and 49 nm	[118]
TTIP, ethanol, hydrochloric acid, deionized water	Stirring: 60 s, under ice-bath Drying: 400 °C, 6 h	TiO ₂ catalyst was synthesised on alumina membrane Pore size: 200 nm	[119]

Table 9 reports some of the TiO₂ photocatalysts that were synthesized using the sol-gel method, which resulted in large ranges of the crystallite sizes and pore diameters. To enhance and control the photocatalyst morphology, a copolymer or template can be added [120]. Addition of a copolymer during the photocatalyst synthesis leads to a TiO₂ mesoporous material with enlarged pores as well as to high purity, homogeneity, low agglomeration tendency, and quite narrow pore size distribution.

3.3.2 Copolymers

These templates are usually surfactants that act as amphiphilic molecules that influence the size, shape, and arrangement of the nanoparticles. The amphiphilic surfactants are used due to their ability to self-assemble into different structures involving Van der Waals and electrostatic forces, hydrogen bonding and π - π interactions. Surfactants can assemble into spherical micelles at lower concentrations and into cylindrical shaped micelles at higher concentrations.

Mesoporous photocatalysts can be synthesized by evaporation-induced self-assembly (EISA). When using this method, alkoxide precursors are dissolved in a solvent (usually ethanol), at ambient temperature. Following the sol-gel method, colloidal structures are formed and dissolved in the alcohol to obtain a sol. These colloidal particles agglomerate forming a gel with a 3D network structure. During the sol-gel photocatalyst preparation, 4 stages take place as shown in Figure 18: (1) alcohol evaporation leads to the self-assembly process; (2) water and solvent reach equilibrium; (3) an organic-inorganic mesoporous structure is formed; and (4) condensation of the inorganic precursor occurs and this forms a mesoporous network[121].

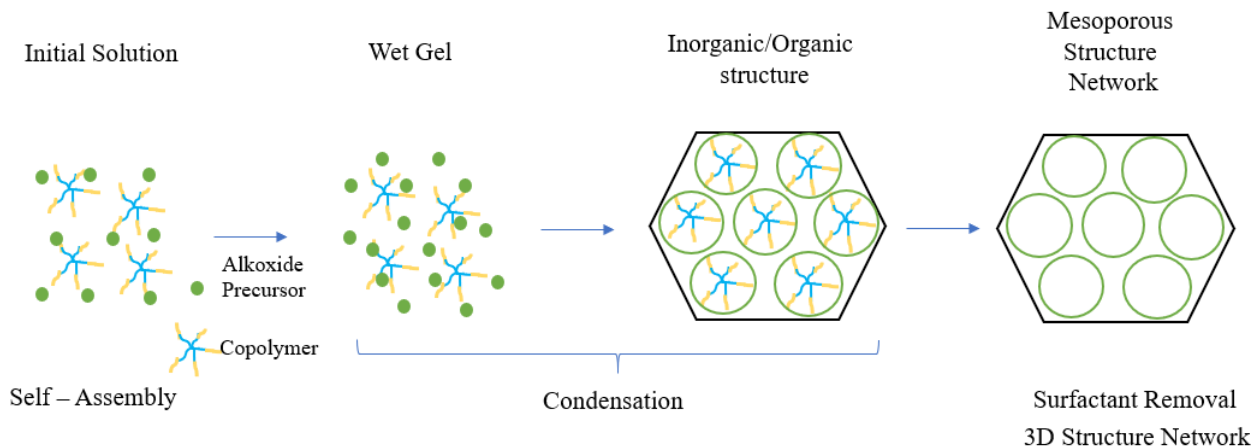


Figure 18 Schematic Diagram of the Formation of the Synthesized Mesoporous TiO₂.

These surfactants can be cationic, anionic, or non-ionic. Cationic surfactants are used to prepare silicates at high temperature conditions. Anionic surfactants are utilized for the preparation of mesoporous alumina catalysts, in an aqueous media. Non-ionic surfactants are used under low pH conditions to synthesize disordered wormhole silicas (HMS, MSU) or ordered structures via sol-gel dip-coating[122].

Non-ionic surfactants can be classified into diblock and triblock copolymers. Most of the mesoporous TiO₂ are synthesized with non-ionic surfactants. One of the copolymers frequently used is Pluronic F-127². The resulting photocatalyst displays a well-ordered TiO₂ structure, and enhanced morphological properties such as porosity, surface area, particle size and crystallinity[123].

Pluronics are non-ionic surfactant poly (ethylene oxide)/poly (propylene oxide) / poly (ethylene oxide) (PEO-PPO³-PEO⁴, MW = 12,600) triblock copolymers. Pluronic F-127 has a central hydrophobic PPO⁵ chain and two hydrophilic PEO⁶ tails, as shown in Figure 19. The

² F stand for the physical state of the copolymer in flake

³ Hydrophobic segment. It is 30% of the block copolymer

⁴ Hydrophilic segment. It is 70% of the block copolymer

⁵ Poly (propylene oxide)

⁶ Poly (ethylene oxide)

hydrophobic core of the copolymer determines the pore size of the TiO₂ mesoporous material[124].

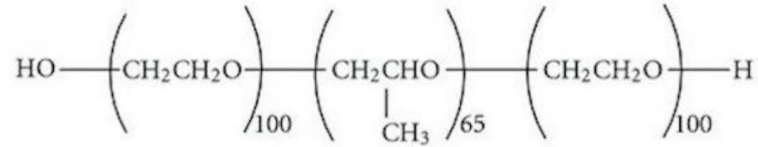


Figure 19 Pluronic F-127 Structure.

Using a non-ionic copolymer such as Pluronic F-127 provides some advantages over other surfactants such as: a) low cost, b) suitability for large scale processes, c) fewer steps for the photocatalyst synthesis, d) adequate properties to modify mesopore surface properties, e) “thermo-responsive” characteristics as it changes its structure with temperature, and f) hydrophobic- hydrophilic polarity for the creation of pores [125], [126].

Thus, after the use of the sol-gel method and by adding a copolymer, a mesoporous TiO₂ photocatalyst is formed, as described in Figure 20. In the first stage, the hydrophobic block (PPO) core is surrounded by the PEO tails (Figure 20a). Then, the PEO tails attach to TiO₂ in the framework structure. The PEO is then encapsulated between the PPO core and the TiO₂ matrix (Figure 20b). Following this, an inorganic-organic hybrid layer is formed with a dominant TiO₂ composition (Figure 20c). Calcination of the formed xerogel yields a TiO₂ photocatalyst with a mesoporous structure. The copolymer is removed during this step, leaving a structured TiO₂ framework (Figure 20d) [127], [128].

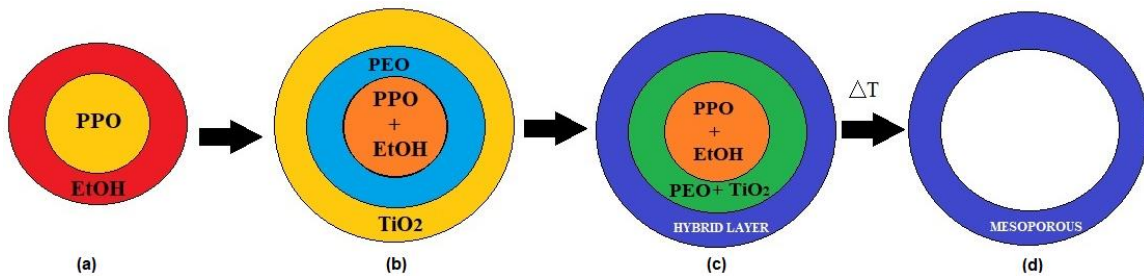


Figure 20 Schematic Diagram of the Formation of the Synthesized Mesoporous TiO₂ [129].

Given the previously explained advantages of using Pluronic F-127 surfactant, it was chosen to be used as co-polymer for the synthesis of the TiO₂ mesoporous photocatalyst in the present study.

3.3.3 Photocatalyst Preparation

Following the sol-gel method, the photocatalyst of the present study was synthesized, as discussed in Section 3.3.1, with the preparation of the photocatalyst using the following reagents: (a) ethanol USP (C₂H₅OH) obtained from commercial alcohols, (b) hydrochloric acid (HCl, 37% purity), (c) Pluronic F-127, (d) anhydrous citric acid, (e) titanium (IV) isopropoxide, and (f) palladium (II) chloride (PdCl₂, 99.9% purity). All the reagents were purchased from Sigma Aldrich (Oakville, Ontario, Canada). Detailed information about the photocatalyst synthesis method is shown in Figure 21.

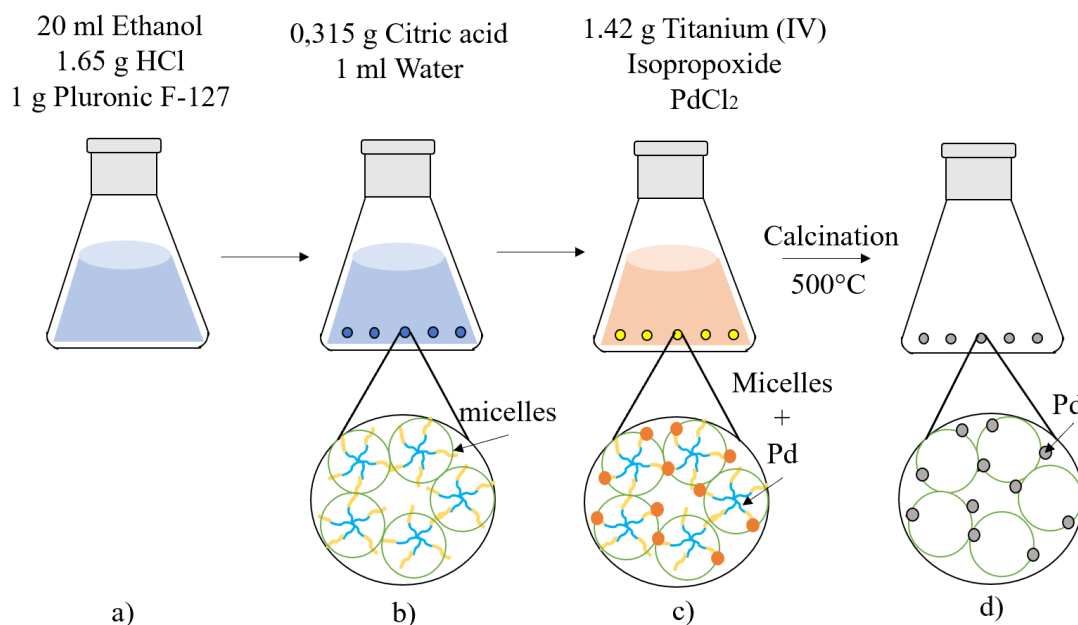


Figure 21 Description of the Four Consecutive Steps Used during Pd-Doped TiO₂ Photocatalyst Preparation: (a) Ethanol enters the interface between the hydrophilic (PEO) and hydrophobic (PPO) chains and attaches to the hydrophobic core, (b) A hydrophobic block (PPO) is placed in a central location surrounded by the PEO tails forming micelles, (c) The PEO tails become attached to the TiO₂, leaving a hybrid outer layer with a dominant TiO₂ composition, and (d) Calcination for 6 to 8 hours at 500°C of the resulting photocatalyst precursor yields a TiO₂ with a 3D mesoporous structure[102], [130], [131].

Considering that palladium oxidizes during the calcination step, the resulting photocatalyst had to be reduced in a subsequent step. To accomplish this, the synthesized semiconductor was placed in a flow reactor under close to atmospheric pressure, 1 cm³/s of Ar/H₂ (g) (90/10%, Praxair) and 500°C for 3 h period [97]. However, from the XPS results, it is possible to observe that metallic palladium was not completely reduced. Therefore, a further and critical Pd-TiO₂ photoreduction step was implemented in the Photo-CREC Water-II (PCW-II). The photocatalyst was irradiated under near-UV light, at room temperature for 60 min, to obtain a more reduced mesoporous material. It is important to mention that all prepared photocatalyst of the present study were subjected to the above-described preparation method.

Note that the sol-gel phase occurred at room temperature, with this phase enhancing strong surface interactions between reagents [132].

Figure 21 shows that ethanol was added at the beginning of the photocatalyst synthesis, given that this was the hydrophilic species to be attached to the PPO chains of the Pluronic F-127. The titanium-rich species (titanium isopropoxide) attach to the hydrophilic PEO tails of the copolymer[133].

Given that anatase is the most photoactive phase of the TiO₂, a high anatase/rutile ratio was wanted. To accomplish this, the addition of hydrochloric acid contributed towards the formation of high anatase levels. Citric acid was also used to control and reduce the pH to 0.74, in order to help functionalize the hydrophilic surface of the TiO₂ chains. This enhanced the particle binding to the hydrophilic (PEO) tails of the F-127. The addition of hydrochloric acid and citric acid to the photocatalyst promoted a rapid hydrolysis process, followed by a slower polymerization stage.

During the drying process, water, ethanol and HCl evaporated, while the remaining copolymer was removed during the calcination step, at temperatures of 500°C.

3.4 Photocatalytic Experiments

The photocatalyst was evaluated using the Photo-CREC Water-II reactor with a BLB near-UV lamp or alternatively with a fluorescent visible light lamp. The hydrogen storage/mixing tank

was loaded with 6000 mL of water and 0.15 g L^{-1} of the TiO_2 photocatalyst. Ethanol was used as sacrificial agent, and the pH was adjusted at the beginning of the reaction to 4 ± 0.05 using H_2SO_4 [2 M].

Prior to the initiation of the experiment, 0.15 g/L of the Pd- TiO_2 photocatalyst was added to the solution with the following steps being considered: (a) 0.9 g in total of Pd- TiO_2 was mixed with 100 mL of water and subjected to sonication for a 10 min period, to ensure good particle distribution and avoid possible agglomeration; (b) once a thorough dispersion of the Pd- TiO_2 particles was achieved, the photocatalyst–water solution was added to the 6 L of water contained in the Photo-CREC Water-II Reactor, (c) Following this, the pump and lamp were turned on for 30 min prior to the reaction, allowing lamp stabilization and better photocatalyst dispersion in the liquid solution. (d) Finally, for 10 min , argon was used as an inert gas for oxygen removal, from the gas phase in the hydrogen storage tank.

Gas and liquid samples were taken every hour, for 6 h of continuous irradiation. For the experiments under visible light, an initial photoreduction step with near-UV light was considered. Before the reaction began, the photocatalyst was photoirradiated for one hour, with near-UV light, to achieve the further reduction of the catalyst. This approach was reported by Rusinque et al.[134].

3.5 Analytical Techniques

The gas phase was analyzed with a Shimadzu GC2010 Gas Chromatograph Inc (Mandel, Guelf, ON, Canada) using argon (Praxair 99.999%) as a carrier gas. This unit was equipped with a HayeSepD 100/120 mesh packed column ($9.1 \text{ m} \times 2 \text{ mm} \times 2 \mu\text{m}$ nominal SS) (Sigma Aldrich, Oakville, ON, Canada) used for the separation of hydrogen from air. Additional details and information regarding the GC analysis of the Pd- TiO_2 photocatalyst are provided in **Appendix A**.

For the liquid phase, the Shimadzu HPLC Model UFLC (ultra-fast liquid chromatography) System was utilized using $0.1\% \text{ H}_3\text{PO}_4$ as a mobile phase. This unit contains a Supelcogel C-

610H 30 cm × 7.8 mm ID column. This quantitative analysis was performed by employing the RID (Refractive Index Detector) 10A due to the polar nature of ethanol. This HPLC separated ethanol from water for further quantification.

A colorimetric method was employed for the quantification of hydrogen peroxide (H_2O_2), being this one of the by-products of the water splitting reaction. H_2O_2 was measured at low concentrations (0–10 mg L⁻¹ approximately). In the colorimetric method, iodide and N-dimethyl-p-phenylenediamine (DPD) were used to detect H_2O_2 during the photocatalytic reaction. The collected sample was mixed with ammonium molybdate that decomposes H_2O_2 in solution and with KI that oxidizes iodide to iodine[135]. Iodine posteriorly oxidizes the DPD compound, generating a pink color. The DPD compound absorbance was then measured, using a spectrophotometer Spectronic 200+, Thermo Spectronic (Thermo Fischer, Mississauga, ON, Canada), which provides a 340 to 950 nm wavelength range and a nominal spectral bandwidth of 20 nm.

The hydrogen peroxide concentration was estimated using a linear calibration for 530 nm, considering the absorption spectra of the sample. All the reagents used for hydrogen peroxide detection were purchased from Hach® (London, ON, Canada). A commercial H_2O_2 technical-grade solution (30% w/w of H_2O_2) was supplied by BioShop Canada (Burlington, ON, Canada).

3.6 Determination of H_2O_2 Concentrations

To determine the amount of H_2O_2 , 0.15 mL of KI solution (20%) and 0.15 mL of Mo (VI) solution (ammonium molybdate in sulfuric acid) were placed in a 10-mL sample. The volumetric flask was capped and shaken for proper mixing. After 6 min of reaction time, one pillow of DPD (bag of N, N-dimethyl-p-phenylenediamine), with a total of 25-mL of chlorine powder, was added to the prepared sample cell. A pink color developed, indicating the presence of H_2O_2 . Subsequently, the sample was transferred to a quartz cuvette, and the absorbance was measured by a spectrophotometer (Spectronic 200+, Thermo Spectronic). The absorbance was obtained at 530 nm, in terms of total chlorine concentration ($[\text{Cl}_2]$), and according to a

calibration curve shown in Figure 22. This methodology allowed the quantification of H₂O₂ in the sample. Deionized water was used as blank.

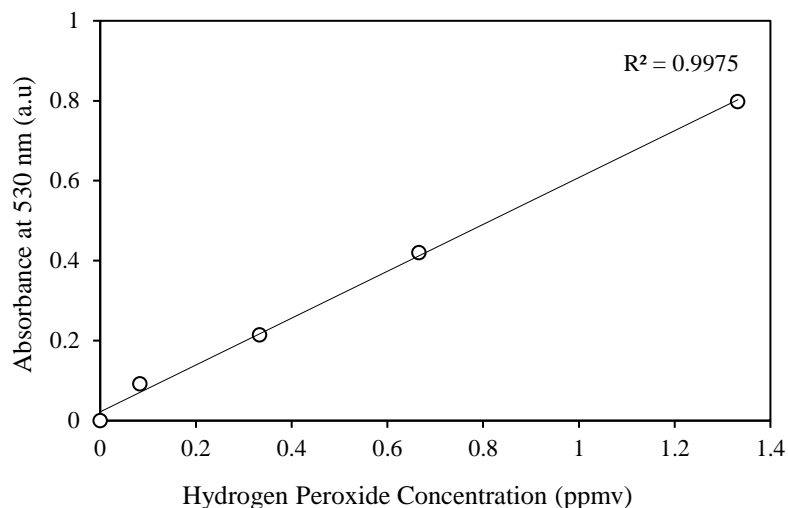


Figure 22. Calibration curve of H₂O₂ measurements by colorimetric method.

The colorimetric and permanganometry methods were compared to determine the best approach for hydrogen peroxide identification, specifically for the present study. The permanganometric titration showed a standard deviation between 9–16%, whereas the colorimetric method displayed a standard deviation in the 1–3% range, for 0.1 to 1.3 mg L⁻¹ H₂O₂ concentrations. Thus, it was proven that the colorimetric methodology provides more reliable results when measuring hydrogen peroxide concentrations.

Additional tests were performed to determine the accuracy of both methods (colorimetric and permanganometric), in the presence of an alcohol. In this case, ethanol was used, given that it is employed as a scavenger in the photocatalytic reaction. It was observed that the permanganometric method yielded a 43% standard deviation, while only a ±1% standard deviation was observed using the colorimetry method in the presence of ethanol. The lower reliability of the permanganometric titration was assigned to the ethanol scavenger interference. Thus, it was proven that the colorimetric methodology provides, in the present study, more reliable results when measuring hydrogen peroxide concentrations.

3.7 pH Measurements

The pH was measured with a digital pH meter Thermo Scientific Orion Star, with an accuracy of ± 0.05 . The pH was monitored in the slurry every hour, to determine its effect during the photocatalytic reaction.

3.8 Conclusions

Regarding Equipment, Materials, Photocatalyst Synthesis and Experimental Methods Section of the present doctoral thesis, these are the main conclusions:

- a) The slurry Photo-CREC Water-II Reactor unit, allows uniform light distribution inside the reactor, uniform catalyst distribution, minimum catalyst fouling, a well-mixed suspension and irradiation measurements, and all this for a controlled photocatalytic water splitting reaction.
- b) The photocatalyst is activated with a low input 15w Near-UV or alternatively with a 15w visible lamp.
- c) The sol-gel method used in this thesis is adequate for the synthesis of a noble metal doped TiO₂ photocatalyst using a Pluronic F-127 surfactant. This polymeric template modifies the mesoporous TiO₂ structure.
- d) Photocatalytic experiments were carried out in the novel unit Photo-CREC Water II Reactor under controlled conditions.
- e) Hydrogen and by-products were evaluated using analytical techniques such as GC chromatography for the gas phase, HPLC for the liquid phase and colorimetry for hydrogen peroxide identification.

Chapter 4

4 Photocatalyst Characterization

This chapter describes the main characterization methods used for assessing the photocatalyst Pd-TiO₂ properties, including chemical composition (elemental composition, and chemical state), physical properties (surface area, pore size distribution and pore size, phase composition, metal dispersion and metal crystallite size), and band structure (band gap).

4.1 N₂ Physisorption

The BET (Brunauer–Emmett–Teller) method provides a specific surface area evaluation based on nitrogen multilayer physisorption, which is measured as a function of relative pressure on a porous material, with an accuracy of $\pm 0.5\%$ as given by the BET manufacturer. The capillary condensation principle is applied to determine the pore volume and the pore size distribution. The area is given in m² g⁻¹ units.

In the BET, it is assumed that the photocatalyst reaches equilibrium under nitrogen atmosphere, with the amount of adsorbed gas being a function of the adsorbate partial pressure [136]. There are 6 types of possible adsorption isotherms, with type IV being the most common for mesoporous materials.

Figure 23 describes the four stages of the nitrogen physisorption process:

- a) *Stage 1*: At low pressures, isolated sites adsorb nitrogen gas molecules.
- b) *Stage 2*: As nitrogen gas pressure increases, the adsorbed nitrogen molecule coverage increases, forming a monolayer. The BET equation can be used at these conditions, to calculate the solid specific surface area.
- c) *Stage 3*: As nitrogen pressure rises further, this causes nitrogen multilayer adsorption surface coverage, with the smaller pores of the sorbent being fully covered first.
- d) *Stage 4*: Finally, increasing the nitrogen gas pressure allows complete filling of the pores. The BJH calculation can be then used to determine pore diameter, volume and distribution.

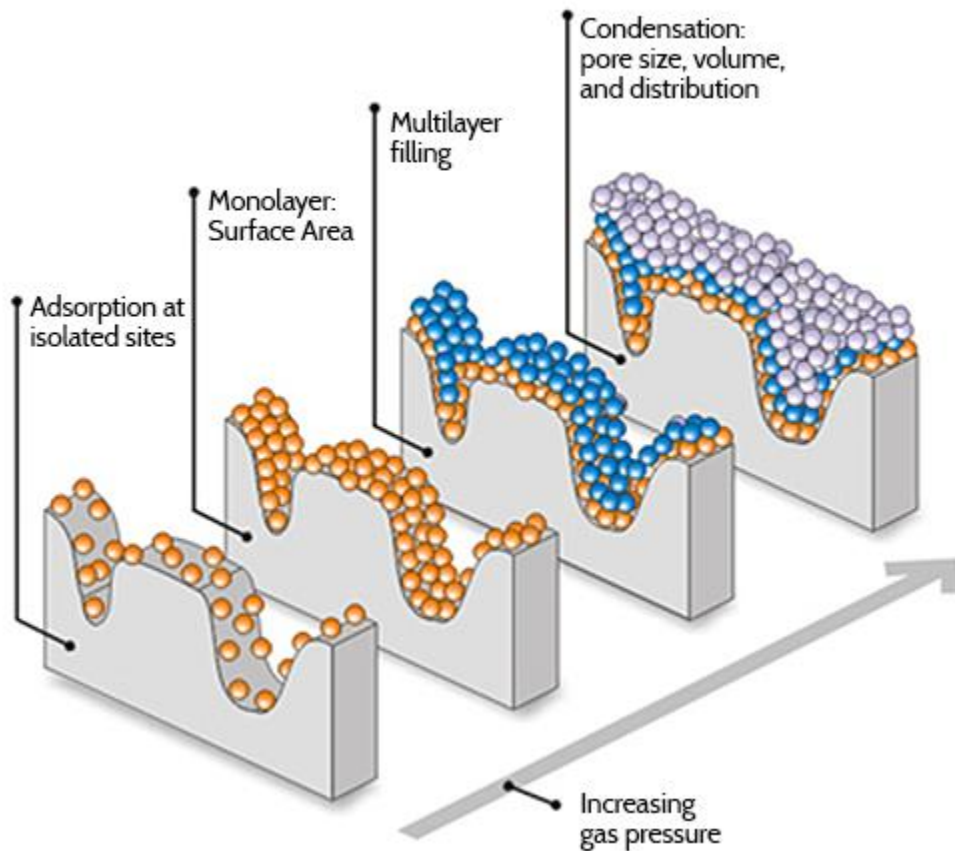


Figure 23 BET and BJH. Process description [137].

In Stage 2, once the nitrogen monolayer is formed, the resulting sorbed volume of nitrogen gas can be calculated.

The photocatalyst surface areas were determined using a BET surface area analyzer (Micrometrics, ASAP 2010) at -195°C . The photocatalyst was degassed at 150°C for (3) hours. Nitrogen was then used to evaluate the sample and to generate adsorption-desorption equilibrium isotherms.

On this basis, the BET surface area can be calculated based on Equation 8:

$$S_{\text{BET}} = \frac{\text{CSA} \times (6.03 \times 10^{23})}{(22414 \text{ cm}^3 \text{ STP}) \times (10^{18} \text{ nm}^2)/\text{m}^2 \times (S + Y_{\text{INT}})} \quad \text{Equation 8}$$

With CSA being the molecular cross-sectional area of the gas used (nm^2) and S and Y the Slope ($S \text{ g/cm}^3 \text{ STP}$) and the intercept ($Y_{\text{INT}} \text{ g/cm}^3 \text{ STP}$) in the $1/(V[(P_0/P) - 1])$ versus P/P_0 of the BET plot.

To determine the average pore diameter (D_p), the BJH method (Barret, Joiyner and Halendaer) can be used. This equation considers the experimental obtained isotherms and the Kelvin equation, which relates the P/P_0 relative pressure in pores of specific size, at which capillary condensation takes place [138]:

$$\ln \frac{P}{P_0} = - \frac{2\gamma V_M}{R_K RT} \text{Cos}\theta \quad \text{Equation 9}$$

Where P represents the equilibrium pressure in atm, P_0 the pressure of vapour in atm, γ the liquid surface tension in N/m, V_M the molar volume of the condensed phase in cm^3/mole , R_K the mean radius of curvature of the liquid meniscus in m, R the gas constant, T the temperature in K and θ the meniscus contact angle. When using nitrogen, a $34.68 \text{ cm}^3/\text{mol}$ V_M , a $8.72 \times 10^{-3} \text{ N/m}$ γ and a zero θ are set [139].

Furthermore, the pore volume (V_p) of the photocatalyst is determined, by relating the liquid nitrogen adsorbed at the P/P_0 relative pressure at 0.99 [121]. Relative pressure (P/P_0) are considered in the 0 to 0.20 range, with a C constant, related to the sorption energy of the first adsorbed layer, in the 100-120 range and this for all photocatalysts studied.

Figure 24 reports the adsorption isotherms for the TiO_2 photocatalyst with different Pd loadings. These are Type IV isotherms with described adsorption and desorption isotherm paths for each semiconductor studied[139].

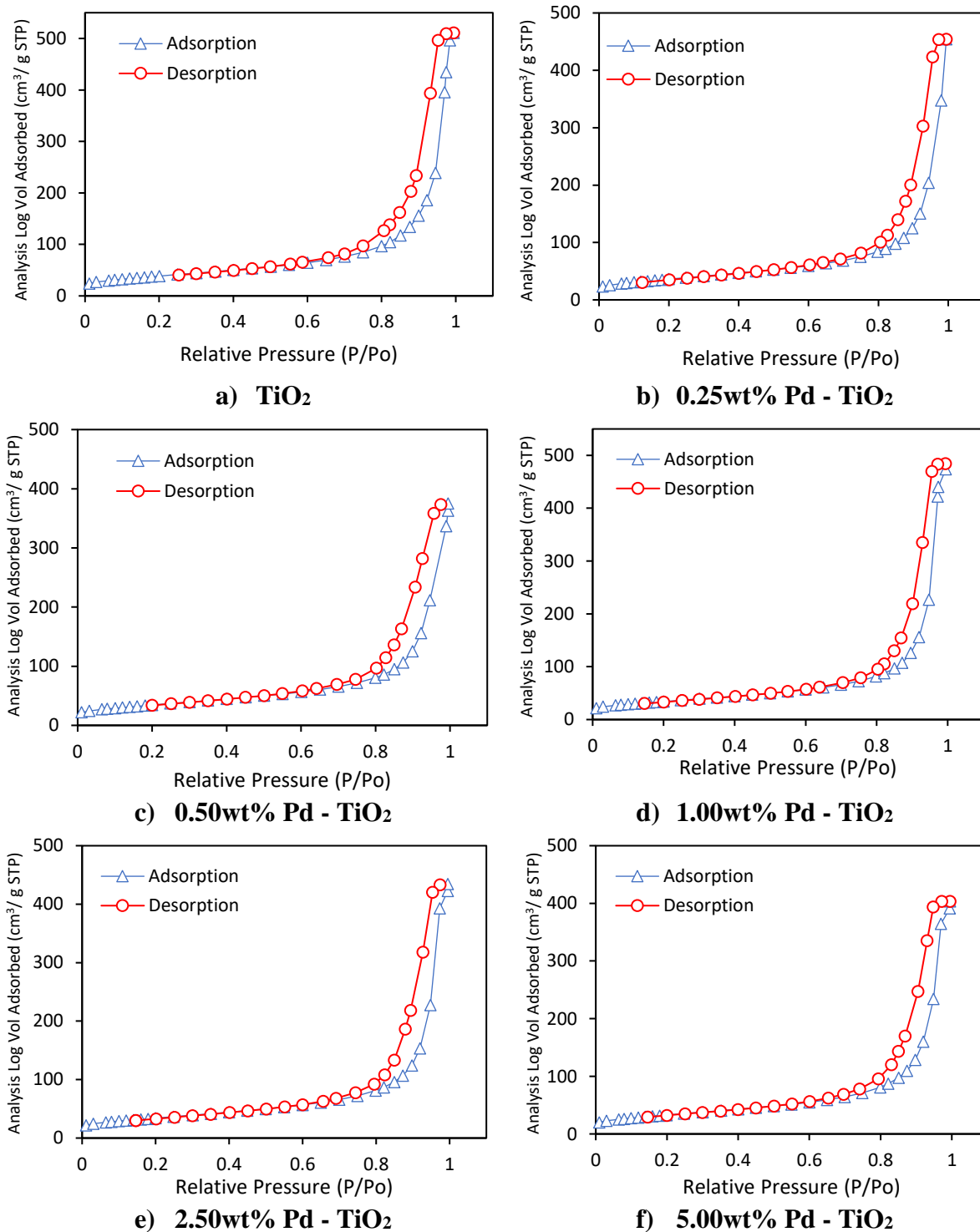


Figure 24 N₂ Adsorption-Desorption Isotherms for Mesoporous TiO₂ at Different Palladium Loadings.

On the basis of the obtained isotherms the Pd-TiO₂ photocatalysts of the present study were characterized. Table 10 reports the specific surface area, the average pore diameter and the specific pore volume for various mesoporous TiO₂ prepared using F-127 template. It is shown that when using this template, the morphological properties of TiO₂ are improved as follows: (a) specific surface areas are increased, (b) average pore diameters are augmented, and (c) specific pore volumes are increased. Furthermore, one can also notice that the F-127-TiO₂, displays both higher porosity and specific surface area than the TiO₂ alone.

Table 10 Surface Area and Pore Diameter Using a Pluronic F-127 Template.

Photocatalyst	S _{BET} (m ² g ⁻¹)	D _p ^{BJH} (4V _p ^{BJH} /S _{BET}) (nm)	V _p ^{BJH} (cm ³ g ⁻¹)
Degussa P-25	59	7.5	0.25
TiO ₂	140	17.5	0.61

According to Table 11, the best results for the specific surface area were obtained with the mesoporous TiO₂ photocatalysts. These photocatalysts display a clear increment of the specific surface area and specific pore volume (D_p) when compared to Degussa P-25 (commercial titania photocatalyst that is commonly used in photocatalytic reactions). Furthermore, for the TiO₂ doped with palladium loadings greater than 0.25 wt%, a decrease in the specific surface area was attributed to a moderate blocking of the small TiO₂ pores, with Pd leading to an increment in the average pore size [140].

Table 11 Surface Area and Pore Diameter Using Palladium.

Photocatalyst	S _{BET} (m ² g ⁻¹)	D _p ^{BJH} (4V _p ^{BJH} /S _{BET}) (nm)	V _p ^{BJH} (cm ³ g ⁻¹)
Anatase	11	7.3	0.05
Rutile	5	4.7	0.05
0.25 wt% Pd-TiO ₂	131	16.5	0.53
0.50 wt% Pd-TiO ₂	124	16.8	0.52
1.00 wt% Pd-TiO ₂	123	21.2	0.65
2.50 wt% Pd-TiO ₂	122	19.9	0.60
5.00 wt% Pd-TiO ₂	119	18.9	0.56

Furthermore, by using the Barrett-Joyner-Halenda (BJH) method with N₂ desorption isotherm, the pore size distribution was determined. The mesoporous pore size distribution was

found to be unimodal for the 0.25 and 0.50 wt% Pd–500 °C thermally treated TiO₂ photocatalysts, with pore sizes in the 18–22 nm range. However, for the photocatalysts with Pd loadings equal or larger than 1.0 wt%, a bimodal pore size distribution was observed, with a second peak at 16–35 nm.

4.2 Temperature Programmed Reduction (TPR)

The chemical state of the Pd dopant is a key parameter that influences photocatalyst performance. To establish this, TPR analysis allows reduction of PdO with hydrogen, yielding Pd⁰. To perform TPR a hydrogen-argon gas blend is used with the temperature of the sample increasing progressively. The hydrogen-argon gas mixture flows through the sample first and through the TCD detector, later. When the critical reduction temperature is reached, hydrogen molecules react with the PdO doped on TiO₂ forming Pd⁰ and water, which is removed by a cold trap. The resulting free of water gas with a hydrogen reduced content, is analyzed on line with a calibrated thermal conductivity detector [141]. The resulting TPR peak is employed to calculate the total amount of hydrogen consumed and consequently the Pd⁰ loading of the TiO₂.

The described H₂ Temperature Programmed Reduction (TPR) analyses of the Pd-TiO₂ photocatalysts were carried out in a Micromeritics AutoChemII Analyzer. A 250 mg photocatalyst sample were placed in the U-shaped tube with an Ar/H₂ (g) (90/10%) gas blend contacting the sample. Reaction temperatures were changed in a 15°C to 600 °C range, using an Ar/H₂ gas flow rate of 50 mL min⁻¹. The amount of H₂ consumed was measured using a thermal conductivity detector (TCD)[142].

TPR analysis showed that palladium oxide reduction [143] yields four distinctive TPR peaks. The first negative peak at 68 °C was attributed to the decomposition of palladium β-hydride, which occurred at the beginning of the TPR. This large negative peak at 68 °C was quite significant at the Pd loadings studied, in excess of 0.25 wt% [144]. This tendency to form palladium β-hydrides increased when the palladium dispersion increases.

The second observed TPR peak was a broad one and was assigned to palladium oxide reduction. This peak started at 200 °C and was completed at 300 °C, the broad peak was attributed to the particle size distribution (18–22 nm)[145], with larger particle sizes moderately increasing the palladium oxide reduction temperature.

Furthermore, as reported in Figure 25, the 0.25 wt%Pd-TiO₂ showed double peaks in the 400–600 °C range. The peak at 415°C can be assigned to the interaction between Pd species with the TiO₂ support and the peak at 594°C can be attributed to the Ti⁺⁴ ions surface reduction species [146][142]. Similar trends to the ones reported in Figure 25 were found for all doped photocatalysts, including the ones in the 0.25 wt% to 5.00 wt% Pd-TiO₂ loading range, It should be noted, however, that the second peak in the 200–300 °C range was considered only, in all the calculations and this to establish the amount of reducible palladium.

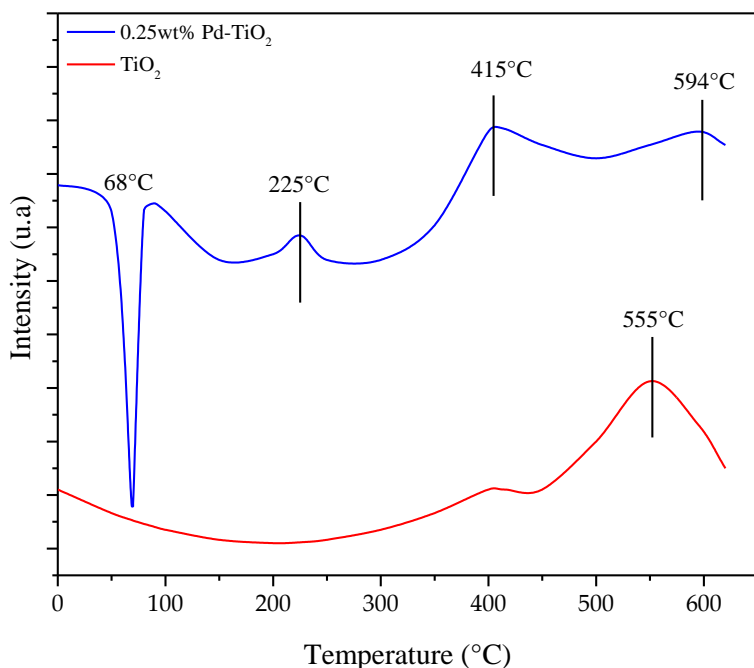


Figure 25 Temperature Programmed Reduction (TPR) of TiO₂ and 0.25 wt% Pd-TiO₂.

In summary, one can see that for the Pd-TiO₂ of the present study, the Pd reduction temperature was above 225 °C, which suggests strong metal-support interactions, potentially leading to high photocatalytic hydrogen production activity [147].

4.3 Pulse Hydrogen Chemisorption

The Pulse Chemisorption analysis determines the metal percentage or active species available for reaction [148].

In Pulse Chemisorption, pulses of hydrogen are contacted with the pretreated photocatalyst to achieve full chemisorption surface coverage. The volume of chemisorbed hydrogen is calculated considering the successive cumulative difference between hydrogen pulses and non-adsorbed hydrogen. Thus, by using hydrogen chemisorption, the total volume of hydrogen adsorbed on photocatalyst active sites is established [149].

Considering that a hydrogen molecule chemisorbs on a single Pd site, the calculation of the metal percent dispersion is given by Equation 10 as follows:

$$PD = 100 \times \left(\frac{V_s \times SF_{calc}}{SW \times 22414} \right) \times MW_{calc} \quad \text{Equation 10[148]}$$

Where PD is the metal dispersion percentage, V_s represents the hydrogen volume adsorbed [cm^3 STP], SF_{calc} stands for the adopted stoichiometry factor, SW expresses the photocatalyst sample weight [g] and MW_{calc} is the molecular weight of the noble metal palladium [g/g-mole].

A pulse chemisorption analysis was carried out in a U-shaped tube filled with 0.15 g of mass sample and then purged with argon at a rate of 50mL/min, to displace any oxygen present in the tube. The analysis started with a TPR evaluation to determine all the reducible available sites, at 500°C. As a result, the volume of hydrogen adsorbed was obtained [150].

Table 12 reports the hydrogen chemisorption analysis developed in the context of the present study, showing the effect of metal loading on metal dispersion. One can thus observed that when Pd is used as a dopant, it is shown that higher metal loadings lead to reduced metal dispersion. By increasing the metal loading, the metal dispersion decreases, with the metal loading remaining at a high 75% metal dispersion for the 0.25 wt% Pd-TiO₂.

Table 12 Chemisorption Analysis: Metal Dispersion.

Photocatalyst	Metal Dispersion (%)
0.25 wt% Pd–TiO ₂	75
0.50 wt% Pd–TiO ₂	27
1.00 wt% Pd–TiO ₂	26
2.50 wt% Pd–TiO ₂	12
5.00 wt% Pd–TiO ₂	8

4.4 X-Ray Diffraction

X-ray diffraction (XRD) is a non-destructive analytical technique that involves measurement of the X-rays scattered over a material. This technique is used to identify the active crystalline phase in a semiconductor material. X-rays are generated by a cathode ray tube and directed towards the sample. X-ray waves are scattered at different positions and angles, by the electron clouds around the atoms, producing constructive and destructive interference. The relationship between the principle of X-ray diffraction and the principle of reflection is given by Bragg's Equation:

$$n\lambda = 2d_{hkl}\sin \theta \quad \text{Equation 11}$$

Where, n represents the order of diffraction, λ the wavelength in nm, d_{hkl} the distance between lattice planes in nm and θ the angle of the incoming radiation in degrees.

Bragg's equation relates the wavelength of electromagnetic radiation to the diffraction angle (2θ) and the lattice spacing in a crystalline sample [151]. For TiO₂, X-ray diffraction allows the determination of the semiconductor structure. This is determined to be tetragonal for anatase and rutile or orthorhombic for brookite.

The XRD spectrum for each material was measured in a Rigaku Rotating Anode X-Ray Diffractometer (Rigaku, Auburn Hills, MI, United States) rated at 45 kV and 160 mA. For the characterization of the atomic structure of the photocatalysts, scans were taken between 20–80°, with a step size of 0.02° and a dwell time of 2 s/step.

XRD patterns for the different photocatalysts, are shown in Figure 26. XRD peaks for DP25, anatase and rutile are also given in Figure 26 in order to compare them with those of the Pd-TiO₂ photocatalysts. XRD peaks at 25°, 38°, 48°, 54°, 63°, 69°, 70.5° and 75° 2θ diffraction angles were assigned to anatase (101), (004), (200), (105), (204), (116), (220) and (215) crystal planes or lattice parameters (h k l), respectively. [JCPDS No. 73-1764], whereas XRD peaks at 40.12° and 46.66° were assigned to Pd (111) and (200) crystalline planes, respectively [JCPDS No. 87-0638].

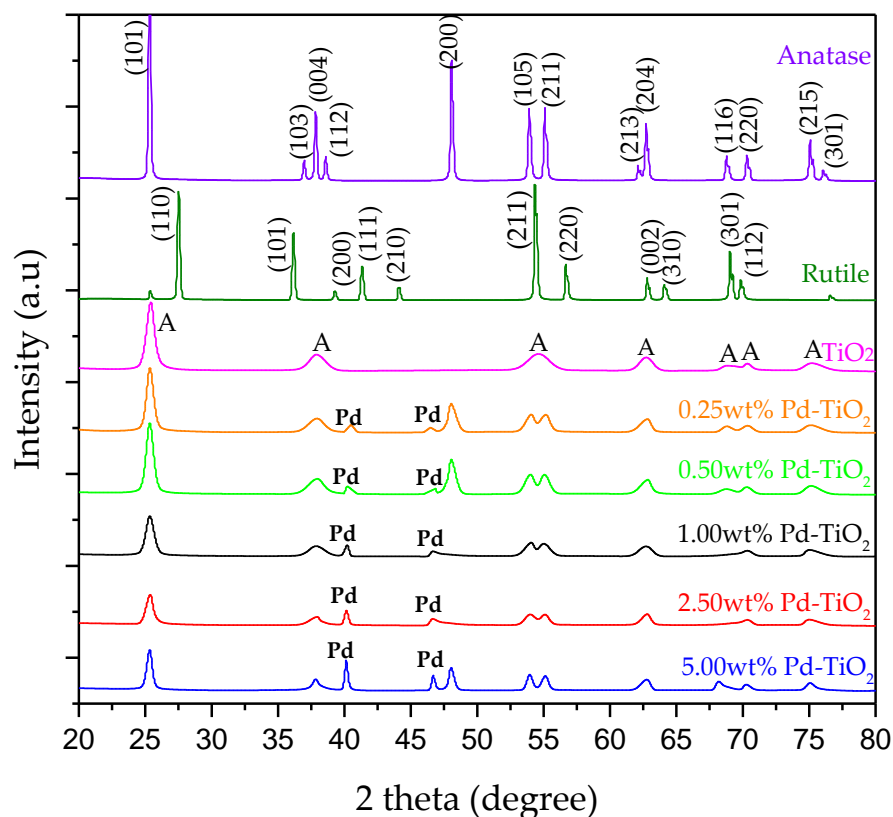


Figure 26 X-Ray Diffractograms for Pd-Doped TiO₂ Photocatalysts. XRDs for A = anatase and Pd = palladium are shown as a reference.

Furthermore, Figure 26 also reports that the XRD diffractograms for Pd-doped TiO₂ consistently showed a significant anatase XRD peak. The nature of the desirable anatase peaks in this semiconductor was confirmed with a 99.7% anatase reference sample from Aldrich [152]. For all the photocatalysts, anatase was the dominant TiO₂ crystalline phase assumed as 100% with no rutile being present. The high anatase content is closely related to the calcination temperature during the photocatalyst synthesis process.

One should mention that a third peak at $2\theta = 68.1^\circ$ (220), obtained when using Pd as a dopant, could overlap with anatase, and as a result, cannot be used for adequate Pd identification [153].

Figure 27 reports a comparative analysis of XRD diffractograms, for the mesoporous photocatalysts before and after exposure to 1 hour of near-UV photoreduction. There is a peak at 34° of the 2θ angle scale, which corresponds to (002) reflections of a tetragonal palladium oxide phase [JCPDS 41-1107]. Furthermore, the peaks at 40° and 46° of the 2θ angle scale relate to the Pd° [JCPDS No. 87-0638]. Thus, there is a structural difference in the semiconductor material after the reduction process, which is the absence of XRD detectable palladium oxides and the formation of metallic palladium hkl (1 1 1) and (2 0 0).

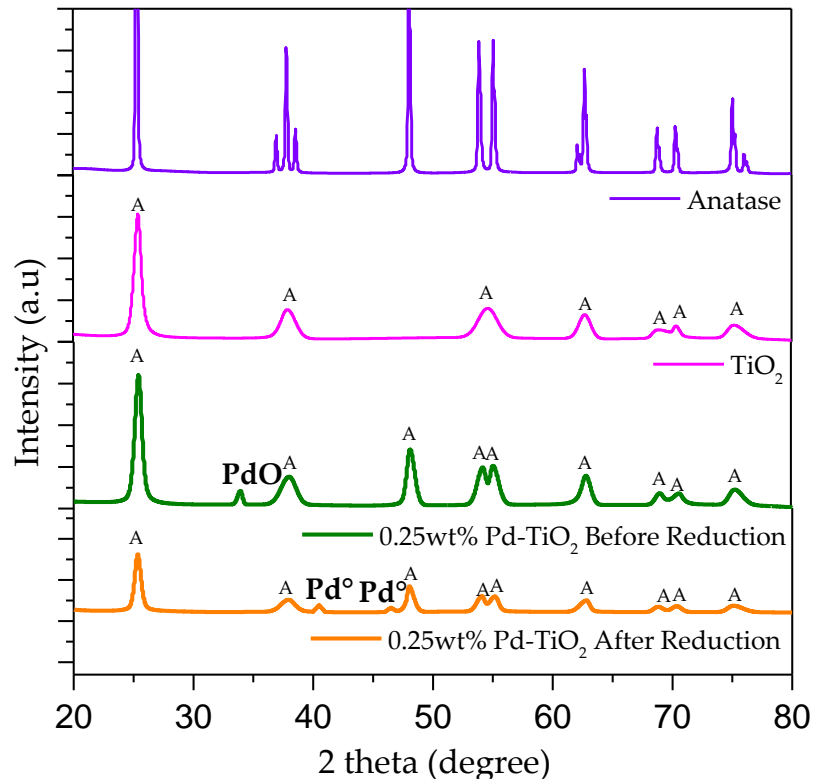


Figure 27 Comparative Analysis of 0.25 wt% Pd-TiO₂ Photocatalysts Before and After Reduction. A = anatase, PdO = palladium oxide and Pd[°] = metallic palladium.

Furthermore, the average size of the crystallites was calculated based on XRD peak broadening using the Scherrer Equation:

$$L_{hkl} = \frac{K\lambda}{\beta_{hkl} \cos \theta} \quad \text{Equation 12}$$

Where K represents the shape factor of 0.94 for cubic grains, L the crystallite mean size, λ is the X-ray wavelength, β the line broadening at half the maximum intensity (FWHM) and θ the Bragg angle.

The calculated crystallite sizes were between 9 and 14 nm and are reported in Table 13.

Table 13 Photocatalyst Crystallite Sizes.

Photocatalyst	Crystallite Size (nm)
DP 25	21
TiO ₂ (this study)	9
0.25 wt% Pd -TiO ₂	11
0.50 wt% Pd -TiO ₂	11
1.00 wt% Pd -TiO ₂	11
2.50 wt% Pd -TiO ₂	13
5.00 wt% Pd -TiO ₂	14

Moreover, the calculated a, b and c lattice constants of the tetragonal anatase unit cells are reported in Table 14. This shows that pure anatase was successfully obtained with the phase structures being maintained at $\alpha = \beta = \gamma = 90^\circ$ angles. These resulting a, b, and c parameters are in close agreement with those reported in the literature [53]. The lattice parameters $a = b \neq c$ and the crystal planes were calculated for the anatase phase as (h k l) = (1 0 1).

Table 14 Lattice Parameters for TiO₂ and Pd doped TiO₂.

Photocatalyst	a = b	c	2 θ (deg)	d (Å)
DP 25 [154]	3.7821	9.5022	25.33	3.5139
TiO ₂ (this study)	3.7679	9.5002	25.41	3.5025
0.25 wt% Pd TiO ₂	3.7832	9.4833	25.33	3.5139
0.50 wt% Pd TiO ₂	3.7858	9.4737	25.31	3.5155
1.00 wt% Pd TiO ₂	3.7825	9.5099	25.32	3.5147
2.50 wt% Pd TiO ₂	3.7748	9.4713	25.38	3.5065
5.00 wt% Pd TiO ₂	3.7691	9.4809	25.41	3.5025

Additionally, X-ray diffraction analyses were developed to determine whether there were changes in the photocatalyst crystalline structure during photocatalytic water splitting reactions. After 6 hours of irradiation, the anatase phase was found remaining predominant in

the TiO₂ photocatalyst. Furthermore, all the anatase peaks remained present in the palladium photocatalysts, except for the (200) peak that overlapped with the noble metal Pd at the 46.66°. Palladium peaks were consistently identified at a 40.12° angle (111) band, before and after the extended 6 hours photocatalytic runs. As can be seen in Figure 28 however, the 46.66° (200) peak was no longer observed where the signal could be too weak for a reliable analysis.

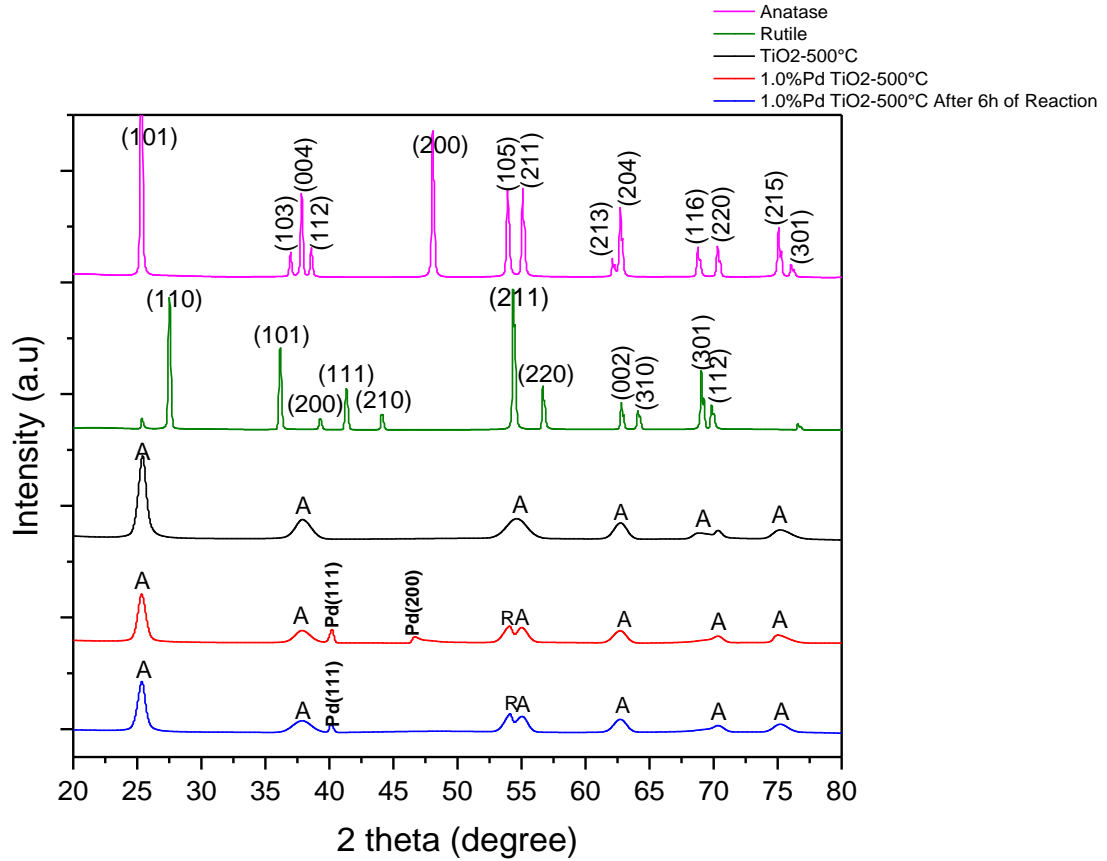


Figure 28 XRD Diffractograms for the Pd-Doped TiO₂ After 6h of Photocatalytic Water Splitting. XRD for anatase, rutile and undoped TiO₂ are reported, as a reference for comparison: A = anatase, R= Rutile, Pd=Palladium.

4.5 Band Gap

Semiconductors display a characteristic band gap in the near-infrared, visible or UV spectrum. Light absorption is null below the absorption edge. It augments once the light energy is high enough to excite electrons[155]. When a photon excites an electron from the valence band, it

jumps to the conduction band creating an electron-hole pair. Based on quantum mechanics, the probability of a photon exciting an electron from an initial to a final quantum state determines the frequency of absorption $\alpha(\nu)$.

An indirect band gap is determined by considering the incremental photon energy:

$$h\nu \geq E_g \quad \alpha \propto (h\nu - E_g - \hbar\Omega)^2 \quad \text{Equation 13[155]}$$

Where:

$\hbar\Omega$ represents the photon energy involved in the transition process and α denotes the absorption coefficient. h is the Planck constant and ν represents the radiation frequency.

To determine the band gap, a UV-VIS-NIR Spectrophotometer (Shimadzu UV-3600, Nakagyo-ku, Kyoto, Japan) equipped with an integrating sphere was used, and employed BaSO₄ as a reference material[156].

By using the Kubelka–Munk (K–M) method, Tauc plots were developed, in order to establish the corresponding band gaps for each photocatalyst, based on Equation 14 [157].

$$\alpha h\nu = A (h\nu - E_g)^m \quad \text{Equation 14}$$

Where A is the optical constant, α represents the absorption coefficient, E_g denotes the optical band gap in eV, m stands for a value equal to 2 for indirect transitions, h is the Planck constant (6.34E-34 J s/photon) and ν represents the radiation frequency ($\nu = c/\lambda$). c is the speed of light under vacuum (3.00E8 m/s²) and λ represents the wavelength in nm.

Figure 29 reports the variation of the " $(\alpha h\nu)^{1/2}$ " function versus the photon energy " $h\nu$ ". By applying the straight-line method proposed by Tauc, the indirect optical band gap is calculated when the straight line intersect the x-axis[158]. It is inferred on that basis that increasing the doping noble metal loading reduces the absorbance.

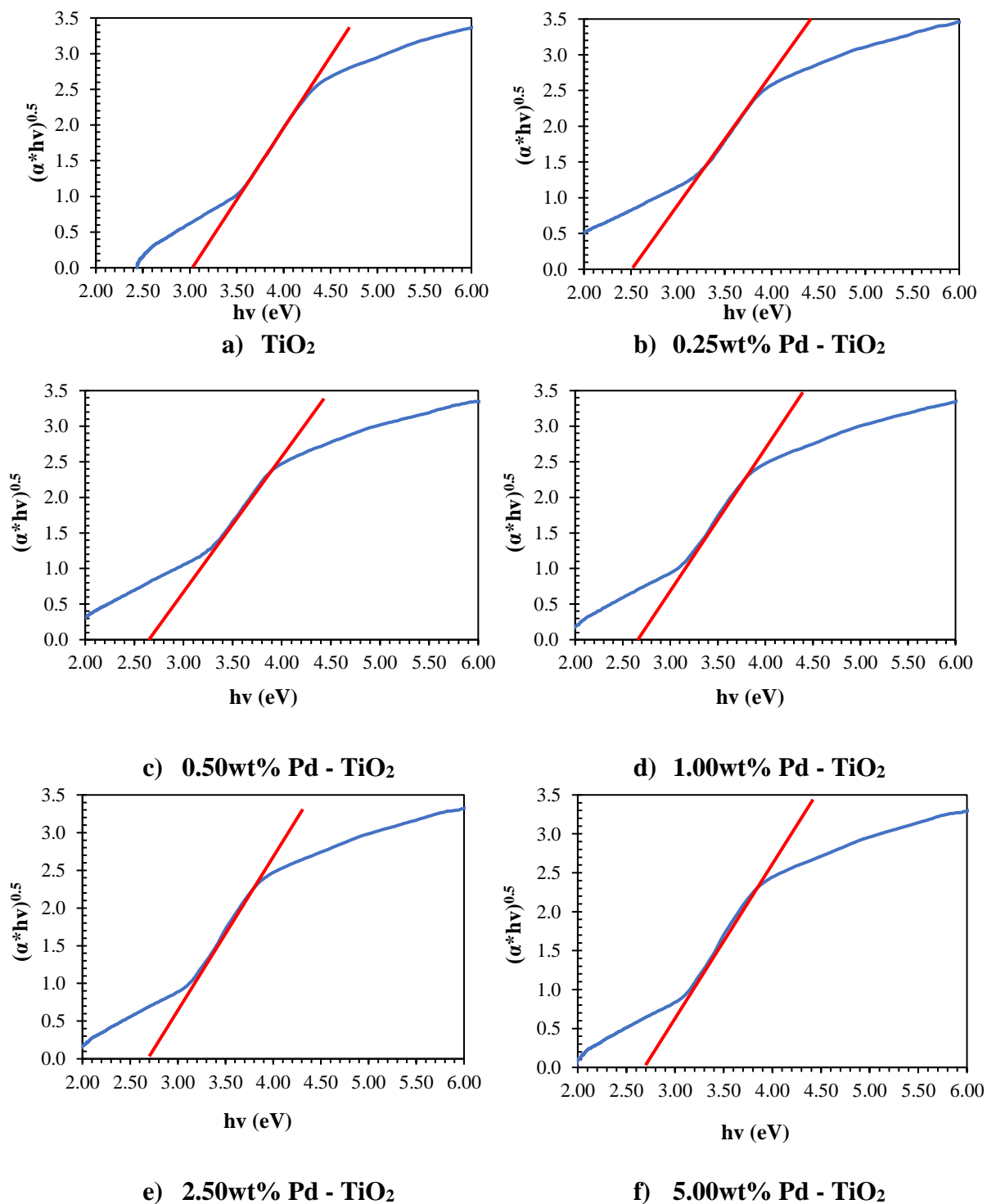


Figure 29 Band Gap Calculation Using the Tauc Plot Method and the Straight Line Extrapolation for the Following Photocatalysts: a) TiO₂, b) 0.25wt%Pd- TiO₂, c) 0.50wt%Pd- TiO₂, d) 1.0wt%Pd- TiO₂, e) 2.5wt%Pd-TiO₂ and f) 5.0wt%Pd-TiO₂.

Figure 29 shows as well, that when using the 0.25 wt% Pd-TiO₂, a linear extrapolation yields a 2.51 eV band gap. This 2.51 eV band gap corresponds to a 494 nm. The 2.51 eV and gap represents a significantly reduced E_{bg} , when compared to the 2.99 eV band gap obtained for mesoporous TiO₂ without Pd, as reported in Table 15. It is also observed in Table 15 that using Pd loadings above 0.25 wt%, yields a reversed trend in the E_{bg} , with band gaps increasing steadily instead.

It could be observed that the higher the noble metal loading, the more that visible light is absorbed. To quantify this effect, Equation 15 is used to calculate the fraction of absorbed light:

$$\%VUI = \frac{\int_{\lambda_{\min}}^{\lambda_{bg}} I d\lambda}{\int_{\lambda_{\min}}^{\lambda_{\max}} I d\lambda} \times 100\% \quad \text{Equation 15[102]}$$

Where VUI represents the visible utilized irradiation, I denotes the irradiance in photon/s, λ_{min} and λ_{max} correspond to the minimum and maximum wavelengths of solar irradiation, respectively and λ_{bg} stands for the band gap wavelength.

The VUI is incremental in the 21-31% range for different noble metal loadings. This effect can be attributed to the palladium crystallite sizes, with being these larger at higher palladium loadings, and displaying an improved visible light absorption [159].

Table 15 Optical Band Gap for a Photocatalyst Modified by Pt and Pd.

	Band gap (eV)	Wavelength (nm)	% of absorbed visible light
DP-25	3.03	410	3.24
TiO ₂	2.99	415	4.91
0.25wt%Pd-TiO ₂	2.51	494	31.34
0.50wt%Pd-TiO ₂	2.55	486	28.75
1.00wt%Pd-TiO ₂	2.60	486	28.75
2.50wt%Pd-TiO ₂	2.67	464	21.47
5.00wt%Pd-TiO ₂	2.67	464	21.47

According to Table 15, there is band gap reduction for the 0.25 wt% Pd-TiO₂, with this change being attributed to the Fermi level changes. This variation can be assigned to the sp-d orbital

exchange interactions between the band electrons and the localized d electrons of the Pd 3d ions, substituting the Ti⁴⁺ cations. The s-d and p-d exchange interactions give rise to a downward shift of the conduction band edge and an upward shift of the valence band edge, leading to a band gap narrowing [156], [158], [160]–[162]. However, at higher than 0.25%wt Pd loadings, it is speculated that the band gap increase is due to the dominant d-d transitions over the sp-d transitions.

It appears that low noble metal loadings (e.g., 0.25%wt Pd-TiO₂) facilitate both charge collection and light absorption[163]. Low Pd loadings give rise to localized energy levels in the band gap of the TiO₂. In this case, the valence band electrons of the TiO₂ are excited at wavelengths longer than 400 nm [164]. Alternatively, excessive noble metal loading may lead to smaller photocatalyst specific surface areas, with larger metal crystallites formed with PdO inclusions [165]. In this respect, XPS confirmed that the PdO presence shields incident photons, blocking light absorption and preventing the generation of semiconductor electron-hole pairs [166].

4.6 X-ray Photoelectron Spectroscopy (XPS)

X-ray photoelectron spectroscopy (XPS) analysis is a non-destructive technique that can be used to identify the elemental composition and the oxidation/reduction states in the first atomic layers of palladium in the synthesized photocatalyst [167].

In the XPS analysis, two cathodes can be used as energy emission sources: a) Al-K α (1,486.6 eV) and b) Mg-K α (1,253.6 eV)[155]. Peaks are the result of the incident light on the sample. Each peak is proportional to the number of atoms present. The chemical state of the emitted atoms affects the shape of the peak and the binding energy[155].

The relation between the binding energy (BE) and the electron kinetic energy (KE) is given by Equation 16.

$$BE = h\nu - KE - \phi \quad \text{Equation 16}$$

Where $h\nu$ represents the incident photon energy and ϕ stands for the work function. The samples were analyzed by X-ray photoelectron spectroscopy (XPS) using a Kratos AXIS Supra X-ray photoelectron spectrometer. XPS can detect all elements except hydrogen and helium. It probes the surface of the sample to a depth of 7 - 10 nanometres and has detection limits ranging from 0.1 - 0.5 atomic percent depending on the element. The survey scan analyses were carried out with an analysis area of 300 x 700 microns and a pass energy of 160 eV. The high-resolution analyses were carried out with an analysis area of 300 x 700 microns and a pass energy of 40 eV. A lower resolution pass energy was used for the high-resolution analyses as the amount of Pd present was very small. The Pd 3d spectrum was also collected for a very long time to achieve sufficient signal/noise.

Quantitative XPS analyses were performed in the present study, for the 0.25 wt% Pd-TiO₂. XPS analyses were carried out before photoreduction and after 60 min photoreduction, under near-UV irradiation. The Pd 3d_{3/2} and Pd 3d_{5/2} spin orbital splitting photoelectrons were observed in both the photoreduced and non-photoreduced 0.25 wt% Pd-TiO₂ photocatalysts.

Figure 30 reports the photoreduced and non-photoreduced 0.25 wt% Pd-TiO₂ photocatalyst XPS peaks. XPS peaks were analyzed via band deconvolution, at the 334.54 eV, 336.38 eV, 339.69 eV, and 341.54 eV characteristic binding energies.

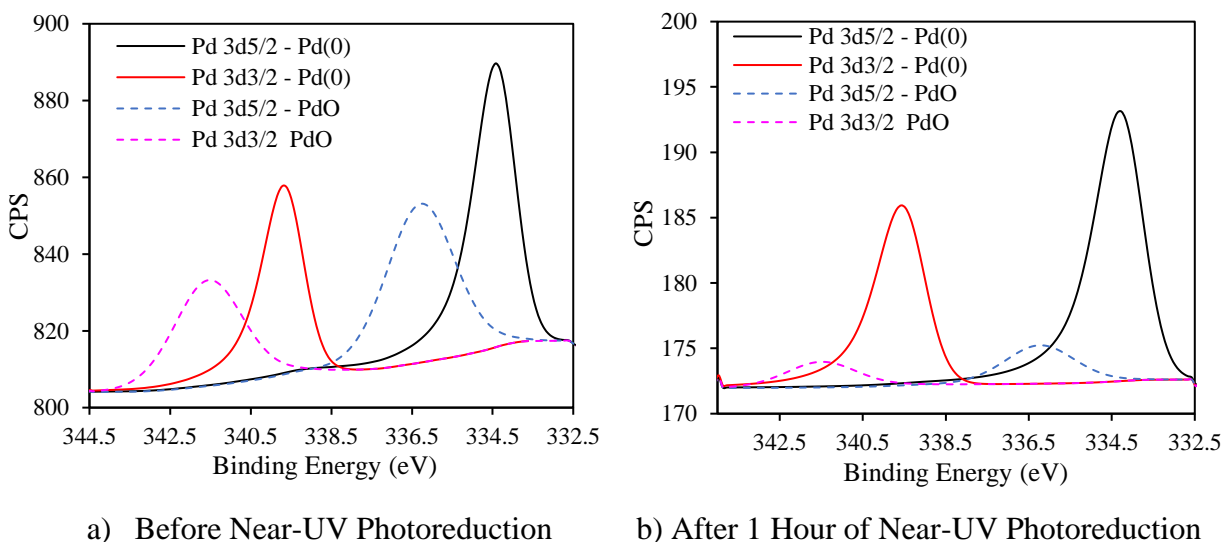


Figure 30 High-Resolution X-Ray Photoelectron Spectroscopy (XPS) Spectra for 0.25 wt% Pd-TiO₂: (a) Before near-UV photoreduction and (b) After 1 hour of near-UV photoreduction. Note: Continuous lines represent Pd⁰ at (i) 3d_{5/2} and (ii) 3d_{3/2}. Broken lines represent PdO at (iii) 3d_{5/2} and (iv) 3d_{3/2}.

The Pd 3d spectrum is curve-fitted with spin-orbital doublets and splitting separation values of 5.26 eV, with doublet constrained FWHMs (the full-widths-at-half-maximum), and peak area ratios of 3:2 (Pd 3d5/2: Pd 3d3/2). The metallic Pd⁰ line-shapes are asymmetric (defined as LA (1.9,7,2) in CasaXPS) and match those of a standard sputter cleaned Pd⁰ spectrum, while the Pd oxides display symmetrical peak shapes. The Pd (II) and Pd (IV) spectra use a 70% Gaussian - 30% Lorentzian product formula mixed line-shape.

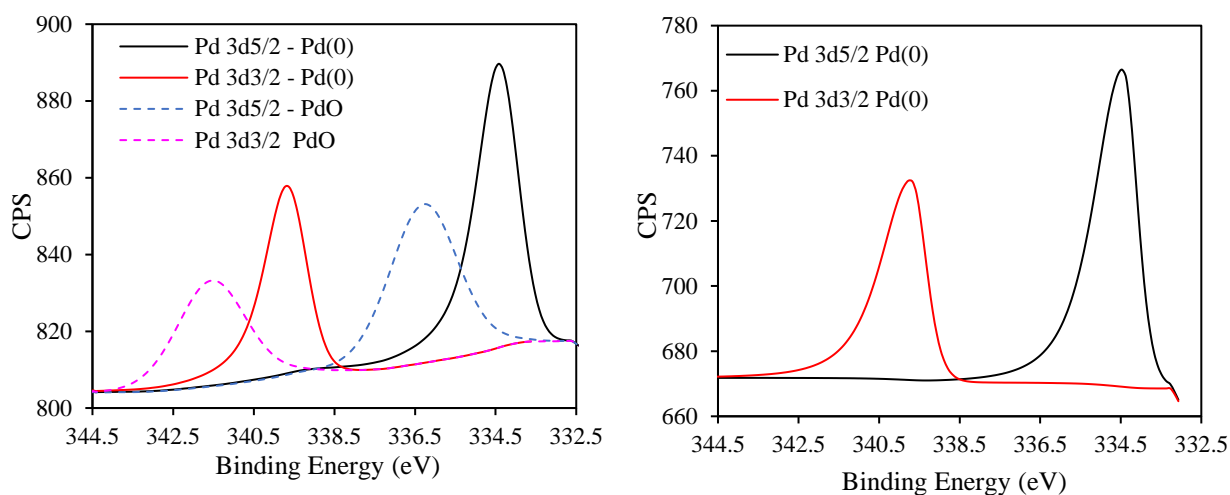
Table 16 reports the observed binding energies, for the 0.25 wt% Pd–TiO₂, with the FWHM and percentual areas.

Table 16 High-Resolution X-Ray Photoelectron Spectroscopy (XPS) Spectra Binding Energies and Peak Areas for the 0.25 wt% Pd–TiO₂, Before Photoreduction and After 60 min of Photoreduction Using Near-UV Irradiation.

Peak Name	Before Photoreduction			After 60 min of Photoreduction Using Near-UV Irradiation		
	Binding Energy	FWHM	% Area	Position	FWHM	% Area
Pd 3d3/2 PdO	341.54	2.00	50.2	341.49	2.00	18.3
Pd 3d3/2 Pd ⁰	339.69	1.13	49.8	339.56	1.29	81.7
Pd 3d5/2 PdO	336.28	2.00	50.2	336.23	2.00	18.3
Pd 3d5/2 Pd ⁰	334.43	1.13	49.8	334.30	1.29	81.7

According to Table 16 and Figure 30, in the XPS analysis, the 0.25 wt% Pd–TiO₂ photocatalyst displays the two most intense peaks, at 334.43 and 339.69 eV. These peaks were assigned to the metallic Pd. Furthermore, there are two other weaker recorded peaks at 336.28 and 341.54 eV, which are attributed to 3d5/2 and 3d3/2 binding energies of the PdO species.

Considering that after 60 min under near-UV photoreduction, 18.3% of PdO remains present in the photocatalyst, an increment in the near-UV exposure time could lead to a more reduced semiconductor. Figure 31 displays the observed binding energies for the 0.25 wt% Pd–TiO₂ before and after 24 hours of near -UV light exposure.



a) Before Near-UV Photoreduction

b) After 24 hours of Near-UV Photoreduction

Figure 31 High-Resolution X-Ray Photoelectron Spectroscopy (XPS) Spectra for 0.25 wt% Pd–TiO₂ Before Near-UV Photoreduction and After 24 Hours of Near-UV Photoreduction.

Table 17 reports a comparison between the XPS binding energies of the 0.25 wt% Pd–TiO₂ photocatalyst before and after 24 hours of near-UV photoreduction. One can see that there is a significantly increased in Pd⁰ content ranging from 49.8% up to 100% after near-UV irradiation, with no PdO presence. This increased Pd⁰ is the result of near-UV electrons reducing the oxidized Pd species.

Table 17 Comparison between High-Resolution X-Ray Photoelectron Spectroscopy (XPS) Spectra Binding Energies and Peak Areas for the 0.25 wt% Pd–TiO₂ Before and After 24 Hours of Near-UV Light Exposure.

Peak Name	Before Photoreduction			After 24 Hours of Photoreduction Using Near-UV Irradiation		
	Binding Energy	FWHM	% Area	Pos	FWHM	% Area
Pd 3d3/2 PdO	341.54	2.00	50.2	339.7	0.90	0.0
Pd 3d3/2 Pd ⁰	339.69	1.13	49.8	-	-	-
Pd 3d5/2 PdO	336.28	2.00	50.2	-	-	-
Pd 3d5/2 Pd ⁰	334.43	1.13	49.8	344.4	0.86	100.0

Furthermore, the XPS analysis of the 0.25%wt Pd-TiO₂ photocatalysts, also showed Ti 2p and O 1s bands at peaks of 454 and 526 eV, respectively (Figure 32). These bands were assigned to the titanium oxide photocatalyst.

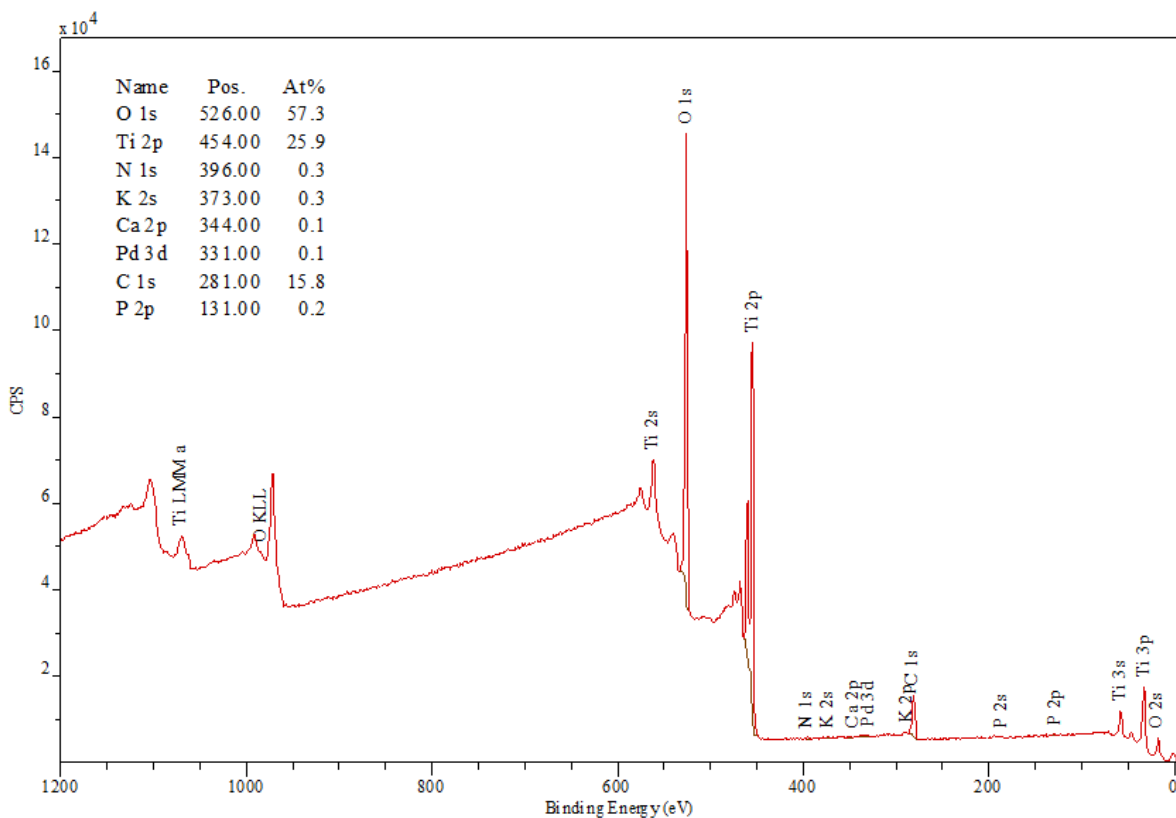


Figure 32 Survey Scan Analysis for 0.25 wt% Pd–TiO₂.

4.7 Conclusions

The following are the main conclusions of the present chapter:

- BET analysis can be used to establish specific surface area and pore size distribution of the synthesized photocatalyst of the present study.
- XRD analysis can provide valuable information on main semiconductor phases in the photocatalyst, as well as on its crystallite sizes.
- Pulse H₂ chemisorption can be employed for the determination of the noble metal dispersion.
- UV-Vis Spectroscopy and the derived Tauc plots can be used to establish the impact of Pd on band gaps. This is a very important consideration for hydrogen production via photocatalytic water splitting.
- Near-UV photocatalyst photoreduction by visible light irradiation can lead to a fully reduced photocatalyst. This may involve effective electron reservoirs, limiting electron hole recombination.

Chapter 5

5 Macroscopic Irradiation Energy Balance (MIEB)

The operation of the Photo-CREC Water-II reactor involves the emission of photons and their absorption in a circulating semiconductor slurry suspension media. To be able to establish the absorbed radiation in the Photo-CREC Water-II Reactor, macroscopic irradiation balances must be established in order to obtain accurate energy efficiency calculations.

5.1 Irradiation and Measurements

Irradiation in the Photo-CREC Water-II reactor (PCW-II) is provided by an inner lamp located at the centre of the reactor. This reactor type that allows homogenous photocatalyst recirculation, can be seen in Figure 33. The reactor unit is equipped with seven (7) silica windows located on the outer polyethylene reactor tube surface. Irradiation measurements are taken along the reactor axis by using these windows.

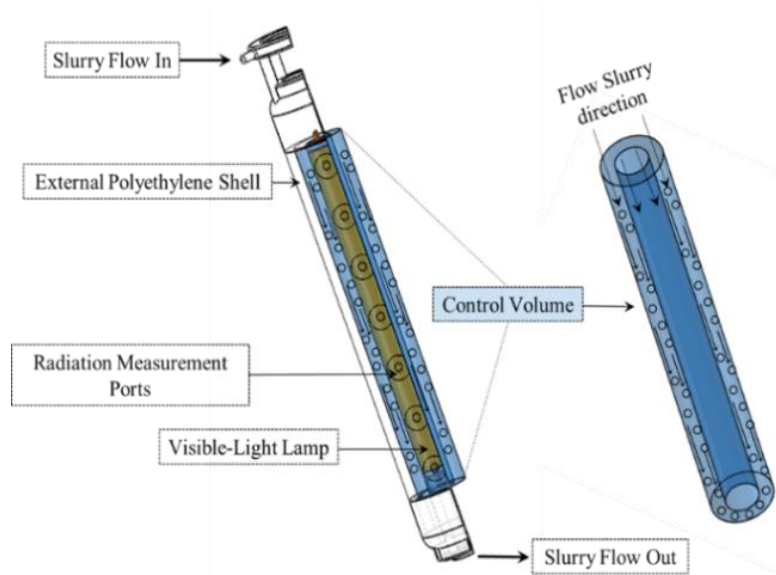


Figure 33 Schematic Representation of the 6000 cm³ Slurry Control Volume Used to Obtain Macroscopic Irradiation Balances.

A fibre optic spectroradiometer StellarNet EPP2000-25 measures the lamp emitted photon irradiation spectra. Measurements were taken in the 300 nm to 420 nm wavelength range for near-

UV experiments and in the 300 to 720 nm wavelength range for visible light spectra. The scanning time for all measures was set at 300 ms, to prevent reading saturation.

As described in Figure 34, the optical fibre spectroradiometer sensor is placed at a central position along the reactor axis to perform measurements. This determines a symmetric radiation profile along the PCW-II axial length. Emitted radiation is detected by the spectroradiometer and evaluated in: a) An empty PCW-II unit, b) A water filled PCW-II unit, c) A suspended photocatalyst filled PCW-II. Evaluation for c) conditions are developed before and after every experimental run.

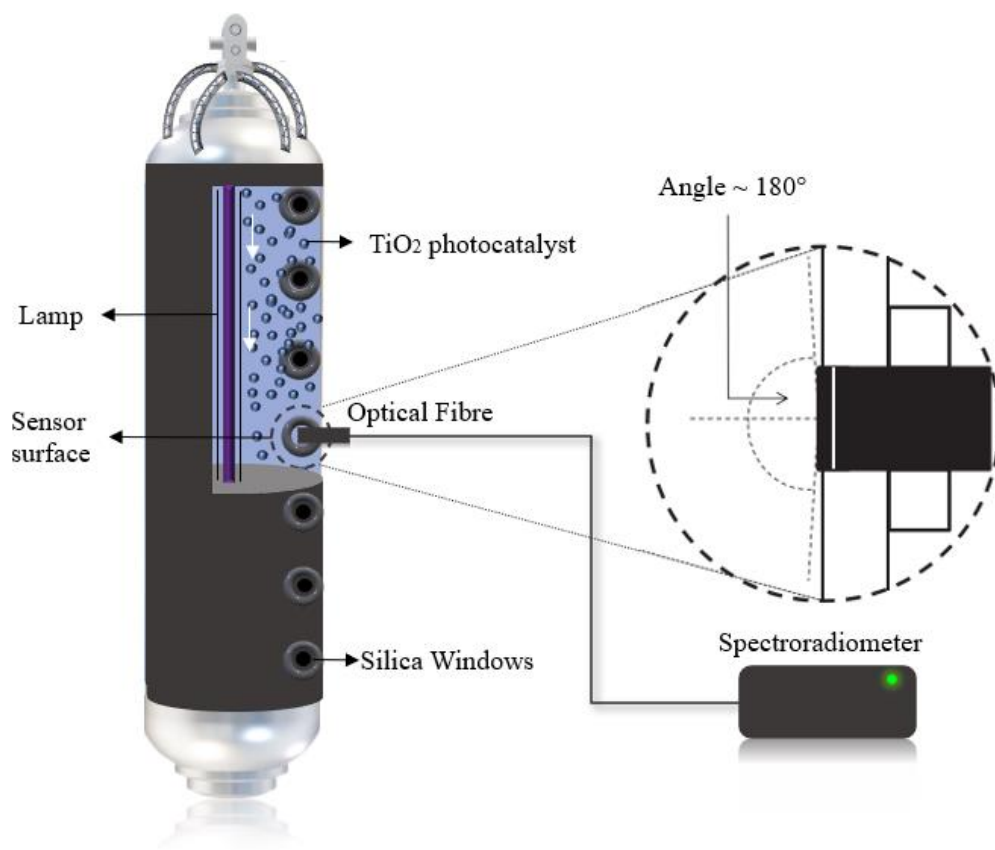


Figure 34 Photo-CREC Water-II Reactor with Optical Fibre Sensors in Place to Measure Transmitted Radiation [168].

5.2 Macroscopic Irradiation Energy Balance (MIEB)

Macroscopic Irradiation Energy Balances can be established using a “photocatalyst control volume” established by Salaices, Serrano and de Lasa [99] as follows:

$$P_a = P_i - P_{bs} - P_t \quad \text{Equation 17}$$

Where P_a is the rate of absorbed photons, P_i the rate of photons reaching the reactor inner surface, P_{bs} the rate of backscattered photons exiting the system, and P_t the rate of transmitted photons in Einstein/s.

Figure 35 describes the various radiation contribution involved in Equation 17:

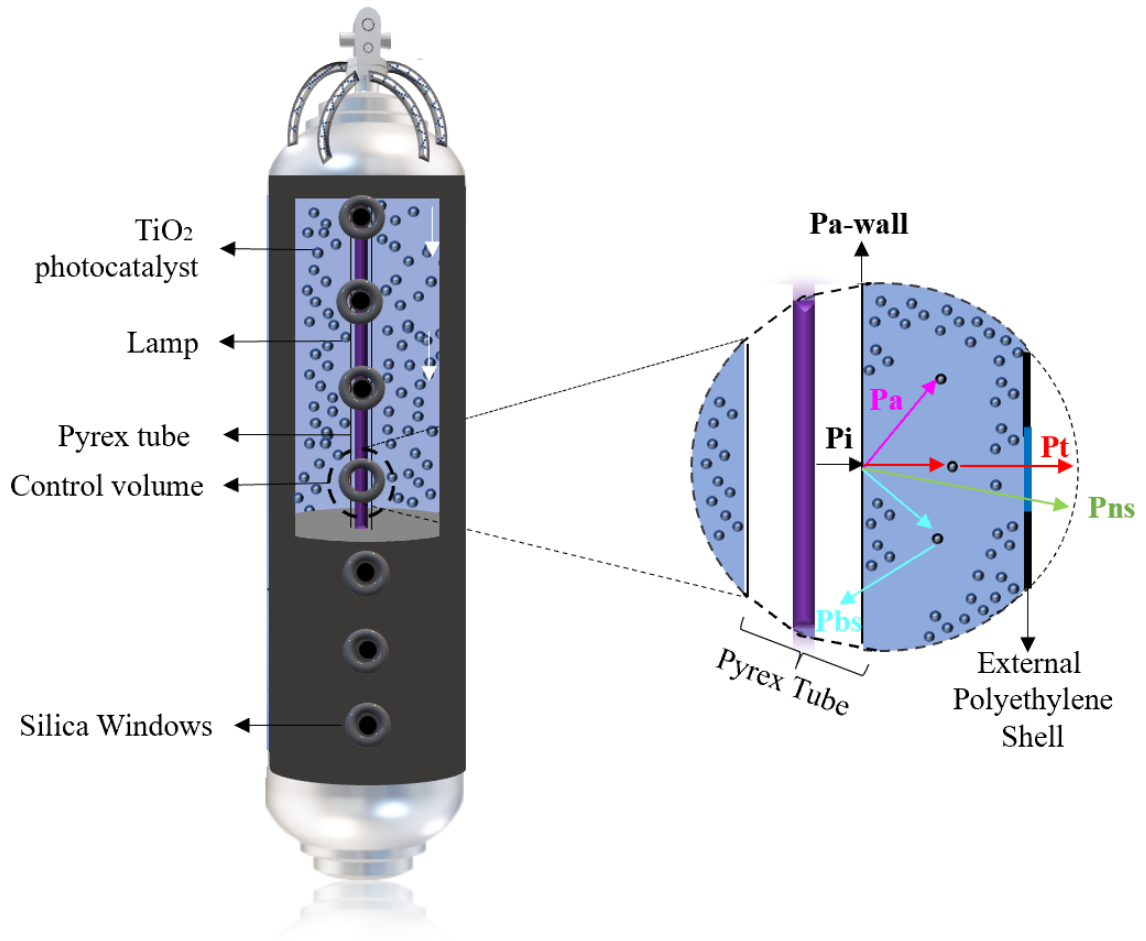


Figure 35 Macroscopic Irradiation Balance in a TiO₂ Water Suspension [99].

Furthermore, P_i which accounts for the rate of incident photons reaching the slurry suspension can be calculated as follows:

$$P_i = P_0 - P_{a-wall} \quad (\text{Einstein/s}) \quad \text{Equation 18}$$

with P_0 being the rate of photons emitted by the lamp, which is estimated from radiometric measurements as follows:

$$P_0 = \int_{\lambda_1}^{\lambda_2} \lambda \int_0^L \int_0^{2\pi} q(\theta, z, \lambda) r d\theta dz d\lambda \quad \text{Equation 19}$$

With $q(\theta, z, \lambda)$ being the radiative flux expressed in $\text{J s}^{-1} \text{m}^{-3}$, λ representing the photon wavelength in nm, r denoting the radial coordinate in m, z being the axial coordinate in m, h representing the Planck's constant in J s, and c denoting the speed of light expressed in m s^{-1} . The P_{a-wall} in Equation 18 represents the rate of photons absorbed and reflected by the inner Pyrex glass surface.

During photocatalytic experiments, photons are absorbed by the photocatalyst and scattered on the photocatalyst surface, while evolving in the slurry phase. In this respect, P_{bs} in Equation 20, accounts for the backscattered photons, with this being the difference between P_i and $P_{t/c \rightarrow 0+}$. $P_{t/c \rightarrow 0+}$ is the rate of photons transmitted at a photocatalyst concentration approaching zero [169] as follows:

$$P_{bs} = P_i - P_{t|_{c \rightarrow 0+}} \quad \text{Equation 20}$$

One should note that the backscattering centres on TiO_2 are assumed to be located on the outer surface layer of photocatalyst, close to the Pyrex wall surface.

Furthermore, P_t accounts for the difference between the transmitted non-scattered radiation (P_{ns}) and the forward-scattered radiation (P_{fs}) as follows:

$$P_t = P_{ns} + P_{fs} \quad \text{Equation 21}$$

$(P_{fs} + P_{ns})$ can be measured by employing aluminum polished collimators, which capture photons reaching the photodetector with large view angles [170].

The described macroscopic balances were originally obtained from experiments using near-UV irradiation in photocatalytic reactors [99]. However, given that macroscopic balances are not photon wavelength dependent, they were extended to visible light irradiation.

5.3 Near-UV-Light MIEB

To assess the P_a as shown in Equation 17, macroscopic balances using near-UV light were established at the central axial position of the PCW-II unit, using a 0.15g/L photocatalyst concentration.

Table 18 reports radiation measurements for various TiO₂ photocatalysts with different metal loadings.

Table 18 Absorbed Photon Rates on TiO₂ Photocatalysts, at Different Pd Metal Loadings, under Near- UV Light.

UV Light	Pt (Einstein/s)	Pt $c \rightarrow 0^+$ (Einstein/s)	Pbs (Einstein/s)	Pa (Einstein/s)	% Abs. Efficiency
TiO ₂	3.09E-06	5.94E-06	1.70E-06	3.11E-06	37.8
0.25wt% Pd	8.17E-07	3.66E-06	2.42E-06	3.18E-06	49.6
0.50wt% Pd	2.53E-07	3.43E-06	2.65E-06	3.52E-06	54.8
1.0wt% Pd	1.85E-06	6.69E-06	1.50E-06	5.11E-06	60.4
2.5wt% Pd	1.67E-06	5.18E-06	3.01E-06	3.77E-06	44.6
5.0wt% Pd	1.18E-06	4.68E-06	3.51E-06	3.76E-06	44.5

Note that for all the runs, the photocatalyst concentration was set at 0.15g/L with : a) Po at 6.75E-06 Einstein/s, for 0.25 to 0.50wt% Pd-TiO₂, b) Po set to 8.87E-06 Einstein/s for 1.00 to 5.00wt% Pd-TiO₂. 96% radiation was transmitted through the Pyrex glass tube, in all cases. All reported data are average values of 3 repeats.

According to Table 18, one can observe that additions of Pd to TiO₂ show that (a) Lower Pd levels (0.25 to 1.00 wt%) lead to an increased P_a and high absorption efficiencies while compared to undoped TiO₂, and (b) Higher Pd levels (2.50 and 5.00 wt% Pd) give smaller P_a and a reduced absorption efficiency. These findings are in line with an increased rate of

transmitted photons when using low Pd loadings, as well as with the incremental photon backscattering that occurs when using higher Pd loadings.

The 1.00wt%Pd-TiO₂ displayed the best photon absorption. However, for this semiconductor, the noble metal loadings added were 4 times greater than the 0.25wt%Pd-TiO₂. An evaluation of the cost-benefit relation indicates that by using the 1.00% wt Pd-TiO₂ semiconductor, the photocatalyst initial cost increases by 400% to obtain just an additional 40% of photon absorption.

Thus, it was considered that the 0.25wt%Pd-TiO₂ photocatalyst was the most suitable option for a more efficient hydrogen production process. Table 19 shows the results obtained when using a 0.25wt%Pd-TiO₂ photocatalyst, at a catalyst concentration of 1.00g/L.

Table 19 Rate of Absorbed Photons at a 1.00 g L⁻¹ Catalyst Concentration under Near-UV Light.

Catalyst (g/L) concentration	Pt (Einstein/s)	Pt $e \rightarrow h^+$ (Einstein/s)	Pbs (Einstein/s)	Pa (Einstein/s)	% Abs. Efficiency
1.00	4.66E-09	1.64E-06	4.44E-06	1.97E-06	30.8

According to Table 19 increasing the photocatalyst concentration reduces photon absorption. This is due to the backscattering phenomenon, where most of the irradiation provided by the light source is lost as backscattering in the slurry medium.

5.4 Visible light MIEB.

The P_a (rate of absorbed photons) was calculated as shown in Table 20, when using the photoreduced photocatalyst, with this photoreduction achieved after 1 hour under near-UV irradiation. One can thus see, that TiO₂ alone absorbs moderately visible light and this due to the modified morphology of the prepared photocatalysts. For 0.25 wt% Pd-TiO₂, there is a significant P_a increase, versus the P_a value obtained when undoped TiO₂ is utilized. However, one can also observe that larger loadings than 0.25 wt% Pd on TiO₂, yield a mildly increased

P_a , with 1.00 wt% Pd on TiO₂ giving a maximum P_a . Larger than 1.00 wt% Pd on TiO₂ yield a modest P_a decrease, while consequently diminishing the absorption efficiency.

Table 20 Visible Light Absorbed Photon Rates on TiO₂ Photocatalysts, at Different Metal Loadings, after 1 Hour of Near-UV Irradiation.

Visible Light	Pt (Einstein/s)	Pt $c \rightarrow 0^+$ (Einstein/s)	Pbs (Einstein/s)	Pa (Einstein/s)	% Abs. Efficiency
TiO ₂	5.83E-06	7.71E-06	1.52E-06	2.23E-06	23.3
0.25wt% Pd	2.45E-06	6.69E-06	2.47E-06	4.37E-06	45.7
0.50wt% Pd	2.55E-06	6.78E-06	2.65E-06	4.36E-06	48.1
1.00wt% Pd	2.68E-06	7.94E-06	1.26E-06	5.62E-06	58.6
2.50wt% Pd	2.68E-06	7.19E-06	2.03E-06	4.87E-06	50.8
5.00wt% Pd	1.73E-06	6.18E-06	3.04E-06	4.81E-06	50.2

The photocatalyst concentration used for the water splitting reactions was 0.15g/L, with $P_o = 9.69E-06$ Einstein/s for 0.25wt% Pd-TiO₂, $P_o = 9.58E-06$ for 0.50wt% Pd-TiO₂ and $P_o = 9.94E-06$ for 1.00 – 5.00wt% Pd-TiO₂, with 96% radiation being transmitted through Pyrex glass tube, for all cases. All reported data are average values of 3 repeats.

An additional evaluation of the pre-reduced 0.25wt%Pd-TiO₂ under visible light was performed using the photocatalyst after 24 h under near-UV irradiation. Table 21 shows that after 24 h under near-UV light, the photocatalyst reduces its photon absorption efficiency from an initial value of 45.7% to 39%, with these results setting excellent prospect for extended application of the 0.25wt%Pd-TiO₂.

Table 21 Rate of Absorbed Photons under Visible Light after 24 h Near-UV Irradiation.

Catalyst (g/L) concentration	Pt (Einstein/s)	Pt $c \rightarrow 0^+$ (Einstein/s)	Pbs (Einstein/s)	Pa (Einstein/s)	% Abs. Efficiency
0.15	2.21E-07	8.39E-06	1.04E-06	3.72E-06	39

5.5 Conclusions

The macroscopic irradiation energy balances obtained under both near-UV light and visible light, are considered in this chapter, with the following being the main conclusions:

- a) Photocatalyst doped with palladium enhances photon absorption efficiencies, and this when compared with the undoped TiO₂. This was found to be true for Pd-TiO₂ photocatalyst irradiated with both near UV and visible light.
- b) Photocatalyst photoreduction during 1 hour using near-UV, favourably influence photon absorption.
- c) The Pd-doped TiO₂ display a similar trend under both near-UV and visible light irradiation, with a moderately increase of the P_a up to 1.00% wt Pd on TiO₂. However, the P_a tends to decrease at higher metal loadings, with this being attributed to augmented photon backscattering.
- d) The Pd-doped TiO₂ photocatalyst displaying the highest photon absorption efficiency (0.25% wt Pd-TiO₂) was selected for hydrogen production via water splitting.

Chapter 6

6 Hydrogen Production Yields and By-Products

Hydrogen production experiments were performed in the Photo-CREC Water-II Reactor under both near-UV light and visible light, before and after photoreducing the photocatalyst. The palladium doped TiO₂ photocatalyst was used, together with ethanol, which acted as an organic scavenger. On this basis, a reaction network is postulated in this chapter, for both near-UV and visible light irradiation sources. All experiments were conducted under an argon atmosphere.

In all cases, the cumulative hydrogen produced is reported in volumetric units, at standard conditions (cm³ STP or cubic centimeters at atmospheric pressure and room temperature).

6.1 Photocatalytic Mechanism

Water splitting reactions under an argon inert atmosphere using ethanol as a sacrificial agent, promote the formation of hydrogen as a main product and other different by-products, as a result of oxidation-reduction reactions. Hydrogen production is feasible when using a palladium-doped titanium dioxide photocatalyst with a reduced band gap, as reported in Chapter 4.

Regarding the photocatalytic reaction, it can be hypothesized that different by-products are formed due to photoredox reactions, as observed in Figure 36. Palladium creates holes, that react with the organic scavenger ethanol, and form by-products. In the gas phase, in addition to hydrogen, the detected by-products include methane, ethane, ethylene, acetaldehyde, CO, and CO₂. In the liquid phase, ethanol and hydrogen peroxide were also identified.

Hydrogen production is reported after 165 experimental runs using different Pd loadings (0.25, 0.50, 1.00, 2.50 and 5.00 wt% Pd) on TiO₂. Mechanistic considerations reported in the present manuscript are established for a 0.25 wt% Pd-TiO₂ semiconductor at a 0.15 g L⁻¹ photocatalyst concentration. The 0.15 g L⁻¹ photocatalyst concentration was found to be the optimum Pd loading for hydrogen production [171]. Regarding the 0.25 wt% Pd-TiO₂, it displayed a reduced band gap of 2.51 eV, as reported in Chapter 4. This allowed hydrogen to be produced,

under visible light, as well. The absorbed radiation was evaluated via macroscopic irradiation energy balances, in Chapter 5.

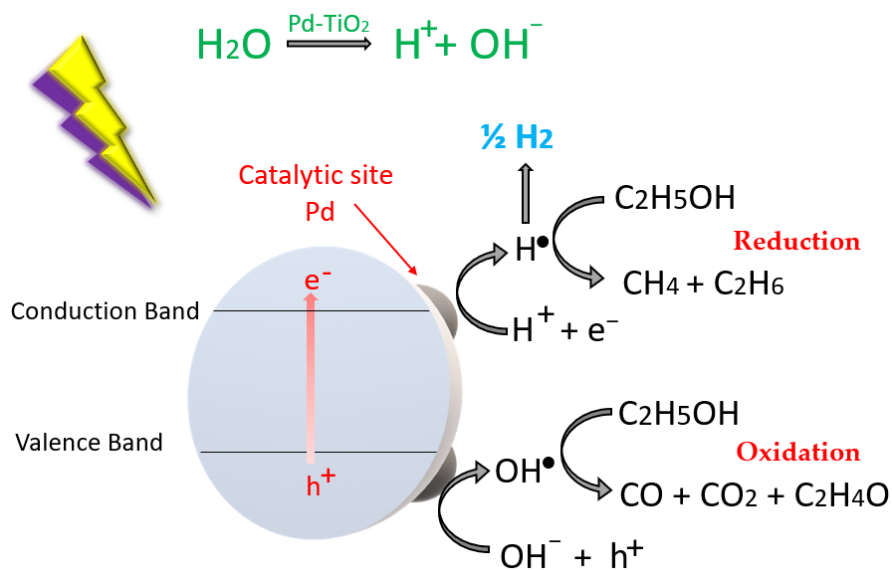
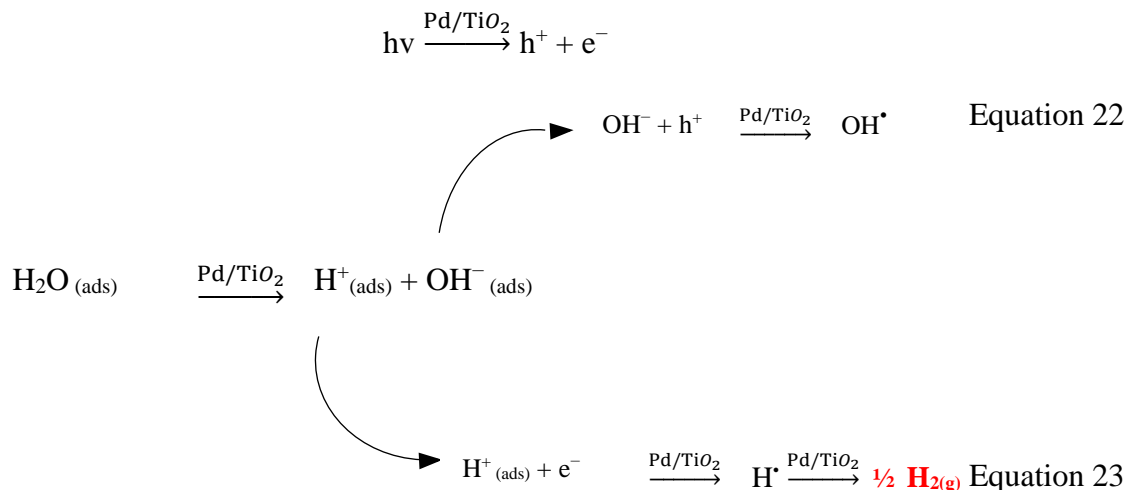


Figure 36 Hydrogen Reactions Steps using Pd-TiO₂ as a Photocatalyst and Ethanol as an Organic Scavenger.

Figure 36 describes hydrogen production via a “series-parallel” redox reaction network as follows:

- a) Near-UV or visible light sources emit photons that reach the photocatalyst surface.
- b) An electron jumps from the valence band to the conduction band, creating an electron-hole pair. The electron must have a higher energy level to surpass the band gap. With a band gap reduction, the gap is narrowed, and the electron can be promoted more easily, from the valence band to the conduction band.
- c) Palladium traps the excited electrons, moving on the semiconductor surface, thus avoiding electron-hole recombination.
- d) Water splits, forming intermediate OH[•] and H[•] radicals, with H[•] reacting further and yielding molecular hydrogen.

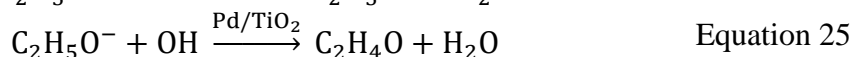
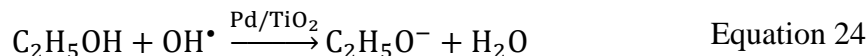
- e) Ethanol, as an OH[•] organic scavenger, is consumed via different reaction pathways, and forms various oxidation by-products, such as acetaldehyde, CO, and CO₂, as described with Equations 24– 28.
- f) Ethanol and ethanol by-products are reduced via the H[•] radicals present, yielding methane, ethane, and ethylene, as reported with Equations 29– 31.



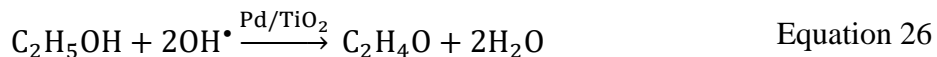
Based on oxidation-reduction reactions, by-products, such as acetaldehyde, CO, and CO₂, methane, ethane, and ethylene are produced.

Oxidation Reactions

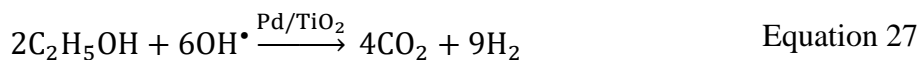
- a) Acetaldehyde



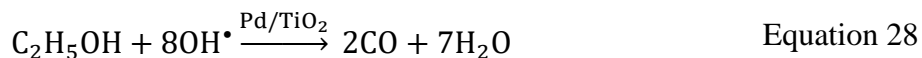
The addition of Equations 24 and 25 yields the following overall equation:



- b) Carbon Dioxide

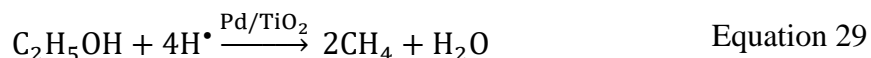


c) Carbon Monoxide



Reduction Reactions

d) Methane



e) Ethane



f) Ethylene



Additionally, hydrogen peroxide is produced, due to the recombination of some of the OH radicals present:



In summary, highly valuable products are generated from the redox reactions, when using the scavenger ethanol. Hydrogen and other hydrocarbon products are formed, with a very small ethanol consumption.

6.2 Hydrogen Production

The performance of the Pd-TiO₂ photocatalyst was evaluated in the Photo-CREC Water-II Reactor. A centrally located BLB UV lamp or Phillips visible light lamp were placed in the PCW-II. This equipment also included a 6000 cm³ storage/mixing tank. Experiments were

carried out either under a near-UV light or under a visible light for 6 hours of continuous irradiation. The lamp was turned on for 30 min before each run, in order to reach stabilization.

In the storage tank, 6000 cm³ of water were loaded together with a 2 v/v% of ethanol, which was used as scavenger. The photocatalyst was sonicated in water for 10 min to avoid the formation of particle agglomerates. The initial pH was adjusted to 4 ± 0.05 with H₂SO₄ [2M], in order to ensure H⁺ availability, for the water splitting process. Argon was circulated for 10 min to displace the oxygen present and to guarantee an inert atmosphere.

Gas samples were analyzed using the Shimadzu GC2010 (gas chromatograph). For ethanol, samples were periodically quantified utilizing a HPLC (UFLC Ultra-Fast Liquid Chromatograph). To identify hydrogen peroxide, the absorbance was measured by a spectrophotometer (Spectronic 200+, Thermo Spectronic).

6.2.1 Hydrogen Production Under Near-UV Light

Palladium was used as co-catalyst to dope the structure of the TiO₂ photocatalyst. It is shown in this PhD dissertation, that Pd noble metal enhances hydrogen production, and this when compared to the undoped mesoporous TiO₂. Nobel metal crystallites reduce the band gap and facilitate electron capture [172]. As a result, Pd reduces the recombination between holes and electrons, promoting a better photocatalytic water splitting performance [173].

Figure 37 reports the influence of the Pd on the TiO₂, in terms of cumulative hydrogen volume.

Figure 37 shows that there is a maximum volume of 140 cm³ STP of hydrogen produced in six hours under near UV irradiation when using 1.00 wt% Pd on TiO₂. This volume is slightly higher than the maximum volume of hydrogen produced when using 0.25 wt% and 0.50 wt% Pd–TiO₂, and three times the volume of hydrogen obtained with undoped TiO₂. One should also note that this volume is close to the 113 cm³ STP of hydrogen produced when palladium is used as a dopant, under the same reaction conditions, but with a reduced metal loading (0.25 wt% Pd) on TiO₂. This makes the 0.25 wt% Pd-TiO₂, an option with a better cost-benefit.

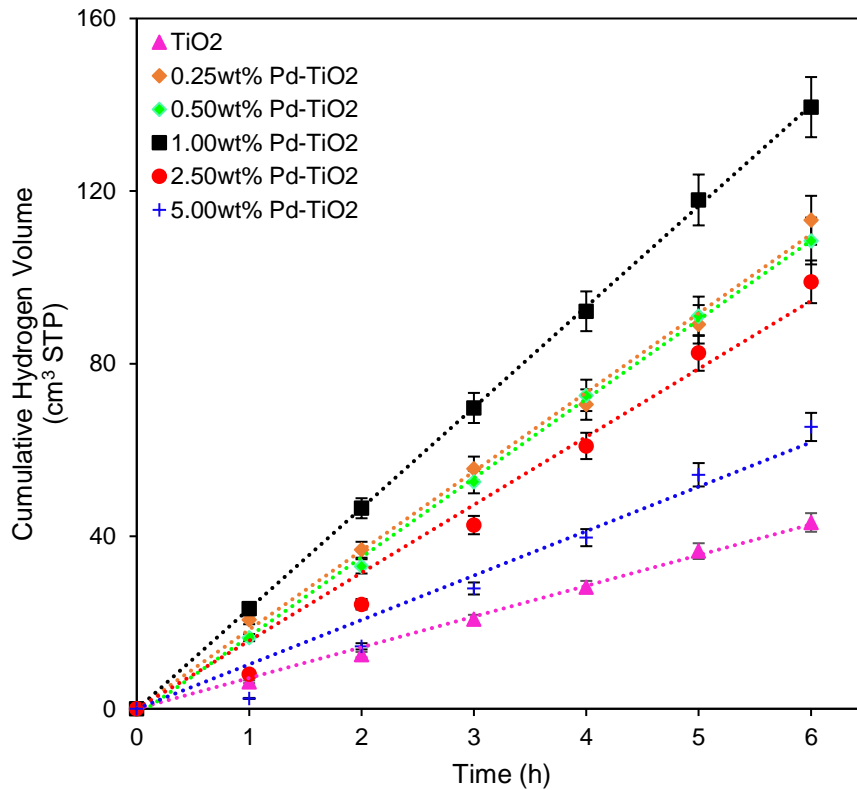


Figure 37. Cumulative Hydrogen Volume STP (standard temperature and pressure) Obtained Using Pd at Different Metal Loadings (0.25, 1.50, 1.00, 2.50 and 5.00 wt%). Conditions: photocatalyst concentration of 0.15 g L^{-1} , 2.0 v/v% ethanol, initial $\text{pH} = 4 \pm 0.05$ and near-UV light.

Furthermore, one should note that the 113 cm^3 STP hydrogen produced in six hours, with 0.25 wt% Pd on TiO_2 , decreased to 60 cm^3 STP, when using higher Pd loadings (2.50 wt% Pd and 5.00 wt% Pd) at STP. The macroscopic radiation energy balance indicates that at the higher Pd loadings, there is increased irradiation backscattering due to possible presence of PdO species, with greater irradiation being reflected and, as a consequence, light absorption being reduced. This is in contrast with the lower Pd loadings evaluated, where the absorption efficiency, as well as the rate of transmitted photons, increases. Thus, a diminished irradiation absorption given by 2.50 wt% Pd and 5.00 wt% Pd, negatively affects the photocatalyst performance[174].

In agreement with this, at the lower palladium loadings studied (0.25, 0.50 and 1.00 wt%) good metal dispersion, with a mildly reduced specific surface area and pore volume were achieved[175]. On the other hand, for 2.50 and 5.00 wt% Pd–TiO₂, poorer metal dispersion with larger metal crystallite sizes was observed, with this being in line with the lower photocatalytic activity [176].

In all cases, palladium doped TiO₂ showed a consistently steady linear hydrogen formation trend. Thus, it was judged that palladium doped TiO₂ was a stable photocatalyst for hydrogen production and this for extended irradiation periods, with no apparent deactivation during 24 h long runs, following consistently a “in series-parallel” reaction mechanism.

These results show that a 0.25 wt% palladium on mesoporous TiO₂ produces valuable hydrogen yields, with this photocatalyst being an excellent replacement for platinum doped TiO₂. As well, Pd is less expensive than Pt, about 20–25% of the platinum cost, making the 0.25 wt% Pd-TiO₂, a more suitable option with a cost-benefit.

In summary, a photocatalyst modified with palladium reduces the band gap, captures the available electrons and reduces electron-hole recombination, promoting a better photocatalytic water splitting performance[173].

6.2.2 Effect of Catalyst Concentration on Hydrogen Production

Previous experimentation was carried out at four different concentrations of TiO₂ catalyst: 0.15, 0.30, 0.50 and 1.00 g L⁻¹ with a 1.00wt%Pd loading. The runs with 1.00g L⁻¹ showed the highest hydrogen production[129]. Thus, considering that the 0.25wt%Pd-TiO₂ photocatalyst displayed the best performance in terms of hydrogen production, suitability, and cost, additional experiments were carried out at Pd loadings of 0.25wt%, at TiO₂ concentrations of 1.00 g L⁻¹, to determine the influence of the catalyst concentration during photoreaction.

It was observed that larger TiO₂ photocatalyst concentrations show more photocatalyst electron-hole availability, resulting in higher hydrogen production rates.

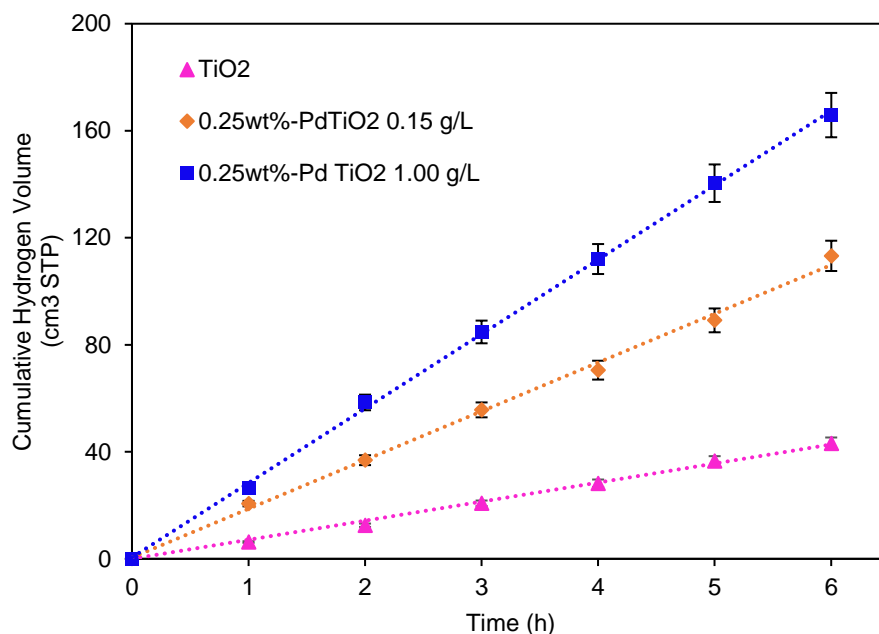


Figure 38 Cumulative Hydrogen Production Using 0.25wt% Pd-TiO₂ at Catalyst Concentrations of 0.15 and 1.00 g L⁻¹. Conditions: 2.0 v/v% ethanol, initial pH=4 ± 0.05 and near-UV light.

Figure 38 indicates that the hydrogen production rate augmented by 74% when using a 1.00g L⁻¹ TiO₂ photocatalyst doped with 0.25wt%-Pd, compared to undoped TiO₂. As well, this increase represented 32% versus the hydrogen production rate obtained using a 0.15g L⁻¹ TiO₂ with a 0.25wt%-Pd dopant. Thus, hydrogen volume augmented 1.5 times, when the photocatalyst concentration augmented seven (7) times, from 0.15 to 1.00 g/L. Given this increment was considered moderate only, the 0.15 gL⁻¹ photocatalyst concentration TiO₂ was used in further experiments.

6.2.3 Gas Phase By-Products Formed during Photocatalytic Hydrogen Production under Near-UV Light

As a result of the photooxidation-photoreduction reactions, different by-products were formed in the photocatalytic water splitting reaction. Detected by-products included methane, ethane, acetaldehyde, ethylene, CO and CO₂, as shown in Figure 39. These by-products were formed in the gas phase, in the presence of ethanol. Samples were taken hourly and analyzed using the Shimadzu GC-2010 chromatograph.

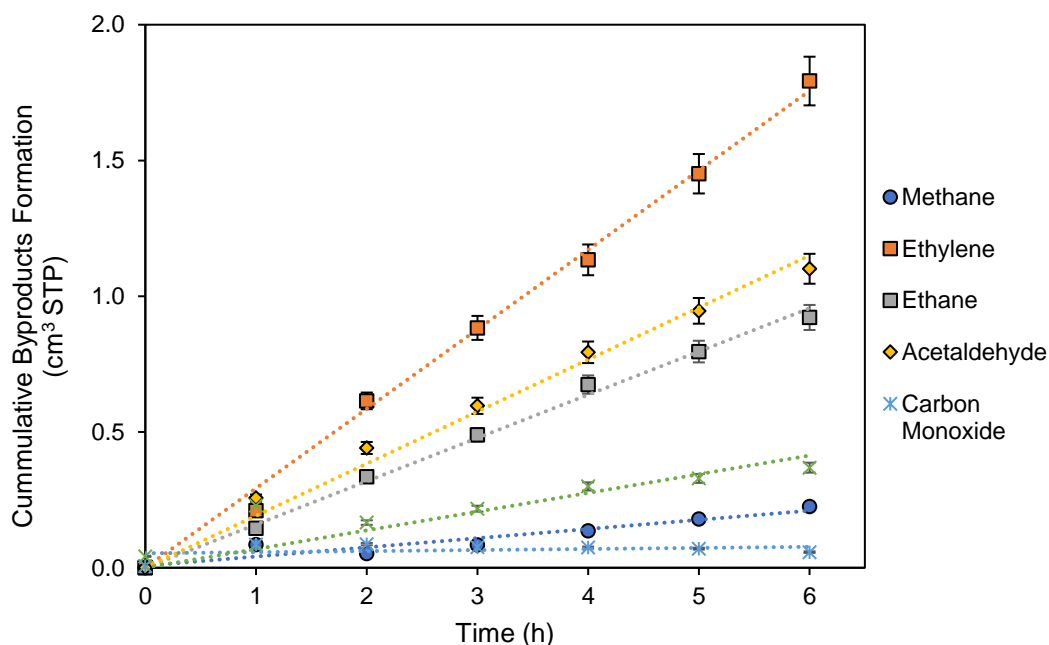


Figure 39. Cumulative Amounts of Carbon Dioxide (CO₂), Methane (CH₄), Acetaldehyde (C₂H₄O), Ethane (C₂H₆), and Ethylene (C₂H₄) Obtained Using a 0.25 wt% Pd-TiO₂. Conditions: photocatalyst concentration of 0.15 g L⁻¹, 2.0 v/v% ethanol, near-UV light irradiation, and argon atmosphere.

6.3 Hydrogen Production under Visible Light

Visible light is a form of electromagnetic radiation where the spectrum is visible to the human eye. This light is considered to be a renewable, inexpensive, and inexhaustible source of energy. Visible light is very valuable and advantageous for photocatalytic reactions.

Titania-based photocatalysts are limited by their wide band gap (E_{bg} ~ 3.2 eV for Anatase), which limits its use to near-UV light ($\lambda \leq 390$ nm)[129]. However, the addition of a noble metal dopant such as palladium, modifies the photocatalyst band structure and serves as an electron trap to prevent electron-hole recombination.

The Pd-TiO₂ photocatalysts of the present study were evaluated in the PCW-II, with respect to their ability to enhance hydrogen production, under the following conditions: (a) by utilizing a photocatalyst concentration of 0.15 g/L, (b) by using a 2.0 v/v% of ethanol as organic scavenger and (c) by utilizing an initial pH = 4 ± 0.05.

Figure 40 reports the cumulative hydrogen volume produced, using TiO₂ doped with different Pd loadings, under visible light. It was shown that Pd-doped TiO₂ semiconductors consistently enhanced hydrogen production, with the best performance being obtained with the 0.25 wt% Pd. It was determined that this mesoporous semiconductor could have an increased scavenging effect of photogenerated electrons, and therefore, could prevent electron–hole pair recombination [177].

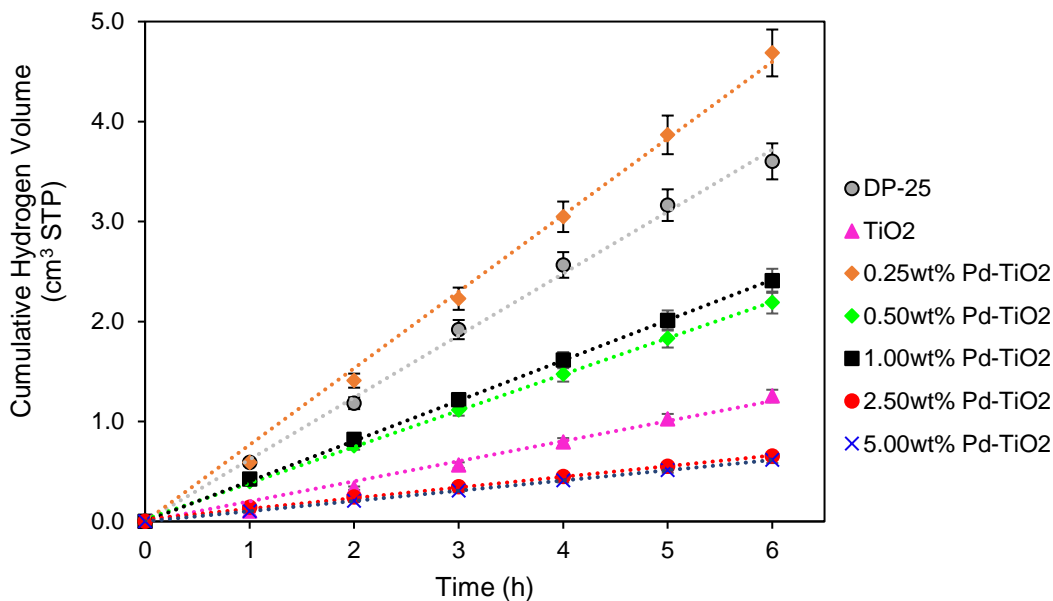


Figure 40 Cumulative Hydrogen Volume STP Produced when Using Pd – TiO₂ at Different Loadings (0.25, 0.50, 1.00, 2.50 and 5.00wt%). Conditions: Photocatalyst concentration: 0.15g L⁻¹, 2.0 v/v% ethanol, pH=4 ± 0.05 and visible light.

Furthermore, it was also observed that when the metal loading of the Pd-TiO₂ was augmented to 0.5 wt% Pd and above, a decreased rate of hydrogen production was obtained. One should notice as well, that the MIEB (Macroscopic Irradiation Energy Balance) as reported in Chapter 5, showed a relatively stabilized visible light absorption, for various Pd-doped TiO₂ photocatalysts. Thus, one can conclude that hydrogen production differences cannot be assigned to changes in electron and hole pair generation [178], but rather to a more effective trapping of electrons in the 0.25 wt%Pd-TiO₂, than in photocatalysts with larger Pd loadings.

Figure 40 also displays that after only 6 h of visible light irradiation, a maximum volume of 4.7 cm³ STP of hydrogen was produced when using the 0.25 wt% Pd on TiO₂ with 0.15g/L of photocatalyst. This hydrogen volume is approximately 4 times higher than the volume produced with undoped mesoporous TiO₂.

6.3.1 Photocatalyst Photoreduction

Palladium is present in a metallic state during the sol-gel photocatalyst preparation. However, palladium can be oxidized during the photocatalyst precursor calcination preparation step. At this stage, it was observed that the photocatalyst showed a reddish color. This was confirmed via X-ray Diffraction Analysis where at 34° (111) of the 2θ angle scale, there was indication of the PdO presence. As well, XPS also showed that 50.2% of palladium was present as PdO, after photocatalyst precursor calcination, as reported in Chapter 4. Thus, one can conclude that palladium species on the semiconductor requires further reduction, to ensure that a substantial amount of palladium species is present as Pd⁰.

Therefore, a special and additional photocatalyst pretreatment was implemented to ensure that most palladium was appropriately reduced to Pd⁰. Metallic palladium (Pd⁰) promotes a high photocatalytic activity of the TiO₂, by generating a Schottky junction between the metal and the photocatalyst. The metal particles trap and store the photogenerated electrons, reducing the rate of the electron hole recombination [179].

With this end and as described in Figure 41, a 15W BLB UV-Lamp was employed to irradiate the prepared semiconductor during 1 h.

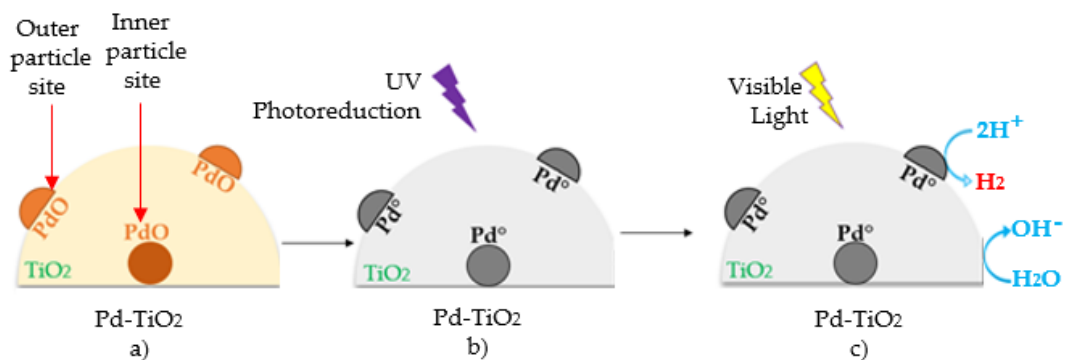


Figure 41. Schematic Representation of: (a) The synthesized photocatalysts following calcination at 500 °C, with most of the Pd being present as PdO, (b) The photoreduction of the PdO to Pd⁰ using a near-UV Lamp, (c) The H₂ production using a photoreduced Pd-TiO₂, with molecular H₂ being generated on the semiconductor.

This PdO photoreduction using near-UV light can be described with the following equation, with the resulting palladium being present as Pd⁰, on the TiO₂ structure:



It is speculated that photoreduction is a very efficient process, with photogenerated electrons migrating from the outer TiO₂ particle surface to the TiO₂ mesoporous inner surface. Formed electrons can reduce the PdO into Pd⁰ [180].

Regarding the present study, following photoreduction, the near-UV lamp was replaced by a visible light lamp. It was observed that when the photocatalyst was photoreduced with near-UV prior to its utilization, this led to an important increase in hydrogen production, under visible light irradiation.

Figure 42 displays an enhanced cumulative hydrogen production under visible light, in the Photo-CREC Water-II Reactor, at different loadings of photocatalyst dopant (0.25, 0.50, 1.00, 2.50 and 5.00 wt%) and after photoreduction of the photocatalyst. It is interesting to see that the same consistent trends were observed using near-UV light [171]. It must be noted as well, that the lower the Pd loadings, the higher the hydrogen production.

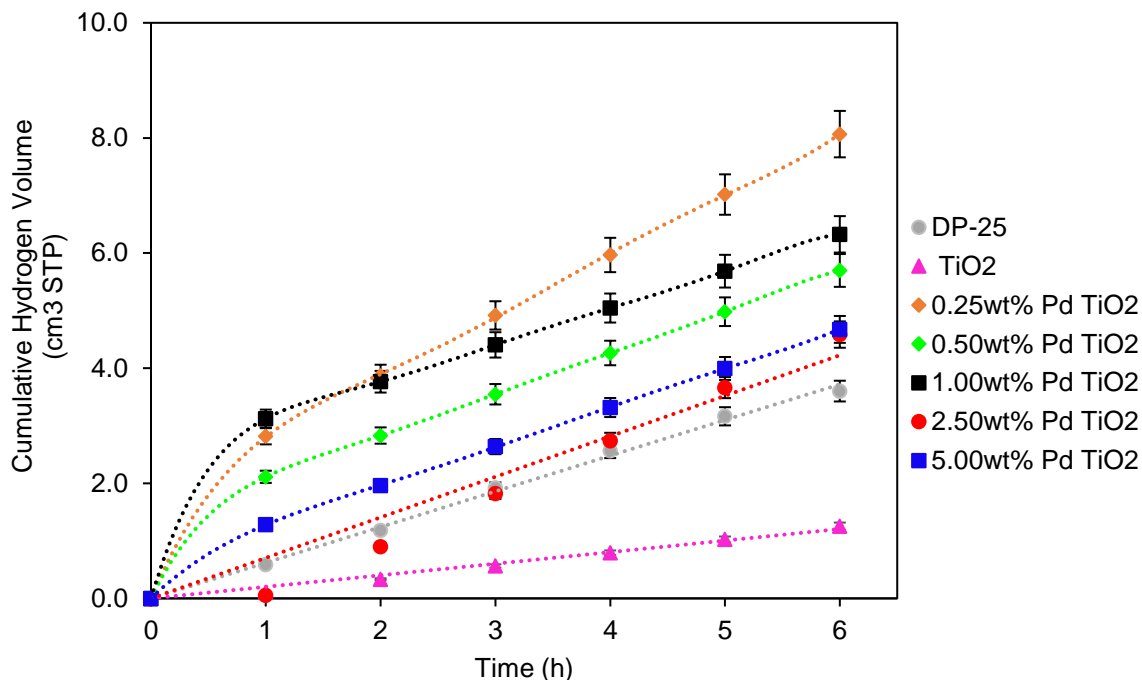


Figure 42 Cumulative Hydrogen Volume Produced at Different 0.25, 0.50, 1.00, 2.50 and 5.00 wt% Pd Loadings on a Photocatalyst Photoreduced with 1 hour Near-UV Light, and Further Exposed to 6 Hours of Visible Light, to Produce Hydrogen. Conditions: Photocatalyst concentration: 0.15 g L^{-1} , 2.0 v/v% ethanol, initial pH = 4 ± 0.05 .

Furthermore, when comparing hydrogen production with and without prior photoreduction, it can be observed that the photoreduced Pd-TiO₂ photocatalyst displayed significantly increased hydrogen production rates. Particularly for the 0.25 wt% Pd-TiO₂ after photoreduction, the maximum hydrogen volume produced was 8.0 cm³ at STP. This is equivalent to a 1.7 time increase in hydrogen formation rate. According to the chemisorption studies, at this low palladium loading, a good metal dispersion of 75% was also observed, with the photocatalyst showing a slightly decreased in both surface area and average pore size [175].

In contrast, when using the 0.50 to 5.00 wt% Pd-TiO₂, lower metal dispersions were observed, with larger metal crystallite sizes being detected. This was in line with their diminished photocatalytic hydrogen production activity [176]. To explain these results, one can consider that when using a Pd-TiO₂ photocatalyst under visible light, photons are both absorbed and scattered. The MIEB as reported in Chapter 5, showed that higher Pd loadings (2.5 and 5.0 wt%- Pd) do not enhance the absorption of visible light, significantly. This phenomenon can be assigned to the presence of larger metal crystallites and TiO₂ particle agglomerates. This

limits photons from reaching the Pd⁰ active metallic sites and from being absorbed [181]. The opposite of this was observed at lower than 1.00 wt% Pd loadings, where the photon absorption increases, positively impacting the semiconductor photoactivity.

On the other hand, it can be hypothesized as well, that the less effective photoreduction of palladium may occur for 2.5 and 5.0wt% Pd on TiO₂, due to the oversupply of noble metal. In this case, layers of PdO could be present on the TiO₂, shielding the TiO₂ from light absorption. The formation of such sites could increase the photocatalyst reflectivity leading to visible light scattering [182]. As well, this phenomenon could also be attributed to the partial blocking of semiconductor pores, which may decrease the TiO₂ specific surface area, as reported in Chapter 4.

Considering and based on the XPS analysis, after 1 hour under near-UV irradiation, a consistent 81.3% conversion of PdO to Pd⁰ was achieved, leaving a 18.3% of PdO present on the photocatalyst. Further noble metal reduction is required to achieve increased hydrogen production rates. Therefore, a 24 hour near-UV irradiation photoreduction was implemented. Results obtained are reported in Figure 43.

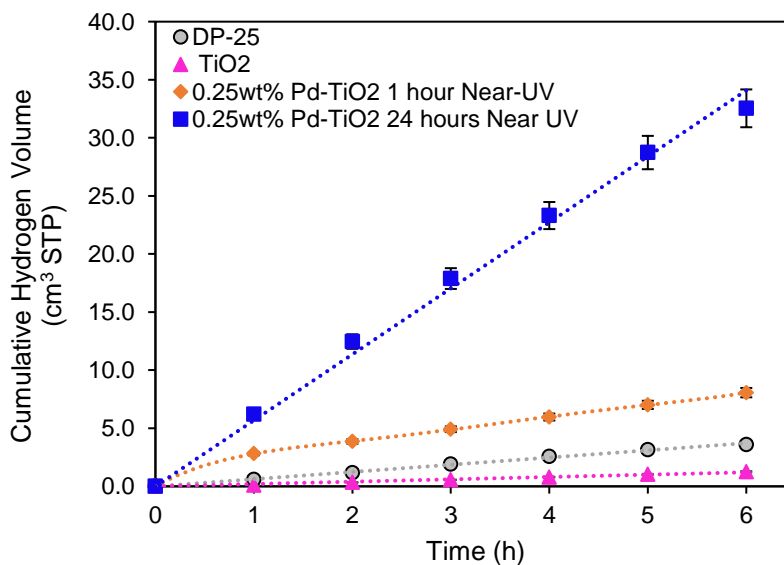


Figure 43. Hydrogen Volume Obtained Using Photocatalysts with 0.25wt% Pd Loadings, Photocatalyst photo-reduced with Near-UV Light during 1 hour and 24 hours prior to a run with visible light. Conditions: Photocatalyst concentration: 0.15g L⁻¹, 2.0 v/v% ethanol, initial pH = 4 ± 0.05.

When studying the cumulative hydrogen formation under visible light, an important issue is the photoreduction palladium state time prior to a run with visible light. To clarify this matter both one-hour and 24-hour under near-UV irradiation photoreduction runs were considered. It was observed that the prior 24-hour extended Pd photoreduction (Pd^0) was advantageous and this to obtain a better photocatalyst performance and therefore, yielding higher hydrogen volumes.

For instance, for the 24-hour near-UV photo-reduced 0.25wt% Pd-TiO₂, the hydrogen volume produced under visible light was 33 cm³STP. This hydrogen volume was 4 times larger than the hydrogen volume achieved with 1-hour of near-UV photoreduction. This hydrogen volume increase was assigned to a close to 100% metallic palladium, as observed in the XPS analysis, a desired situation, considering that Pd⁰ acts as an electron reservoir to prevent electron-hole recombination.

6.3.2 By-Product Formation during the Photocatalytic Hydrogen Production under Visible Light in the Gas Phase

Figure 44 reports that under visible light together with hydrogen, the photogenerated holes created by the noble metal react with the organic scavenger ethanol, forming by-products such as acetaldehyde, ethane, ethylene, CO, CO₂ and methane, as is shown in Figure 44. The amounts of these by-products increase progressively with irradiation time.

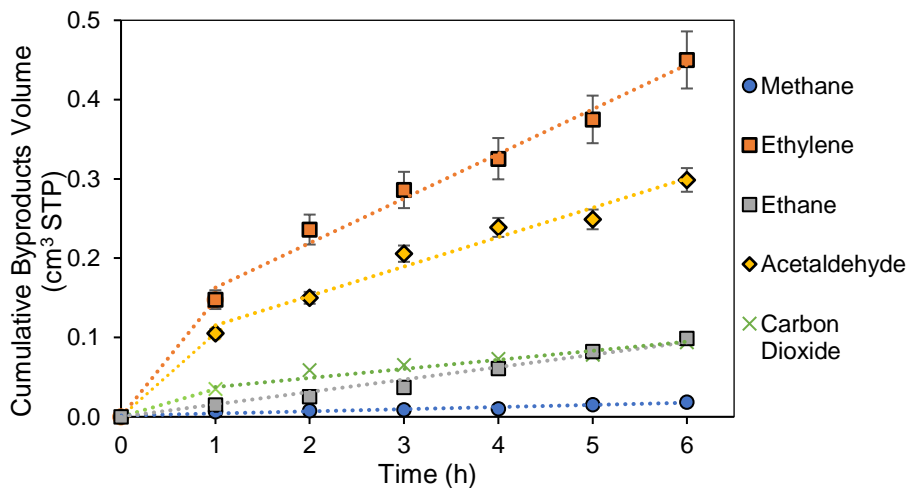


Figure 44 By-Product Changes with Irradiation Time: a) Methane (CH₄), b) Ethane (C₂H₆), c) Ethylene (C₂H₄), d) Acetaldehyde(C₂H₄O) and e) Carbon dioxide (CO₂) at 0.25% w/w Pd-TiO₂. 1 hour near-UV light and 6 hours of visible light were used to produce hydrogen. Conditions: Photocatalyst concentration: 0.15g L⁻¹, 2.0 v/v% ethanol, initial pH=4 ± 0.05.

6.3.3 By-Product Formation during the Photocatalytic Hydrogen Production in the Liquid Phase

During photocatalytic hydrogen formation under visible light, ethanol and hydrogen peroxide in the liquid phase were detected. Ethanol was initially added as an organic scavenger and hydrogen peroxide was formed due to the recombination of some of the OH radicals. For ethanol measurements, a UFLC (Ultra-Fast Liquid Chromatography) technique was used. On the other hand, and to determine the hydrogen peroxide formed, a colorimetric methodology already described in Chapter 3 was employed.

6.3.3.1 Ethanol Consumption-Formation

Figure 45 shows a stable ethanol concentration during the 6 hours of visible light irradiation. It is hypothesized that the net ethanol consumption-formation balance is influenced by a CO photoreduction, when using the 0.25wt% Pd-TiO₂ photocatalyst.

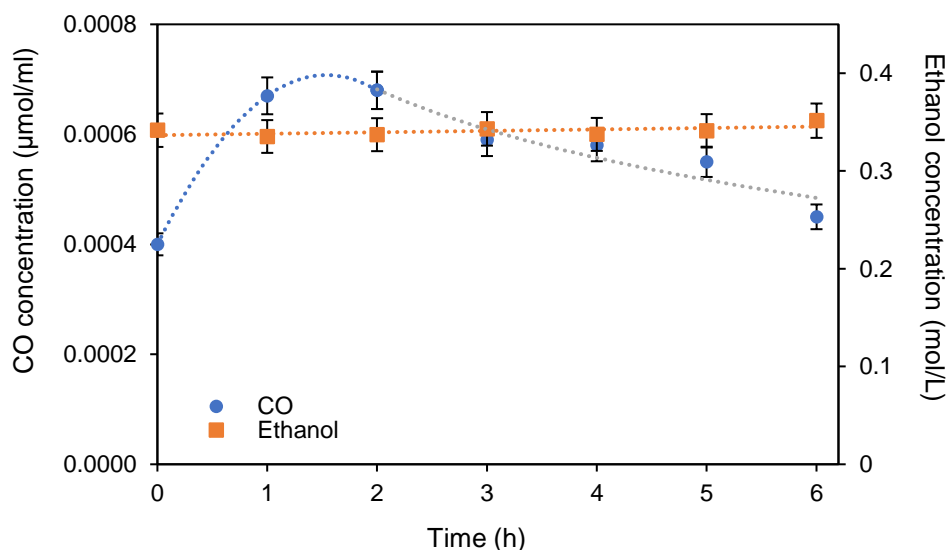


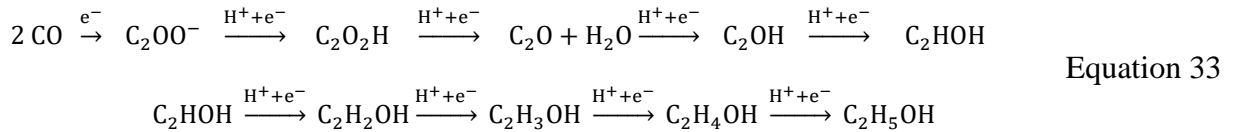
Figure 45 Ethanol and CO Changes with Irradiation Time. Conditions: Photocatalyst concentration 0.15g L⁻¹, at 0.25% w/w Pd-TiO₂, 2.0 v/v% ethanol, initial pH=4 ± 0.05, 6 hours of visible light. Notes: a) Ethanol and CO concentrations are defined considering ethanol in the liquid phase, and CO in the gas phase, b) Ethanol in the gas phase and CO in the liquid phase are considered negligible in this analysis.

During the 165 runs developed, a consistently small overall ethanol consumption was observed. This can be explained given that palladium is one of the strongest C-C coupling catalysts and can also form C₂H₅OH via CO photoreduction, during the water splitting reaction as follows [183]:

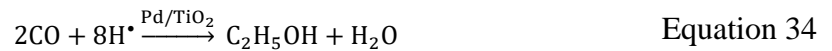
- (a) CO molecules are strongly adsorbed onto a Pd-TiO₂ surface, leading via bimolecular CO interaction to C-C coupling.
- (b) Due to the reduced band gap of the photocatalyst (2.51 eV), electrons jump from the valence band to the conduction band and are trapped by palladium.
- (c) The photogenerated electrons are used to activate and reduce the CO, which leads to ethanol formation via hydrogenation.

Thus, the following reaction mechanism can be postulated for ethanol formation as follows[184]:

- (a) C-C coupling involves electron transfer, with this leading to the formation of the *C₂O₂-intermediate.
- (b) Once the *C₂O₂-intermediate is formed, hydrogenation and electron transfer can take place, with the *C₂O₂H forming ethanol.



Thus, various reaction steps in Equation 33, may lead to ethanol synthesis as follows:



In summary, ethanol consumption and ethanol formation may both coexist during hydrogen formation.

6.3.3.2 Hydrogen Peroxide Formation

Regarding the hydrogen peroxide formed under near-UV light, it is considered to be competition of a rate of OH[•] dimerization, and the rate of H₂O₂ decomposition, as explained later in Chapter 7. To quantify H₂O₂ during photocatalytic hydrogen production, liquid samples were periodically analyzed, using a colorimetric method. As reported in Figure 46, during 6 h of near-UV irradiation, the hydrogen peroxide concentration steadily increased, with a maximum of 0.0022 cm³ of H₂O₂ being produced.

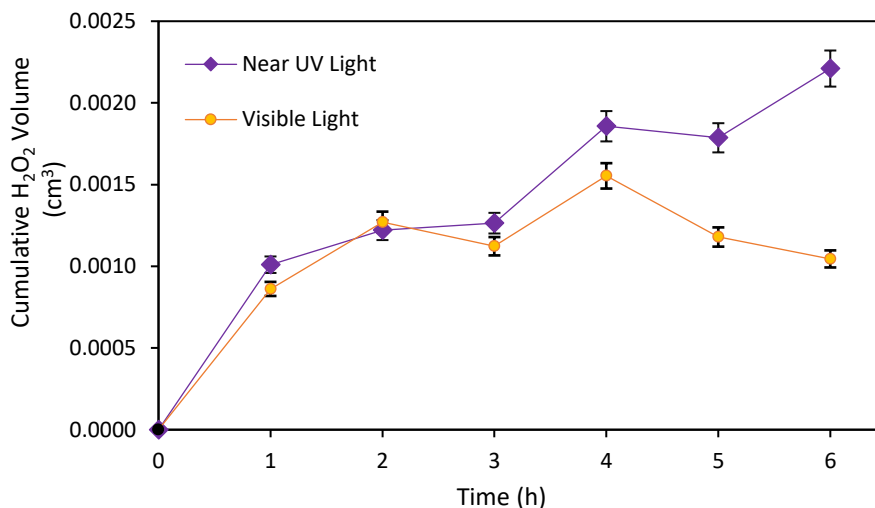


Figure 46. Cumulative H₂O₂ Volume Formed as a Function of Irradiation Time, in the Presence of 0.25 wt% Pd-TiO₂, under: a) Near-UV and b) Visible light (1 h photoreduction under Near-UV followed by 5 h of visible light irradiation). Conditions: Photocatalyst concentration 0.15g L⁻¹, 2.0 v/v% ethanol, initial pH=4 ± 0.05.

On the other hand, Figure 46 also shows that OH[•] dimerization plays an important role under visible light irradiation. In this case, the reaction pathway involves H₂O₂, which is mainly formed during the first hour of near-UV photoreduction, with a modest additional H₂O₂ observed during the next five following hours of visible light.

6.4 Conclusions

This chapter describes hydrogen and by-product formation rates, under near-UV light and visible light. The following are the most important conclusions:

- a) The synthesized Pd-TiO₂ is a suitable photocatalyst for hydrogen production, in the Photo-CREC Water-II Reactor unit under near-UV and visible light, reaching a significant hydrogen volume produced after 6 h of irradiation.
- b) Photoreduction of the Pd-TiO₂ with near UV, is a key step prior to photocatalytic water splitting for water splitting using visible light.
- c) A 0.25wt%Pd-TiO₂ photocatalyst is a most suitable semiconductor for hydrogen production, being highly efficient and inexpensive, and this while compared to other photocatalysts with higher noble metal loadings.
- d) Increasing the photocatalyst concentration up to 1.00g L⁻¹ yields an improvement in the hydrogen formation rates, under near-UV light.
- e) The Pd-TiO₂ photocatalysts display for water splitting an in “series–parallel” reaction network, with hydrogen, methane, ethane, ethylene, acetaldehyde, carbon monoxide, and carbon dioxide products being formed in the gas phase. Hydrogen peroxide is also formed in the liquid phase.

Chapter 7

7 Analysis of the Reaction Mechanism, Carbon Element Balance, OH• and H• radicals Balances

Photocatalytic water splitting reactions using Pd-TiO₂ and ethanol as an organic scavenger, lead to hydrogen production, as well as by-products formation such as methane, ethane, ethylene, acetaldehyde, CO, CO₂ and hydrogen peroxide. These various chemical species allow carbon element balance analysis, as well as OH• and H• radical balances to be performed, as explained in this chapter. Hydrogen peroxide, and pH variations have also to be considered in the reported balance analysis.

Regarding semiconductors, it was found in this PhD dissertation that the 0.25wt% Pd-TiO₂ provides a most suitable option for hydrogen production under near-UV light and visible light, as explained in chapter 6. As a result, the carbon element balance and the OH• and H• radical balances presented in this chapter, were established for the 0.25wt% Pd-TiO₂ photocatalyst.

In this chapter, the photocatalyst is designated as *Pd-TiO₂-nUV* for reactions under near-UV light and *Pd-TiO₂-VIS* for reactions under visible light.

7.1 Photocatalytic Hydrogen Production under Near-UV Light and Visible Light using 0.25wt% Pd-TiO₂

Figure 47 reports a 5055 μmoles cumulative hydrogen produced after six hours of near-UV irradiation, with a 0.25wt% Pd-TiO₂ with 0.15 g L⁻¹, 2.0 v/v% of ethanol, and with an initial pH of 4 ± 0.05. This is equivalent to a hydrogen volume of 113 cm³ STP (standard temperature and pressure). One should note that the Pd-TiO₂-UV performance after 6 h of reaction, is very favourable and this while compared, to the 1927.8 μmoles obtained with undoped mesoporous TiO₂, and the 696.7 moles of H₂ acquired with commercial DP-25 TiO₂. This increased formed hydrogen with the 0.25 wt% Pd-TiO₂-nUV, is equivalent to almost 300% of the hydrogen volume obtained with undoped mesoporous TiO₂ [171].

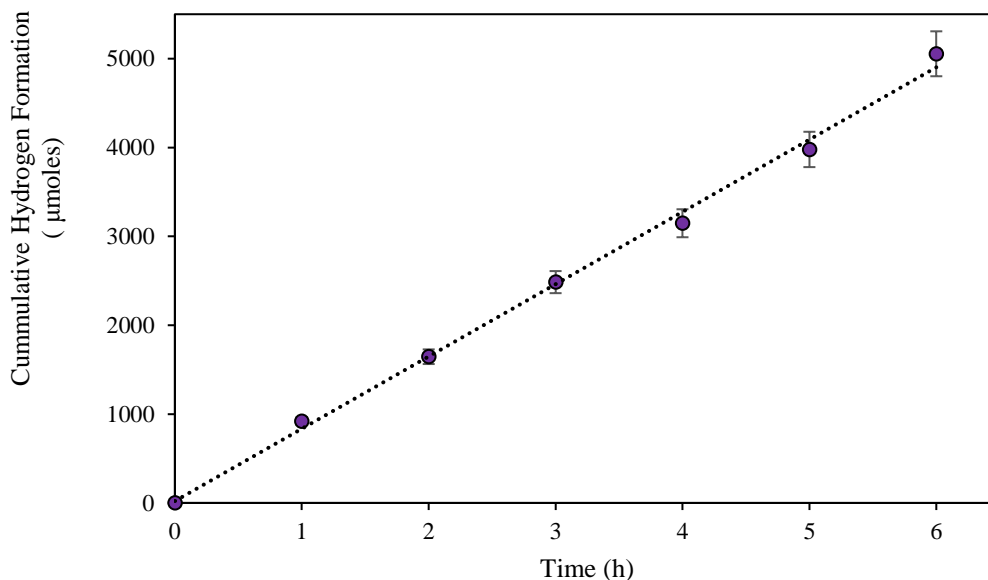


Figure 47. Cumulative Hydrogen Formed Using the 0.25 wt% Pd-TiO₂-near UV.
 Conditions: photocatalyst concentration: 0.15 g/L, 2.0 v/v% ethanol.

The Pd-TiO₂ photocatalyst, was evaluated additionally in the PCW-II reactor as follows: (a) a first photoreduction with near-UV light radiation for one hour, (b) An additional five hours with visible light irradiation. These runs designated as Pd-TiO₂-VIS runs in this PhD dissertation, were conducted under the following conditions: 0.15 g L⁻¹ of catalyst concentration, 2.0 v/v% of ethanol, and initial pH = 4 ± 0.05.

Figure 48 reports the Pd-TiO₂-VIS cumulative hydrogen formed during a first hour of near-UV irradiation, followed by an extra 5 hours of visible light. Thus, the Pd-TiO₂-VIS photocatalyst shows a positive performance for hydrogen production likely diminishing electron-hole pair recombination, and consequently contributing to higher hydrogen yields, under both near-UV and visible light irradiation.

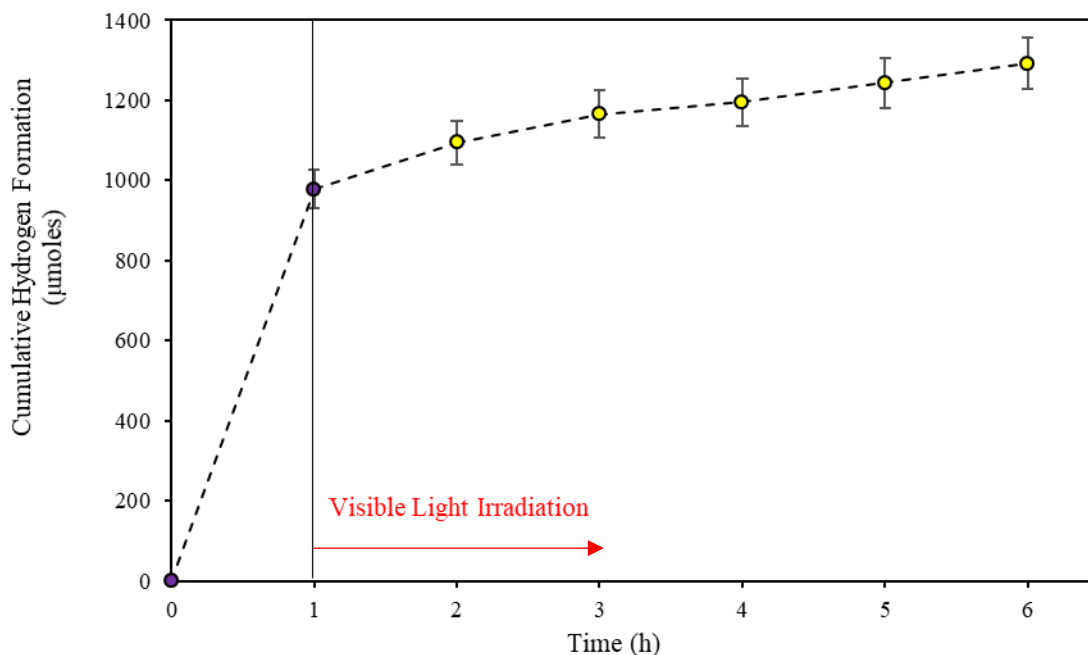


Figure 48. Cumulative Hydrogen Formed with a 0.25 wt% Pd-TiO₂-VIS Photocatalyst, which was Photoreduced during 1 h of Near-UV Light Exposure, and then Exposed to 5 h of Visible Light. Conditions: photocatalyst concentration: 0.15 g L⁻¹, scavenger concentration: 2.0 v/v% ethanol.

Figure 48 reports that during the first hour of near-UV photoreduction 979 µmoles (29 cm³ STP) of hydrogen were formed, while an extra of 314 µmoles (8.0 cm³ STP) of hydrogen were produced during the following 5 hours. One should note that the 314 µmoles of extra hydrogen formed during the 5 extra hours under visible light, compares favourably with the 46 µmoles of hydrogen produced, under the same conditions using an undoped mesoporous TiO₂ photocatalyst. This performance is also greater than the 141.2 µmoles of H₂ obtained with the commercial DP-25 TiO₂. Thus, this represents, altogether, a 76% hydrogen production increase.

7.2 By-Product Formation under Near-UV Light and Visible Light using a 0.25wt% Pd-TiO₂ Photocatalyst

Figure 49 and Figure 50 show the carbon containing products formed using the 0.25 wt% Pd-TiO₂ led as follows: (a) methane and ethane, and (b) CO, CO₂, and acetaldehyde. Thus, both reduced and oxidized carbon containing species were formed during photocatalytic runs, with these formed species being valuable to support the reaction mechanism described in Chapter 6, involving H and OH radicals.

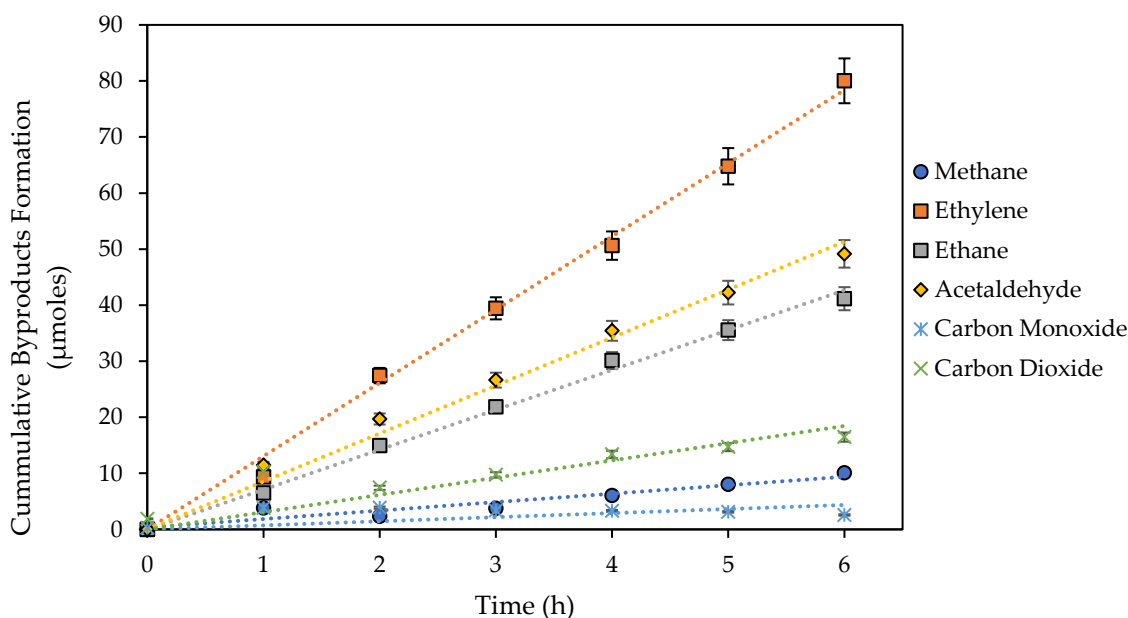


Figure 49. Cumulative Carbon Dioxide (CO₂), Methane (CH₄), Acetaldehyde (C₂H₄O), Ethane (C₂H₆), and Ethylene (C₂H₄) obtained using a 0.25 wt% Pd-TiO₂-nUV. Conditions: photocatalyst concentration of 0.15 g/L, 2.0 v/v% ethanol, near-UV light irradiation, and argon atmosphere.

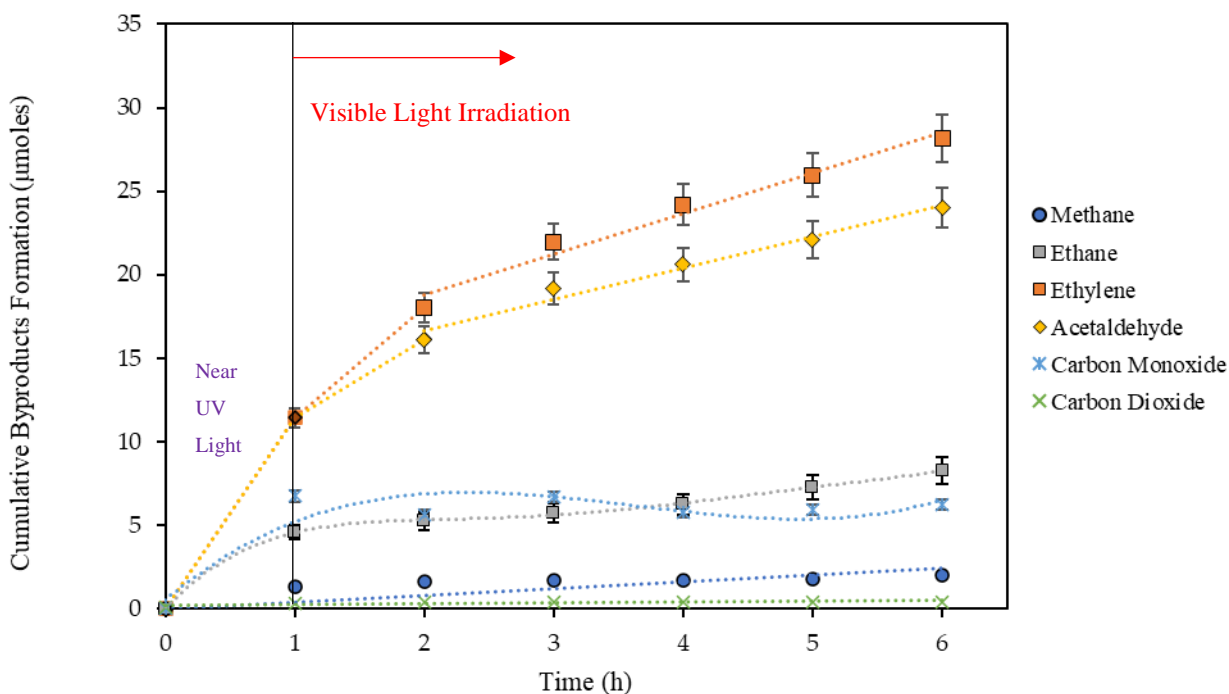


Figure 50. Cumulative Amounts of Carbon Dioxide (CO₂), Methane (CH₄), Acetaldehyde (C₂H₄O), Ethane (C₂H₆), and Ethylene (C₂H₄) Obtained using a 0.25 wt% Pd-TiO₂-VIS. Conditions: combined near-UV irradiation (1h) and visible light irradiation (5 h), photocatalyst concentration of 0.15 g/L, 2.0 v/v% ethanol, and argon atmosphere.

7.3 Carbon Element Balance

Carbon element balances can help to validate the proposed reaction mechanistic steps. These element balances shall involve all carbon containing species present during photocatalytic hydrogen formation: methane, ethane, ethylene, carbon dioxide, carbon monoxide, and acetaldehyde. Figure 51 reports a 99.8% typical element carbon balance closure, for experiments developed using the 0.25 wt% Pd-TiO₂-nUV photocatalyst.

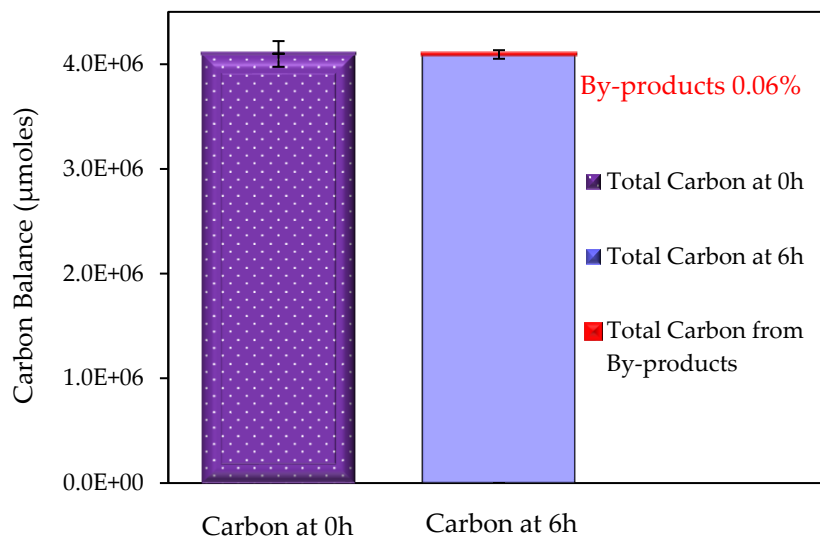


Figure 51. Total Elemental Carbon from Carbon Containing Species, at the Beginning of the Reaction and after 6 Hours of Near-UV Irradiation. Conditions: argon atmosphere, 0.25 wt% Pd-TiO₂-nUV photocatalyst, 2.0 v/v% ethanol. SD for repeats: $\pm 0.2\%$.

Figure 51 reports the following significant findings: (a) 4.10×10^6 μmoles of carbon in ethanol, at the beginning of the run, and (b) 4.09×10^6 μmoles of carbon in ethanol and all carbon containing products, after 6 h of near-UV irradiation. All carbon containing by-products after the 6 h run represent 0.06% of the total carbon present only or 2400 μmoles . Thus, photocatalytic experiments take place under close to constant ethanol scavenger concentration. The minor overall ethanol consumption, is attributed to the concurrent ethanol photo-regeneration, as described in Chapter 6. **Appendix B** provides additional details about the elemental carbon balances.

Figure 52 further reports similar elemental carbon balance results as in Figure 51, including all carbon containing species, using the 0.25 wt% Pd-TiO₂-VIS photocatalyst. In this case, from the 3.92×10^6 μmoles of carbon contained in ethanol, 3.74×10^6 μmoles of carbon, were detected in products after 6 h. This provided a 95.4% carbon balance closure and 2688 μmoles of carbon contained in products. This represented 0.07% of the total carbon and shows once again, that under the conditions studied, ethanol, while being important in acting as an OH[•] scavenger, remains at a “quasi-constant” concentration during the entire run.

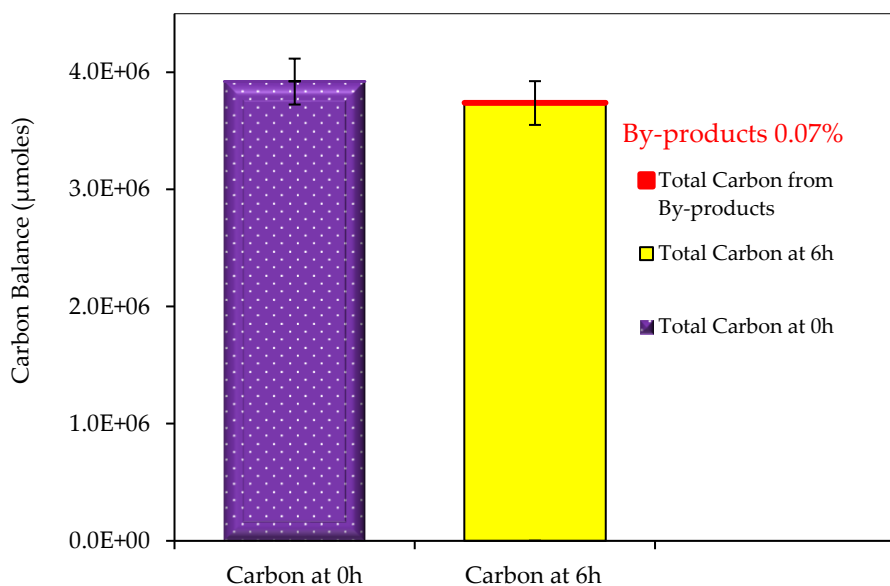
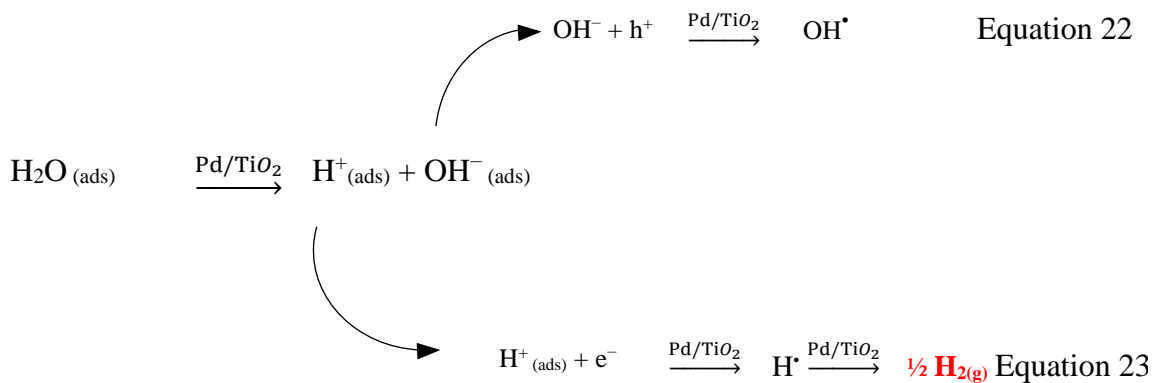
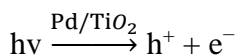


Figure 52. Total Carbon in all Carbon Containing Species at the Beginning of the Reaction and after Combined Near-UV Irradiation (1 h) and Visible Light Irradiation (5 h). Conditions: argon atmosphere, 0.25 wt% Pd-TiO₂-VIS photocatalyst, 2.0 v/v% ethanol. SD for repeats: $\pm 4.6\%$.

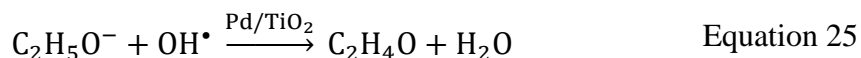
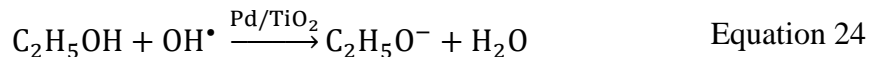
7.4 H[•] and OH[•] Radical Balance

Initial photocatalytic reaction steps can be described via Equation 22 and 23.

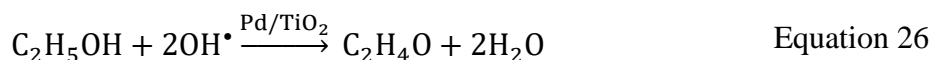


Furthermore, based on observed oxidation by-products, such as acetaldehyde, CO, and CO₂, methane, ethane, and ethylene the following oxidation-reduction reactions can be postulated.

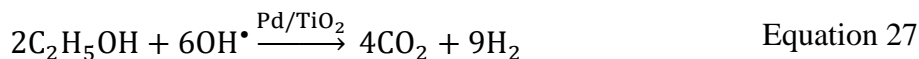
g) Acetaldehyde



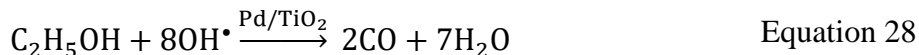
The addition of Equations 24 and 25 yields the following overall equation:



h) Carbon Dioxide

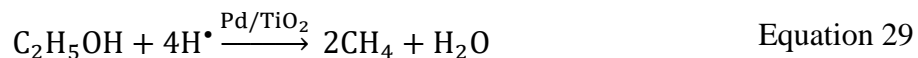


i) Carbon Monoxide

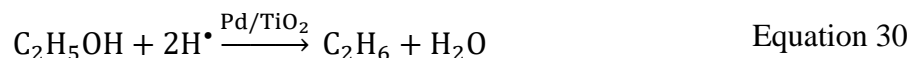


Furthermore, and using as a reference the observed reduced species the following reactions steps can be considered,

j) Methane



k) Ethane



l) Ethylene



Additionally, hydrogen peroxide can be formed due to the recombination of OH radicals being present in the solution:



In this regard, the concentration of the OH[•] and H[•] radicals calculated as a result of the stoichiometric balance during a run, can be considered to be the outcome of a net formation and consumption balance of radicals, with this leading to various observed oxidation and reduction products. More specifically, the formation of OH[•] radicals is the result of OH⁻ ion and h⁺ site interactions, as described Equation 22. On the other hand, H[•] radicals are generated, as the outcome of a H⁺ ion accepting an electron, as shown with Equation 23.

Thus, if the aforementioned proposed reaction mechanism is sound and appropriate, there must also comply with OH[•] and H[•] radicals balance. To thoroughly test this assumption, the following can be considered:

- a) The formed H[•] radicals can be calculated from the experimentally obtained hydrogen, as postulated in Equation 23, and from the consumed H[•] for various reduced by-products (e.g. methane, ethane) to be formed, as given by Equations 29 – 30.
- b) The formed OH[•] can be quantified by considering the OH[•] radicals consumed, according to the stoichiometric requirements for oxidation reactions to proceed, leading to acetaldehyde, carbon monoxide, carbon dioxide, and hydrogen peroxide species and as given by Equations 24 – 28 and 32.

Table 22 reports the calculated total moles of H[•] and OH[•] formed, during the water splitting photocatalytic reaction, under both near-UV and visible light.

Table 22. Net μMoles of H^\bullet formed and OH^\bullet consumed, following 6 h of irradiation using the Pd-TiO₂-nUV and Pd-TiO₂-VIS.

	$\mu\text{moles of OH}^\bullet$ Consumed Equations (24)– (27) (a)	$\mu\text{moles of H}^\bullet$ Formed Equations (23), (29), and (30) (b)
Pd-TiO ₂ -nUV.	2169.6	10,191.5
Pd-TiO ₂ -VIS	2342.4	2620.3

Note: (a) The μmoles of OH^\bullet radicals are calculated based on oxidized carbon containing products (CO_2 , acetaldehyde), (b) the μmoles of H^\bullet radicals are calculated on the basis of H_2 and reduced carbon species (methane, ethane).

In this regard, Table 22 shows a significant imbalance between the moles of H^\bullet produced and the moles of OH^\bullet radicals consumed, with only 21.3% of the moles of OH^\bullet radicals contributing to the formation of by-products under near-UV light. On the other hand, under visible light, 89.4% of the total moles of OH^\bullet radicals, led to carbon containing oxidation by-products. Thus, under both near-UV and visible light, the proposed redox mechanism, as postulated, for the total moles of H^\bullet and OH^\bullet , is deficient with respect to the moles of OH^\bullet radicals consumed and further refinements regarding the moles of OH^\bullet radicals involved in the postulated reaction mechanism, are required.

7.4.1 OH^\bullet Radical Analysis Including Hydrogen Peroxide

Regarding the hydrogen peroxide species produced under near-UV and visible light, they can be considered to be the net result of the rate of OH^\bullet dimerization, as shown in Equation 32, and the rate of H_2O_2 decomposition, as explained later via Equations 36-38.

7.4.1.1 Hydrogen Peroxide Evaluation Method

As explained in Chapter 3, to determine H_2O_2 at any time during a run, a colorimetric method was used considering that this provides more reliable hydrogen peroxide concentrations in the water slurry mixture from photocatalytic runs. H_2O_2 was estimated using a spectrophotometer Spectronic 200+, Thermo Spectronic (Thermo Fischer, Mississauga, ON, Canada), while using a linear calibration for 530 nm. The calibration curve was used considering the absorption spectra of the sample is shown in Figure 53.

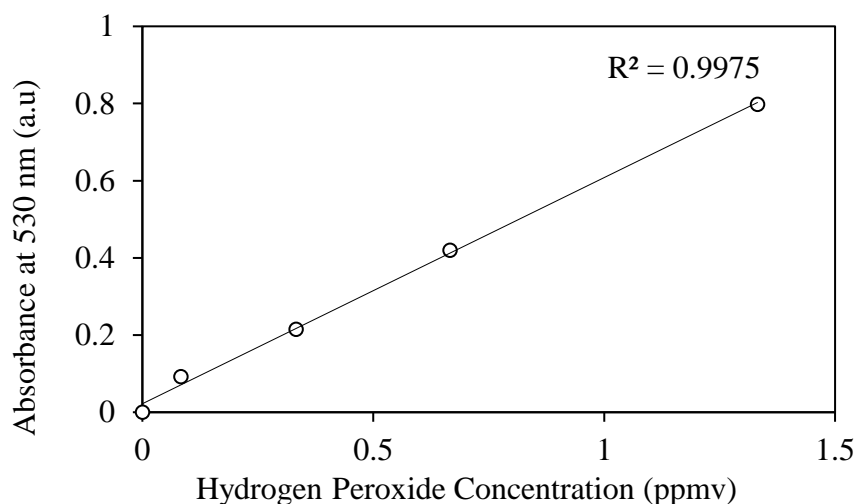


Figure 53. Calibration Curve of H₂O₂ Measurements by Colorimetric Method.

7.4.2 Hydrogen Peroxide Formation from OH[•] Radicals

To account for the H₂O₂ formation, during the photocatalytic hydrogen production, liquid samples were periodically analyzed, using a colorimetric method. As reported in Figure 54, during 6 h of near-UV irradiation, the hydrogen peroxide concentration consistently increased, with a maximum of 94.2 μmoles of H₂O₂ being obtained.

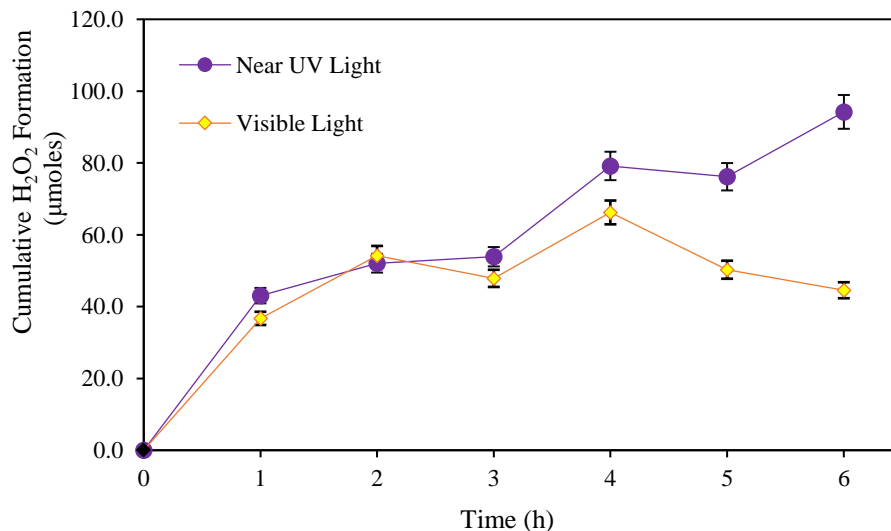


Figure 54. Cumulative H₂O₂ Formed as a Function of Irradiation Time, using a 0.25 wt% Pd-TiO₂-nUV and 0.25 wt% Pd-TiO₂-VIS (1 h photoreduction under near-UV followed by 5 h of visible light irradiation). Conditions: argon atmosphere, 0.15 g/L Pd-TiO₂ photocatalyst, 2.0 v/v% ethanol.

Figure 54 also shows that OH[•] dimerization plays an important role, as described via Equation 32, under visible light irradiation. In this case, the reaction pathway involves H₂O₂, which is formed during the first hour of near-UV irradiation, with modest additional H₂O₂ formed during the five following hours of visible light.

Table 23 reports the cumulative OH[•] consumption that leads to H₂O₂ formation. Hydrogen peroxide is detected in the liquid phase in both Pd-TiO₂-nUV or Pd-TiO₂-VIS runs. It can be observed that the OH[•] consumption due to H₂O₂ generation, only modifies the cumulative moles of OH[•] by 1.8% and 3.4% of the total amount, respectively.

Table 23. Cumulative H[•] Formed/Consumed, and OH[•] Consumed Considering H₂ and Gas Phase By-Products as established in this study.

	μmoles of H[•] Formed Equations (23), (29), and (30)	Cumulative μmoles of OH[•] Consumed Forming H₂O₂ Equation (32) (Liquid Phase)	Cumulative μmoles of OH[•] Consumed Equations (24)– (27) and (32)
Pd-TiO ₂ -nUV.	10,191.5	188.4	2359
Pd-TiO ₂ -VIS	2620.3	89.1	2431

7.4.3 Adsorption of Hydrogen Peroxide

Hydrogen peroxide formed may also adsorb on Pd-TiO₂ [185]. This adsorption may affect the balance of moles of OH[•]. Thus, to evaluate this effect, adsorption measurements under dark conditions were effected[186].

The adsorption analysis of hydrogen peroxide was carried out in the Photo-CREC Water-II Reactor at 25 ± 1 °C. Working conditions for the reactor were identical to the ones during photocatalytic runs, being however without irradiation. First, the reactor was loaded with 6 L of water at certain reagent concentrations (0 to 1.3 ppm-H₂O₂). Following this, 0.15 g/L of the TiO₂ catalyst was added to the solution. The liquid slurry was recirculated for one hour to reach adsorption equilibrium. During this period, a liquid sample was taken every 10 min, and the H₂O₂ concentration in the liquid at equilibrium (C_e) was measured, using the colorimetric method[186]. Based on the experimental data, the maximum adsorption capacity was given by the following relation:

$$Q_e = \frac{Q_{e,\max} K C_e}{(1 + K C_e)} \quad \text{Equation 35}$$

where Q_e is the H_2O_2 equilibrium adsorbent-phase concentration; C_e is the H_2O_2 equilibrium concentration in the liquid (mg L^{-1}); $Q_{e,\max}$ is the H_2O_2 maximum adsorption capacity (mg g^{-1}); and K is the adsorption constant [187].

Figure 55a describes the obtained Langmuir chemisorption isotherm ($Q_e = Q_{e,\max} K C_e / (1 + K C_e)$), showing the H_2O_2 adsorption equilibrium concentration. Through Langmuir equation linearization (Figure 55b), the H_2O_2 adsorption parameters were calculated, for the 0.25 wt% Pd-TiO₂, as shown in Table 24.

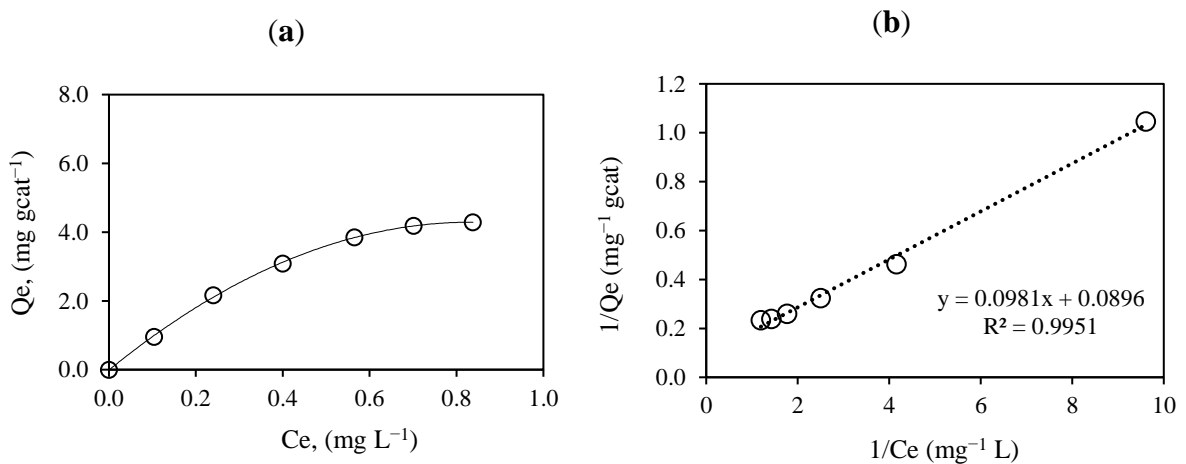


Figure 55. (a) Hydrogen Peroxide Adsorption Isotherm on a Pd-TiO₂ Photocatalyst and (b) Linearized Langmuir Equilibrium Isotherm for Hydrogen Peroxide on Pd-TiO₂.

Table 24 reports both the adsorption constant, K , and the maximum adsorption capacity, $Q_{e,\max}$, for a hydrogen peroxide adsorption isotherm. The obtained $Q_{e,\max}$ differs from the one reported by Sahel [188], who found a $Q_{e,\max}$ of $7.48 \text{ mg}^{-1} \text{L}$ value, for a undoped TiO₂ photocatalyst. This value is lower than the $11.1 \text{ mg}^{-1} \text{g}_{\text{cat}}$ maximum adsorption capacity reported in the present study. The higher $Q_{e,\max}$ reported here, can be justified given the higher surface area of the palladium photocatalyst ($131 \text{ m}^2 \text{ g}^{-1}$), with pore sizes in the 16–20

nm range. Thus, the surface area of our mesoporous semiconductor was almost three times larger than the one reported by Sahel, where the TiO₂ surface area was 50 m² g⁻¹ only [188].

Table 24. Adsorption Constants for Hydrogen Peroxide

K	Q_{e,max}
0.93 mg ⁻¹ L	11.1 mg ⁻¹ g _{cat}

Thus, it can be established that there is an extra 45% of hydrogen peroxide formed and adsorbed on the photocatalyst. On this basis, the μmoles of OH[•] consumed during the runs have to be revised, as shown in Table 25.

Table 25. Cumulative H[•] Formed/Consumed and OH[•] Consumed Considering H₂O₂ Formation and Adsorption.

	Cumulative μmoles of H[•] Formed Equations (23), (29), and (30)	Cumulative μmoles of OH[•] Forming H₂O₂ (Adsorbed)	Cumulative μmoles of OH[•] Consumed Equations (24)– (27) and (32), and OH [•] Adsorbed
Pd-TiO ₂ -nUV	10,191	84.4	2444
Pd-TiO ₂ -VIS	2620	40.1	2472

Table 25 data also show that the addition of the adsorbed H₂O₂ species accounts for 0.82% for Pd-TiO₂-nUV and 1.52% for Pd-TiO₂-VIS, in the context of H[•] and OH[•] mole balance only. Thus, there is still an important difference between the calculated OH[•] radicals consumed and H[•] radicals produced that must be accounted for.

7.4.4 Effect of the pH on the Photocatalytic Reaction

In water splitting for hydrogen production, an important factor that should be considered is the pH and pH changes of the water solution during the run. This is the case given its potential influence on the photocatalytic process efficiency [189].

To account for this, the pH of the solution was measured with a digital pH meter Thermo Scientific Orion Star, with an accuracy of ± 0.05 . The pH was monitored in the slurry every hour, to determine its effect during the photocatalytic reaction.

7.4.4.1 OH[•] Radical Formed Based on pH Influence in the Photocatalytic Reaction

Redox reactions in photocatalysis are influenced by hydrogen formation, due to the combination of excited electrons and H⁺ protons, adsorbed on the photocatalyst. It was proven, in this respect, that hydrogen production is favoured under these conditions, due to availability of dissolved H⁺ ions[190].

Regarding pH, during the photocatalytic water splitting under near-UV, using the Pd-TiO₂, a significant pH change with irradiation time was noticed, as shown in Figure 56. At the beginning of each experiment, the pH of the water-ethanol solution was set to 4.0 ± 0.005 . Upon completion of the photocatalytic reaction, after 6 hours of near-UV light irradiation, the pH increased to 5.89 ± 0.005 , which was close to the TiO₂ isoelectric point [191].

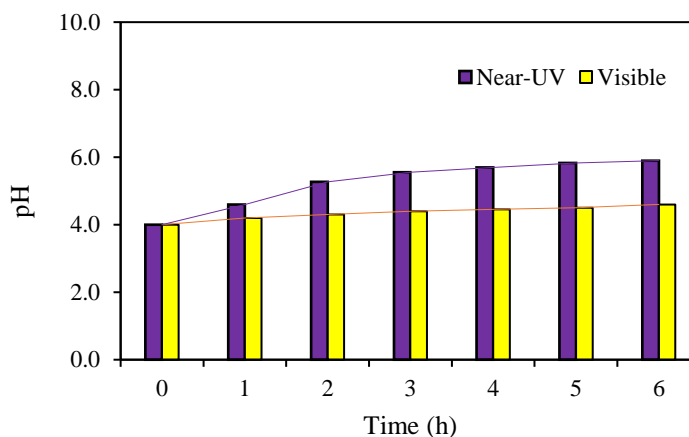
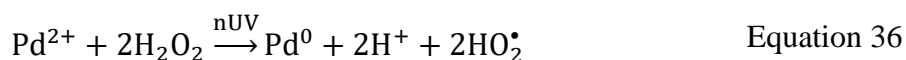


Figure 56. pH Changes with Irradiation time Using a 0.25 wt% Pd-TiO₂-nUV and a 0.25 wt% Pd-TiO₂-VIS.

On the other hand, as shown in Figure 56, for 0.25 wt% Pd-TiO₂-VIS runs, the pH increased after 1 hour of near-UV photoreduction and 5 hours of visible light, from 4.0 ± 0.005 to 4.60 ± 0.005.

Concerning the reported pH variation, it could be attributed to an electron exchange between the photocatalyst and the splitted water molecules. An electron can be donated by the photocatalyst surface, in order for the active Pd⁰ sites to yield HO[•] and OH⁻ ion free radicals[192]. Furthermore, it can be hypothesized that a fraction of the pH change can occur due to H₂O₂ decomposition. One can consider that for both the Pd-TiO₂-nUV and Pd-TiO₂-VIS, the near-UV irradiation leads to the following chain of reactions:



It can be postulated that the photocatalyst accepts electrons, with the Pd²⁺ ion sites yielding a HO₂[•] radical, as described in Equation 36. This HO₂[•] radical gives OH⁻ ions via Equation 37 and Equation 38[192].

Thus, the total moles of OH[•] radicals consumed can be revised further, accounting for the change in pH. Table 26, Figure 57a and Figure 58a report that the accounting of the cumulative moles of OH[•] consumed via a pH change provides a 97–99% balance of the moles of H[•] formed and the moles OH[•] consumed while using Pd-TiO₂-nUV and Pd-TiO₂-VIS.

Table 26. Cumulative H[•] Formed/Consumed and Cumulative μmoles of OH[•] Consumed Considering H₂O₂ (formation, adsorption, dissociation), and pH Changes.

	Cumulative μmoles of H [•] Equation (23), (29), and (30)	Cumulative μmoles of OH [•] via pH Change	Cumulative μmoles of OH [•] Consumed Equations (24)- (27), and (32) Based on H ₂ O ₂ Adsorbed and pH Change	Percentual H [•] OH [•] Balance Closure (%)
Pd-TiO ₂ -UV	10,191	7662.5	10,106.3	99.2
Pd-TiO ₂ -VIS	2620	81.9	2553.5	97.5

Figure 57b and Figure 58b also show that these consistent balances of H^\bullet and OH^\bullet μ moles were also observed at various other irradiation times, providing significant strength and validation to the photocatalytic reaction mechanism for both Pd-TiO₂-UV and Pd-TiO₂-VIS. **Appendix C** provides additional details of the H^\bullet and OH^\bullet mole balance calculations.

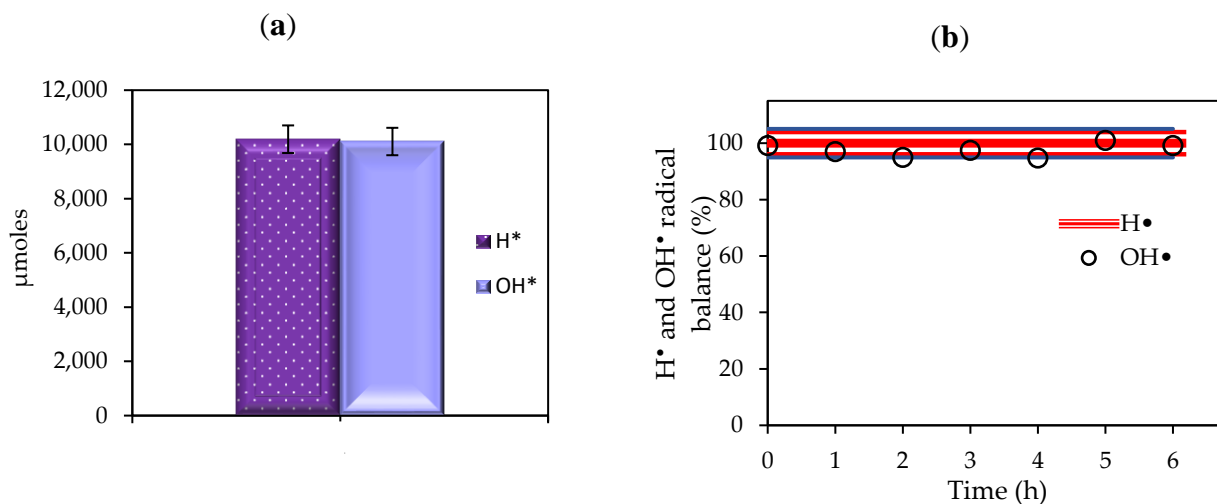


Figure 57. (a) μ moles of OH^\bullet and H^\bullet Radicals Formed after 6 h of Photocatalytic Hydrogen Production under Near-UV Light, and (b) Percentual H^\bullet and H^\bullet μ mole Balances at Different Irradiation Times under Near-UV Light. The 95% confidence and prediction intervals are reported in red and blue, respectively. SD for the repeats: $\pm 0.8\%$

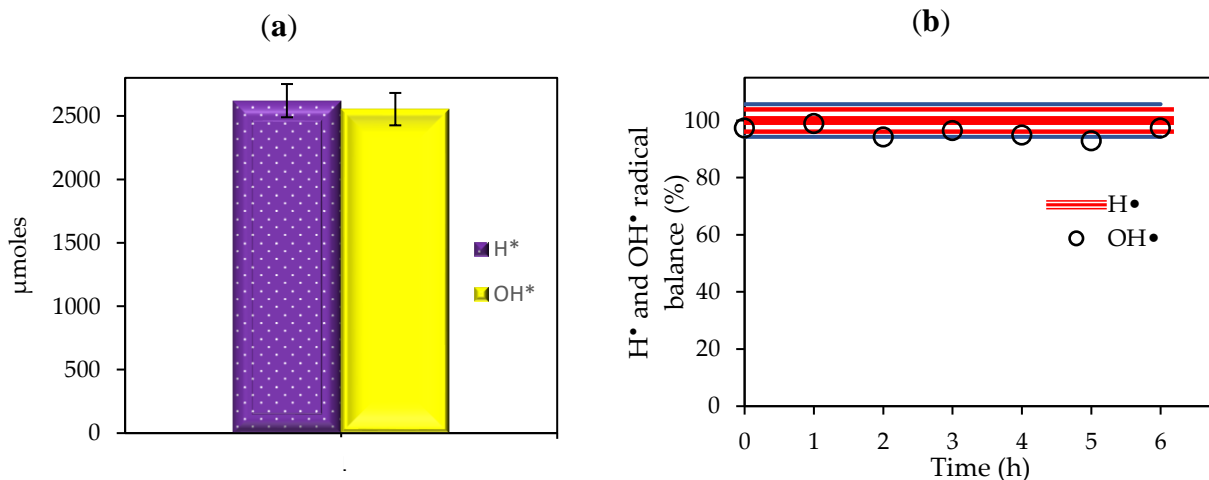


Figure 58. (a) μ Moles of OH^\bullet and H^\bullet Radicals Formed after 6 h of Photocatalytic Hydrogen Production (1 Hour of Near-UV Light Photoreduction and 5 Hours of Visible Light), and (b) Percentual OH^\bullet and H^\bullet Balances at Different Irradiation Times under Visible Light. The 95% confidence and prediction intervals are reported in red and blue, respectively. SD for the repeats: $\pm 2.5\%$

7.5 Conclusions

Given the reported results the following mechanistic steps can be considered for water splitting

- a) Hydrogen is a main product from the photocatalytic water splitting when having 2.00v/v% ethanol as an organic scavenger and a 0.25 wt% Pd-TiO₂-nUV or alternatively, a 0.25 wt% Pd-TiO₂-VIS.
- b) Formed photoreduction species (methane, ethane) and photooxidation species (CO₂, acetaldehyde) are all important observed carbon containing by-products.
- c) Hydrogen peroxide, present in the liquid phase, is formed and adsorbed on the photocatalyst during water splitting.
- d) OH⁻ species in the water solution progressively increase with irradiation time, with this leading to a pH increase of the water solution.

Chapter 8

8 Kinetics for Hydrogen Production and Formation of By-Products

Mechanistic based kinetics can be used to describe the progress of a reaction. This type of model accounts for every reaction step of a reaction network. One possible approach is to consider every reaction step, taking place on a photocatalyst, by following the Langmuir-Hinshelwood (L-M) model, which includes both intrinsic reactions and adsorption phenomena.

This type of heterogenous based kinetics can also be used to describe the photocatalytic water splitting rate with hydrogen formation and the concurrent conversion of the selected organic scavenger. Product formation can be accounted by using an anticipated *in series-parallel* reaction network, as described in Chapter 6.

Following the L-H approximation, reacting molecules are adsorbed on the photocatalyst surface at equilibrium, reacting later, on the photocatalyst surface. All this leads to molecular hydrogen formation.

Altogether the L-H model provides a set of ordinary differential equations, with a number of kinetic constants. These kinetic constants have to be estimated using statistical analysis, defining confidence intervals, cross-correlation coefficients, and residuals.

The objective of this chapter is to provide rates of hydrogen and by-product formation. Given the value of the Pd-TiO₂ photocatalyst, for hydrogen production via water splitting, under either near-UV or visible irradiation, kinetic parameters were established, in the context of this PhD dissertation, for the best performing 0.25wt% Pd-TiO₂ photocatalyst.

8.1 Langmuir-Hinshelwood Model

The L-H kinetics can be established in terms of the gas phase species concentrations as follows:

$$r_i = \text{LVRPA } f[\text{H}^+] \frac{k_i^I K_i^A C_i}{1 + \sum_{j=1}^n K_j^A C_j} = \frac{k_i^* K_i^A C_i}{1 + \sum_{j=1}^n K_j^A C_j} \quad \text{Equation 39}$$

Where r represents the rate of reaction over time, $LVRPA$ is the local rate of photon absorption, $f[H^+]$ denotes the pH influence on the photocatalytic reaction, k_i^* stands for the limiting rate constant of the reaction, under the given experimental conditions ($\text{mol g}_{\text{cat}}^{-1} \text{h}^{-1}$), K represents the equilibrium constant for the adsorption of the chemical species on the photocatalyst (L mol^{-1}), and C is the chemical species concentration at any time t (mol L^{-1}).

One should note that k_i^* and K parameters in Equation 39 are considered function of the initial concentration, C_0 , and the concentration at equilibrium, C_e . These can be predicted by simplifying Equation 40.

$$r_j \approx \frac{K_j^A C_j}{1 + K_0^A C_0} \quad \text{Equation 40}$$

By using Equation 40, an expression can be obtained for each individual chemical species formed during the photocatalytic water splitting reaction (hydrogen and by-products). Thus, a set of ordinary differential equations can be established, for the *in series-parallel* reaction network.

Furthermore, the L-H kinetic parameters also involve the adsorption constants of the organic scavenger, ethanol. In order to determine this constant, ethanol adsorption runs were carried out in the Photo-CREC Water-II Reactor under dark conditions. The adsorption runs were the same than the ones set for the water splitting reactions. First, the reactor was loaded with 6 L of water, at different ethanol concentrations (0.5 to 4% v/v). Following this, 0.15 g/L of the TiO_2 catalyst was added to the solution. The liquid slurry was recirculated for one hour to reach adsorption equilibrium. During this period, a liquid sample was taken every 10 min, and the ethanol concentration in the liquid at equilibrium (C_e) was measured using ultra fast liquid chromatography (UFLC). Based on the experimental data, the maximum adsorption capacity was given by the following relation:

$$Q_e = \frac{Q_{e,\text{max}} K C_e}{(1 + K C_e)} \quad \text{Equation 35}$$

Where Q_e is the ethanol equilibrium adsorbent-phase concentration; C_e is the equilibrium concentration in the liquid (mol L^{-1}); $Q_{e,\text{max}}$ is the maximum adsorption capacity (mol g^{-1}); and K is the adsorption constant (L mol^{-1}) [187].

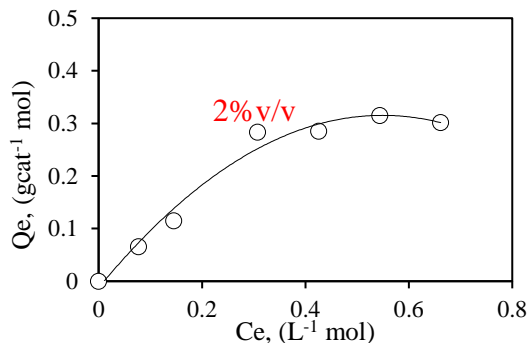


Figure 59. Ethanol Adsorbed on 0.25wt% Pd-TiO₂ Photocatalyst.

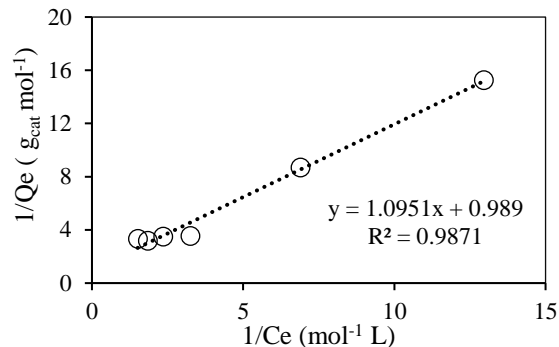


Figure 60. Linearized Langmuir Equilibrium Isotherm for Ethanol on 0.25wt% Pd-TiO₂.

Figure 59 describes the Langmuir chemisorption isotherm obtained with the data acquired in this research for ethanol ($Q_e = Q_{e,\text{max}} K C_e / (1 + K C_e)$). It shows the chemisorption character of the ethanol adsorption. One can also obtain by using a Langmuir linearized equation, as shown in Figure 60, ethanol adsorption parameters for 0.25 wt% Pd-TiO₂.

Table 27. Adsorption Constants for Ethanol for the 0.25wt% Pd-TiO₂

K	Q_{e, max}
1.26 mol ⁻¹ L	1.01 mol ⁻¹ g _{cat}

One can notice that the results reported in Table 27 differ from those obtained by Escobedo [97], who found that ethanol adsorbs on 1%Pt-TiO₂ with a $Q_{e,\text{max}}$ of 0.163 mol⁻¹ g_{cat}. This is considerably lower than the $Q_{e,\text{max}} = 1.01 \text{ mol}^{-1} \text{ g}_{\text{cat}}$ reported in Table 27, with this result being assigned to the 131 m²g⁻¹ specific surface area, with the 16–20 nm pores of the palladium-doped photocatalyst, of the present study.

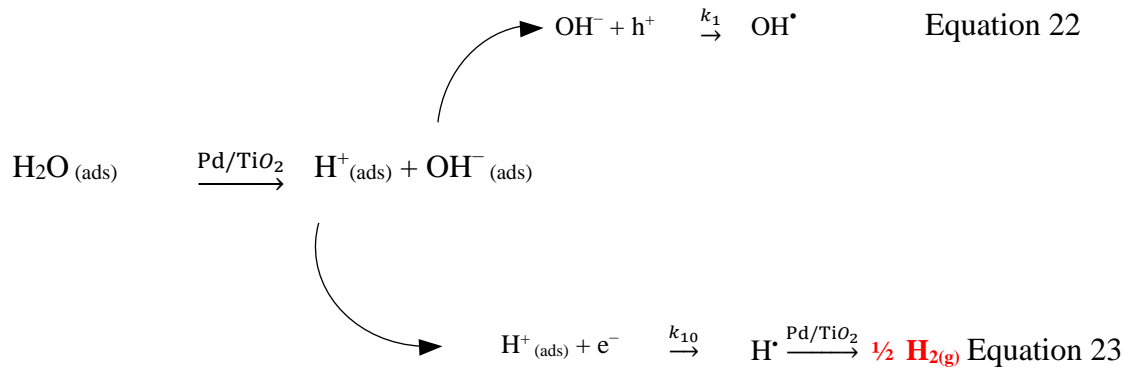
The ethanol adsorption isotherm shows that for ethanol concentrations over 2.0% v/v, the equilibrium adsorbent-phase concentration remains constant over the photocatalyst surface reaching saturation. Therefore, increment of the ethanol concentration surpassing 2.0% v/v in the photocatalytic water splitting reaction, will not enhance the hydrogen production rate.

Thus, one can see that optimal ethanol equilibrium adsorbent-phase concentration on the TiO₂ surface is reached at 2.0% v/v ethanol.

8.2 Reaction Mechanism for the *In Series-Parallel* Kinetic Reaction Network

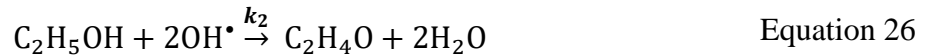
Photocatalytic water splitting reactions using Pd-TiO₂ semiconductors and ethanol as organic scavenger, lead to hydrogen formation as well as several by-products such as methane, ethane, ethylene, acetaldehyde, CO, CO₂ and hydrogen peroxide. This network of redox chemical reactions species can be modelled using an *in series-parallel* reaction network as follows:

Hydrogen Formation

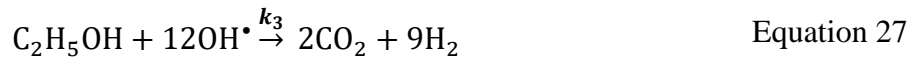


Oxidation Reactions

a) Acetaldehyde



b) Carbon Dioxide



c) Hydrogen Peroxide

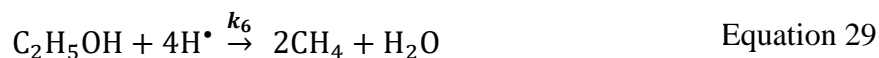


d) pH variation



Reduction Reactions

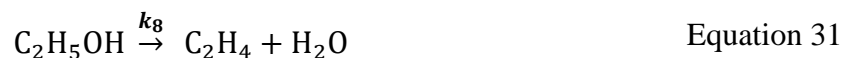
e) Methane



f) Ethane



g) Ethylene



The proposed kinetics as given by the above equations is based on the following statements[193]:

- (a) Reactions take place on the photocatalyst surface.
- (b) Reactions are elementary.
- (c) Chemical species adsorbed are in equilibrium with those in the bulk solution.
- (d) Concentration of water on the photocatalyst surface is constant.
- (e) Rate of electron-hole generation is proportional to the LVRPA or local volumetric rate of photon absorption.
- (f) The photocatalytic water splitting reactions take place in the Photo CREC Water-II Reactor, with a 0.15 g L^{-1} photocatalyst loading, 0.25wt%Pd in TiO_2 and 2.0v/v% ethanol.
- (g) Water splits, forming intermediate OH^\bullet and H^\bullet radicals, with H^\bullet reacting further, and yielding molecular hydrogen.

- (h) Ethanol, as an OH[·] organic scavenger, is consumed via different reaction pathways, and forms various oxidation by-products, such as acetaldehyde, CO, and CO₂.
- (i) Ethanol and ethanol by-products are reduced via the H[·] radicals present, yielding methane, ethane, and ethylene.

Using both the L-H approximation and an in series-parallel network, a set of ordinary equations were obtained, with these equations containing the kinetic constants, required to be evaluated using statistical data analysis.

8.3 L-H Equations Applied to the Proposed *In Series-Parallel* Reaction Network

The Langmuir-Hinshelwood (L-H) rate-based equations can be used to describe each one of the steps involved in the water splitting reaction for all chemical species formed as described by Equation 40.

Given that ethanol concentration was significantly higher comparatively to all other carbon containing by-products, hence, the following inequality could be considered:

$$K_{EtOH}^A C_{EtOH} \gg K_{H_2}^A C_{H_2} + K_{CH_4}^A C_{CH_4} + K_{C_2H_6}^A C_{C_2H_6} + K_{C_2H_4}^A C_{C_2H_4} + K_{C_2H_4O}^A C_{C_2H_4O} + K_{CO_2}^A C_{CO_2}$$

Then, the ethanol equilibrium adsorbent-phase concentration, Q_{EtOH} :

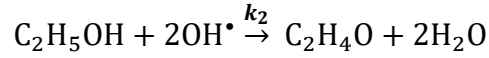
$$Q_{EtOH} = \frac{K_{EtOH}^A C_{EtOH}}{1 + K_{EtOH}^A C_{EtOH}} \cong K_{EtOH}^A C_{EtOH} \quad \text{Equation 42}$$

With this approximation being true if $1 > K_{EtOH}^A C_{EtOH}$.

On this basis, the various kinetic expressions for each one of the carbon-containing chemical species were described.

Let us consider the exponent n_m as the reaction rate order for each by-product.

(a) Acetaldehyde (C₂H₄O)



$$-r_{\text{EtOH}} = -\frac{1}{2}r_{\text{OH}\cdot} = r_{\text{C}_2\text{H}_4\text{O}} = \frac{1}{2}r_{\text{H}_2\text{O}}$$

$$-r_{\text{OH}\cdot} = 2 r_{\text{C}_2\text{H}_4\text{O}}$$

$$-r_{\text{OH}\cdot} = 2 k_2 Q_{\text{EtOH}} Q_{\text{OH}\cdot}^{n_1}$$

$$r_{\text{C}_2\text{H}_4\text{O}} = k_2 Q_{\text{EtOH}} Q_{\text{OH}\cdot}^{n_1} \quad \text{Equation 43}$$

(b) Carbon Dioxide (CO₂)



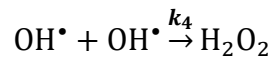
$$-r_{\text{EtOH}} = -\frac{1}{12}r_{\text{OH}\cdot} = \frac{1}{2}r_{\text{CO}_2} = \frac{1}{9}r_{\text{H}_2\text{O}}$$

$$-r_{\text{OH}\cdot} = 6 r_{\text{CO}_2}$$

$$-r_{\text{OH}\cdot} = 6 k_3 Q_{\text{EtOH}} Q_{\text{OH}\cdot}^{n_2}$$

$$r_{\text{CO}_2} = k_3 Q_{\text{EtOH}} Q_{\text{OH}\cdot}^{n_2} \quad \text{Equation 44}$$

(c) Hydrogen Peroxide (H₂O₂)



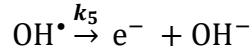
$$-\frac{1}{2}r_{\text{OH}\cdot} = r_{\text{H}_2\text{O}_2}$$

$$-r_{\text{OH}\cdot} = 2 r_{\text{H}_2\text{O}_2}$$

$$-r_{\text{OH}\cdot} = 2 k_4 Q_{\text{OH}\cdot}^3$$

$$r_{\text{H}_2\text{O}_2} = k_4 Q_{\text{OH}\cdot}^{n_3} \quad \text{Equation 45}$$

(d) pH variation



$$-r_{\text{OH}^\bullet} = r_{\text{OH}^-}$$

$$-r_{\text{OH}^\bullet} = k_5 Q_{\text{OH}^\bullet}^4$$

$$r_{\text{OH}^-} = k_5 Q_{\text{OH}^\bullet}^4 \quad \text{Equation 46}$$

(e) Hydroxyl Radical (OH[•]) Consumption – Formation

$$r_{\text{OH}^\bullet} = k_1 - 2 k_2 Q_{\text{EtOH}} Q_{\text{OH}^\bullet}^{n_1} - 6 k_3 Q_{\text{EtOH}} Q_{\text{OH}^\bullet}^{n_2} - 2 k_4 Q_{\text{OH}^\bullet}^{n_3} - k_5 Q_{\text{OH}^\bullet}^{n_4} \quad \text{Equation 47}$$

Applying the steady state $\frac{dN_{\text{OH}^\bullet}}{dt} = 0$ and the ethanol concentration approximations, the following:

$$k_1 = 2 k_2 Q_{\text{EtOH}} Q_{\text{OH}^\bullet}^{n_1} + 6 k_3 Q_{\text{EtOH}} Q_{\text{OH}^\bullet}^{n_2} + 2 k_4 Q_{\text{OH}^\bullet}^{n_3} + k_5 Q_{\text{OH}^\bullet}^{n_4}$$

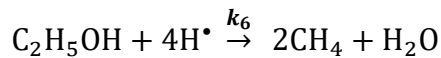
From all the OH[•] radicals formed, only a third of them were consumed, as indicated by the quantum yield (QY < 69.4%) and as described in Chapter 9. Therefore, in this case, the concentration of hydroxyl radicals was approximately constant ($Q_{\text{OH}^\bullet} \cong \text{constant}$) and could be expressed as follows:

Equation 48

$$k_1 = 2 k_2' Q_{\text{EtOH}} + 6 k_3' Q_{\text{EtOH}} + 2 k_4' + k_5'$$

Note: $k'i = ki Q_{\text{OH}^\bullet}$

(f) Methane (CH₄)



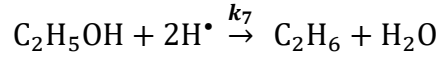
$$-r_{\text{EtOH}} = -\frac{1}{4} r_{\text{H}^\bullet} = \frac{1}{2} r_{\text{CH}_4} = r_{\text{H}_2\text{O}}$$

$$-r_{H\cdot} = 2r_{CH_4}$$

$$-r_{H\cdot} = 2 k_6 Q_{EtOH} Q_{H\cdot}^{n_5}$$

$$r_{CH_4} = k_6 Q_{EtOH} Q_{H\cdot}^{n_5} \quad \text{Equation 49}$$

(g) Ethane (C₂H₆)



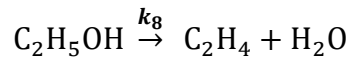
$$-r_{EtOH} = -\frac{1}{2}r_{H\cdot} = r_{C_2H_6} = r_{H_2O}$$

$$-r_{H\cdot} = 2r_{C_2H_6}$$

$$-r_{H\cdot} = 2 k_7 Q_{EtOH} Q_{H\cdot}^{n_6}$$

$$r_{C_2H_6} = k_7 Q_{EtOH} Q_{H\cdot}^{n_6} \quad \text{Equation 50}$$

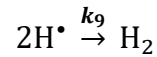
(h) Ethylene (C₂H₄)



$$-r_{EtOH} = r_{C_2H_4} = r_{H_2O}$$

$$r_{C_2H_4} = k_8 Q_{EtOH} \quad \text{Equation 51}$$

(i) Hydrogen (H₂)



$$-\frac{1}{2}r_{H\cdot} = r_{H_2}$$

$$-r_{H\cdot} = 2 r_{H_2}$$

$$-r_{H\cdot} = 2 k_9 Q_{H\cdot}^{n_7}$$

$$r_{H_2} = k_9 Q_{H\cdot}^{n_7} \quad \text{Equation 52}$$

(j) H[•] consumption - formation

$$r_{H^{\bullet}} = r_{H^{\bullet}} - 2r_{CH_4} - 2r_{C_2H_6} - 2r_{H^{\bullet}} \quad \text{Equation 53}$$

Considering, $r_{H^{\bullet}} = r_{OH^{\bullet}}$

$$r_{H^{\bullet}} = k_1 - 2k_6 Q_{EtOH} Q_{H^{\bullet}}^{n_5} - 2k_7 Q_{EtOH} Q_{H^{\bullet}}^{n_6} - 2k_9 Q_{H^{\bullet}}^{n_7} \quad \text{Equation 54}$$

By applying the steady-state approximation $\frac{dN_{H^{\bullet}}}{dt} = 0$, and the ethanol concentration inequality, this results in Equation 42:

$$k_1 = 2k_6 Q_{EtOH} Q_{H^{\bullet}}^{n_5} + 2k_7 Q_{EtOH} Q_{H^{\bullet}}^{n_6} + 2k_9 Q_{H^{\bullet}}^{n_7}$$

Considering a quantum yield of QY < 69.4% (Chapter 9), one can conclude that the concentration of hydrogen radicals is approximately constant ($C_{H^{\bullet}} \cong \text{constant}$).

Note: $k'i = ki Q_{H^{\bullet}}$

$$k_1 = 2k_6' Q_{EtOH} + 2k_7' Q_{EtOH} + 2k_9' \quad \text{Equation 55}$$

Experimental data obtained in the present study confirms that k_1 , which is related to OH radical formation, is constant along the reaction time.

Furthermore, at a set ethanol concentration of 2.0v/v%, the reaction rate for each chemical species resulting from both water splitting and redox OH[•] and H[•] reactions is given by the expressions in Table 28. These reaction rates are based on experimental observations.

Table 28. Reaction Rates for the Chemical Species Involved in the Photocatalytic Water Splitting Reaction using Ethanol as an Organic Scavenger.

Chemical Species	Reaction Rate
Acetaldehyde	$r_{C_2H_4O} = k_2' Q_{EtOH}$
Carbon Dioxide	$r_{CO_2} = k_3' Q_{EtOH}$
Hydrogen Peroxide	$r_{H_2O_2} = k_4'$
Methane	$r_{CH_4} = k_6' Q_{EtOH}$
Ethane	$r_{C_2H_6} = k_7 Q_{EtOH}$
Ethylene	$r_{C_2H_4} = k_8' Q_{EtOH}$
Hydrogen	$r_{H_2} = k_9'$

8.4 Kinetic Parameters Estimation

The proposed kinetics of the present study, for hydrogen production, as reported in Table 28 involves 7 reactions, and their respective parameters. These parameters were evaluated using experimental data which involved a 0.25wt% Pd-TiO₂ photocatalyst, 2.0v/v% ethanol concentration, 0.15 g L⁻¹ photocatalyst loading and initial pH = 4.0.

To accomplish this, a linear fit regression analysis of an objective function to a minimum value involving a kinetic model prediction and experimental data was considered. Adjustment of kinetic parameters was developed until the sum of the square residuals is minimized as:

$$\sum_{i=1}^n (V_{i,exp} - V_{i,model})^2 = \text{minimum} \quad \text{Equation 56}$$

With $V_{i,exp}$ being the experimentally observed volume at STP conditions and this for each chemical species, and $V_{i,model}$ representing the calculated volume at STP using the proposed kinetic model.

8.4.1 Kinetic Parameters Estimation under Near-UV Light

Comparison of model predictions and experimental data using the 0.25wt% Pd-TiO₂ photocatalyst of present study with 2.0v/v% ethanol as an organic scavenger and under 6 hours of near-UV irradiation, are reported in Figures 61-67.

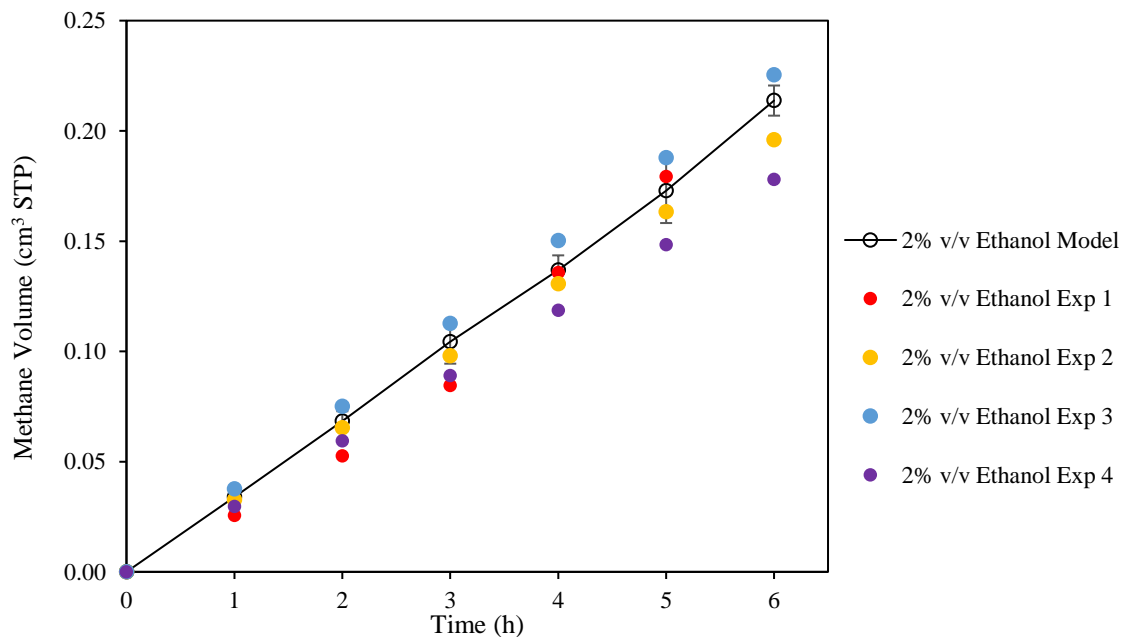


Figure 61. Cumulative Methane Volume (STP) after 6 Hours of Irradiation. Experimentally observed runs are represented by (○). Model predictions are represented by (—). Experimental conditions: a) near-UV irradiation, b) 0.25wt% Pd-TiO₂ photocatalyst and 0.15 g L⁻¹ photocatalyst loading, c) Initial pH = 4.0.

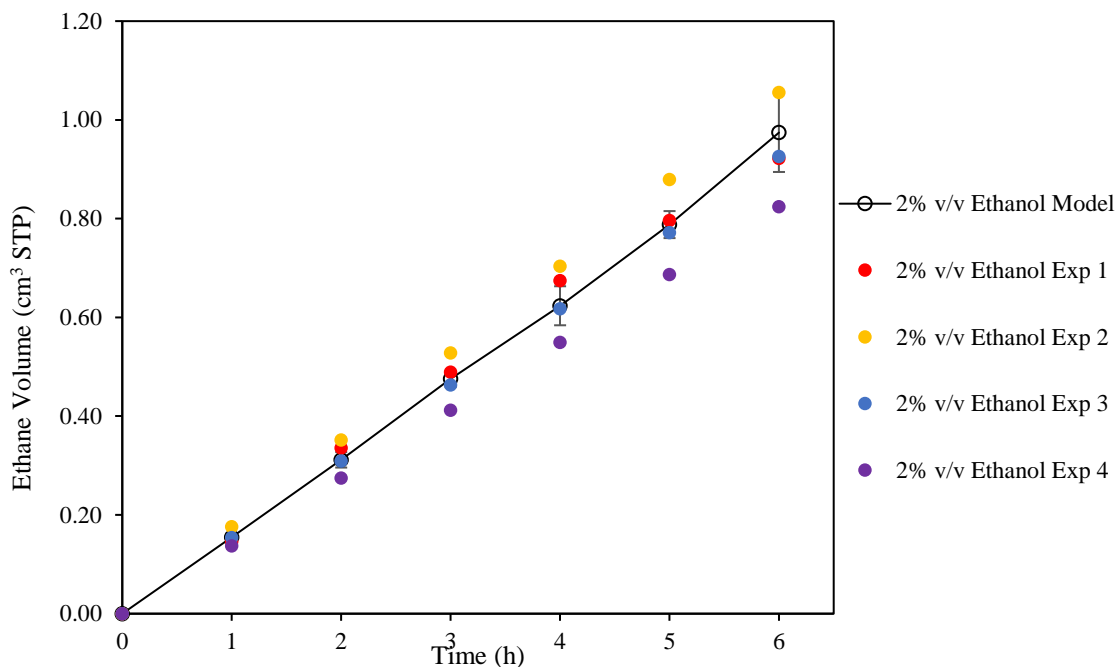


Figure 62. Cumulative Ethane Volume (STP) Obtained after 6 Hours of Irradiation. Experimentally observed runs are represented by (○). Model predictions are represented by (—). Experimental conditions: a) near-UV irradiation, b) 0.25wt% Pd-TiO₂ photocatalyst and 0.15 g L⁻¹ photocatalyst loading, c) Initial pH = 4.0.

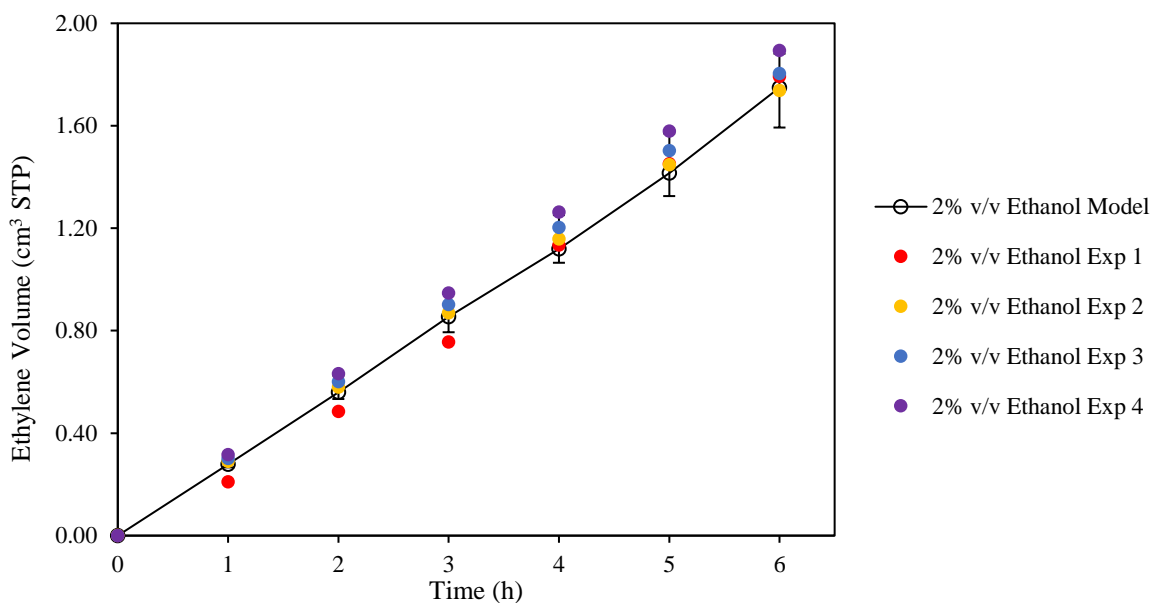


Figure 63. Cumulative Ethylene Volume (STP) Obtained after 6 Hours of Irradiation. Experimentally observed runs are represented by (○). Model predictions are represented by (—). Experimental conditions: a) near-UV irradiation, b) 0.25wt% Pd-TiO₂ photocatalyst and 0.15 g L⁻¹ photocatalyst loading, c) Initial pH = 4.0.

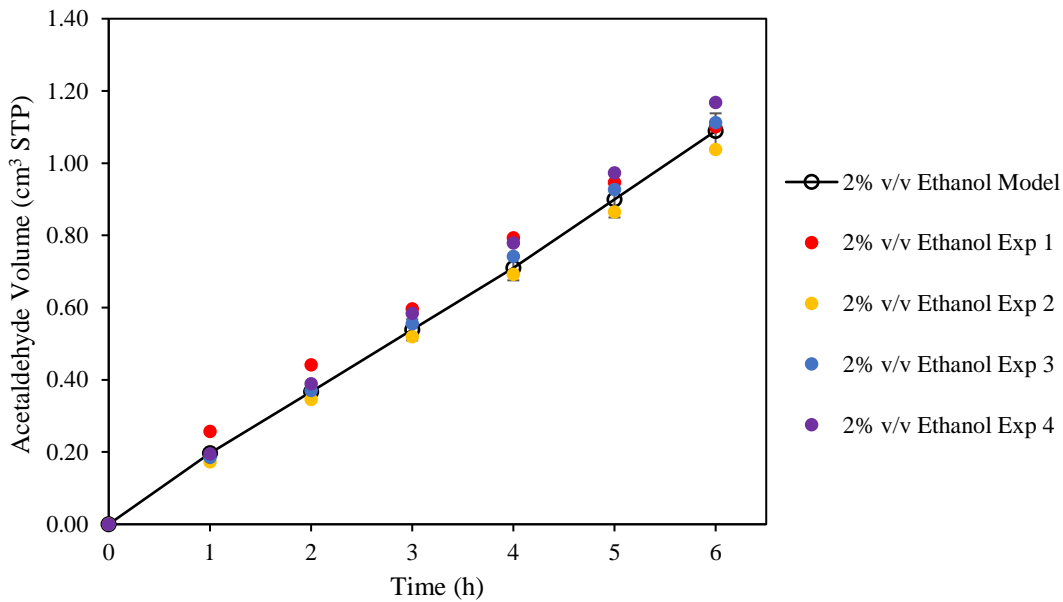


Figure 64. Cumulative Acetaldehyde Volume Obtained after 6 Hours of Irradiation. Experimentally observed runs are represented by (○). Model predictions are represented by (—). Experimental conditions: a) near-UV irradiation, b) 0.25wt% Pd-TiO₂ photocatalyst and 0.15 g L⁻¹ photocatalyst loading, c) Initial pH = 4.0.

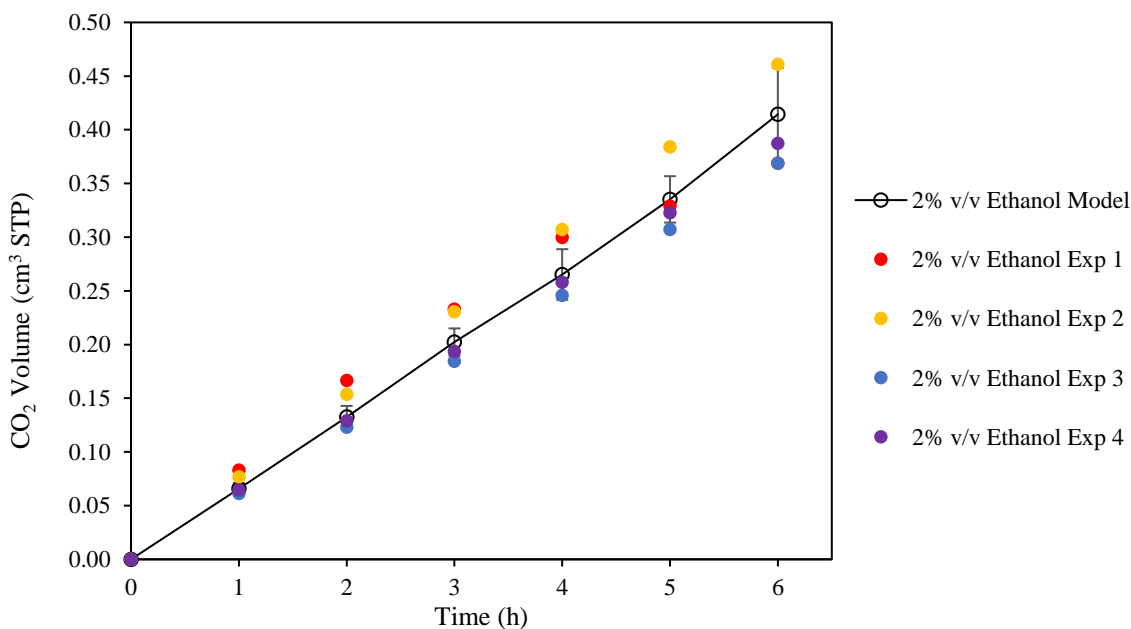


Figure 65. Cumulative CO₂ Volume after 6 Hours of Irradiation. Experimentally observed runs are represented by (○). Model predictions are represented by (—). Experimental conditions: a) near-UV irradiation, b) 0.25wt% Pd-TiO₂ photocatalyst and 0.15 g L⁻¹ photocatalyst loading, c) Initial pH = 4.0.

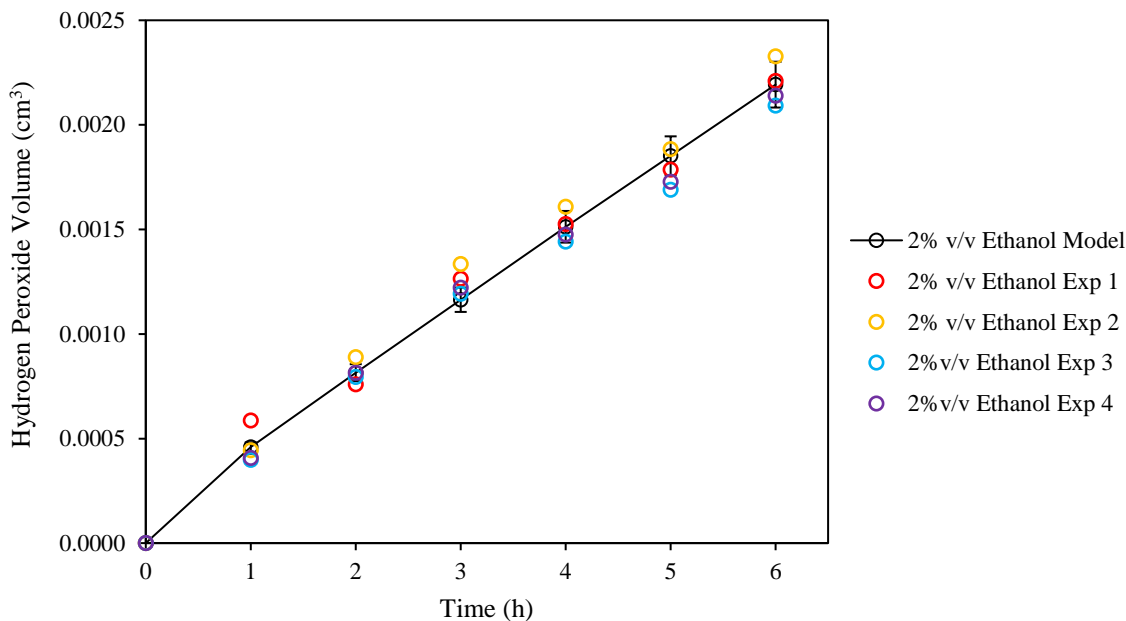


Figure 66. Cumulative Hydrogen Peroxide Volume Obtained after 6 Hours of Irradiation. Experimentally observed runs are represented by (○). Model predictions are represented by (—). Experimental conditions: a) near-UV irradiation, b) 0.25wt% Pd-TiO₂ photocatalyst and 0.15 g L⁻¹ photocatalyst loading, c) Initial pH = 4.0.

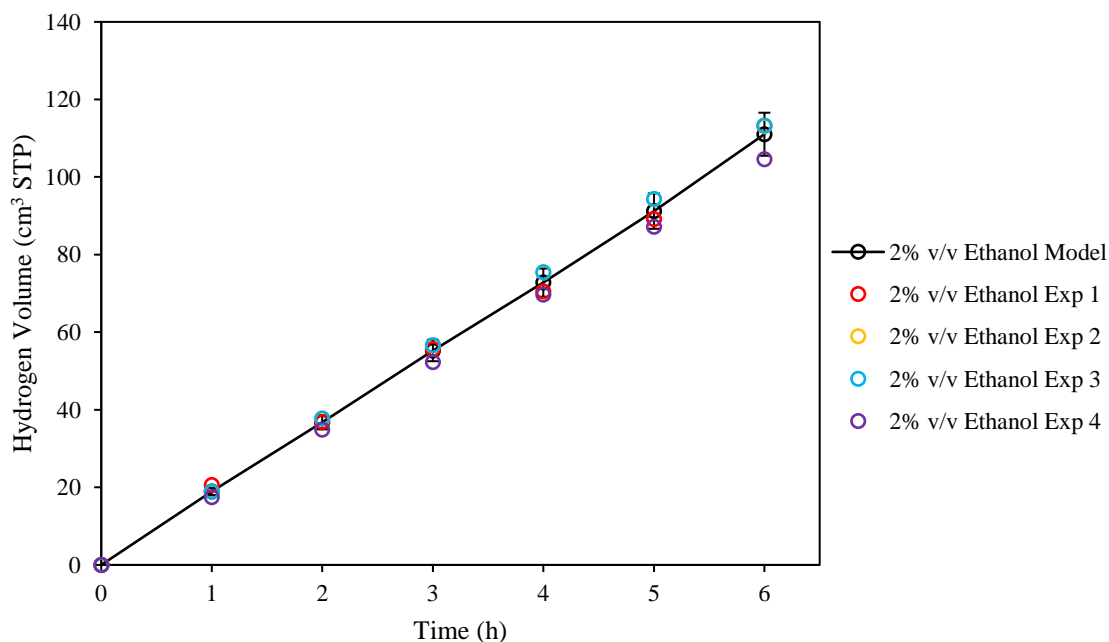


Figure 67. Cumulative Hydrogen Volume Obtained after 6 Hours of Irradiation. Experimentally observed runs are represented by (○). Model predictions are represented by (—). Experimental conditions: a) near-UV irradiation, b) 0.25wt% Pd-TiO₂ photocatalyst and 0.15 g L⁻¹ photocatalyst loading, c) Initial pH = 4.0.

One significant feature of the Figures 61-67 reported, is the common linear trend, representing a steady increase of the obtained STP volume of all chemical species during the 6 hours of irradiation, with no photoactivity decay.

Based on the proposed kinetics and the experimental data, the k_2' , k_3' , k_4' , k_6' , k_7' , k_8' and k_9' intrinsic kinetic rate constants, are reported in Table 29, along with their standard deviations and their confidence intervals.

Table 29. Intrinsic Kinetic Rate Constants for Hydrogen and By-Products under Near-UV light at 2.0% v/v Ethanol. The adsorption constant for ethanol was set to $1.26 \text{ mol}^{-1} \text{ L}$, as shown in Section 8.1.

	Intrinsic kinetic Rate Constant (h^{-1})	STD (\pm)	Confidence Interval
k_2'	3.44E-03	9.21E-05	1.35E-04
k_3'	1.25E-03	1.24E-04	2.00E-04
k_4'	2.60E-03	1.06E-04	1.60E-04
k_6'	6.24E-04	6.60E-05	1.13E-04
k_7'	2.90E-03	3.17E-04	4.72E-04
k_8'	5.64E-03	3.77E-04	5.21E-04
k_9'	1.43E-01	4.60E-03	3.37E-03

The reported intrinsic kinetic rate constants of Table 29 can be determined with limited standard deviations. This points to the adequacy of the intrinsic rate constants selected, for the photocatalytic water splitting reaction, under near-UV light.

Furthermore, the intrinsic kinetic rate constant for k_1 is $1.71\text{E-}03 \text{ h}^{-1}$ corresponding to the OH radical formation, and for k_5 is $3.13\text{E-}01 \text{ h}^{-1}$ corresponding to the OH^- or pH change. It is however, recommended to analyse the validity of this functionality in future studies.

8.4.2 Kinetic Parameters Estimation under Visible Light

Kinetic parameter estimations for the “in series-parallel” model under visible light, are reported in the upcoming figures of this chapter. The proposed kinetic model was evaluated using experimental data obtained for the 0.25wt%Pd-TiO₂ photocatalyst, at 2.0v/v% ethanol concentration, using 0.15 g L⁻¹ photocatalyst and an initial pH of 4.0. The adsorption constant for ethanol used for the model was 1.265 mol⁻¹ L. The photocatalyst was pre-reduced under near-UV irradiation for 1 hour, proceeding after this with 5 hours of visible light.

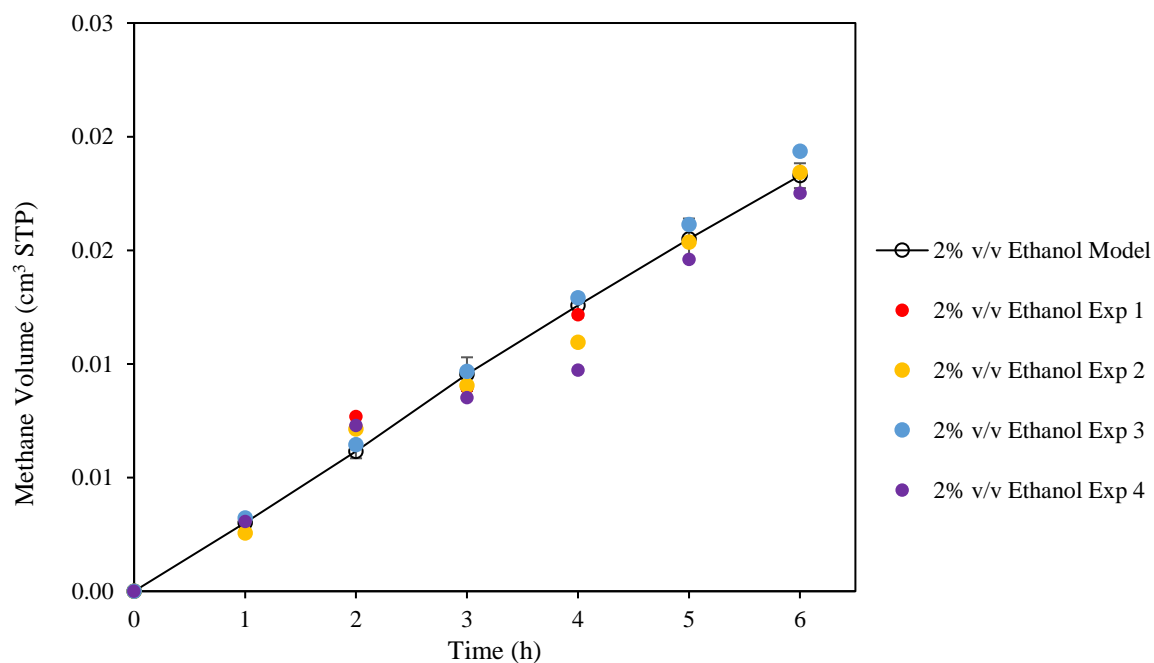


Figure 68. Cumulative Methane Volume after 6 hours of Irradiation. Experimentally observed runs are represented by (○). Model predictions are represented by (—). Experimental conditions: a) 0.25wt% Pd-TiO₂ photocatalyst and 0.15 g L⁻¹ photocatalyst loading, b) Initial pH = 4.0, c) 1 hour near-UV light plus 5 hours under visible light.

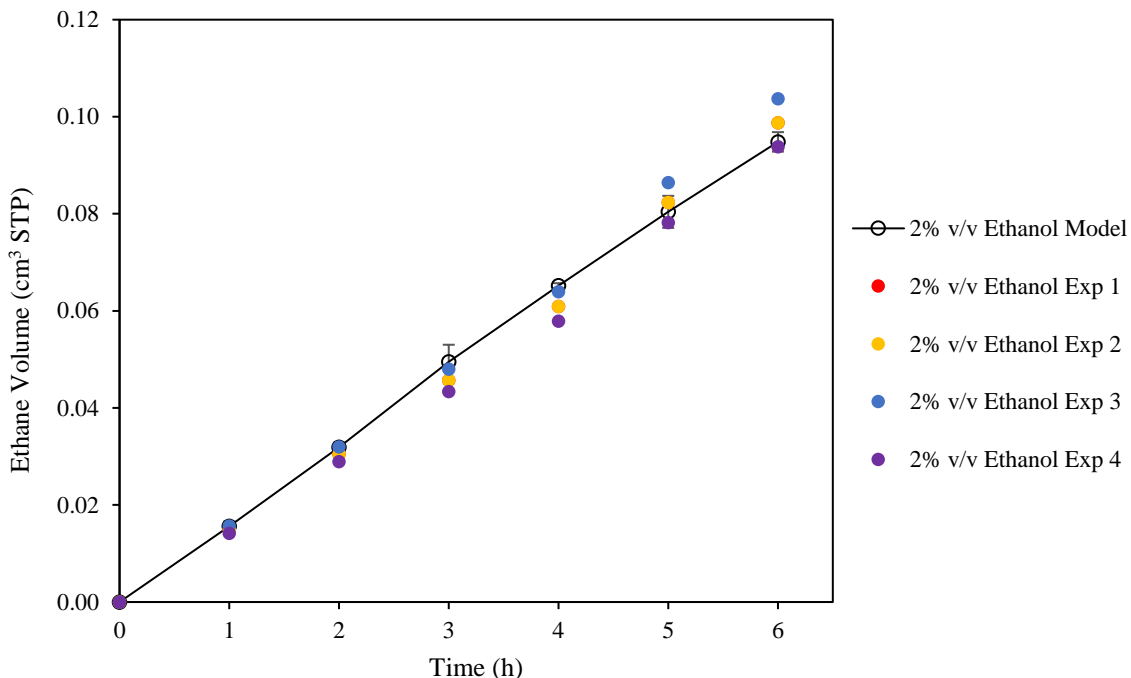


Figure 69. Cumulative Ethane Volume after 6 Hours of Irradiation. Experimentally observed runs are represented by (○). Model predictions are represented by (—). Experimental conditions: a) 0.25wt% Pd-TiO₂ photocatalyst and 0.15 g L⁻¹ photocatalyst loading, b) Initial pH = 4.0, c) 1 hour near-UV light plus 5 hours under visible light.

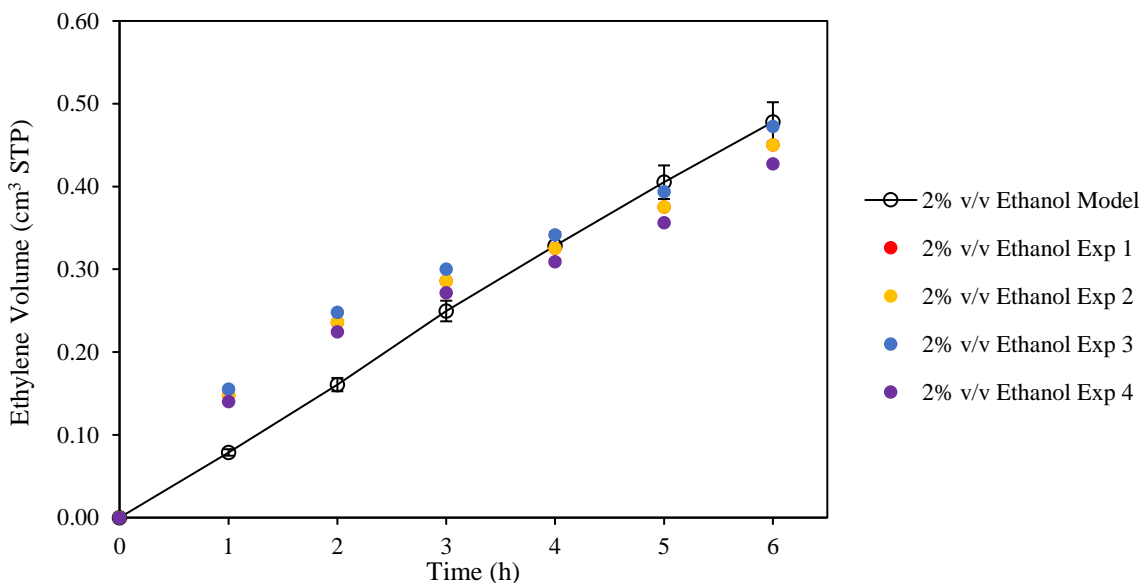


Figure 70. Cumulative Ethylene Volume after 6 Hours of Irradiation. Experimentally observed runs are represented by (○). Model predictions are represented by (—). Experimental conditions: a) 0.25wt% Pd-TiO₂ photocatalyst and 0.15 g L⁻¹ photocatalyst loading, b) Initial pH = 4.0, c) 1 hour near-UV light plus 5 hours under visible light.

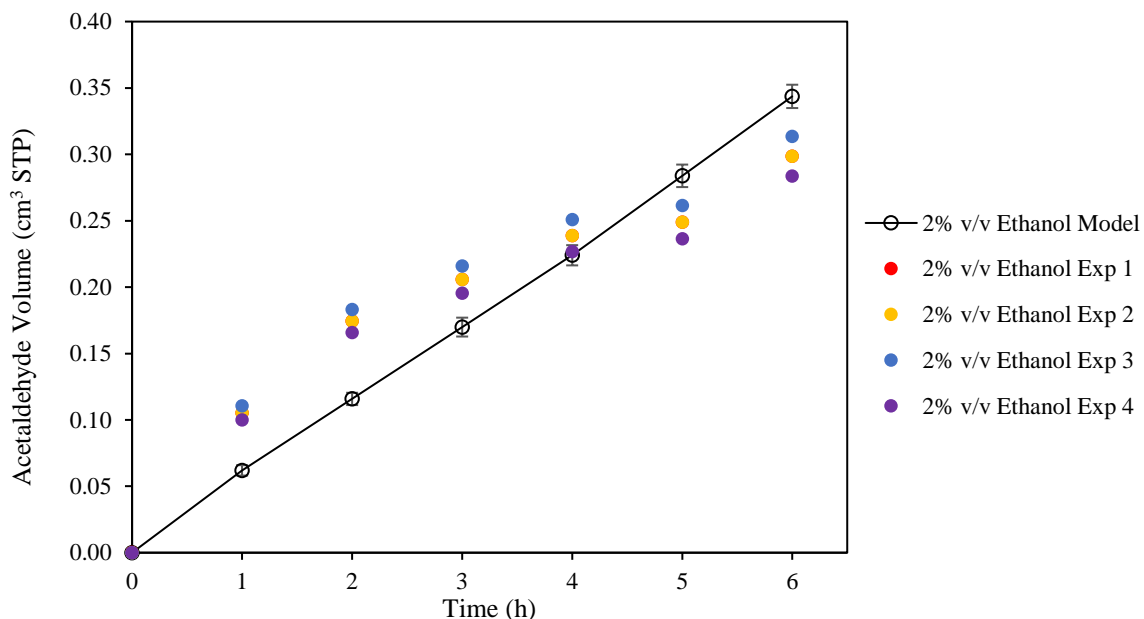


Figure 71. Cumulative Acetaldehyde Volume after 6 Hours of Irradiation. Experimentally observed runs are represented by (○). Model predictions are represented by (—). Experimental conditions: a) 0.25wt% Pd-TiO₂ photocatalyst and 0.15 g L⁻¹ photocatalyst loading, b) Initial pH = 4.0, c) 1 hour near-UV light plus 5 hours under visible light.

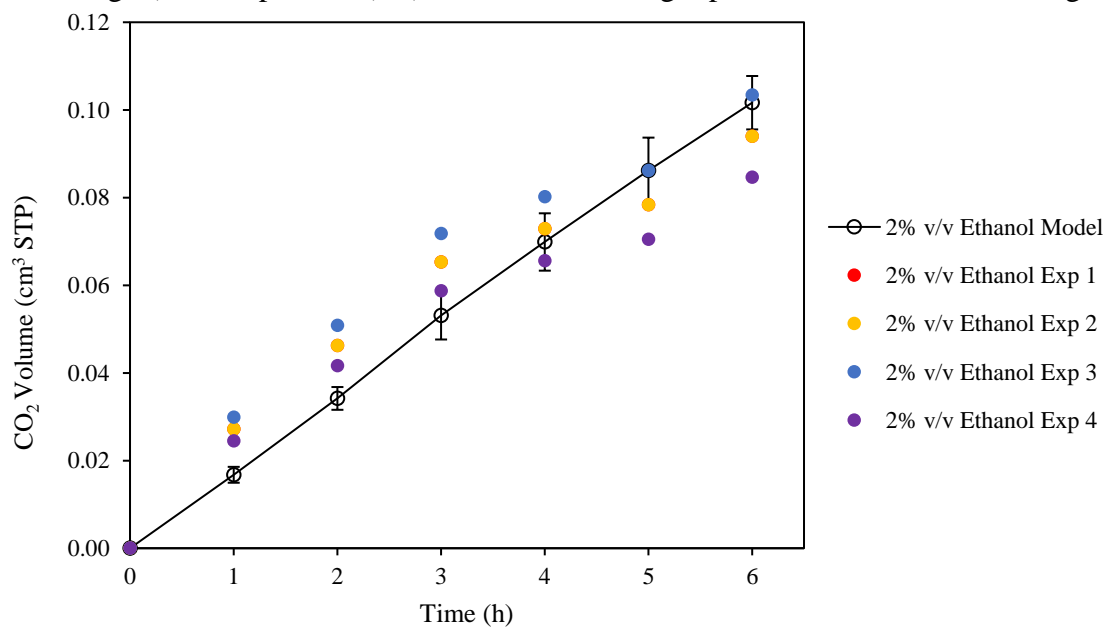


Figure 72. Cumulative CO₂ Volume after 6 Hours of Irradiation. Experimentally observed runs are represented by (○). Model predictions are represented by (—). Experimental conditions: a) 0.25wt% Pd-TiO₂ photocatalyst and 0.15 g L⁻¹ photocatalyst loading, b) Initial pH = 4.0, c) 1 hour near-UV light plus 5 hours under visible light.

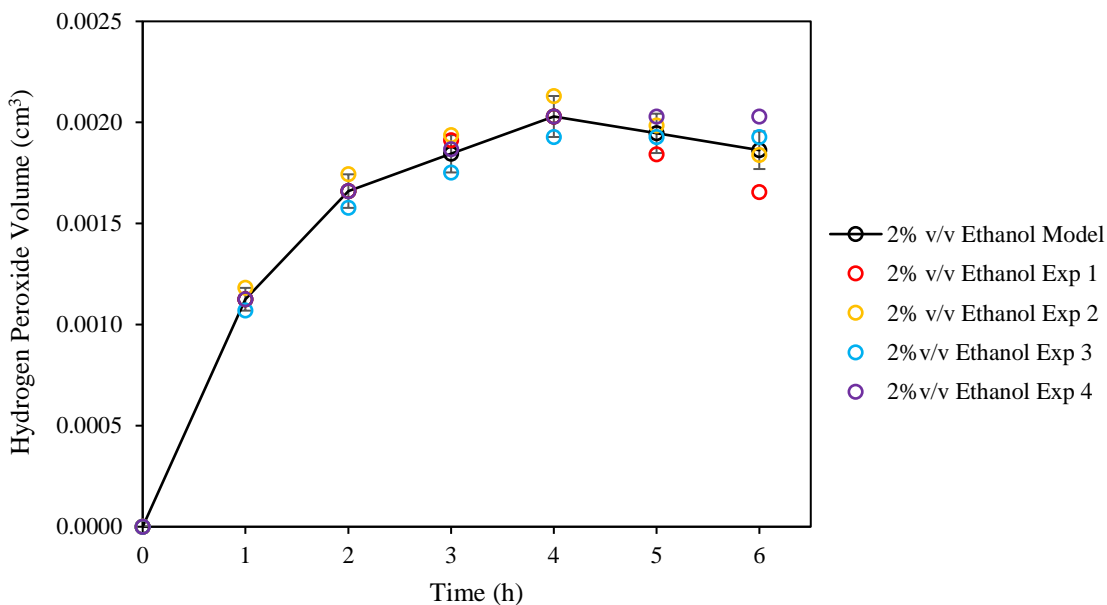


Figure 73. Cumulative Hydrogen Peroxide Volume after 6 Hours of Irradiation. Experimentally observed runs are represented by (○). Model predictions are represented by (—). Experimental conditions: a) 0.25wt% Pd-TiO₂ photocatalyst and 0.15 g L⁻¹ photocatalyst loading, b) Initial pH = 4.0, c) 1 hour near-UV light plus 5 hours under visible light.

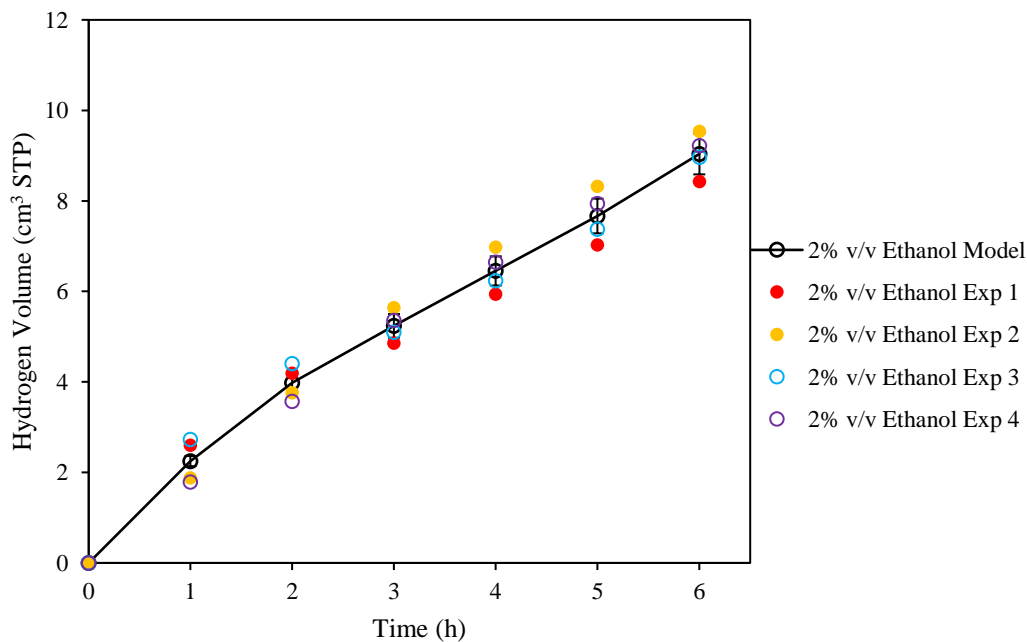


Figure 74. Cumulative Hydrogen Volume after 6 hours of Irradiation. Experimentally observed runs are represented by (○). Model predictions are represented by (—). Experimental conditions: a) 0.25wt% Pd-TiO₂ photocatalyst and 0.15 g L⁻¹ photocatalyst loading, b) Initial pH = 4.0, c) 1 hour near-UV light plus 5 hours under visible light.

Figures 68-74 display a common linear trend consisting in the increase of the production of hydrogen and in the formation of by-products with irradiation time. For the acetaldehyde, ethylene, and CO₂ however there is a slight deviation from the proposed kinetics, in the initial 0-2 hours. This can be explained by the photoreduction effect on the photocatalyst, during the near-UV 1-hour irradiation period, which causes a higher productivity of all 3 carbon containing by-products.

Furthermore, during the remaining hours under visible light, the production of carbon containing by-products (with the exception of hydrogen peroxide) is steady, showing a linear trend. For hydrogen peroxide however, there is an unsteady formation-consumption of the OH radicals forming H₂O₂.

Thus, one can see that the proposed model describes well the experimental data from the photocatalytic water splitting reactions with a steady increase in hydrogen STP volume over the 5 hours of visible light and this following the first hour of near-UV irradiation.

Table 30 reports the 7 determined intrinsic kinetic constants along with the standard deviations and the 95% confidence intervals.

Table 30. Intrinsic Kinetic Rate Constants for Hydrogen and By-Products under Visible Light at 2% v/v Ethanol.

	Intrinsic kinetic Rate Constant (h⁻¹)	STD (±)	95% Confidence Interval
k ₂ '	1.06E-03	6.90E-05	1.13E-04
k ₃ '	3.28E-04	3.16E-05	5.67E-05
k ₄ '	1.48E-03	1.07E-04	1.70E-04
k ₆ '	5.83E-05	4.23E-06	8.50E-06
k ₇ '	3.07E-04	1.96E-05	3.53E-05
k ₈ '	1.54E-03	9.98E-05	1.58E-04
k ₉ '	1.13E-02	1.00E-03	1.27E-03

Note: k₁ corresponds to the formation of OH radicals with an intrinsic rate constant of 3.11E-04 h⁻¹ and k₅ corresponds to the increase in pH with an intrinsic rate constant of 9.11E-02 h⁻¹.

Cross-correlation analysis provides a way of establishing the numerical interactions between the determined kinetic parameters. Table 31 reports cross-correlation coefficients, which in

most cases, much smaller than 1, indicating the desirable low numerical interactions between determined parameters.

For example, from the cross-correlation matrix reported in Table 31, one can see that the methane intrinsic kinetic rate constant (k_6') is weakly correlated to acetaldehyde, carbon dioxide and hydrogen peroxide parameters (k_2' , k_3' , k_4'), given the 0.236, 0.035, -0.205 obtained coefficient values. One can notice that k_2' - k_4' and k_3' - k_4' pairs are the exception with cross-correlation values of -0.98 and 0.97, respectively.

Table 31. Cross-Correlation Coefficients for Photocatalytic Hydrogen Production via Water Splitting, under Near-UV Light.

	k_2'	k_3'	k_4'	k_6'	k_7'	k_8'	k_9'
k_2'	1						
k_3'	-0.935	1					
k_4'	-0.980	0.970	1				
k_6'	0.236	0.035	-0.205	1			
k_7'	-0.685	0.863	0.720	0.532	1		
k_8'	0.420	-0.344	-0.277	-0.389	-0.532	1	
k_9'	-0.276	0.544	0.326	0.857	0.889	-0.474	1

Table 32 reports the cross-correlation coefficients for the model fitted kinetic parameters for photocatalytic runs under visible light. In this case, it is observed that most of the cross-correlation coefficients show the desirable absolute values lower than the k_7' - k_8' , k_2' - k_6' , k_3' - k_9' pairs, being the exception.

Table 32. Cross-Correlation Coefficients for Photocatalytic Hydrogen Production via Water Splitting under Visible Light.

	k_2'	k_3'	k_4'	k_6'	k_7'	k_8'	k_9'
k_2'	1						
k_3'	0.359	1					
k_4'	-0.093	-0.526	1				
k_6'	0.951	0.564	-0.381	1			
k_7'	0.783	0.702	-0.672	0.937	1		
k_8'	0.776	0.729	-0.669	0.933	0.999	1	
k_9'	-0.100	-0.964	0.572	-0.342	-0.547	-0.576	1

Thus, the proposed kinetic modelling shows an overall good selection of kinetic parameters, based on the smaller than one cross-correlation parameters, in the cross-correlation matrix.

The next step in the process of the kinetic model developed is to establish reconciliation plots, as reported in Figure 75 and Figure 76 for experiments and predictions, under near-UV and visible light irradiation cases. It was observed in this respect, that the proposed kinetics provide a good prediction of the experimental data, under near-UV light for all chemical species. However, for the reactions under visible light, the predicted species volumes at STP, appear to be somewhat more scattered. These deviations are attributed to larger errors when evaluating chemical species with smaller volumes at STP, leading to increased data dispersion.

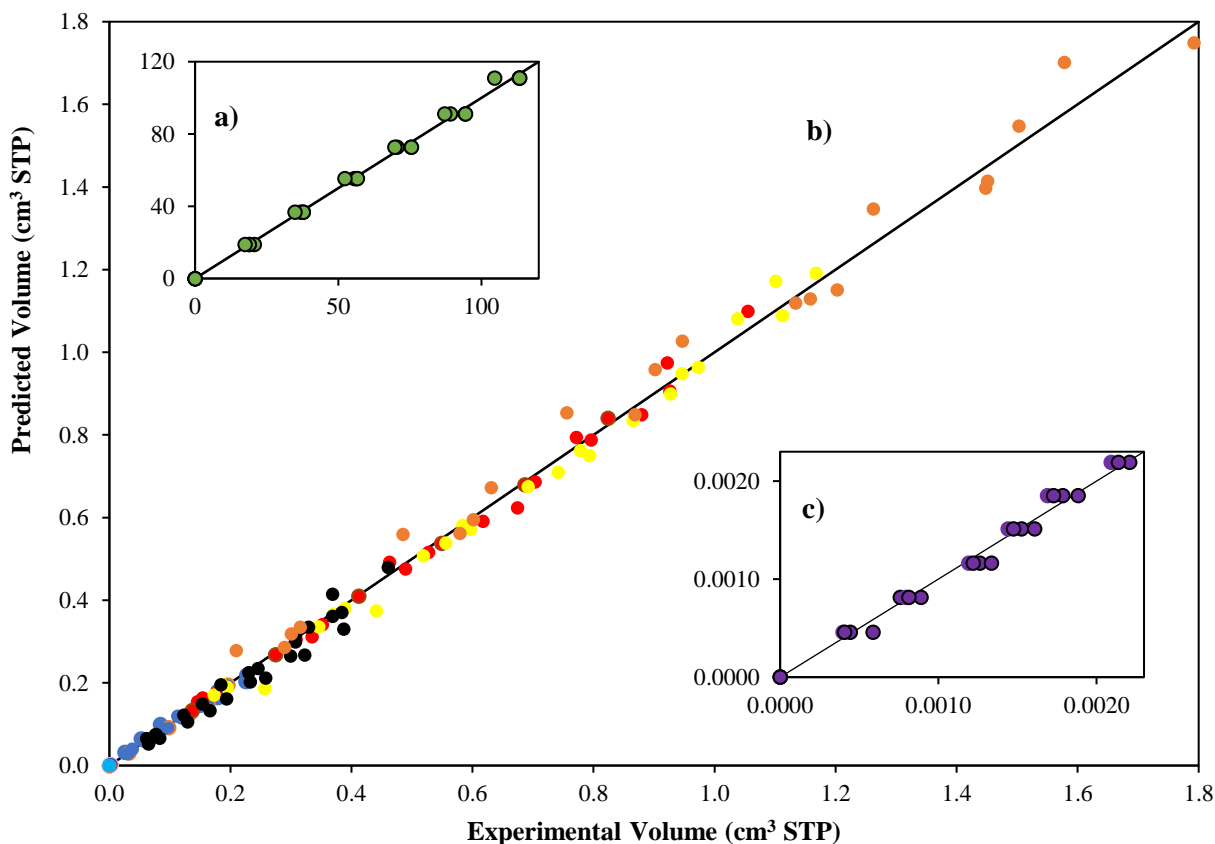


Figure 75. Reconciliation Plot for Predicted and Experimentally Observed Volumes at STP for CO_2 , H_2O_2 , CH_4 , $\text{C}_2\text{H}_4\text{O}$, C_2H_6 , C_2H_4 , and H_2 . Notes: a) Species Volumes: 0 to 113 cm^3 STP, b) Species Volumes: 0 to 1.8 cm^3 , and c) Species Volumes: 0 to 0.0022 cm^3 STP. Conditions: 0.25wt% Pd-TiO₂ photocatalyst, Near-UV Light irradiation and Experimental error: $\pm 5.8\%$ Legends: Blue: Methane, Red: Ethane, Yellow: Acetaldehyde, Black: Carbon Dioxide, Violet: Hydrogen Peroxide, Orange: Ethylene and, Green: Hydrogen

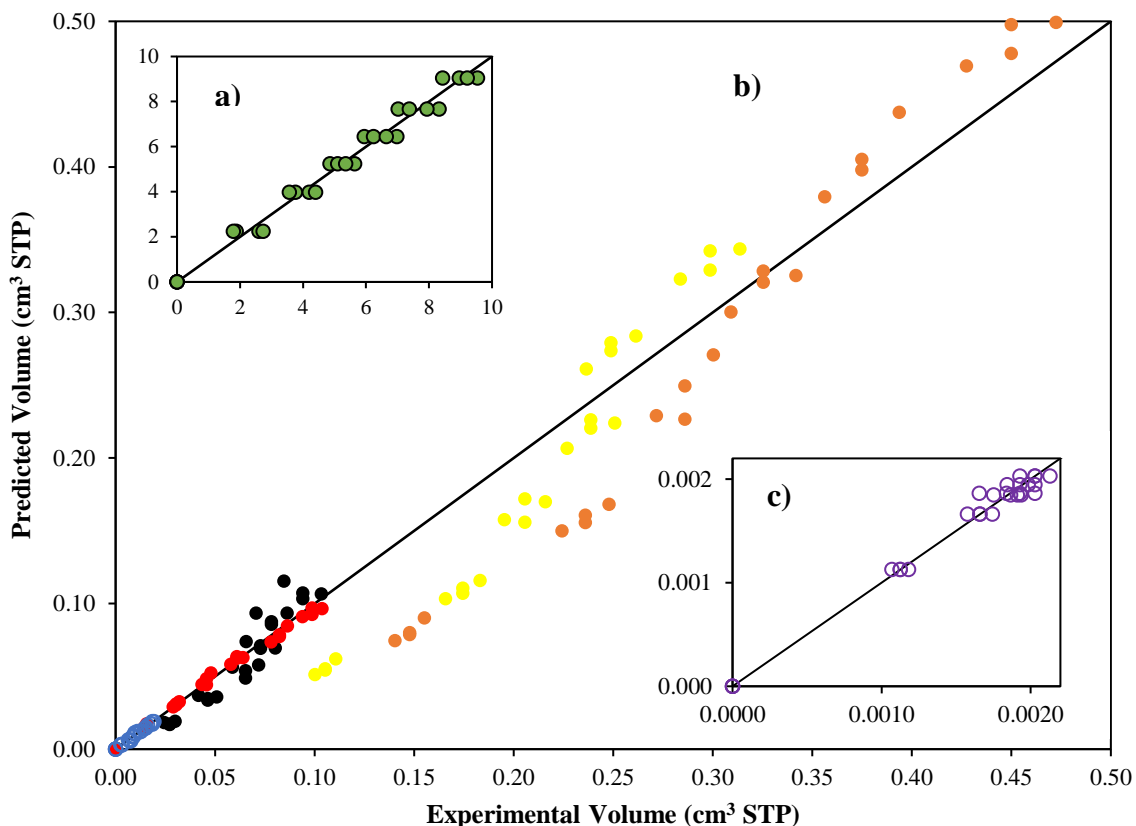


Figure 76. Reconciliation Plot for Predicted and Experimentally Observed Volumes at STP for CO_2 , H_2O_2 , CH_4 , $\text{C}_2\text{H}_4\text{O}$, C_2H_6 , C_2H_4 , and H_2 . Notes: a) Species Volumes: 0 to 10 cm^3 STP, b) Species Volumes: 0 to 0.5 cm^3 , and c) Species Volumes: 0 to 0.0022 cm^3 STP. Conditions: 0.25wt% Pd-TiO₂ photocatalyst, Visible Light irradiation and Experimental error: $\pm 15\%$ Legends: Blue: Methane, Red: Ethane, Yellow: Acetaldehyde, Black: Carbon Dioxide, Violet: Hydrogen Peroxide, Orange: Ethylene and, Green: Hydrogen

On this basis, one can conclude that the proposed kinetic model adequately described the experimental data, when using near-UV and/or visible light irradiation, and for the experimental conditions studied.

Figure 77 and Figure 78 display the residuals for the estimated kinetic model, it was observed that the residual values were symmetrically distributed. Each chemical species demonstrated a trend to cluster towards the x-axis. The positive and negative values were clustered in the y-axis, with a deviation no larger than ± 0.1 , which is almost negligible. Therefore, it is concluded that the proposed kinetic model provided a good prediction of the experimental data.

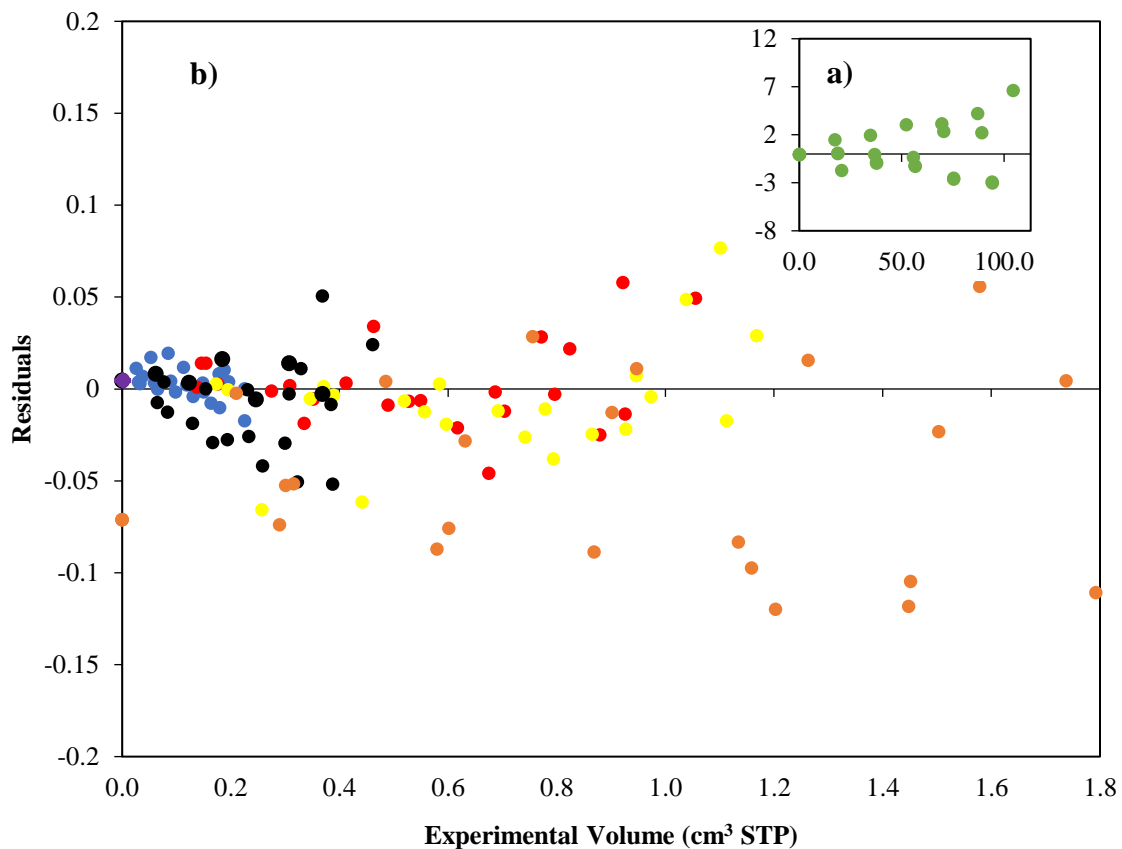


Figure 77. Residuals Plot for the Photocatalytic Hydrogen Generation 0.25wt% Pd-TiO₂ under Near-UV Light. Notes: a) Residual volumes between 0 to 113 cm³ STP, and b) Residual volumes between 0 and 1.8 cm³ at STP. Legends: Blue: Methane, Red: Ethane, Yellow: Acetaldehyde, Black: Carbon Dioxide, Violet: Hydrogen Peroxide, Orange: Ethylene and, Green: Hydrogen

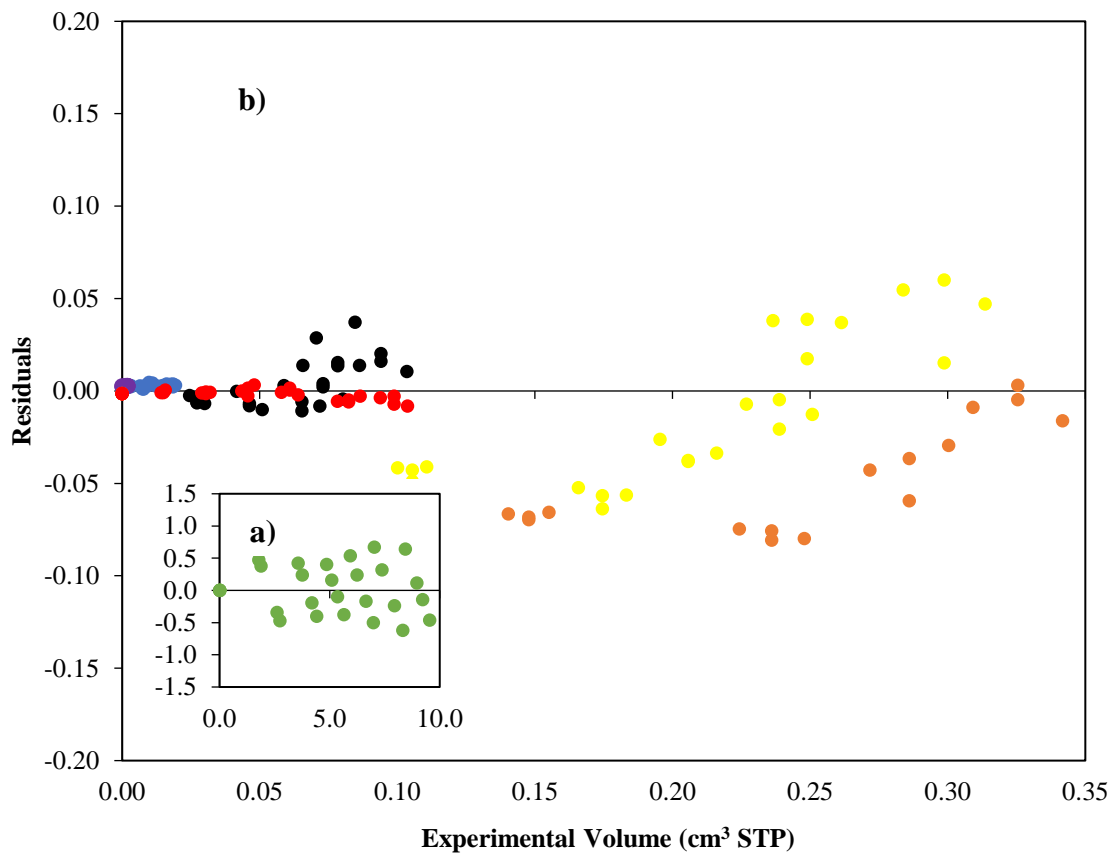


Figure 78. Residuals Plot for the Photocatalytic Hydrogen Generation 0.25wt% Pd-TiO₂ under Near-UV Light. Notes: a) Residual volumes between 0 to 10 cm³ STP, and b) Residual volumes between 0 and 0.35 cm³ at STP. Legends: Blue: Methane, Red: Ethane, Yellow: Acetaldehyde, Black: Carbon Dioxide, Violet: Hydrogen Peroxide, Orange: Ethylene and, Green: Hydrogen

8.5 Conclusions

This chapter reports the kinetic modelling and the statistical analysis, for hydrogen production and the formation of by-products via photocatalytic water splitting, using the 0.25wt% Pd-TiO₂ photocatalyst and 2.0% v/v ethanol concentration. On this basis, the following can be concluded:

- a) The Langmuir-Hinshelwood model accurately describes the in series-parallel reaction network for the production of hydrogen and the formation of by-products.
- b) The proposed kinetics provides a good prediction of the experimental data, for photocatalytic water splitting reactions, under near-UV and visible light, using ethanol as an organic scavenger.
- c) The developed statistical analysis confirms the suitability of the proposed kinetics, with 95% confidence intervals, low cross-correlated parameters, and good data prediction.

Chapter 9

9 Quantum Yield (QY) Evaluation

The quantum yield (QY) is a parameter used to evaluate the photon utilization efficiency in photocatalytic reactors [194]. For hydrogen production reactions, the quantum yield has to be defined in terms of the hydrogen radical production rate over the absorbed photon rate onto the photocatalyst surface. Therefore, QY can be determined as follows:

$$QY_{H\cdot} = \frac{\text{moles of } H\cdot/s}{\text{moles of photons absorbed by the photocatalyst/s}} \quad \text{Equation 57}$$

Equation 57 is equivalent to:

$$\%QY = \frac{\left[\frac{dN_{H\cdot}}{dt}\right]}{Pa} \times 100 \quad \text{Equation 58}$$

Where $\frac{dN_{H\cdot}}{dt}$ stands for the rate of moles of hydrogen radicals formed over the photocatalyst absorbed photon rate.

The QY calculation requires the Pa absorbed photon rate. To establish Pa , a macroscopic balance is needed, with the assessment of P_t transmitted photons, P_i incident photons and P_{bs} backscattered photons. Determination of these parameters are described in Chapter 5.

One should note that some authors report the QY% in terms of incident photons, using a numerical solution of a radiation equation[195]. However, this approach may involve significant error and therefore, Equation 58 is considered a better approach.

9.1 Evaluation of Quantum Yields under Near-UV Light

Table 33 and Figure 79 report QY% for the mesoporous photocatalysts, doped with palladium, at different metal loadings (0.25, 0.50, 1.00, 2.50 and 5.00 wt%), using photocatalyst concentrations of 0.15 g L^{-1} , 2.0 v/v% ethanol, initial pH = 4 ± 0.05 and near-UV light.

Table 33. Quantum Yield (%QY) for the Pd–TiO₂ photocatalyst when using 0.15g/L of TiO₂ under near-UV irradiation. All reported data are average values of three repeats.

Semiconductor	QY (%)
F-127 TiO ₂	5.0
F-127–0.25 wt% Pd–TiO ₂	13.7
F-127–0.50 wt% Pd–TiO ₂	12.8
F-127–1.00 wt% Pd–TiO ₂	10.9
F-127–2.50 wt% Pd–TiO ₂	9.6
F-127–5.00 wt% Pd–TiO ₂	8.5

While the result of Table 33 shows an improved quantum yield, when compared to the 8% QY reported by Escobedo [97] for DP25 doped with Pt, one can also observe that: a) the QY% increases with the Pd loadings in the 0.25 to 1.00 wt% Pd–TiO₂ range, b) The QY% decreases with higher than 1wt% Pd-TiO₂ loadings (2.50 to 5.00 wt% Pd–TiO₂) range.

Figure 79 reports a consistent and steady QY% over 6 hours of near-UV irradiation, for all photocatalyst loadings. It is observed that in the first hour of irradiation, QY% increased linearly until it reached a stable value. During the remaining 5 hours, QY% continued unchanged at the same levels, with this showing a stable performance of the palladium photocatalysts.

Detailed QY% calculation is provided in **Appendix D**.

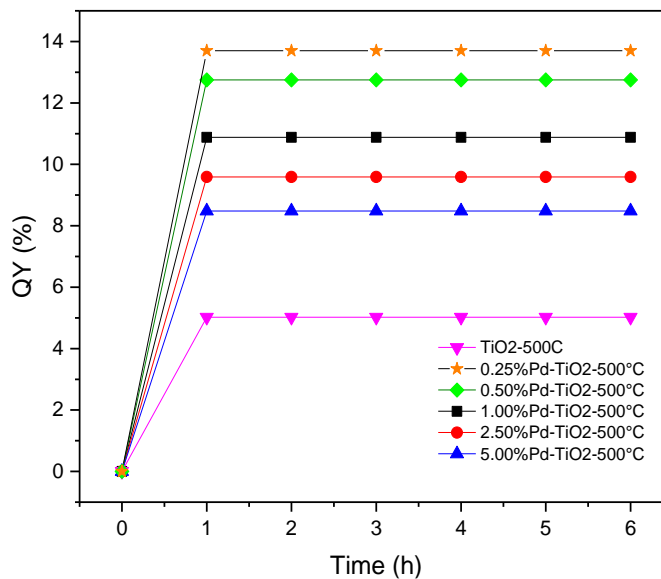


Figure 79. QY% at Various Irradiation Times, under Near-UV Light and 0.15 g L^{-1} of Photocatalyst Concentration, and Using Pd at Different Loadings (0.25, 0.50, 1.00, 2.50 and 5.00 wt%).

9.1.1 Effect of Photocatalyst Concentration on Quantum Yields

Further QY% evaluations were developed, for the 0.25 wt% Pd–TiO₂, by changing the photocatalyst concentration. Figure 80 reports the QY% obtained, by augmenting the photocatalyst concentration up to 1.00 g L^{-1} , under the following conditions: (a) 2.0 v/v% ethanol, (b) initial pH = 4 ± 0.05 , and (c) under near-UV light irradiation. It was observed that there was a noticeable increase of the QY% in the first hour of irradiation, followed by a stable QY% in the next 5 h of irradiation, with no photocatalyst activity decay.

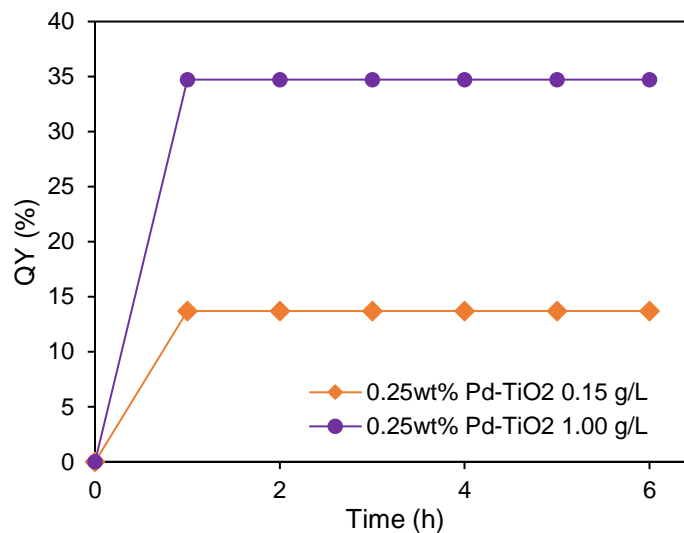


Figure 80. QY% at various Irradiation Times under near-UV Irradiation Using 0.15, and 1.00g L⁻¹ Photocatalyst Concentrations. Note: Loading was 0.25 wt% Pd on TiO₂.

Thus, using the 1.00 g L⁻¹ photocatalyst concentration, a 0.25 wt% Pd loading on TiO₂, and near-UV light, led to a steady and favourable quantum yield of 34.7%.

9.2 Evaluation of Quantum Yields under Visible Light

Table 34 and Figure 81 report the QY% for the mesoporous photocatalysts, doped with palladium at different metal loadings (0.25, 0.50, 1.00, 2.50, and 5.00 wt%) under the following conditions: (a) Photocatalyst slurry concentrations of 0.15 g L⁻¹, (b) 2.0 v/v% ethanol, (c) pH = 4 ± 0.05 and (d) Visible light. Regarding these QY%_s, the photocatalyst was evaluated under two scenarios: a) photocatalyst irradiated with visible light only for the entire 6 hours, and b) photocatalyst photoreduced for 1 hour first under near-UV light, and irradiated with visible light for the remaining 5 hours.

Table 34. QYs% for Pd-TiO₂ Photocatalysts at Different Metal Loadings (0.25, 0.50, 1.00, 2.50, and 5.00 wt%) under: (a) Visible light irradiation only, (b) Using near-UV light for 1hour, followed by visible light irradiation for 5 hours.

Photocatalyst	QY (%) (a)	QY (%) (b)
TiO ₂	0.23	-
0.25 wt% Pd TiO ₂	1.13	1.58
0.50 wt% Pd TiO ₂	0.34	1.07
1.00 wt% Pd TiO ₂	0.30	0.80
2.50 wt% Pd TiO ₂	0.10	0.79
5.00 wt% Pd TiO ₂	0.10	0.78

One can observe in Table 34 that the QYs% obtained with visible light irradiation only, were in the low 0.10–1.13% range, with this reflecting a modest improvement versus the 0.23% obtained for the undoped TiO₂. These low QYs% can be attributed to the limited ability of the Pd-TiO₂ photocatalysts to produce hydrogen under visible light, with only 49.8 wt% of the loaded palladium as Pd⁰.

It was also observed on the other hand, that the near-UV photoreduced photocatalysts reached higher QYs% values under visible light, as high as 1.6% for the 0.25wt%Pd-TiO₂. Thus, it was concluded that the prior photocatalyst photoreduction is of critical importance to make the photocatalyst active under visible light, for hydrogen production, while having 81.7 wt% of the loaded palladium present as Pd⁰.

Note that Ravishankar[196] reported a maximum quantum yield, within the 0.36 to 0.43% range, for 0.1 to 0.4 wt% Pd-TiO₂ photocatalysts, under visible light. In the present study, the reported QY% are 3-4 times larger, than the QY% obtained by Ravishankar[3]. This is accomplished using rigorous experimentally evaluated absorbed photons rate, which was determined via MIEB (macroscopic irradiation energy balances).

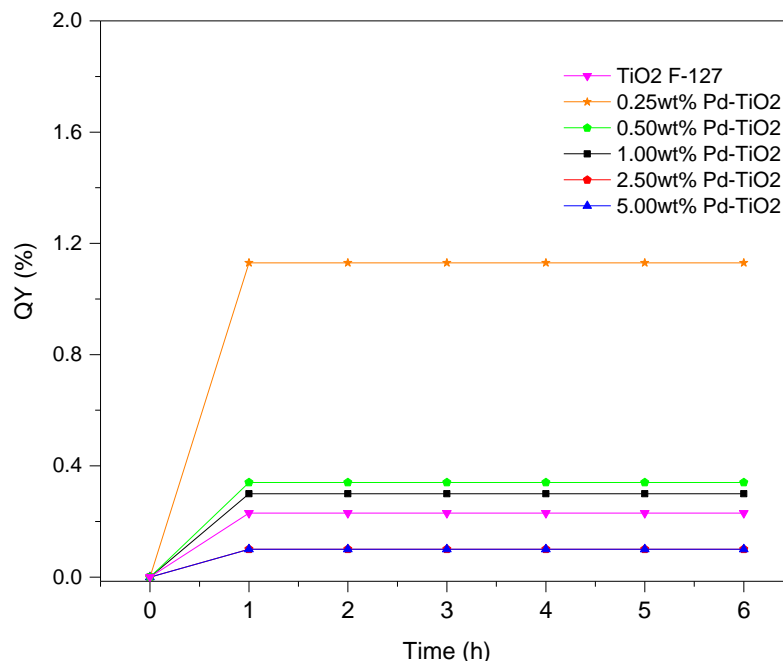


Figure 81. QY% at Various Irradiation Times, under Visible Light, using a 0.15 g L^{-1} Photocatalyst Concentration. Note: Pd-TiO₂ photocatalyst with different palladium loadings: 0.25, 0.50, 1.00, 2.50, and 5.00 wt% are used.

Furthermore, Figure 82 reports the consistent QY% trends, observed for Pd-doped TiO₂ photocatalysts, under the following conditions: (a) During the first hour near-UV irradiation, the QY% increases progressively until it reaches a stable value; and (b) During the additional five hours of visible irradiation, the QY% remains essentially unchanged, with the photocatalysts displaying a stable performance. It can also be observed in this respect, that there is a significant increase of QY% when using 0.25 and 0.50 wt% Pd-TiO₂, whereas higher Pd loadings led to a decrease in the QY%.

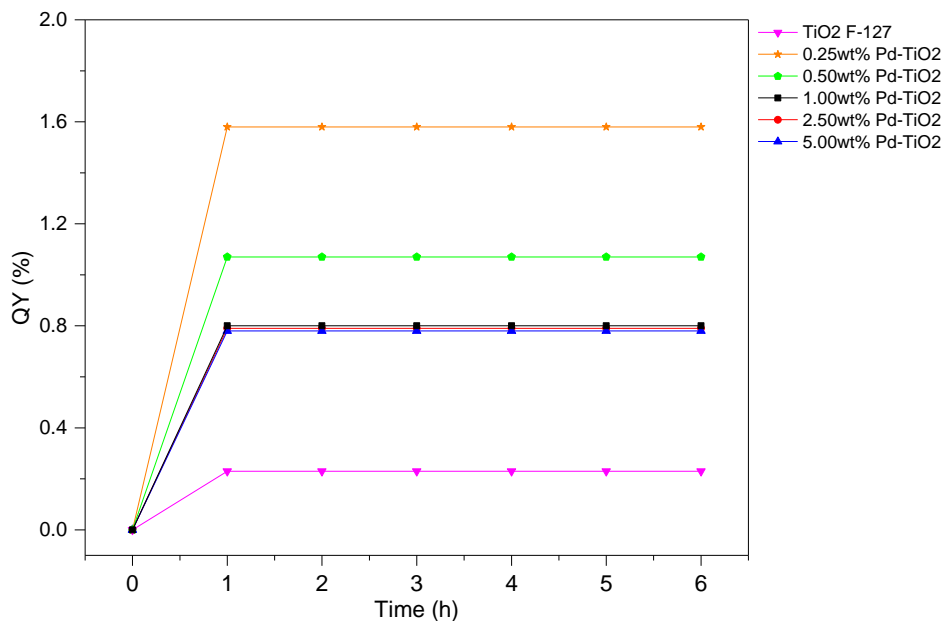


Figure 82. QY% at Various Irradiation Times, under Visible Light, and Using a 0.15g L^{-1} TiO_2 Photocatalyst Concentration. Photocatalysts were photoreduced using Near-UV light during the first 1 hour.

It is also interesting to notice in Figure 82, that the photoreduced semiconductors of the present study displayed good and stable QYs%, showing their significant ability to produce hydrogen, without photocatalyst deactivation. This photocatalyst QY% stability was also established with 4 consecutive hydrogen production photocatalytic run repeats, each lasting 6 h or the equivalent of 24 h under visible light irradiation.

9.2.1 Effect of Photoreduction Time on Quantum Yields

Given that the highest QY% observed for the 0.25 wt% Pd– TiO_2 photocatalyst, during 1 hour under Near-UV was 1.6%, further QY% evaluations were developed by changing the near-UV irradiation time of the photocatalyst. Figure 83 reports the QY% obtained, when increasing the near-UV photoreduction exposure time up to 24 hours, followed by 6 hours of visible light

irradiation. The reaction conditions remained unchanged as in previous experimental runs: (a) 2.0 v/v% ethanol, (b) initial pH = 4 ± 0.05 and (c) 0.15 g L^{-1} of TiO_2 .

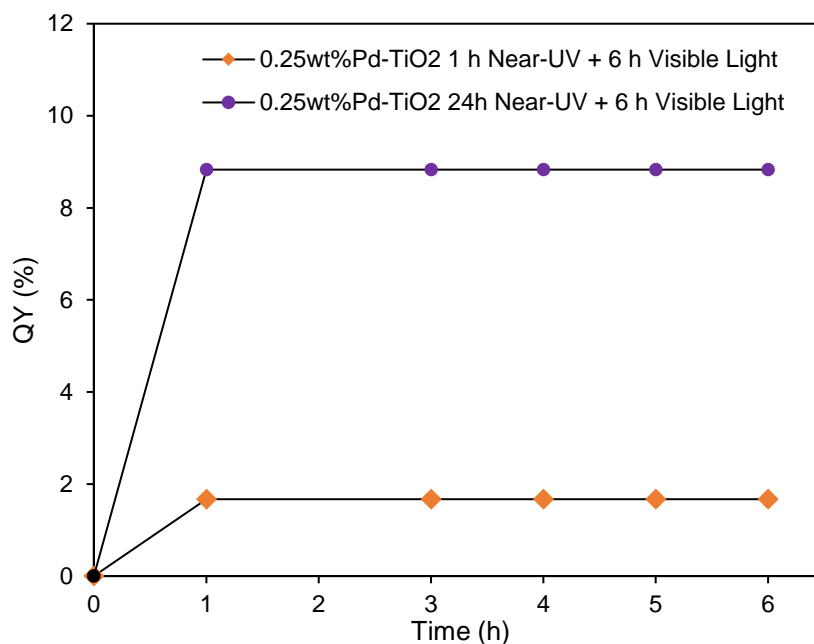


Figure 83. QY% at Various Irradiation Times under 1 hour near-UV photoreduction, followed by 6 hours of visible light irradiation, and 24 hours near-UV photoreduction, followed by 6 hours of visible light irradiation. Note that the reactions were performed using a 0.15 g L^{-1} photocatalyst concentration and 0.25 wt% Pd on TiO_2 .

It was observed that there was a noticeable increase in the QY%, with 24 hours of near-UV photoreduction rather than 1 hour of near-UV photoreduction, under visible light irradiation, with this being as high as 8.8%. This quantum yield was five times the one reported with 1 hour of near-UV photoreduction. The rise in the QY% was attributed to a close to 100 wt% of the loaded palladium being present as Pd^0 , as demonstrated by the XPS analysis in Chapter 4. Note that the QY% achieved remained steady with no apparent photocatalyst activity decay.

9.3 Theoretical Quantum Yields

The "*Theoretical Quantum Yields*" are based on the photon stoichiometric requirements for H[•] radical production over the number of photons absorbed in the palladium on TiO₂ photocatalysts.

$$\%QY = \frac{[\frac{dN_{H^{\bullet}}}{dt}]}{P_a} \times 100 = 2 \times \frac{[\frac{dNH_2}{dt}]}{P_a} \times 100 \quad \text{Equation 59}$$

Therefore, by using Equation 59, one can determine the values of the "*Theoretical Quantum Yield*" under near UV light and visible light irradiation as reported in Table 35:

Table 35. Theoretical Quantum Yields using 0.25% wt Pd – TiO₂ photocatalyst

Conditions	QY (%) = $\frac{[\frac{dN_{H^{\bullet}}}{dt}]}{P_a} \times 100$	QY (%) = $2 \times \frac{[\frac{dNH_2}{dt}]}{P_a} \times 100$
Near UV light Photocatalyst concentration: 1.00 g L ⁻¹ Ethanol concentration: 2% v/v Initial pH: 4 ± 0.05	34.7	69.4
Visible Light after 24 hours under Near UV irradiation. Photocatalyst concentration: 0.15 g L ⁻¹ Ethanol concentration: 2% v/v Initial pH: 4 ± 0.05	8.80	17.6

Considering that H⁺ protons form H[•] radicals, the "*Theoretical Quantum Yield*" equals 1 or 100%. However, due to the presence of the ethanol scavenger and the subsequent oxidation – reduction reactions, an estimated average theoretical QY is 0.8 or 80%.

9.4 Conclusions

From the various QYs% reported in this chapter, the following can be concluded:

- a) The QYs% is a valuable parameter that determines the energy usage efficiency, when using photocatalytic reactors for hydrogen production.
- b) The QYs% can be determined based on the hydrogen production rate, and the absorbed photon rate, with the absorbed photon rates being calculated using macroscopic irradiation energy balances.
- c) The QYs% using near-UV irradiation can be enhanced with 0.25wt% Pd-TiO₂, 1.0 g L⁻¹ photocatalyst and 2.0%/v ethanol scavenger, yielding a favourable 69.4% maximum QY% value.
- d) The QYs% of Pd-TiO₂ photocatalyst under visible light was in the 0.10-1.13 range and was enhanced with 1 hour or 24 hours of photoreduction, under near-UV light. This 1 hour or 24-hour of photoreduction demonstrated the importance of having palladium present as Pd⁰ on the photocatalyst, for hydrogen production.
- e) The QYs% can be improved using 24 hours extended photoreduction period under near-UV irradiation. Using the 0.25wt%Pd-TiO₂ photocatalyst, at 0.15 gL⁻¹ photocatalyst concentrations and 2.0%v/v ethanol, it yielded a 17.6 QYs% under visible light.

Chapter 10

10 Conclusions and Recommendations

Photocatalysis is a promising technology that involves the use of light to split water, by taking advantage of semiconductor material properties. These semiconductors under photon irradiation can generate electron hole pairs and produces hydrogen. This technology requires suitable photocatalysts, to achieve better radiation and sunlight utilization efficiencies. A sacrificial agent or scavenger is also required, to reduce the electron-hole h^+/e^- recombination by being an electron donor.

Hydrogen as an energy carrier has important advantages, such as high-energy density (143 MJ/kg) and zero-CO₂ combustion emissions. It can be produced and stored on site and used to produce thermal energy and electricity.

This PhD thesis addresses some of the challenges in photocatalytic water splitting such as: a) enhancing the efficiency of hydrogen production by modifying the TiO₂ photocatalyst, b) reducing electron-hole pair recombination, b) decreasing semiconductor band gaps to absorb visible light, and c) achieving photocatalyst chemical stability under redox conditions.

In order to accomplish this, a mesoporous titanium dioxide photocatalyst was modified and synthesized using palladium, as a noble metal dopant. The prepared photocatalyst was evaluated in the Photo-CREC Water-II Reactor, and characterized using physical and chemical techniques, under both near-UV and visible light, while using ethanol as a renewable scavenger.

10.1 Conclusions

The main findings and conclusions of this PhD thesis can be summarized as follows:

- A TiO₂ mesoporous photocatalyst material was synthesized using a Pluronic F-127 soft template, following the sol-gel method. The semiconductor was successfully doped using a palladium-noble metal. A photoreduction approach was also considered to fully

reduce the Pd on the TiO₂, with metallic formed sites fully contributing, as effective electron traps.

- The developed Pd-TiO₂ photocatalyst was characterized using several analytical techniques such as: XRD, BET, H₂-chemisorption, XPS, TPR, and UV-Vis spectra. These techniques allowed determining the photocatalyst specific surface area (131m² g⁻¹), Pd metal dispersion (75%), crystallite sizes (9 to 14 nm range), the high degree of Pd reduction (100% Pd⁰), and the band gap (2.51 eV), of the synthesized 0,25%Pd-TiO₂ photocatalysts.
- The performance of the Pd-TiO₂ photocatalyst in terms of photon absorption, was adequately assessed using Macroscopic Irradiation Energy Balances (MIEB). For the synthesized Pd-TiO₂ photocatalysts, photon absorption efficiencies were established in the 45 to 60% range, under both near-UV and visible light irradiation.
- The 0.25wt% Pd-TiO₂ photocatalyst was proved to be the best photocatalyst in various experiments under inert argon atmosphere, in the Photo-CREC Water-II Reactor unit, for hydrogen production, using ethanol as a scavenger.
- The developed 0.25wt% Pd-TiO₂ photocatalyst used for water splitting, led to hydrogen formation via a “*in series-parallel*” reaction network, with the formation of methane, ethane, ethylene, hydrogen peroxide, carbon monoxide, carbon dioxide and acetaldehyde, in small quantities.
- The 0.25wt% Pd-TiO₂ photocatalyst used for water splitting led to a “*in series-parallel*” redox reaction network. This network was successfully evaluated via carbon element balances, as well as OH• and H• radical balances, and was established for both 6 h of near-UV or 1 hour of near-UV followed by 5 hours of visible light irradiation.
- The photocatalytic water splitting rates for the 0.25wt% Pd-TiO₂ at a 0.15g L⁻¹ photocatalyst concentration were accurately described via a Langmuir-Hinshelwood rate model including chemical species adsorption and intrinsic reaction steps. The resulting kinetics provided a good representation of the experimental data and predicted

well the volumes of photocatalytic water splitting products, at STP conditions, under near-UV and visible light.

- The Pd-TiO₂ photon utilization efficiency was satisfactorily established, using quantum yields. The synthesized 0.25wt%Pd-TiO₂ photocatalyst, 2.0% v/v ethanol, under near-UV showed a best QY% of 69.4%. It was also observed that extending the photo reduction period to 24 hours followed by 5 hours of visible light, the photocatalyst achieved a high QY% of 17.6%.

10.2 Recommendations

The following future work is recommended based on the results of this research:

- To study the effect of higher irradiation densities, by using LED lamps, with lower power consumption and as a result, higher power utilization efficiency.
- To develop irradiation models in the Photo-CREC Water-II Reactor accounting for: a) irradiation absorption, b) forward and backward scattering, for different Pd loadings, on the TiO₂ photocatalyst. These models could include the proposed reaction kinetics and could be valuable to establish best photocatalyst loadings.
- To evaluate the Pd-TiO₂ photocatalyst, under different photoreduction conditions. For example, reducing the metal loading below 0.25 wt% Pd and determining its band gap after reaction. This would allow determining the best photocatalyst photoreduction conditions, prior to visible light irradiation, in order to obtain an optimal performance for hydrogen production.
- To determine the Photochemical Thermodynamic Efficiency Factor (PTEF), during photocatalytic hydrogen production, in the PCW-II reactor, in order to evaluate the photon energy efficiency.
- To evaluate the possibility of scaling up the process including the Photo CREC Water II reactor, from the laboratory up to industrial scale, analyzing costs and identifying critical variables that might affect the efficiency of the photocatalytic water splitting reaction for hydrogen production.

Bibliography

- [1] T. Chang, H.-P. Chu, and W.-Y. Chen, “Energy consumption and economic growth in 12 Asian countries: panel data analysis,” *Appl. Econ. Lett.*, vol. 20, no. 3, pp. 282–287, 2013.
- [2] “Renewable energy facts,” *Government of Canada*, 2018. [Online]. Available: <https://www.nrcan.gc.ca/energy/facts/renewable-energy/20069>. [Accessed: 31-Mar-2021].
- [3] J. Maloney, “Strategic Electricity Interties Report of the Standing Committee on Natural Resources,” no. December, 2017.
- [4] Natural Resources Canada (NRCan), *Seizing the Opportunities for Hydrogen*. Natural Resources Canada, 2020.
- [5] S. H. Jensen, P. H. Larsen, and M. Mogensen, “Hydrogen and synthetic fuel production from renewable energy sources,” *Int. J. Hydrogen Energy*, vol. 32, no. 15 SPEC. ISS., pp. 3253–3257, 2007.
- [6] K. Mazloomi and C. Gomes, “Hydrogen as an energy carrier: Prospects and challenges,” *Renew. Sustain. Energy Rev.*, vol. 16, no. 5, pp. 3024–3033, 2012.
- [7] D. Ipsakis, S. Voutetakis, P. Seferlis, F. Stergiopoulos, and C. Elmasides, “Power management strategies for a stand-alone power system using renewable energy sources and hydrogen storage,” *Int. J. Hydrogen Energy*, vol. 34, no. 16, pp. 7081–7095, 2009.
- [8] J. Bockris, *Comments on: Hydrogen futures: toward a sustainable energy system*, vol. 28. 2003.
- [9] M. Momirlan and T. N. Veziroglu, “The properties of hydrogen as fuel tomorrow in sustainable energy system for a cleaner planet,” *Int. J. Hydrogen Energy*, vol. 30, no. 7, pp. 795–802, 2005.
- [10] M. M. Rashid, M. K. Al Mesfer, H. Naseem, and M. Danish, “Hydrogen Production by Water Electrolysis: A Review of Alkaline Water Electrolysis, PEM Water Electrolysis and High Temperature Water Electrolysis,” *Int. J. Eng. Adv. Technol.*, no. 3, pp. 2249–8958, 2015.
- [11] A. J. Haider, “Exploring potential Environmental applications of TiO₂ Nanoparticles,” *Energy Procedia*, vol. 119, pp. 332–345, 2017.

- [12] S. Y. Lee and S. J. Park, "TiO₂ photocatalyst for water treatment applications," *J. Ind. Eng. Chem.*, vol. 19, no. 6, pp. 1761–1769, 2013.
- [13] C. Change, "G w a p h c d i a," vol. 11, no. 2, pp. 44–58, 2007.
- [14] X. Chen, S. Shen, L. Guo, and S. S. Mao, "Semiconductor-based photocatalytic hydrogen generation.," *Chem. Rev.*, vol. 110, no. 11, pp. 6503–70, 2010.
- [15] C. Acar, "Review of photocatalytic water-splitting methods for sustainable hydrogen production," *Energy Res.*, vol. 40, pp. 1449–1473, 2016.
- [16] S. K. Cushing, L. Jiantian, F. Manke, T. Senty, S. Suri, M. Zhi, M. Li, A. Bristow and N. Wu., "Photocatalytic activity enhanced by plasmonic resonant energy transfer from metal to semiconductor," *J. Am. Chem. Soc.*, vol. 134, no. 36, pp. 15033–15041, 2012.
- [17] M. Balat, "Potential importance of hydrogen as a future solution to environmental and transportation problems," *Int. J. Hydrogen Energy*, vol. 33, no. 15, pp. 4013–4029, Aug. 2008.
- [18] S. Ramesohl and F. Merten, "Energy system aspects of hydrogen as an alternative fuel in transport," *Energy Policy*, vol. 34, no. 11, pp. 1251–1259, 2006.
- [19] L. Barreto, A. Makihira, and K. Riahi, "The hydrogen economy in the 21st century: A sustainable development scenario," *Int. J. Hydrogen Energy*, vol. 28, no. 3, pp. 267–284, 2003.
- [20] K. Maeda, K. Teramura, D. Lu, T. Takata, N. Saito, Y. Inoue, D. Kazunari., "Photocatalyst releasing hydrogen from water," *Nature*, vol. 440, no. 7082, p. 295, 2006.
- [21] I. Dincer, "Green methods for hydrogen production," *Int. J. Hydrogen Energy*, vol. 37, no. 2, pp. 1954–1971, 2012.
- [22] I. Dincer, "Sustainable hydrogen production options and the role of IAHE," *Int. J. Hydrogen Energy*, vol. 37, no. 21, pp. 16266–16286, 2012.
- [23] M. Ni, M. K. H. Leung, K. Sumathy, and D. Y. C. Leung, "Potential of renewable hydrogen production for energy supply in Hong Kong," *Int. J. Hydrogen Energy*, vol. 31, no. 10, pp. 1401–1412, 2006.
- [24] F. Khalid, "Model development and analysis of a novel high-temperature electrolyser for gas phase electrolysis of hydrogen chloride for hydrogen production," *Int. J. Hydrogen Energy*, vol. 43, no. 19, pp. 9112–9118, 2018.
- [25] H. Ozcan, "Performance investigation of magnesium–chloride hybrid thermochemical

- cycle for hydrogen production,” *Int. J. Hydrogen Energy*, vol. 39, no. 1, pp. 76–85, 2018.
- [26] V. Kyriakou, “A protonic ceramic membrane reactor for the production of hydrogen from coal steam gasification,” *J. Memb. Sci.*, vol. 553, no. 1, pp. 163–170, 2018.
- [27] N. Muradov, “Low to near-zero CO₂ production of hydrogen from fossil fuels: Status and perspectives,” *Int. J. Hydrogen Energy*, vol. 42, no. 20, pp. 14058–14088, 2018.
- [28] D. Sengmee, “Biophotolysis-based hydrogen and lipid production by oleaginous microalgae using crude glycerol as exogenous carbon source,” *Int. J. Hydrogen Energy*, vol. 42, no. 4, pp. 1970–1976, 2017.
- [29] R. García-Sánchez, “Photofermentation of tequila vinasses by *Rhodospseudomonas pseudopalustris* to produce hydrogen,” *Int. J. Hydrogen Energy*, 2018.
- [30] S. Fukuzumi, “Artificial photosynthesis for production of hydrogen peroxide and its fuel cells,” *Biochim. Biophys. Acta - Bioenerg.*, vol. 1857, no. 5, pp. 604–611, 2016.
- [31] I. Dincer, “Photonic Energy Production,” in *Comprehensive Energy Systems*, 2018, pp. 707–754.
- [32] O. M. Yardimci, “Employing plasma as catalyst in hydrogen production,” *Int. J. Hydrogen Energy*, vol. 23, no. 12, pp. 1109–1111, 1998.
- [33] A. . Adesina, “Thermolysis of hydrogen sulphide in an open tubular reacto,” *Int. J. Hydrogen Energy*, vol. 20, no. 10, pp. 777–783, 1995.
- [34] E. Kao, “Electropolymerized polythiophene photoelectrodes for photocatalytic water splitting and hydrogen production,” *Sensors Actuators A Phys.*, vol. 277, no. 1, pp. 18–25, 2018.
- [35] J. Wang, “Fermentative hydrogen production using various biomass-based materials as feedstock,” *Renew. Sustain. Energy Rev.*, vol. 92, pp. 284–306, 2018.
- [36] P. Parthasarathy, “Hydrogen production from steam gasification of biomass: Influence of process parameters on hydrogen yield – A review,” *Renew. Energy*, vol. 66, pp. 570–579, 2014.
- [37] J. Kennedy, “Hydrogen generation by photocatalytic reforming of potential biofuels: Polyols, cyclic alcohols, and saccharides,” *J. Photochem. Photobiol. A Chem.*, vol. 356, no. 1, pp. 451–456, 2018.
- [38] H. Tebibel, “Comparative performance analysis of a grid connected PV system for

- hydrogen production using PEM water, methanol and hybrid sulfur electrolysis,” *Int. J. Hydrogen Energy*, vol. 43, no. 6, pp. 3482–3498, 2018.
- [39] P. Nikolaidis and A. Poullikkas, “A comparative overview of hydrogen production processes,” *Renew. Sustain. Energy Rev.*, vol. 67, pp. 597–611, 2017.
- [40] A. V Puga, “Photocatalytic production of hydrogen from biomass-derived feedstocks,” *Coord. Chem. Rev.*, vol. 315, pp. 1–65, 2016.
- [41] C. a Linkous, D. Slattery, T. Teets, S. D. Nocera, C, Liao, C. Huang, J. Wu. “Solar Photocatalytic Hydrogen Production From Water Using a Dual Bed Photosystem,” *Chem. Commun.*, vol. 47, no. 33, p. CP-570-28890, 2011.
- [42] C. Byrne, “Recent advances in photocatalysis for environmental applications,” *J. Environ. Chem. Eng.*, vol. 6, no. 3, pp. 3531–355, 2018.
- [43] H. Wang, “Recent progress in ultrathin two-dimensional semiconductors for photocatalysis,” *Mater. Sci. Eng. R Reports*, vol. 130, pp. 1–39, 2018.
- [44] J. Moulijn, *Catalysis. An integrated approach to homogeneous, heterogenous and industrial catalysis*. Amsterdam, The Netherlands: Elsevier, 1993.
- [45] Y. L. Can Li, *Bridging Heterogeneous and Homogeneous Catalysis: Concepts, Strategies, and applications*. Book. Wiley-VCH. 2014.
- [46] N. Ahmed, “Heterogeneous photocatalysis and its potential applications in water and wastewater treatment: a review,” *Nanotechnology*, vol. 29, no. 34, 2018.
- [47] R. de Fátima, “Mass transfer and photocatalytic degradation of leather dye using TiO₂/UV,” *J. Appl. Electrochem.*, vol. 35, no. 7–8, pp. 821–829, 2005.
- [48] K. Takanebe, “Photocatalytic Water Splitting: Quantitative Approaches toward Photocatalyst by Design,” *ACS Catal.*, vol. 7, no. 11, pp. 8006–8022, 2017.
- [49] T. Li Hsiung, “Chemical structure of photocatalytic active sites in nanosize TiO₂,” *J. Phys. Chem. Solids*, vol. 69, no. 2–3, pp. 383–385, 2018.
- [50] W.-N. Zhao, “Mechanism and active site of photocatalytic water splitting on titania in aqueous surroundings,” *Chem. Sci.*, no. 6, 2014.
- [51] S. Zhu, “Photocatalysis: Basic Principles, Diverse Forms of Implementations and Emerging Scientific Opportunities,” *Advanve Energy Mater.*, vol. 7, no. 23, 2017.
- [52] S. Somiya, *Handbook of Advanced Ceramics*, 2nd ed. Academic Press Inc, 2013.
- [53] A. Currao, “Photoelectrochemical Water Splitting,” *Chim. Int. J. Chem.*, vol. 61, no. 12,

- pp. 815–819, 2007.
- [54] M. G. Walter, E. Warren, J. McKone, S. Boettcher, Q. Mi, E. Santori, N. Lewis. “Solar water splitting cells” *Chem. Rev.*, vol. 110, no. 11, pp. 6446–6473, 2010.
- [55] H. Ahmad, S. K. Kamarudin, L. J. Minggu, and M. Kassim, “Hydrogen from photocatalytic water splitting process: A review,” *Renew. Sustain. Energy Rev.*, vol. 43, pp. 599–610, 2015.
- [56] A. Galińska, “Photocatalytic Water Splitting over Pt–TiO₂ in the Presence of Sacrificial Reagents,” *Energy & Fuels*, vol. 19, no. 3, pp. 1143–1147, 2005.
- [57] R. Abe, “Significant effect of iodide addition on water splitting into H₂ and O₂ over Pt-loaded TiO₂ photocatalyst: suppression of backward reaction,” *Chem. Phys. Lett.*, vol. 371, no. 3–4, pp. 360–364, 2003.
- [58] A. Mills, “An overview of semiconductor photocatalysis,” *J. Photochem. Photobiol. A Chem.*, vol. 108, no. 1, pp. 1–35, 1997.
- [59] A. Mills, “Photosensitised dissociation of water using dispersed suspensions of n-type semiconductors,” *J. Chem. Soc. Faraday Trans. 1 Phys. Chem. Condens. Phases*, vol. 12, no. 78, pp. 3659–3669, 1982.
- [60] S. Cho, J. W. Jang, K. H. Lee, and J. S. Lee, “Research update: Strategies for efficient photoelectrochemical water splitting using metal oxide photoanodes,” *APL Mater.*, vol. 2, no. 1, 2014.
- [61] R. H. Gonzalves, B. H. R. Lima, and E. R. Leite, “Magnetite colloidal nanocrystals: A facile pathway to prepare mesoporous hematite thin films for photoelectrochemical water splitting,” *J. Am. Chem. Soc.*, vol. 133, no. 15, pp. 6012–6019, 2011.
- [62] G. Wang, Y. Ling, and Y. Li, “Oxygen-deficient metal oxide nanostructures for photoelectrochemical water oxidation and other applications,” *Nanoscale*, vol. 4, no. 21, pp. 6682–6691, 2012.
- [63] M. M. Khan, S. F. Adil, and A. Al-Mayouf, “Metal oxides as photocatalysts,” *J. Saudi Chem. Soc.*, vol. 19, no. 5, pp. 462–464, 2015.
- [64] P. Holloway and G. McGuire, *Handbook of Compound Semiconductor*. New Jersey, USA: Noyes Publications, 1995.
- [65] L. Forni, “Mass and heat transfer in catalytic reactions,” *Catal. Today*, vol. 52, no. 2–3, pp. 147–152, 1999.

- [66] J. Brinker and G. W. Schere, *Sol-Gel Science: The Physics and Chemistry of Sol-Gel Processing*. San Diego, California: Academic Press Inc, 1990.
- [67] D. A. Ward, “Preparing Catalytic Materials by the Sol-Gel Method,” *I&EC Res.*, vol. 34, no. 2, pp. 421–433, 1995.
- [68] M. . Cauqui, “Application of the sol-gel methods to catalyst preparation,” *J. Non. Cryst. Solids*, vol. 147, pp. 724–738, 1992.
- [69] A. L. Castro, “Synthesis of anatase TiO₂ nanoparticles with high temperature stability and photocatalytic activity,” *Solid State Sci.*, vol. 10, no. 5, pp. 602–606, 2008.
- [70] W. L. Chin, F. Wah Low, S. Weng Chong, and S. Bee Abd Hamid, “An Overview: Recent Development of Titanium Dioxide Loaded Graphene Nanocomposite Film for Solar Application,” *Curr. Org. Chem.*, vol. 19, 2015.
- [71] R. Verma, J. Gangwar, and A. K. Srivastava, “Multiphase TiO₂ nanostructures: A review of efficient synthesis, growth mechanism, probing capabilities, and applications in bio-safety and health,” *RSC Adv.*, vol. 7, no. 70, pp. 44199–44224, 2017.
- [72] I. Ali, M. Suhail, Z. A. Allothman, and A. Alwarthan, “Recent advances in syntheses, properties and applications of TiO₂ nanostructures,” *RSC Adv.*, vol. 8, no. 53, pp. 30125–30147, 2018.
- [73] Y. Zhang, J. Liu, G. Wu, and W. Chen, “Porous graphitic carbon nitride synthesized via direct polymerization of urea for efficient sunlight-driven photocatalytic hydrogen production,” *Nanoscale*, vol. 4, no. 17, pp. 5300–5303, 2012.
- [74] G. Hasegawa, *Studies on Porous Monolithic Materials Prepared via Sol–Gel Processes*. Japan: Springer Science, 2013.
- [75] B. Guo, H. Shen, K. Shu, Y. Zeng, and W. Ning, “The study of the relationship between pore structure and photocatalysis of mesoporous TiO₂,” *J. Chem. Sci.*, vol. 121, no. 3, pp. 317–321, 2009.
- [76] X. He, *Recent Progress in Fabrication of Nanostructured Carbon Monolithic Materials*. Book. Mdpi AG. 2017.
- [77] C.-H. Liao, C.-W. Huang, and J. C. S. Wu, “Hydrogen Production from Semiconductor-based Photocatalysis via Water Splitting,” *Catalysts*, vol. 2, no. 4, pp. 490–516, 2012.
- [78] D. Jing Jing, L. Guo, L. Zhao, X. Zhang, H. Liu, M. Li, S. Shen, G. Liu, X. Hu, X. Zhang, K. Zhang, L. Ma, P. Guo. “Efficient solar hydrogen production by photocatalytic

- water splitting: From fundamental study to pilot demonstration,” *Int. J. Hydrogen Energy*, vol. 35, no. 13, pp. 7087–7097, 2010.
- [79] M. Tahir and N. S. Amin, “Advances in visible light responsive titanium oxide-based photocatalysts for CO₂ conversion to hydrocarbon fuels,” *Energy Convers. Manag.*, vol. 76, pp. 194–214, Dec. 2013.
- [80] K. Nakata and A. Fujishima, “TiO₂ photocatalysis: Design and applications,” *J. Photochem. Photobiol. C Photochem. Rev.*, vol. 13, no. 3, pp. 169–189, 2012.
- [81] J. Schneider, “Understanding TiO₂ Photocatalysis: Mechanisms and Materials,” *Chem. Rev.*, vol. 114, no. 19, pp. 9919–9986, 2014.
- [82] J. Yang, “Roles of Cocatalysts in Photocatalysis and Photoelectrocatalysis,” *Acc. Chem. Res.*, vol. 46, no. 8, pp. 1900–1909, 2013.
- [83] P. V. Kamat, “Manipulation of charge transfer across semiconductor interface. A criterion that cannot be ignored in photocatalyst design,” *J. Phys. Chem. Lett.*, vol. 3, no. 5, pp. 663–672, 2012.
- [84] P. D. Vaidya and A. E. Rodrigues, “Glycerol reforming for hydrogen production: A review,” *Chem. Eng. Technol.*, vol. 32, no. 10, pp. 1463–1469, 2009.
- [85] M. A. Nadeem, M. A. Khan, A. A. Ziani, and H. Idriss, “An overview of the photocatalytic water splitting over suspended particles,” *Catalysts*, vol. 11, no. 1, pp. 1–25, 2021.
- [86] M. Ismael, “A review and recent advances in solar-to-hydrogen energy conversion based on photocatalytic water splitting over doped-TiO₂ nanoparticles,” *Sol. Energy*, vol. 211, no. July, pp. 522–546, 2020.
- [87] V. Kumaravel, S. Mathew, J. Bartlett, and S. C. Pillai, “Photocatalytic hydrogen production using metal doped TiO₂: A review of recent advances,” *Appl. Catal. B Environ.*, vol. 244, no. September 2018, pp. 1021–1064, 2019.
- [88] V. Etacheri, C. Di Valentin, J. Schneider, D. Bahnemann, and S. C. Pillai, “Visible-light activation of TiO₂ photocatalysts: Advances in theory and experiments,” *J. Photochem. Photobiol. C Photochem. Rev.*, vol. 25, pp. 1–29, 2015.
- [89] P. C. Ricci, C. Carbonaro, L. Stagi, M. Salis, A. Casu, S. Enzo, F. Delogu, “Anatase-to-rutile phase transition in TiO₂ nanoparticles irradiated by visible light,” *J. Phys. Chem. C*, vol. 117, no. 15, pp. 7850–7857, 2013.

- [90] B. J. Clark, *UV Spectroscopy: Techniques, instrumentation and data handling*. London, England, Book. Springer Netherlands. 1993.
- [91] V.-H. Nguyen, “Recent developments in the design of photoreactors for solar energy conversion from water splitting and CO₂ reduction,” *Appl. Catal. A Gen.*, vol. 550, pp. 122–141, 2018.
- [92] T. Jafari, E. Moharreri, A. S. Amin, R. Miao, W. Song, and S. L. Suib, “Photocatalytic water splitting - The untamed dream: A review of recent advances,” *Molecules*, vol. 21, no. 7, 2016.
- [93] A. K. Seferlis and S. G. Neophytides, “On the kinetics of photoelectrocatalytic water splitting on nanocrystalline TiO₂films,” *Appl. Catal. B Environ.*, vol. 132–133, pp. 543–552, 2013.
- [94] M. Wang, S. Shen, L. Li, Z. Tang, and J. Yang, “Effects of sacrificial reagents on photocatalytic hydrogen evolution over different photocatalysts,” *J. Mater. Sci.*, vol. 52, no. 9, pp. 5155–5164, 2017.
- [95] C. R. López, E. P. Melián, J. A. Ortega Méndez, D. E. Santiago, J. M. Doña Rodríguez, and O. González Díaz, “Comparative study of alcohols as sacrificial agents in H₂production by heterogeneous photocatalysis using Pt/TiO₂ catalysts,” *J. Photochem. Photobiol. A Chem.*, vol. 312, pp. 45–54, 2015.
- [96] K. C. Christoforidis and P. Fornasiero, “Photocatalytic Hydrogen Production: A Rift into the Future Energy Supply,” *ChemCatChem*, vol. 9, no. 9, pp. 1523–1544, 2017.
- [97] S. E. Salas and H. De Lasa, “Photocatalytic Water Splitting using a Modified Pt- TiO₂. Kinetic Modeling and Hydrogen Production Efficiency,” 2013.
- [98] S. Escobedo and H. De Lasa, “Photocatalytic Water Splitting using a Modified Pt- TiO₂. Kinetic Modeling and Hydrogen Production Efficiency,” Thesis. The University of Western Ontario, 2013.
- [99] H. De Lasa, B. Serrano, and M. Salaiques, *Photocatalytic Reaction Engineering*. Book. Springer US. London, Ontario, 2004.
- [100] K. V. Kumar, K. Porkodi, and F. Rocha, “Langmuir-Hinshelwood kinetics - A theoretical study,” *Catal. Commun.*, vol. 9, no. 1, pp. 82–84, Jan. 2008.
- [101] H. De Lasa, B. S. Rosales, J. Moreira, and P. Valades-Pelayo, “Efficiency Factors in Photocatalytic Reactors: Quantum Yield and Photochemical Thermodynamic

- Efficiency Factor,” *Chem. Eng. Technol.*, vol. 39, no. 1, pp. 51–65, 2016.
- [102] J. F. Guayaquil-Sosa, B. Serrano-Rosales, P. J. Valadés-Pelayo, and H. de Lasa, “Photocatalytic hydrogen production using mesoporous TiO₂ doped with Pt,” *Appl. Catal. B Environ.*, vol. 211, pp. 337–348, 2017.
- [103] H. de Lasa, B. Serrano, and M. Salaices, *Photocatalytic Reaction Engineering*. US: Springer. Science, 2005.
- [104] B. S. Rosales, J. Moreira Del Rio, J. F. Guayaquil, and H. De Lasa, “Photodegradation Efficiencies in a Photo-CREC Water-II Reactor Using Several TiO₂ Based Catalysts,” *Int. J. Chem. React. Eng.*, vol. 14, no. 3, pp. 685–701, 2016.
- [105] Y.-L. He, S.-Z. Qin, C. J. Lim, and J. R. Grace, “Particle velocity profiles and solid flow patterns in spouted beds,” *Can. J. Chem. Eng.*, vol. 72, no. 4, pp. 561–568, 1994.
- [106] S. M. Systems, M. Fiber, O. Spectrometers, L. Sources, F. O. Cables, and S. Accessories, “Extreme Spectrometer Instrumentation Stellar Net Catalog,” *Spectroscopy*, Florida, USA. 2007.
- [107] Ushio, “Uv-b, bl & blb.”.Catalog. USA. 2016.
- [108] B. Serrano, A. Ortíz, J. Moreira, and H. I. De Lasa, “Energy efficiency in photocatalytic reactors for the full span of reaction times,” *Ind. Eng. Chem. Res.*, vol. 48, no. 22, pp. 9864–9876, 2009.
- [109] M. J. Garcia, “Photocatalytic Reactors for Air Treatment : Energy Efficiencies and Kinetic Modeling,” no. April, p. 147, 2012.
- [110] M.Salaices, B. Serrano, and H. I. de Lasa, “Photocatalytic Conversion of Organic Pollutants Extinction Coefficients and Quantum Efficiencies,” *Ind. Eng. Chem.*, 40, 23, 5455–5464. 2001.
- [111] S. P. Guo, J. C. Li, Q. T. Xu, Z. Ma, and H. G. Xue, “Recent achievements on polyanion-type compounds for sodium-ion batteries: Syntheses, crystal chemistry and electrochemical performance,” *J. Power Sources*, vol. 361, pp. 285–299, 2017.
- [112] D. Ficai and A. Mihai Grumezescu, *Nanostructures for Novel Therapy*. Bucharest, Romania: Elsevier Inc, 2017.
- [113] M. Parashar, V. K. Shukla, and R. Singh, “Metal oxides nanoparticles via sol–gel method: a review on synthesis, characterization and applications,” *J. Mater. Sci. Mater. Electron.*, vol. 31, no. 5, pp. 3729–3749, 2020.

- [114] C. De Coelho Escobar and J. H. Z. Dos Santos, "Effect of the sol-gel route on the textural characteristics of silica imprinted with Rhodamine B," *J. Sep. Sci.*, vol. 37, no. 7, pp. 868–875, 2014.
- [115] B. E. Yoldas, "Monolithic glass formation by chemical polymerization," *J. Mater. Sci.*, vol. 14, no. 8, pp. 1843–1849, Aug. 1979.
- [116] H. Luo, C. Wang, and Y. Yan, "Synthesis of mesostructured titania with controlled crystalline framework," *Chem. Mater.*, vol. 15, no. 20, pp. 3841–3846, 2003.
- [117] R. S. Dubey, "Temperature-dependent phase transformation of TiO₂ nanoparticles synthesized by sol-gel method," *Mater. Lett.*, vol. 215, pp. 312–317, Mar. 2018.
- [118] A. O. Araoyinbo, M. M. A. B. Abdullah, A. Rahmat, A. I. Azmi, P. Vizureanu, and W. M. F. Wan Abd Rahim, "Preparation of Heat Treated Titanium Dioxide (TiO₂) Nanoparticles for Water Purification," in *IOP Conference Series: Materials Science and Engineering*, 2018, vol. 374, no. 1, p. 012084.
- [119] B. B. Lakshmi, P. K. Dorhout, and C. R. Martin, "Sol-Gel Template Synthesis of Semiconductor Nanostructures," *Chem. Mater.*, vol. 9, no. 3, pp. 857–862, 1997.
- [120] D. V. Aware and S. S. Jadhav, "Synthesis, characterization and photocatalytic applications of Zn-doped TiO₂ nanoparticles by sol-gel method," *Appl. Nanosci.*, vol. 6, no. 7, pp. 965–972, 2016.
- [121] J. C. Yu, X. Wang, and X. Fu, "Pore-Wall Chemistry and Photocatalytic Activity of Mesoporous Titania Molecular Sieve Films," *Chem. Mater.*, vol. 16, no. 8, pp. 1523–1530, 2004.
- [122] D. Y. Zhao, P. D. Yang, N. Melosh, J. L. Feng, B. F. Chmelka, and G. D. Stucky, "Continuous mesoporous silica films with highly ordered large pore structures," *Adv. Mater.*, vol. 10, no. 16, pp. 1380–1385, 1998.
- [123] E. M. Samsudin, S. B. A. Hamid, J. C. Juan, and W. J. Basirun, "Influence of triblock copolymer (pluronic F127) on enhancing the physico-chemical properties and photocatalytic response of mesoporous TiO₂," *Appl. Surf. Sci.*, vol. 355, pp. 959–968, 2015.
- [124] T. Wang, D. Chen, J. Ma, S. Wen, and Q. Liu, "Synthesis and characterisation of pore-expanded mesoporous silica materials," *Micro & Nano Lett.*, vol. 10, no. 2, pp. 140–144, 2015.

- [125] E. H. D. Donkers. "*Block copolymers with polar and non-polar blocks : combination of living anionic polymerization and RAFT- mediated polymerization*". Eindhoven University of Technology Library. Book. 2006.
- [126] T. Křížek, P. Coufal, E. Tesařová, J. Sobotníková, and Z. Bosáková, "Pluronic F-127 as the buffer additive in capillary entangled polymer electrophoresis: Some fundamental aspects," *J. Sep. Sci.*, vol. 33, no. 16, pp. 2458–2464, 2010.
- [127] J. Wang, H. Li, H. Li, C. Zou, H. Wang, and D. Li, "Mesoporous TiO₂ thin films exhibiting enhanced thermal stability and controllable pore size: Preparation and photocatalyzed destruction of Cationic Dyes," *ACS Appl. Mater. Interfaces*, vol. 6, no. 3, pp. 1623–1631, 2014.
- [128] J. Wang, J. Wu, and L. Hongyi, "A Review of Mesoporous TiO₂ Thin Films," *Key Lab Adv. Funct. Mater. Sch. Mater. Sci. Eng. Beijing Univ. Technol. Beijing 100124, China*.
- [129] B. Rusinque, "Hydrogen Production by Photocatalytic Water Splitting Under Near-UV and Visible Light Using Doped Pt and Pd TiO₂," Thesis, 2018.
- [130] S. K. Das, M. K. Bhunia, and A. Bhaumik, "Self-assembled TiO₂ nanoparticles: Mesoporosity, optical and catalytic properties," *Dalt. Trans.*, vol. 39, no. 18, pp. 4382–4390, 2010.
- [131] B. Rusinque, "Hydrogen Production by Photocatalytic Water Splitting under Near-UV using Pd doped Mesoporous TiO₂," in *Nam 26. 2019 North American Catalysis Society Meeting*, 2019.
- [132] H. Oveisi, N. Suzuki, A. Beitollahi, and Y. Yamauchi, "Aerosol-assisted fabrication of mesoporous titania spheres with crystallized anatase structures and investigation of their photocatalytic properties," *J. Sol-Gel Sci. Technol.*, vol. 56, no. 2, pp. 212–218, 2010.
- [133] M. Cargnello, T. R. Gordon, and C. B. Murray, "Solution-phase synthesis of titanium dioxide nanoparticles and nanocrystals," *Chem. Rev.*, vol. 114, no. 19, pp. 9319–9345, 2014.
- [134] B. Rusinque, S. Escobedo, and H. de Lasa, "Photoreduction of a Pd-Doped Mesoporous TiO₂ Photocatalyst for Hydrogen Production under Visible Light," *Catalysts*, pp. 1–24, 2020.
- [135] L. Domínguez-Henao, A. Turolla, D. Monticelli, and M. Antonelli, "Assessment of a colorimetric method for the measurement of low concentrations of peracetic acid and

- hydrogen peroxide in water,” *Talanta*, vol. 183, no. February, pp. 209–215, 2018.
- [136] G. Fagerlund, “Determination of specific surface by the BET method,” *Matériaux Constr.*, vol. 6, no. 3, pp. 239–245, 1973.
- [137] Micromeritics Instrument Corporation, “Gas Adsorption Theory,” [Online]. Available: http://www.micromeritics.com/Repository/Files/Gas_Adsorption_Theory_poster.pdf, [Accessed: 31-Mar-2021].
- [138] Micromeritics, *ASAP 2020 Operator’s Manual*, no. October. 2006.
- [139] A. T. Hubbard, *Encyclopedia of Surface and Colloid Scienc*, Volume 1. New York, USA: Marcel Dekker, Inc, 2002.
- [140] X. Pan and Y. J. Xu, “Defect-mediated growth of noble-metal (Ag, Pt, and Pd) nanoparticles on TiO₂ with oxygen vacancies for photocatalytic redox reactions under visible light,” *J. Phys. Chem. C*, vol. 117, no. 35, pp. 17996–18005, 2013.
- [141] Micromeritics, “AutoChem II 2920,” no. Figure 1, p. 2920, 2000.
- [142] V. Bratan, C. Munteanu, C. Hornoiu, A. Vasile, F. Papa, R. State, S. Preda, D. Culita, N. Ionescu. “CO oxidation over Pd supported catalysts —In situ study of the electric and catalytic properties,” *Appl. Catal. B Environ.*, vol. 207, no. October, pp. 166–173, 2017.
- [143] V. G. Deshmane, S. L. Owen, R. Y. Abrokwah, and D. Kuila, “Mesoporous nanocrystalline TiO₂ supported metal (Cu, Co, Ni, Pd, Zn, and Sn) catalysts: Effect of metal-support interactions on steam reforming of methanol,” *J. Mol. Catal. A Chem.*, vol. 408, pp. 202–213, Nov. 2015.
- [144] C. M. Mendez, H. Olivero, D. E. Damiani, and M. A. Volpe, “On the role of Pd β -hydride in the reduction of nitrate over Pd based catalyst,” *Appl. Catal. B Environ.*, vol. 84, no. 1–2, pp. 156–161, Oct. 2008.
- [145] A. Baylet, P. Marécot, D. Duprez, P. Castellazzi, G. Groppi, and P. Forzatti, “In situ Raman and in situ XRD analysis of PdO reduction and Pd⁰ oxidation supported on γ -Al₂O₃ catalyst under different atmospheres,” *Phys. Chem. Chem. Phys.*, vol. 13, no. 10, p. 4607, Feb. 2011.
- [146] C. S. L. Alencar, A. R. N. Paiva, J. C. M. Da Silva, J. M. Vaz, and E. V. Spinace, “One-step synthesis of AuCu/TiO₂ catalysts for CO preferential oxidation,” *Mater. Res.*, vol. 23, no. 5, pp. 2–7, 2020.

- [147] C. A. González, A. N. Ardila, C. Montes De Correa, M. A. Martínez, and G. Fuentes-Zurita, "Pd/TiO₂ Washcoated Cordierite Minimonoliths for Hydrodechlorination of Light Organochlorinated Compounds," *Ind. Eng. Chem.* 46, 24, 7961–7969. 2007.
- [148] *AutoChem 2920 Automated Catalyst Characterization System Operator's Manual*, no. July. 2014.
- [149] W. F. Bleam, *Soil and Environmental Chemistry*. Elsevier, 2012.
- [150] S. Kuhaudomlap, O. Mekasuwandumrong, P. Praserttham, S.-I. Fujita, M. Arai, and J. Panpranot, "The H₂-Treated TiO₂ Supported Pt Catalysts Prepared by Strong Electrostatic Adsorption for Liquid-Phase Selective Hydrogenation," *Catalysts*, vol. 8, no. 2, p. 87, 2018.
- [151] B. E. Warren, *X-Ray Diffraction*. United States: Dover publications, 1990.
- [152] J. Zhang, P. Zhou, J. Liu, and J. Yu, "New understanding of the difference of photocatalytic activity among anatase, rutile and brookite TiO₂," *Phys. Chem. Chem. Phys.*, vol. 16, no. 38, pp. 20382–20386, 2014.
- [153] D. Rodriguez-Vindas, "Synthesis of palladium with different nanoscale structures by sputtering deposition onto fiber templates," *J. Nanophotonics*, vol. 2, no. 1, p. 021925, 2008.
- [154] P.W.Treacy, H. Hussain, X. Torrelles, D. Grinter, G. Cabailh, O. Bikondoa, C. Nicklin, S. Selcuk, A. Selloni, R. Lindsay, G. Thornton, , "Geometric structure of anatase TiO₂(101)," *Phys. Rev. B*, vol. 95, no. 7, pp. 1–7, 2017.
- [155] A. Hernandez and I. Medina. *Photocatalytic Semiconductors: Synthesis, Characterization and Environmental Applications*. Springer. Mexico. 2015.
- [156] N. Sobana, M. Muruganadham, and M. Swaminathan, "Nano-Ag particles doped TiO₂ for efficient photodegradation of Direct azo dyes," *J. Mol. Catal. A Chem.*, vol. 258, no. 1–2, pp. 124–132, 2006.
- [157] A. Slav, "Optical characterization of TiO₂-Ge nanocomposite films obtained by reactive magnetron sputtering," *Dig. J. Nanomater. Biostructures*, vol. 6, no. 3, pp. 915–920, 2011.
- [158] A. Tauc, J. Grigorovici, R. Vancu, "Optical Properties and Electronic Structure of Amorphous Germanium," *Basic Solid State Phys.*, vol. 15, no. 2, 1966.
- [159] Y. Xiong, J. Chen, B. Wiley, Y. Xia, Y. Yin, and Z. Y. Li, "Size-dependence of surface

- plasmon resonance and oxidation for Pd nanocubes synthesized via a seed etching process,” *Nano Lett.*, vol. 5, no. 7, pp. 1237–1242, 2005.
- [160] B. Santara, B. Pal, and P. K. Giri, “Signature of strong ferromagnetism and optical properties of Co doped TiO₂ nanoparticles,” *J. Appl. Phys.*, vol. 110, no. 11, 2011.
- [161] W. Khairy, M. Zakaria, “Effect of metal-doping of TiO₂ nanoparticles on their photocatalytic activities toward removal of organic dyes,” *Egypt. J. Pet.*, vol. 23, pp. 419–426, 2014.
- [162] O. Ola and M. M. Maroto-Valer, “Transition metal oxide based TiO₂ nanoparticles for visible light induced CO₂ photoreduction,” *Appl. Catal. A Gen.*, vol. 502, pp. 114–121, 2015.
- [163] K. Hon Leong, H. Ye Chu, S. Ibrahim, and P. Saravanan, “Palladium nanoparticles anchored to anatase TiO₂ for enhanced surface plasmon resonance-stimulated, visible-light-driven photocatalytic activity,” *Beilstein J. Nanotechnol.*, vol. 6, pp. 428–437, 2015.
- [164] X. Yang, F. Ma, K. Li, Y. Guo, J. Hu, W. Li, M. Huo, Y. Guo. “Mixed phase titania nanocomposite codoped with metallic silver and vanadium oxide: New efficient photocatalyst for dye degradation,” *J. Hazard. Mater.*, vol. 175, no. 1–3, pp. 429–438, 2010.
- [165] A. T. Kuvarega, R. W. M. Krause, and B. B. Mamba, “Nitrogen / Palladium-Codoped TiO₂ for Efficient Visible Light Photocatalytic Dye Degradation,” pp. 22110–22120, 2011.
- [166] Y. Lee, E. Kim, Y. Park, J. Kim, W. Ryu, J. Rho, K. Kim. “Photodeposited metal-semiconductor nanocomposites and their applications,” *J. Mater.*, vol. 4, no. 2, pp. 83–94, 2018.
- [167] D. Briggs, “X: X-Ray Photoelectron Spectroscopy,” *Handb. Adhes. Second Ed.*, pp. 621–622, 2005.
- [168] P. J. Valades-Pelayo, J. Moreira, B. Serrano, and H. De Lasa, “Boundary conditions and phase functions in a photo-crec water-II reactor radiation field,” *Chem. Eng. Sci.*, vol. 107, pp. 123–136, 2014.
- [169] S. Escobedo, B. Serrano, A. Calzada, J. Moreira, and H. De Lasa, “Hydrogen production using a platinum modified TiO₂ photocatalyst and an organic scavenger. Kinetic

- modeling,” *Fuel*, vol. 181, pp. 438–449, 2016.
- [170] M. Salaices, B. Serrano, and H. I. De Lasa, “Experimental evaluation of photon absorption in an aqueous TiO₂ slurry reactor,” *Chem. Eng. J.*, vol. 90, no. 3, pp. 219–229, 2002.
- [171] B. Rusinque, S. Escobedo, and H. de Lasa, “Photocatalytic hydrogen production under near-UV using Pd-doped mesoporous TiO₂ and ethanol as organic scavenger,” *Catalysts*, vol. 9, no. 1, 2019.
- [172] J. M. Thornton and D. Raftery, “Efficient photocatalytic hydrogen production by platinum-loaded carbon-doped cadmium indate nanoparticles,” *ACS Appl. Mater. Interfaces*, vol. 4, no. 5, pp. 2426–2431, 2012.
- [173] H. Yoshida, K. Hirao, J. Nishimoto, K. Shimura, S. Kato, H. Itoh, H. Hideaki, T. Hattori. “Hydrogen production from methane and water on platinum loaded titanium oxide photocatalysts,” *J. Phys. Chem. C*, vol. 112, no. 14, pp. 5542–5551, 2008.
- [174] N. Zhang, S. Liu, X. Fu, and Y. J. Xu, “Synthesis of M@TiO₂ (M = Au, Pd, Pt) core-shell nanocomposites with tunable photoreactivity,” *J. Phys. Chem. C*, vol. 115, no. 18, pp. 9136–9145, 2011.
- [175] S. Riyapan, Y. Boonyongmaneerat, O. Mekasuwandumrong, H. Yoshida, F. Hiroshi, I. Shin, M. Arai, J. Panpranot, “Improved catalytic performance of Pd/TiO₂ in the selective hydrogenation of acetylene by using H₂-treated sol-gel TiO₂,” *J. Mol. Catal. A Chem.*, vol. 383–384, pp. 182–187, 2014.
- [176] S. Akbayrak, Y. Tonbul, and S. Özkar, “Nanoceria supported palladium(0) nanoparticles: Superb catalyst in dehydrogenation of formic acid at room temperature,” *Appl. Catal. B Environ.*, vol. 206, pp. 384–392, 2017.
- [177] J. Peng and S. Wang, “Performance and characterization of supported metal catalysts for complete oxidation of formaldehyde at low temperatures,” *Appl. Catal. B Environ.*, vol. 73, no. 3, pp. 282–291, 2007.
- [178] J. F. Gomes, I. Leal, K. Bednarczyk, M. Gmurek, M. Stelmachowski, M. Diak, M. Quinta-Ferreira, R. Costa, R. Quinta-Ferreira, R. Martins. “Photocatalytic ozonation using doped TiO₂ catalysts for the removal of parabens in water,” *Sci. Total Environ.*, vol. 609, pp. 329–340, 2017.
- [179] M. Maicu, M. C. Hidalgo, G. Colón, and J. A. Navío, “Comparative study of the

- photodeposition of Pt, Au and Pd on pre-sulphated TiO₂ for the photocatalytic decomposition of phenol,” *J. Photochem. Photobiol. A Chem.*, vol. 217, no. 2–3, pp. 275–283, Jan. 2011.
- [180] H. Bahruji, M. Bowker, P. R. Davies, D. J. Morgan, C. A. Morton, T. A. Egerton, J. Kennedy, W. Jones. “Rutile TiO₂–Pd Photocatalysts for Hydrogen Gas Production from Methanol Reforming,” *Top. Catal.*, vol. 58, no. 2–3, pp. 70–76, 2015.
- [181] H. Zhang, J. Sun, V. L. Dagle, B. Halevi, A. K. Datye, and Y. Wang, “Influence of ZnO facets on Pd/ZnO catalysts for methanol steam reforming,” *ACS Catal.*, vol. 4, no. 7, pp. 2379–2386, 2014.
- [182] W. G. Onderwaater, A. Taranovskyy, G. C. Van Baarle, J. W. M. Frenken, and I. M. N. Groot, “In Situ Optical Reflectance Difference Observations of CO Oxidation over Pd(100),” *J. Phys. Chem. C*, vol. 121, no. 21, pp. 11407–11415, 2017.
- [183] S. Bai, Q. Shao, P. Wang, Q. Dai, X. Wang, and X. Huang, “Highly Active and Selective Hydrogenation of CO₂ to Ethanol by Ordered Pd-Cu Nanoparticles,” *J. Am. Chem. Soc.*, vol. 139, no. 20, pp. 6827–6830, 2017.
- [184] Y. Song, W. Chen, W. Wei, and Y. Sun, “Advances in clean fuel ethanol production from electro-, photo- and photoelectro-catalytic CO₂ reduction,” *Catalysts*, vol. 10, no. 11, pp. 1–25, 2020.
- [185] C. Arrouvel, M. Digne, M. Breysse, H. Toulhoat, and P. Raybaud, “Effects of morphology on surface hydroxyl concentration: A DFT comparison of anatase-TiO₂ and γ -alumina catalytic supports,” *J. Catal.*, vol. 222, no. 1, pp. 152–166, Feb. 2004.
- [186] J. Moreira, B. Serrano, A. Ortiz, and H. de Lasa, “A unified kinetic model for phenol photocatalytic degradation over TiO₂ photocatalysts,” *Chem. Eng. Sci.*, vol. 78, pp. 186–203, 2012.
- [187] L. Liu, X. B. Luo, L. Ding, and S. L. Luo, “Application of Nanotechnology in the Removal of Heavy Metal From Water,” in *Nanomaterials for the Removal of Pollutants and Resource Reutilization*, Elsevier, 2018, pp. 83–147.
- [188] K. Sahel, L. Elsellami, I. Mirali, F. Dappozze, M. Bouhent, and C. Guillard, “Hydrogen peroxide and photocatalysis,” *Appl. Catal. B Environ.*, vol. 188, pp. 106–112, Jul. 2016.
- [189] H. Enzweiler, P. H. Yassue-Cordeiro, M. Schwaab, E. Barbosa-Coutinho, M. H. N. Olsen Scaliante, and N. R. C. Fernandes, “Catalyst concentration, ethanol content and

- initial pH effects on hydrogen production by photocatalytic water splitting,” *J. Photochem. Photobiol. A Chem.*, vol. 388, no. December 2018, p. 112051, 2020.
- [190] M. Kosmulski, “The significance of the difference in the point of zero charge between rutile and anatase,” *Advances in Colloid and Interface Science*, vol. 99, no. 3. Elsevier, pp. 255–264, 02-Dec-2002.
- [191] M. J. Arlos, M. Hatat-Fraile, R. Liang, L. Bragg, N. Zhou, S. Andrews, M. Servos. “Photocatalytic decomposition of organic micropollutants using immobilized TiO₂ having different isoelectric points,” *Water Res.*, vol. 101, pp. 351–361, Sep. 2016.
- [192] S. B. Kanungo, K. M. Parida, and B. R. Sant, “Studies on MnO₂-III. The kinetics and the mechanism for the catalytic decomposition of H₂O₂ over different crystalline modifications of MnO₂,” *Electrochim. Acta*, vol. 26, no. 8, pp. 1157–1167, 1981.
- [193] H. M. G. Tambago and R. L. de Leon, “Intrinsic Kinetic Modeling of Hydrogen Production by Photocatalytic Water Splitting Using Cadmium Zinc Sulfide Catalyst,” *Int. J. Chem. Eng. Appl.*, vol. 6, no. 4, pp. 220–227, Aug. 2015.
- [194] H. Ibrahim and H. De Lasa, “Novel photocatalytic reactor for the destruction of airborne pollutants reaction kinetics and quantum yields,” *Ind. Eng. Chem. Res.*, vol. 38, no. 9, pp. 3211–3217, 1999.
- [195] A. Rioja-Cabanillas, D. Valdesueiro, P. Fernández-Ibáñez, and J. A. Byrne, “Hydrogen from wastewater by photocatalytic and photoelectrochemical treatment,” *JPhys Energy*, vol. 3, no. 1. IOP Publishing Ltd, p. 12006, 01-Jan-2021.
- [196] T. N. Ravishankar, M. de O. Vaz, T. Ramakrishnappa, S. Teixeira, J. Dupont, R. Pai, G. Banuprakash. “The heterojunction effect of Pd on TiO₂ for visible light photocatalytic hydrogen generation via water splitting reaction and photodecolorization of trypan blue dye,” *J. Mater. Sci. Mater. Electron.*, vol. 29, no. 13, pp. 11132–11143, Jul. 2018.

Appendices

Appendix A. Detection of H₂ and Carbon Containing Species by a Shimadzu CG 2010

The several gases produced, as a result of the photocatalytic water splitting with ethanol as a scavenger, were evaluated using a Shimadzu GC2010 Gas Chromatograph (Nakagyo-ku, Kyoto, Japan). Samples were taken every hour during a 6 h period. To accomplish this, argon (Praxair 99.999%) was used as a gas carrier. The GC was equipped with two detectors: A Flame Ionization Detector (Nakagyo-ku, Kyoto, Japan) (FID) coupled with a methanizer and a Thermal Conductivity Detector (TCD). As a result, the analytical equipment employed was able to detect hydrogen (H₂), carbon monoxide (CO), methane (CH₄), carbon dioxide (CO₂), ethane (C₂H₆), ethylene (C₂H₄), acetaldehyde (C₂H₄O), and ethanol (C₂H₅OH).

The GC method used for the gas phase analysis is described as follows:

Column:

Temperature: 50 °C Equilibration time: 0.2 min

Column Oven Temperature Program

Rate	Temperature (°C)	Hold Time (min)
-	50	4
20.0	200	18.5

FID

Temperature: 230 °C Sample Rate: 40 msec Make up gas: Hydrogen

TCD

Temperature: 210 °C Sample Rate: 40 msec Make up gas: Argon

Typical chromatograms obtained, for both hydrogen and carbon containing by-products, using the employed programmed oven temperature method, are reported in Figures A1 and A2. One should note that the air detected via the TCD was attributed to the air contained in the needle, when injecting the gas sample into the GC. This air gas volume is negligible and was disregarded in the product analysis.

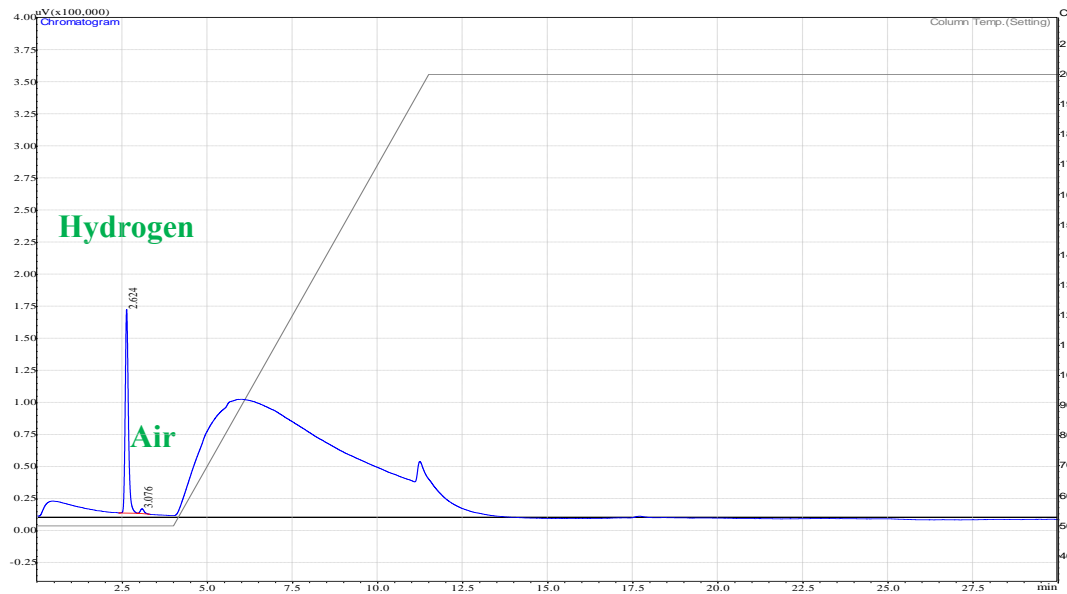


Figure A1. Hydrogen peak as detected by the TCD.

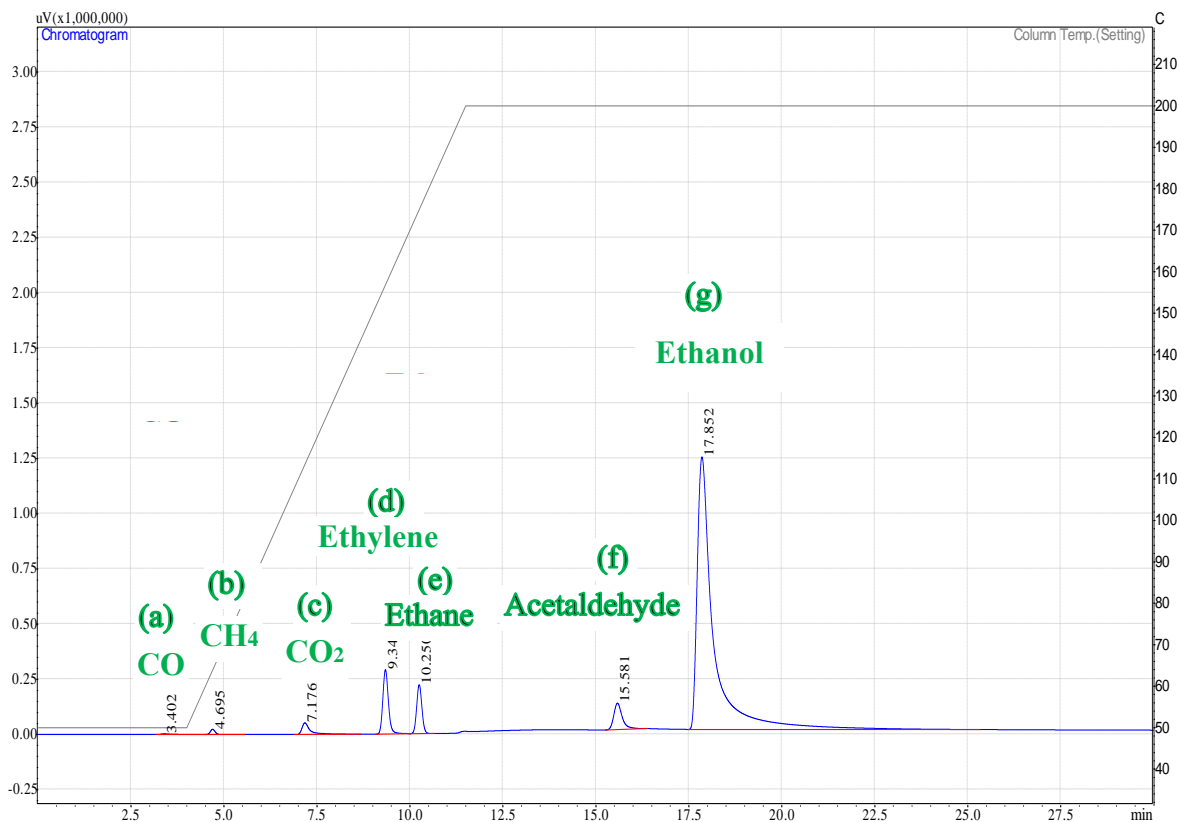


Figure A2. Carbon containing product species peaks as detected by the FID for: (a) carbon monoxide (CO), (b) methane (CH₄), (c) carbon dioxide (CO₂), (d) ethylene (C₂H₄), (e) ethane (C₂H₆), (f) acetaldehyde (C₂H₄O), and (g) ethanol (C₂H₅OH).

H₂ peak measurements were quantified using the TCD calibration, as reported in Figure A3. Calibration was established by using a H₂ certified standard gas mixture sample (10% H₂ and 90% He Praxair), and different known hydrogen volumes (0.1, 0.2, 0.3, 0.4, 0.5, and 0.6 mL). Sample volumes in the syringe were at room temperature, and pressure conditions (25 °C and 1 atm).

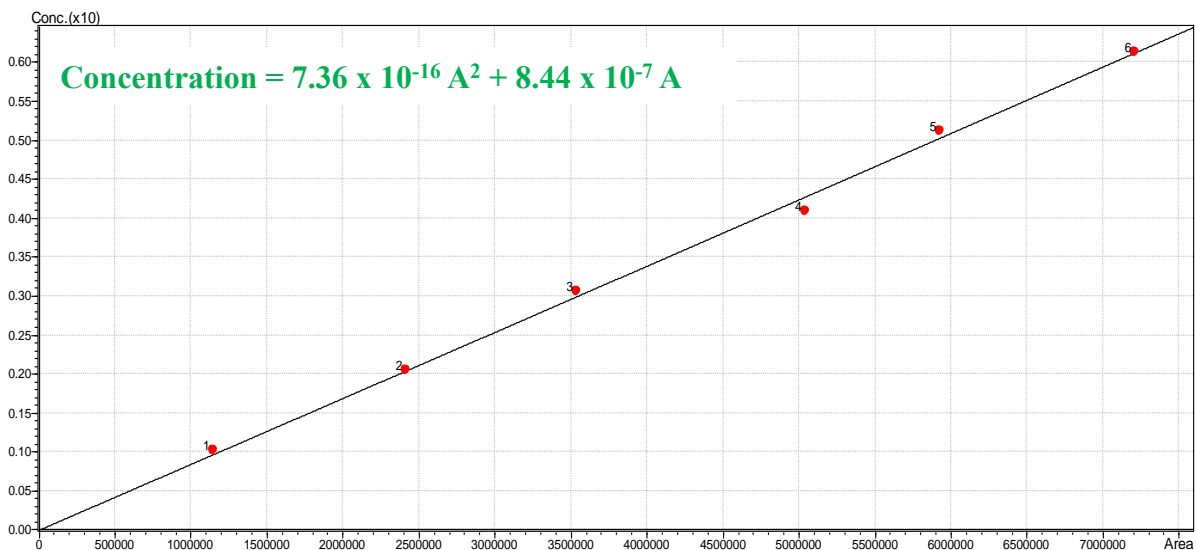


Figure A3. Calibration curve using the Shimadzu GC 2010 for Hydrogen.

Appendix B. Carbon Containing Species Balance

This appendix reports a typical calculation of the moles carbon balance for the 0.25 wt% Pd-TiO₂ catalyst under near-UV light. Note that the Photo-CREC Water II Reactor, at the beginning of the reaction, was loaded with 6 L of slurry suspension. In addition, the Photo-CREC Water II Reactor is equipped with a sealed storage tank with a total volume of 5716 mL for collecting the gas phase products.

- Moles of carbon at t = 0 h in the liquid phase:

$$n_C = 0.34171 \text{ mole L}^{-1} * (6.0 \text{ L}) * \left(\frac{2 \text{ moles of Carbon}}{1 \text{ mole of Ethanol}} \right) = 4.10 \text{ mole of Carbon}$$

- Moles of carbon at t = 6 h in the liquid phase:

$$n_C = 0.34110 \text{ moles L}^{-1} * (6.0 \text{ L}) * \left(\frac{2 \text{ moles of Carbon}}{1 \text{ moles of Ethanol}} \right) = 4.09 \text{ moles of Carbon}$$

- Ethanol in the gas phase:

$$\begin{aligned} n_C &= 0.1776 \text{ } \mu\text{moles mL}^{-1} * (5716 \text{ mL}) * \left(\frac{2 \text{ moles of Carbon}}{1 \text{ moles of Ethanol}} \right) \\ &= 2.03 \times 10^{-3} \text{ moles of Carbon} \end{aligned}$$

- Methane in the gas phase:

$$\begin{aligned} n_C &= 0.018 \text{ } \mu\text{moles mL}^{-1} * (5716 \text{ mL}) * \left(\frac{1 \text{ mole of Carbon}}{1 \text{ mole of Methane}} \right) \\ &= 1.01 \times 10^{-5} \text{ moles of Carbon} \end{aligned}$$

- Ethane in the gas phase:

$$\begin{aligned} n_C &= 0.0072 \text{ } \mu\text{moles mL}^{-1} * (5716 \text{ mL}) * \left(\frac{2 \text{ moles of Carbon}}{1 \text{ mole of Ethane}} \right) \\ &= 8.23 \times 10^{-5} \text{ moles of Carbon} \end{aligned}$$

- Ethylene in the gas phase:

$$\begin{aligned} n_C &= 0.0140 \text{ } \mu\text{moles mL}^{-1} * (5716 \text{ mL}) * \left(\frac{2 \text{ moles of Carbon}}{1 \text{ mole of Etylenel}} \right) \\ &= 1.60 \times 10^{-4} \text{ moles of Carbon} \end{aligned}$$

- Acetaldehyde in the gas phase:

$$\begin{aligned} n_C &= 0.0086 \text{ } \mu\text{moles mL}^{-1} * (5716 \text{ mL}) * \left(\frac{2 \text{ moles of Carbon}}{1 \text{ mole of Acetaldehyde}} \right) \\ &= 9.83 \times 10^{-5} \text{ moles of Carbon} \end{aligned}$$

- Carbon monoxide in the gas phase:

$$n_C = 0.0005 \mu\text{mole mL}^{-1} * (5716 \text{ mL}) * \left(\frac{1 \text{ mole of Carbon}}{1 \text{ mole of Carbon Monoxide}} \right)$$

$$= 2.57 \times 10^{-6} \text{ moles of Carbon}$$

- Carbon dioxide in the gas phase:

$$n_C = 0.0029 \mu\text{moles mL}^{-1} * (5716 \text{ mL}) * \left(\frac{1 \text{ mole of Carbon}}{1 \text{ mole of Carbon Dioxide}} \right)$$

$$= 1.65 \times 10^{-5} \text{ moles of Carbon}$$

The addition of the moles of carbon after 6 h of irradiation can be established as:

$$n_{t=6h} = \text{mol of byproducts} + \text{mol of ethanol}$$

$$n_{t=6h} = 2.40 \times 10^{-3} \text{ moles of Carbon} + 4.09 \text{ moles of Carbon} = 4.096 \text{ moles of Carbon}$$

Thus, comparing this amount to the 4.10 moles of carbon fed as ethanol at $t = 0$, the percentual difference in a mole carbon balance is 0.12% only. Furthermore, one can note that the combined moles of carbon containing products are 2.4×10^{-3} . This shows that one can assume with confidence that the photocatalytic hydrogen production takes place with a small overall variation of ethanol concentration as observed in Table B1.

Table B1. Cumulative ethanol formed/consumed at different irradiation times.

Time (h)	Concentration (M)
0	0.34171
1	0.33529
2	0.33714
3	0.34312
4	0.33742
5	0.33960
6	0.34110

Appendix C. H[•] and OH[•] Radicals Balance

Regarding the H[•] and OH[•] balances reported from experiments using 0.25 wt% Pd-TiO₂, after 6 h of irradiation, under near-UV light, in the Photo-CREC Water-II Reactor, the following can be considered:

$$H_{H_2}^{\bullet} = H_{2(g)} \left(\frac{2H^{\bullet} \text{ moles}}{1 \text{ mole of } H_2} \right)$$

At the end of the photocatalytic reaction, 5.055×10^{-3} moles of H₂ are generated from water splitting:

$$\begin{aligned} H_{H_2}^{\bullet} &= 0.8844 \mu\text{mole mL}^{-1} * 5716 \text{ mL} * \left(\frac{2H^{\bullet} \text{ moles}}{1 \text{ mole of } H_2} \right) \\ &= 1.01 \times 10^{-2} \text{ moles of } H_2^{\bullet} \end{aligned}$$

$$\begin{aligned} H_{CH_4}^{\bullet} &= 0.0018 \mu\text{moles mL}^{-1} * 5716 \text{ mL} * \left(\frac{4H^{\bullet} \text{ moles}}{1 \text{ mole of } H_2} \right) \\ &= 4.02 \times 10^{-5} \text{ moles of } H_2^{\bullet} \end{aligned}$$

$$\begin{aligned} H_{C_2H_6}^{\bullet} &= 0.0072 \mu\text{mole mL}^{-1} * 5716 \text{ mL} * \left(\frac{1H^{\bullet} \text{ mole}}{1 \text{ mole of } H_2} \right) \\ &= 4.12 \times 10^{-5} \text{ moles of } H_2^{\bullet} \end{aligned}$$

The total amount of H[•] radicals is:

$$H_{\text{Total}}^{\bullet} = H_{H_2}^{\bullet} + H_{CH_4}^{\bullet} + H_{C_2H_6}^{\bullet}$$

$$H_{\text{Total}}^{\bullet} = 1.019 \times 10^{-2} \text{ moles of } H^{\bullet}$$

Furthermore, the OH[•] formed as per stoichiometric requirements accounts for:

$$\begin{aligned} OH_{\text{Total}}^{\bullet} &= OH_{\text{intermediate}}^{\bullet} + OH_{CO_2 \text{ Total}}^{\bullet} + OH_{H_2O_2 \text{ (Formation)}}^{\bullet} \\ &\quad + OH_{\text{pH Change}}^{\bullet} \end{aligned}$$

With the “intermediate” subscript related to the OH[•] being consumed as:

$$\text{OH}_{\text{intermediate}}^{\bullet} = \text{OH}_{\text{Acetaldehyde gas}}^{\bullet}$$

$$\begin{aligned}\text{OH}_{\text{Acetaldehyde gas}}^{\bullet} &= 0.0086 \mu\text{moles mL}^{-1} * 5716 \text{ mL} * \left(\frac{2 \text{ OH}^{\bullet} \text{ moles}}{1 \text{ mole acetaldehyde}}\right) \\ &= 9.83 \times 10^{-5} \text{ moles OH}^{\bullet}\end{aligned}$$

Furthermore, and regarding the total OH[•] consumed, one can mention that it is required for the formation of CO₂, based on the following relation:

$$\text{OH}_{\text{CO}_2}^{\bullet} = \text{OH}_{\text{CO}_2(\text{gas})}^{\bullet} + \text{OH}_{\text{CO}_2(\text{dissolved})}^{\bullet}$$

The OH radicals in the gas and liquid phase are calculated as:

$$\text{OH}_{\text{CO}_2(\text{gas})}^{\bullet} = 0.00288 \mu\text{moles mL}^{-1} * 5716 \text{ mL} * \left(\frac{6 \text{ OH}^{\bullet} \text{ moles}}{1 \text{ mole CO}_2}\right) = 9.88 \times 10^{-5} \text{ moles OH}^{\bullet}$$

$$\text{OH}_{\text{CO}_2(\text{dissolved})}^{\bullet} = 3.29 \times 10^{-4} \mu\text{moles} * \left(\frac{6 \text{ OH}^{\bullet} \text{ moles}}{1 \text{ mole CO}_2}\right) = 1.97 \times 10^{-3} \text{ moles OH}^{\bullet}$$

The required total number of moles of OH radicals needed to form CO₂ are:

$$\text{OH}_{\text{CO}_2 \text{ Total}}^{\bullet} = 2.07 \times 10^{-3} \text{ moles OH}^{\bullet}$$

For the H₂O₂ formation, during the photocatalytic reaction, one should consider the OH radicals consumed and the 45% of hydrogen peroxide adsorbed on the photocatalyst:

$$\begin{aligned}\text{OH}_{\text{H}_2\text{O}_2(\text{Formation})}^{\bullet} &= 94,217 \mu\text{moles H}_2\text{O}_{2(\text{L})} * \left(\frac{2 \text{ OH}^{\bullet} \text{ moles}}{1 \text{ mole H}_2\text{O}_2}\right) * 1.45 \\ &= 2.73 \times 10^{-4} \text{ OH}^{\bullet} \text{ moles}\end{aligned}$$

Furthermore, considering the pH change as a function of the OH radicals:

$$\text{OH}_{\text{pH Change}}^{\bullet} = 7.81 \times 10^{-3} \text{ OH}^{\bullet} \text{ moles}$$

Thus, the total number of moles of OH radicals are the result of the following addition:

$$\text{OH}_{\text{Total}}^{\bullet} = \text{OH}_{\text{intermediate}}^{\bullet} + \text{OH}_{\text{CO}_2\text{Total}}^{\bullet} + \text{OH}_{\text{H}_2\text{O}_2(\text{Formation})}^{\bullet} + \text{OH}_{\text{pH Change}}^{\bullet}$$

$$\begin{aligned}\text{OH}_{\text{Total}}^{\bullet} &= 9.83 \times 10^{-5} + 2.07 \times 10^{-3} + 2.73 \times 10^{-4} + 7.81 \times 10^{-3} \\ &= 1.01 \times 10^{-2} \text{ moles OH}^{\bullet}\end{aligned}$$

In summary, and if one compares the number of moles of H[•] produced/consumed to the OH[•] moles involved in various product formation reactions (H[•] moles and OH[•] moles balance), after 6 h of irradiation, one can see that the mole balance closure with the hypothesized reactions is very good with a percentual error of 0.84% only.

Appendix D. Quantum Yield Calculation

As stated in Chapter 9, QY% can be defined as the number of moles of hydrogen radical produced per absorbed photons on the photocatalyst surface:

$$\%QY = \frac{\left[\frac{dN_{H\cdot}}{dt}\right]}{P_a} \times 100 \quad (D1)$$

where $\frac{dN_{H\cdot}}{dt}$ represents the rate of moles of hydrogen radicals formed and P_a stands for the moles of photons absorbed.

As well, and according to the Macroscopic Irradiation Energy Balances (MIEB) in the Photo-CREC Water Reactor II, P_a was calculated as follows:

$$P_a = P_i - P_{bs} - P_t \quad (D2)$$

where, P_i is the rate of photons reaching the reactor at the inner reactor surface, P_{bs} represents the rate of backscattered photons, and P_t is the rate of transmitted photons (Einstein s^{-1}).

A sample calculation is given below considering a hydrogen production rate of 0.2159 $\mu\text{mol}\cdot\text{cm}^{-3}\text{ h}$ using: (a) 0.25 wt.% Pd-TiO₂, (b) a photocatalyst concentration of 1.0g L⁻¹, (c) ethanol at 2.0 v/v%, (d) initial pH = 4 ± 0.05, (e) near-UV Light, (f) gas phase volume in the reactor of 5716 cm³ and (g) $P_a = 1.97 \times 10^{-06}$ Einstein/s.

$$QY_{H\cdot} = \frac{2 * \left(0.2159 \frac{\mu\text{mol}}{\text{cm}^3\text{h}}\right) * \left(6.022 \times 10^{23} \frac{\text{photon}}{\text{mol H}_2}\right) * \left(\frac{1\text{h}}{3600\text{s}}\right)}{1.97 \times 10^{-06} \text{ Einsteins/s}}$$

$$QY_{H\cdot} = 34.7\%$$

Curriculum Vitae

Name: Bianca Rusinque

Post-secondary Education and Degrees:

The University of Western Ontario
London, Ontario, Canada
2018-2021 PhD. Chemical Engineering

The University of Western Ontario
London, Ontario, Canada
2016-2018 MEdSc. Chemical Engineering

Universidad de America
Bogota, Colombia
2007-2015 B.A Petroleum Engineering

Universidad de America
Bogota, Colombia
2007-2013 B.A Chemical Engineering

Related Work Experience

Research/Teaching Assistant
The University of Western Ontario
2016-2021

Project Engineer
Aci Proyectos
2015-2016

Junior Project Engineer
Aci Proyectos
2014-2015

Trainee Development area
Cepsa Colombia
2013-2014

Trainee Research and Development
Carboquimica S.A.S
2011